

DEPARTAMENTO DE ASTROFISICA

Universidad de La Laguna

**Study of Very High Energy Gamma Ray Sources:  
Discovery of the Blazars PKS 1222+21 and  
1ES 1215+303**

Memoria que presenta  
Dña. Josefa Becerra González  
para optar al grado de  
Doctor en Ciencias Físicas.

INSTITUTO DE ASTROFISICA DE CANARIAS  
septiembre de 2011

Fecha de examen: Julio de 2011.

Directores de Tesis: Ramón J. García López & Markus Gaug & Carlos Delgado Méndez.

©Josefa Becerra González 2011

Parte del material incluido en este documento ya ha sido publicado en *The Astrophysical Journal Letters*.

*Por robar rayos de sol a los días nublados,  
por arrancar sonrisas siempre a tu paso,  
por acompañarme siempre en este sueño,  
y por una lista interminable de “por qués”...  
para tí, wely.*



# Contents

<b>Summary</b>	<b>1</b>
<b>Resumen</b>	<b>3</b>
<b>1 Introduction to Gamma Ray Astrophysics</b>	<b>5</b>
1.1 Cosmic rays . . . . .	5
1.2 Gamma rays . . . . .	6
1.2.1 Emission processes of $\gamma$ -rays . . . . .	6
1.2.2 Interaction and absorption processes . . . . .	9
1.3 Classes of Gamma-ray Emitters . . . . .	9
1.3.1 Galactic sources . . . . .	10
1.3.2 Extragalactic sources . . . . .	13
1.3.3 Dark Matter (DM) search . . . . .	14
<b>2 Active Galactic Nuclei</b>	<b>17</b>
2.1 The Unified Model and the structure of AGNs . . . . .	19
2.2 Jets . . . . .	22
2.2.1 Jet emission models . . . . .	24
2.3 Spectral Energy Distribution . . . . .	31
2.4 Gamma-ray absorption . . . . .	32
2.4.1 Background Radiation . . . . .	34
2.4.2 EBL Models . . . . .	37
2.4.3 Effects on the VHE spectra . . . . .	39
<b>3 Cherenkov Technique</b>	<b>41</b>
3.1 Air showers . . . . .	41
3.1.1 Electromagnetic air showers . . . . .	42
3.1.2 Hadronic air showers . . . . .	44
3.2 Emission from Air Showers . . . . .	47
3.2.1 Cherenkov radiation . . . . .	47
3.2.2 Fluorescence . . . . .	50
3.3 The Cherenkov imaging technique . . . . .	50

---

<b>4 The MAGIC telescopes</b>	<b>55</b>
4.1 The telescope structure and drive system . . . . .	55
4.2 The mirrors . . . . .	56
4.3 The camera . . . . .	57
4.4 The starguider . . . . .	59
4.5 The trigger . . . . .	59
4.6 The readout system . . . . .	60
4.7 The calibration system . . . . .	61
4.8 Observation modes . . . . .	63
4.9 The GRB alert system . . . . .	64
4.10 The KVA telescope . . . . .	64
<b>5 The Analysis Chain</b>	<b>65</b>
5.1 Data types . . . . .	65
5.2 Analysis scheme . . . . .	67
5.3 The signal extraction and calibration . . . . .	68
5.4 The image cleaning . . . . .	68
5.4.1 The standard cleaning . . . . .	69
5.4.2 The Sum cleaning . . . . .	70
5.5 Shower parametrization . . . . .	70
5.5.1 The image parameters . . . . .	71
5.5.2 The timing parameters . . . . .	72
5.6 Quality selection . . . . .	72
5.7 Calculation of stereoscopic parameters . . . . .	73
5.8 The stereo DISP reconstruction . . . . .	73
5.9 Gamma-hadron separation . . . . .	74
5.10 The energy reconstruction . . . . .	77
5.11 The signal search . . . . .	77
5.11.1 The <i>alpha</i> plot . . . . .	78
5.11.2 The $\theta^2$ ( $\theta^2$ ) plot . . . . .	78
5.11.3 The skymap . . . . .	79
5.12 Flux estimation . . . . .	79
5.13 The unfolding . . . . .	80
5.14 Spectral de-absorption . . . . .	80
5.15 The telescopes performance . . . . .	81
5.16 Systematic uncertainties . . . . .	82
<b>6 Discovery of the Blazar PKS 1222+21 in VHE <math>\gamma</math>-Rays</b>	<b>83</b>
6.1 Introduction . . . . .	83
6.2 The observations . . . . .	84
6.3 Data analysis and results . . . . .	84
6.3.1 The VHE spectrum . . . . .	86
6.3.2 Source variability . . . . .	89
6.4 Fermi data . . . . .	91
6.4.1 Spectral energy distribution of PKS 1222+21 . . . . .	92

---

6.5	Discussion of the results . . . . .	94
6.5.1	EBL limits . . . . .	94
6.5.2	Implications for jet emission models . . . . .	96
<b>7</b>	<b>Emission Model for PKS 1222+21</b>	<b>101</b>
7.1	Introduction . . . . .	101
7.2	A scheme of the model . . . . .	102
7.3	The spectral energy distribution . . . . .	104
7.4	Modelling of the spectral energy distribution . . . . .	105
<b>8</b>	<b>Discovery of VHE <math>\gamma</math>-Ray Emission from 1ES 1215+303</b>	<b>113</b>
8.1	Introduction . . . . .	113
8.2	The observations . . . . .	114
8.3	Data analysis and results . . . . .	116
8.3.1	The VHE spectrum of 1ES 1215+303 . . . . .	116
8.4	Study of variability from multi-frequency data . . . . .	119
8.5	An EBL study from the observations of 1ES 1215+303 . . . . .	127
8.6	Spectral energy distribution of 1ES 1215+303 . . . . .	134
<b>9</b>	<b>Observation of the BL Lac 1ES 1218+304 at VHE <math>\gamma</math>-Rays</b>	<b>139</b>
9.1	Introduction . . . . .	139
9.2	Observations . . . . .	140
9.3	Data analysis and results . . . . .	140
9.3.1	The VHE spectrum of 1ES 1218+304 . . . . .	143
9.4	Variability study in optical and VHE band . . . . .	146
9.5	An EBL study from the observations of 1ES 1218+304 . . . . .	150
<b>10</b>	<b>Conclusions and Outlook</b>	<b>155</b>
<b>11</b>	<b>Conclusiones y Trabajo Futuro</b>	<b>159</b>
<b>A</b>	<b>Appendix</b>	<b>163</b>
A.1	Searching the data . . . . .	163
A.2	Star . . . . .	164
A.3	Checking the data . . . . .	166
A.4	Quality selection . . . . .	167
A.5	Superstar . . . . .	169
A.6	MC selection . . . . .	170
A.7	Calculation of the DISP parameter . . . . .	171
A.8	Random Forest . . . . .	172
A.9	Look-up tables . . . . .	173
A.10	Melibea . . . . .	173
A.11	Signal search . . . . .	175
A.11.1	Odie . . . . .	175
A.11.2	Caspar . . . . .	180
A.11.3	Zinc . . . . .	180

A.12 Fluxlc . . . . .	182
A.13 Unfolding . . . . .	187
<b>List of Figures</b>	<b>204</b>
<b>List of Tables</b>	<b>207</b>
References . . . . .	209
<b>Bibliography</b>	<b>216</b>

# Summary

Very High Energy (VHE,  $E > 100$  GeV)  $\gamma$ -rays constitute still nowadays a largely unexplored observing window to the Universe. Due to the opacity of the Earth's atmosphere, the direct observation of these VHE  $\gamma$ -photons is not possible from ground installations. Moreover, observation from Space by satellites results unfeasible for energies higher than  $\sim 300$  GeV due to the low fluxes and, therefore, the necessity of large collection area detectors which cannot yet be launched into Space. This problem can be circumvented by making use of the relatively new Cherenkov technique as indirect method for measuring the VHE  $\gamma$ -rays from ground.

This work is devoted to the study of VHE  $\gamma$ -ray sources from ground using the Imaging Atmospheric Cherenkov Telescopes (IACT) MAGIC. Since autumn 2009, the two MAGIC telescopes have been operated in stereoscopic mode, with a sensitivity two times better than the previous single telescope observations. A detailed analysis of a large sample of data taken in this mode is presented, in particular Active Galactic Nuclei (AGNs) have been studied. The study of this type of sources in VHE  $\gamma$ -rays is of crucial importance in order to understand the emission mechanisms in their jets since most of their energy is released in the VHE band. AGNs are also important for the study of the Extragalactic Background Light (EBL) which imprints its characteristics on the VHE spectrum of distant sources, distorting the VHE spectra due to the absorption of the  $\gamma$ -photons by the interaction with the EBL photons leading to pair production of electrons and positrons. The study of the EBL has cosmological implications since it is composed of all redshifted emission from the different epochs of the Universe.

Only 46 AGNs have been detected up to now in the VHE range and the discovery of two of them is presented in this work. First, the discovery of the Flat Spectrum Radio Quasar (FSRQ) PKS 1222+21 close to the highest possible MeV/GeV flare state is presented. This detection was performed contemporaneously with a measurement by the *Fermi* satellite, resulting in a differential energy spectrum which can be described by a simple power-law ranging from  $\sim 3$  GeV up to 400 GeV. A cut-off can be excluded for energies lower than 130 GeV. This fact, together with the fast variability on a time scale of  $\sim 10$  minutes detected by MAGIC, heavily challenges the current emission models for FSRQs. In chapter 7, an improved emission model for this source is proposed, which consists of two emitting regions: one standard region modeled as a sphere whose diameter corresponds to the section of the jet, and a smaller and compacter region inside the jet travelling at different velocity than the rest of the surrounding jet matter.

Later, the first detection of the blazar 1ES 1215+303 in VHE  $\gamma$ -rays is presented in chapter 8. A multi-frequency study of its variability has been carried out, showing that the emission from this object can be modeled using the standard Self-Synchrotron Compton model which typically is used to explain the emission from BL Lacs.

The last chapter of this thesis is devoted to a long-term study of the blazar 1ES 1218+304, which is found in the same FoV as 1ES 1215+303. For the first time, the detection of two sources in the same MAGIC FoV was possible, and a non-standard analysis had to be performed. 1ES 1218+304 has been detected in a steady state, compatible with previous observations.

For all these sources, the present generation of EBL models has been tested. Despite different approaches used in most of the models, all the tested currently accepted EBL models result compatible with the observations presented in this thesis.

In the appendix, a detailed explanation on how to analyze the stereoscopic MAGIC data can be found.

## Objetives

The main goals of this thesis is the study of VHE  $\gamma$ -rays sources making use of the MAGIC stereoscopic system. This work has been mainly focused on the following issues:

- Test and understand the first stereoscopic MAGIC data.
- Make use of the improved capabilities of the MAGIC telescopes in stereoscopic mode to discover new VHE  $\gamma$ -ray sources, in particular AGNs.
- Test the present jet emission models for AGNs.
- Test the present generation of EBL models.

UNESCO codes: 2101.03, 2101.04, 2101.09

# Resumen

Los rayos  $\gamma$  de muy alta energía (en inglés “Very High Energy” -VHE-, con energías  $>100$  GeV) son todavía hoy en día una ventana de observación del Universo poco explorada. Debido a la opacidad de la atmósfera terrestre, la observación directa de estos fotones de VHE no es posible desde instalaciones terrestres. Además, la observación desde el Espacio haciendo uso de satélites resulta inviable para energías mayores de  $\sim 300$  GeV debido a que el flujo es tan bajo que se necesitarían detectores con grandes áreas colectoras que no pueden ser todavía puestos en órbita. Este problema puede evitarse haciendo uso de la técnica Cherenkov, relativamente nueva, como método indirecto de medida de rayos  $\gamma$  de VHE desde tierra.

Este trabajo está dedicado al estudio de fuentes de rayos  $\gamma$  de VHE desde tierra usando los *Imaging Atmospheric Cherenkov Telescopes (IACT)* MAGIC. Desde otoño de 2009, los dos telescopios MAGIC han operado en modo estereoscópico, con una mejora un factor dos en sensibilidad comparado con las observaciones previas con un único telescopio. Un análisis detallado de una amplia muestra de datos observados en este modo son presentados en este trabajo, en particular se han estudiado Galaxias con Núcleos Activos (AGNs según sus siglas en inglés). El estudio de este tipo de fuentes en rayos  $\gamma$  de VHE es crucial en el entendimiento de los mecanismos de emisión en sus *jets* o chorros, puesto que la mayor parte de su energía es emitida en la banda VHE. Los AGNs son también muy importantes en el estudio de la Luz Extragaláctica de Fondo (EBL según sus siglas en inglés), la cual deja huella de sus características en el espectro VHE de fuentes lejanas, distorsionando los espectros VHE debido a la absorción de fotones  $\gamma$  como resultado de la interacción con fotones del EBL, induciendo la creación de pares de electrones y positrones. El estudio del EBL tiene implicaciones cosmológicas puesto que está constituida por la emisión integrada en las diferentes épocas del Universo.

Sólo 46 AGNs han sido detectados hasta ahora en el rango de VHE y el descubrimiento de dos de ellos se presenta en este trabajo. En primer lugar, se presenta el descubrimiento del *Flat Spectrum Radio Quasar (FSRQ)* PKS 1222+21 durante un estado de alta actividad cercano a la máxima actividad posible para este objeto, en la banda MeV/GeV. Esta detección fue llevada a cabo contemporáneamente con una medida por el satélite *Fermi*, resultando un espectro diferencial de energía que puede ser descrito por una ley de potencias desde 3 GeV hasta 400 GeV. Se puede excluir una caída exponencial en el espectro para energías menores de 130 GeV. Este hecho, junto con la rápida variabilidad detectada por MAGIC en una escala temporal de  $\sim 10$  minutos, desafía fuertemente los actuales modelos

de emisión para FSRQs. En el capítulo 7, se propone un modelo de emisión mejorado para esta fuente que consiste en dos regiones de emisión: una región estándar modelada como una esfera cuyo diámetro corresponde a la sección del *jet*, y una región más pequeña y compacta dentro del *jet* viajando a una velocidad diferente que el resto del la materia circundante.

A continuación, la primera detección del blazar 1ES 1215+303 en rayos  $\gamma$  de VHE se presenta en el capítulo 8. Se ha llevado a cabo un estudio multifrecuencia de su variabilidad, mostrando que la emisión de este objeto puede ser modelada usando el modelo estándar Self-Synchrotron Compton que es normalmente usado para explicar la emisión en BL Lacs.

El último capítulo de esta tesis está dedicado a un estudio a largo plazo del blazar 1ES 1218+304, el cual se encuentra en el mismo campo de visión que 1ES 1215+303. Por primera vez, ha sido posible la detección de dos fuentes en el mismo campo de visión de MAGIC, y un análisis no estándar ha sido aplicado. 1ES 1218+304 ha sido detectado en estado estacionario, compatible con observaciones previas.

Para todas estas fuentes, la generación actual de modelos de EBL han sido testeados. A pesar de que diferentes enfoques han sido usados en la mayoría de ellos, todos los modelos actualmente aceptados que han sido testeados resultan compatibles con las observaciones presentadas en esta tesis.

En el apéndice, se encuentra una explicación detallada de cómo analizar datos estereoscópicos tomados con los telescopios MAGIC.

## Objetivos

El principal objetivo de esta tesis es el estudio de fuentes de rayos  $\gamma$  de VHE haciendo uso del sistema estereoscópico MAGIC. Este trabajo se ha enfocado principalmente en las siguientes cuestiones:

- Testear y entender los primeros datos de MAGIC observados en modo estereoscópico.
- Hacer uso de la mejora en las capacidades de los telescopios MAGIC en modo estereoscópico para descubrir nuevas fuentes de rayos  $\gamma$  de VHE, en particular AGNs.
- Testear los actuales modelos de emisión para *jets* en AGNs.
- Testear la actual generación de modelos de EBL.

Códigos UNESCO: 2101.03, 2101.04, 2101.09

---

# 1

---

## Introduction to Gamma Ray Astrophysics

The Earth is continuously bombarded by charged particles, photons and neutrinos covering a wide energy range. These particles mainly consist of protons, electrons and atomic nuclei, with a small contribution of gamma rays, and receive the name of cosmic rays. When these high energy particles reach the Earth's atmosphere, they start to interact with the air molecules and produce showers of particles, as will be described in Chapter 3. Due to the interaction with the atmosphere, only products of the interactions can be found at ground level. Therefore, direct measurements can only be performed in Space, using satellites. This is possible up to an energy range of about 300 GeV, since for higher energies the fluxes decrease with energy and the necessary collection area of the detectors would be too large and heavy and cannot be launched into Space. Several indirect methods have been developed to study the cosmics rays of high energy with the use of ground based-experiments, in particular this thesis makes use of the *Cherenkov technique* in order to study  $\gamma$ -rays. Since both the discovery of  $\gamma$ -rays and the *Cherenkov technique* are closely related to cosmic rays, I will introduce phenomenology of the cosmic rays before focussing on  $\gamma$ -ray physics.

### 1.1 Cosmic rays

The origin extraterrestrial of the cosmic rays were discovered in 1912 by Victor Hess who, onboard a balloon detected permanent ionization of the atmosphere (Hess, 1912). Most of the cosmic rays ( $\sim 98\%$ ) are nuclei, while there is  $\sim 2\%$  of free electrons and positrons. About 89% of the nuclei are hydrogen atoms, 10% is helium and the resting 1% is due to heavier nuclei where essentially all the chemical elements are present. There is an overabundance of some elements with respect to the composition of the Solar System, such as Li, Be or B which shows that the nucleosynthesis of cosmic rays and the Solar System was different and that cosmic rays should originate from outside the Solar System. There is also a neutral component composed of  $\gamma$ -rays, neutrons and neutrinos. For the study of cosmic rays,  $\gamma$ -rays are preferred since neutrons typically don't reach the Earth due to their short life time and the detection of neutrinos is very difficult because of their very small interaction cross-sections. The  $\gamma$ -ray component is essential for the study of the origin of the cosmic rays

since they are not charged and don't interact with the galactic and intergalactic magnetic fields during their travel, thus in contrast to the all charged cosmic rays they point directly to their origins.

Regarding the spectrum, cosmic rays cover a very wide energy range, it have been measured from  $\sim 10^8$  to  $\gtrsim 10^{20}$  eV. At lower energies, the solar wind interacts with the charged particles. As shown in Fig. 1.1, the most powerful accelerator built on Earth (the Large Hadron Collider -LHC-) can only accelerate particles up to  $\sim 10^{13}$  eV while cosmic rays can reach much higher energies. This means that cosmic rays have to be created or at least accelerated in very powerful accelerators. Different sources have been suggested, while their individual contributions are still under debate: Supernova Remnants, Gamma-ray Bursts or Active Galactic Nuclei. It is important to note in Fig. 1.1 that there are changes in the spectral slope (the so-called knee at  $\sim 10^{15}$  eV and the ankle at  $\sim 10^{18}$ - $10^{19}$  eV) which suggest that different parts of the spectrum probably are due to different acceleration processes from different types of sources. Given the large energy range covered by the spectrum, its study requires a joint effort from a lot of different techniques and instruments, e.g. PAMELA satellite (Picozza et al., 2011) and KASCADE-Grande experiment (Apel et al., 2010).

The most energetic cosmic rays are called *Ultra-High Energy Cosmic Rays* (UHECR) which present a very low flux (below the ankle) and interact with the Cosmic Microwave Background (CMB) causing the GreisenZatsepinKuzmin (GZK) cut-off at  $\sim 10^{20}$  eV (Greisen, 1966; Zatsepin and Kuzmin, 1966).

## 1.2 Gamma rays

Gamma rays (or  $\gamma$ -rays) is the name received by the photons with frequencies higher than  $10^{20}$  Hz or 512 keV. They are named Very High Energy  $\gamma$ -rays if the photons are more energetic than  $\sim 100$  GeV. The principal emission and absorption processes of  $\gamma$ -rays will be explained hereafter.

### 1.2.1 Emission processes of $\gamma$ -rays

Mainly there are five processes which are responsible for the production of  $\gamma$ -rays (see Fig. 1.2):

- **Bremsstrahlung:** The emission of radiation by this process is due to the interaction by a moving charged particle with an electric field, created by the presence of a charged nucleus. It consists in slowing down the particles velocity and deviating its trajectory. The deceleration depends on the intensity of the electric field and the distance to the nuclei. The spectrum emitted by a population of electrons which follows a power-law and which are affected by *Bremsstrahlung*, results in a power-law with the same spectral index as the one of the accelerated particles. This process is typically responsible for X-ray emission in the accretion disk of an Active Galactic Nucleus and can produce  $\gamma$  photons up to  $\sim 100$  MeV. This mechanism is also operative in the development of particle showers in the Earth's atmosphere. The importance of this effect depends strongly on the density of the medium, the denser the more important the effect.

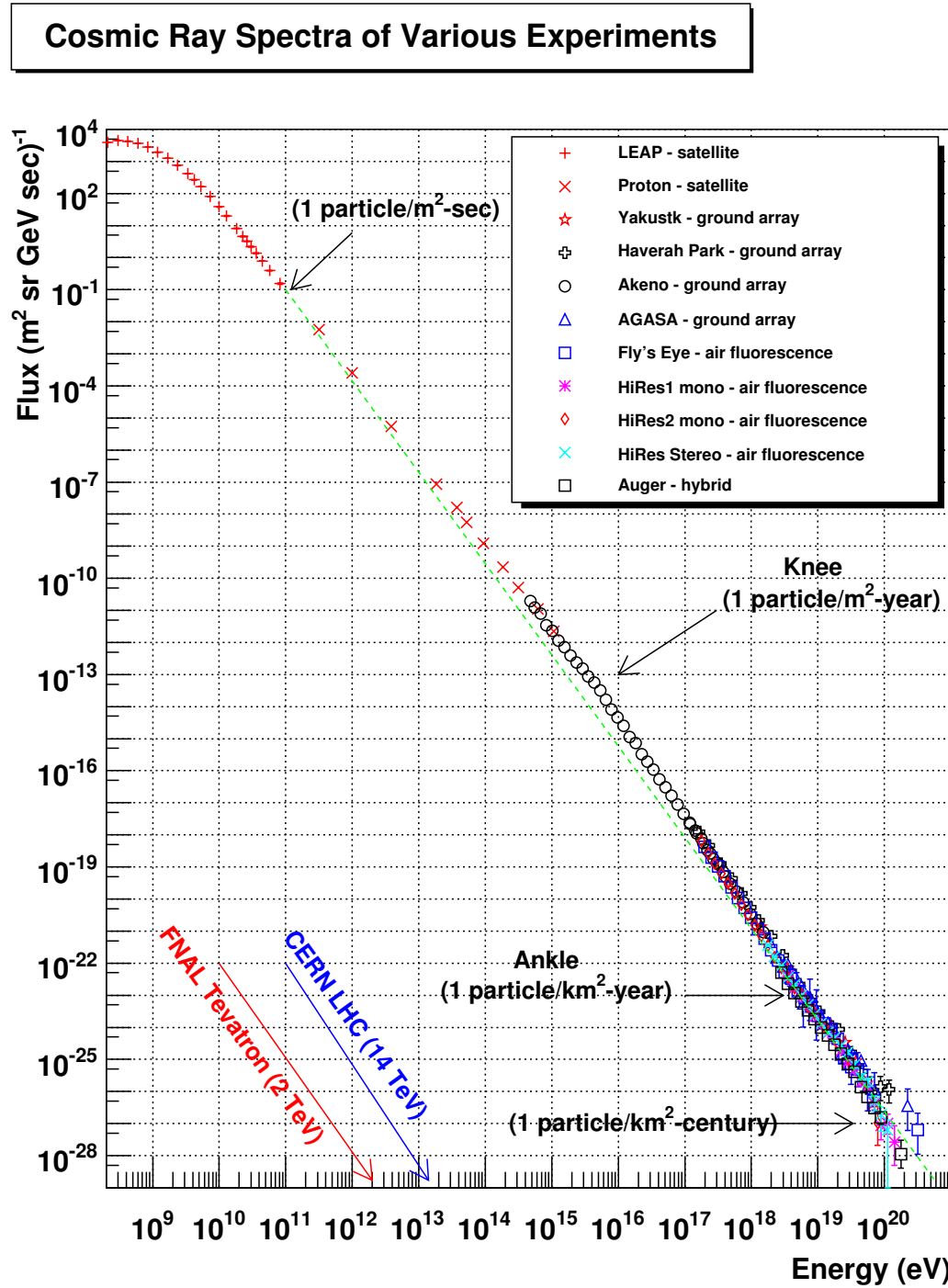


Figure 1.1: All particle cosmic rays spectrum, taken from <http://www.physics.utah.edu/~whanlon/spectrum.html>.

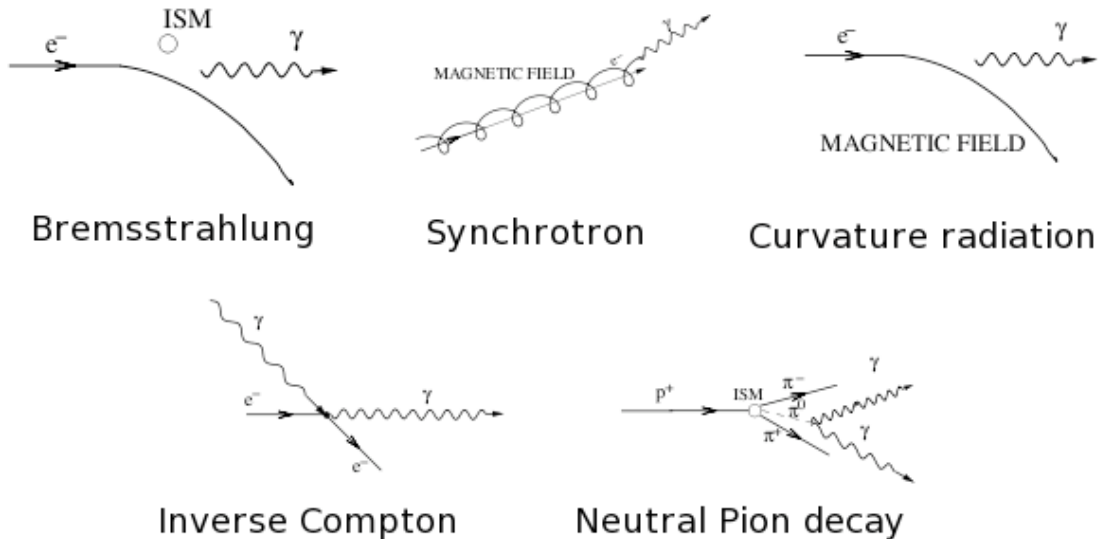


Figure 1.2: Sketch of the main  $\gamma$ -ray emission processes.

- **Synchrotron radiation:** This type of radiation occurs when a charged particle travels within a magnetic field producing an acceleration which forces the particle to rotate around the magnetic field lines. The spectrum usually covers from radio to X-rays. However, UHECRs can also produce  $\gamma$ -rays. A detailed discussion of this process for the case of Active Galactic Nuclei (AGNs) will be presented in Sec. 2.2.1.
- **Curvature radiation:** This process affects charged particles crossing very strong magnetic fields of the order of  $10^8\text{-}10^9$  G. In this case, instead of rotating around the magnetic field lines, the charged particles tend to follow the lines. Thus, if the magnetic field lines are curved the particles will be accelerated and emit as in case of *Synchrotron* radiation. The electrons and positrons emit in the GeV range, this type of emission is important for sources like pulsars with strong magnetic fields.
- **Inverse Compton (IC) scattering:** The interaction between very energetic particles, like relativistic electrons or protons, with low energy photons via IC scattering produces a transfer of kinetic energy from the charged particle to the photon. Typically for astrophysical sources, the emission peak by this mechanism lies in the GeV-TeV range, leading to  $\gamma$ -ray emission. A particular modelling of this process in the case of AGNs is presented in Sec. 2.2.1.
- **Neutral Pion decay:** As a result of collisions between protons and energetic nuclei, pions can be created. They can be charged ( $\pi^+, \pi^-$ ) or neutral ( $\pi^0$ ), being produced with the same probability each of them. However, the life times and the decay chains are different. While  $\pi^+$  and  $\pi^-$  decay with a typical life time of  $\sim 2.6 \cdot 10^{-8}$  s in a leptonic chain producing muons and neutrinos,  $\pi^0$  have a shorter life time of  $\sim 10^{-16}$  s

(which means they will mostly decay before interacting with the medium) and the most probable decay is the creation of two photons :

$$\pi^0 \rightarrow \gamma + \gamma \quad (P = 99\%) \quad (1.1)$$

$$\pi^0 \rightarrow e^- + e^+ + \gamma \quad (P = 1\%) \quad (1.2)$$

The emitted two photons have a low energy limit of  $\sim 70$  MeV in the observer rest frame (half of the  $\pi^0$  mass at rest) which means, accelerated  $\pi^0$  are a powerful source of  $\gamma$  photons.

### 1.2.2 Interaction and absorption processes

Photons are not affected by magnetic fields but can interact and be absorbed in other ways:

- **Photoelectric absorption:** In the interaction between photons and atoms, the photon energy can be absorbed by an electron of the atom which in turn gets kicked off the atom. It is the dominant process for radiation with energies below  $\sim 100$  keV.
- **Compton scattering:** On the contrary to *IC scattering*, in the *direct Compton scattering* the interaction between low energetic particles and high energy photons leads to a total or partial absorption of the photon energy by the particle. The characteristics of the interaction is the same as that of the IC scattering but in this case instead of an increase of the photon energy a reduction of its energy is achieved. This process is important from  $\sim 0.1$  MeV to few MeV.
- **Pair creation:** Because of the interaction of two photons, an electron-positron pair ( $e^- e^+$ ) is created, that is to say, this process is able to produce matter and antimatter from radiation. The interaction is only possible if the sum of the photon energies amounts at least the rest mass of the  $e^- e^+$  pair. Most of the absorption of  $\gamma$ -rays from far sources is due to pair creation processes because of the Extragalactic Background Light, which is able to interact with the emitted photons and absorb them. More explanations will be found in Sec. 2.4.

## 1.3 Classes of Gamma-ray Emitters

There are different objects in the Universe able to produce  $\gamma$ -rays. Depending on their nature and characteristics, the dominant emission process as well as the interaction and absorption will depend strongly on the medium, its density, the magnetic field, the involved velocity fields, etc. Thus,  $\gamma$ -rays are very important in order to study these huge physics laboratories which can not be recreated on Earth due to the high energetic processes involved.

Fig. 1.3 shows the distribution in the sky of all sources detected up to now in the VHE spectral range. Several unidentified sources have been detected in VHE without a counterpart. The most important types of  $\gamma$ -ray emitters will be briefly described below.

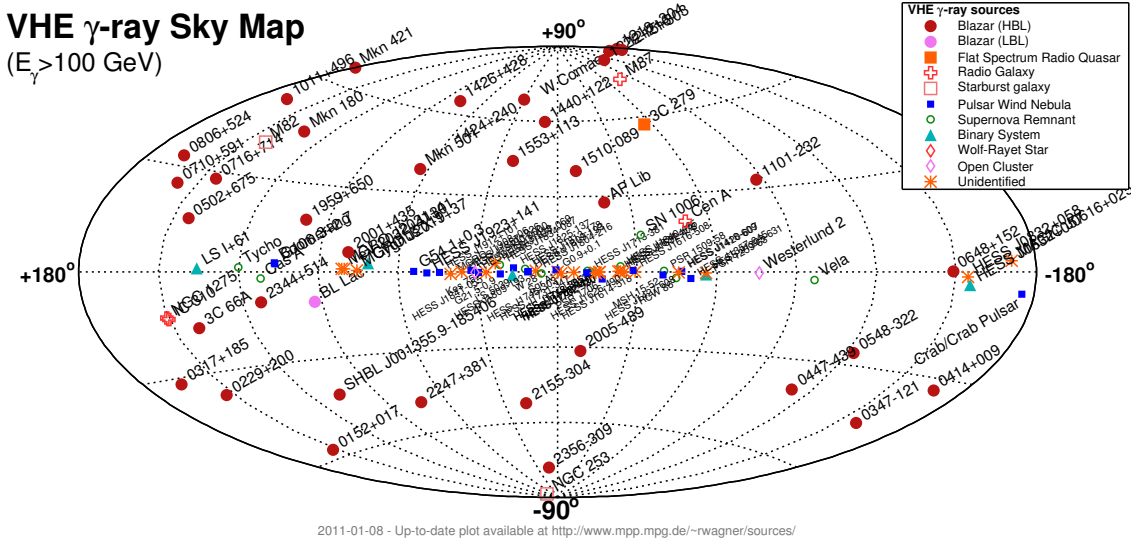


Figure 1.3: Sky map of discovered VHE sources, taken from <http://www.mpp.mpg.de/~rwagner/sources>.

The section will be divided in three parts, galactic sources, extragalactic sources and dark matter searches. The main differences come from the particular environments producing different leading emission and absorption processes. For example, in case of galactic sources the absorption due to the interaction with EBL is negligible while it is an important issue in case of extragalactic emitters. This means that galactic sources can be detected at higher energies than extragalactic ones. However, the low energy parts of the spectra from galactic sources are more contaminated by the emission from the galactic center where most of the galactic sources are concentrated, as detected in the HESS galaxy plane scan (Aharonian et al., 2006c), see Fig. 1.4.

### 1.3.1 Galactic sources

## Galactic Center

Gamma-rays coming from the Galactic Center (GC) have been detected as a steady flux. The nature of the emitter is still unknown, but there are several candidates as the Black Hole *Sgr A\** which produces jets where the  $\gamma$ -rays could be emitted (Aharonian et al., 2009a). However, this hypothesis is unlikely due to the steady flux measured. Other possibilities are Supernova Remnants, massive stellar clusters or Pulsars.

## Supernova Remnants

Supernovae Remnants are the final stage of a super-massive star. Once such a star finishes the nuclear processes in its core, the central part of the star collapses creating a compact object. Depending on the mass, it will evolve into a Pulsar or a Black Hole while the outer layers are violently expelled to the surrounding Interstellar Medium (ISM). During the explosion of the super-massive star, the supernova, shock waves are able to accelerate

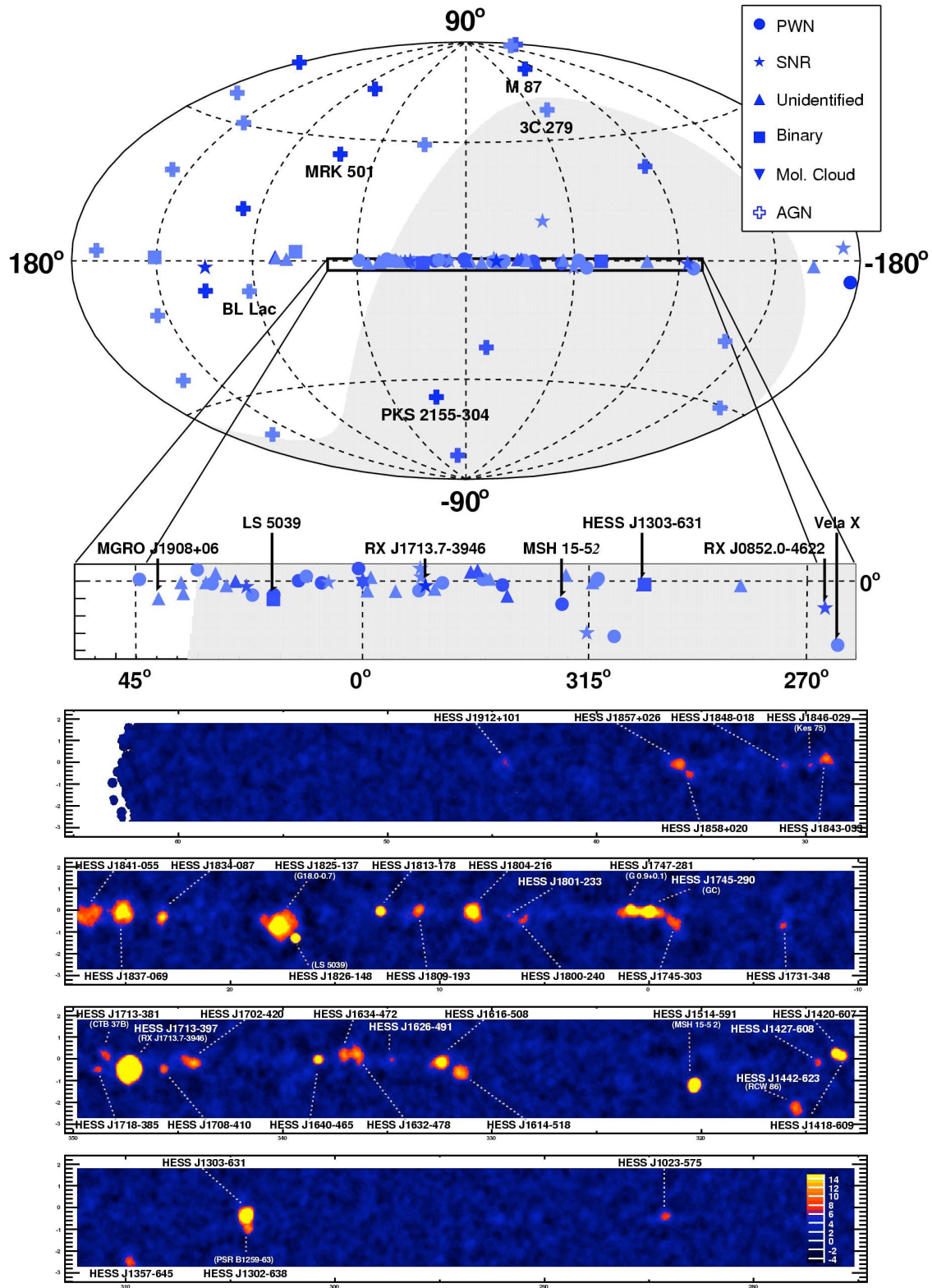


Figure 1.4: VHE survey of the galactic plain by HESS (Hinton and Hofmann, 2009).

particles which reach relativistic velocities. The principal  $\gamma$ -ray emission process in this scenario is the *inverse Compton scattering* due to the interaction between the relativistic charged particles and the synchrotron photons, the called *Syncrhotron-self Compton* (see Sec. 2.2.1 for more details). Supernova remnants are considered the major source of galactic cosmic rays.

### Pulsars and Pulsar Wind Nebulae

Pulsars are very compact objects, neutron stars and possible remainders of a supernova explosion. They rotate very fast and their extremely strong magnetic fields produce an effect of collimation of the emission along the magnetic field axis. In general, this axis is different from the rotational axis and thus the emission can only be observed when the magnetic field axis is pointing to the Earth. This occurs at the rotation frequency of the pulsar and the emission is then visible as a pulsating signal. The typical rotation frequencies range covers from  $\sim 0.1$  to  $\sim 10^9$  Hz. Pulsars are believed to produce the strongest magnetic fields in the universe. MAGIC detection from the Crab Pulsar (Aliu et al., 2008) ruled out the polar cap model.

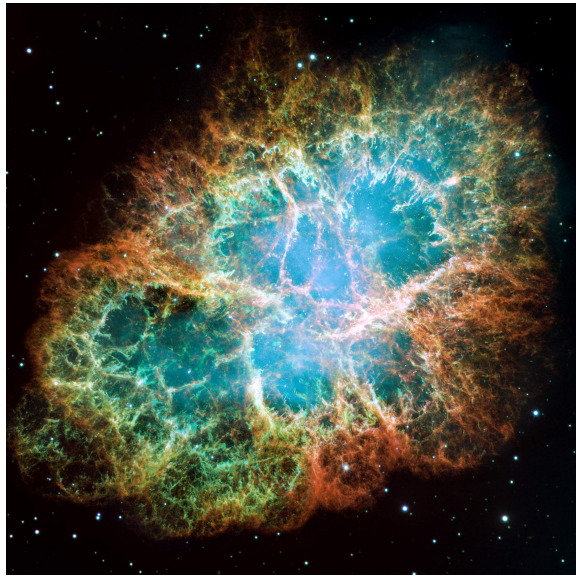


Figure 1.5: The Crab Nebula is one of the most studied and strongest VHE  $\gamma$ -ray emitters in the sky. Here, a picture taken from the Hubble Space Telescope in the optical is shown. Taken from <http://hubblesite.org/newscenter/archive/releases/2005/37/image/a/>.

A pulsar wind nebula is a nebula powered by the pulsar wind of a pulsar. At the early stages (first few thousands of years) of their evolution, pulsar wind nebulae are often found inside the shells of supernova remnants. However, pulsar wind nebulae have also been found around older pulsars whose supernova remnants have disappeared. Fig. 1.5 shows a picture, taken in the optical, of the most important representative of this class of objects, the Crab

Nebula which is typically used as candle in the VHE range<sup>1</sup>.

### Gamma-ray binary systems

This type of objects typically is composed of a very compact object like a Black Hole or a neutron star and a companion star. There are two different approaches in the VHE  $\gamma$ -ray emission theories. The first one considers the compact object as a structure similar to the AGN accretion zone, called *microquasar* (see Fig. 1.6), and the emission mechanics would be rather similar to the AGN case, but at much smaller scales. The second approach assumes the emission is produced in a system composed of a pulsar and massive star, where the  $\gamma$ -rays are generated in the shock from the pulsar wind interacting with the massive companion.

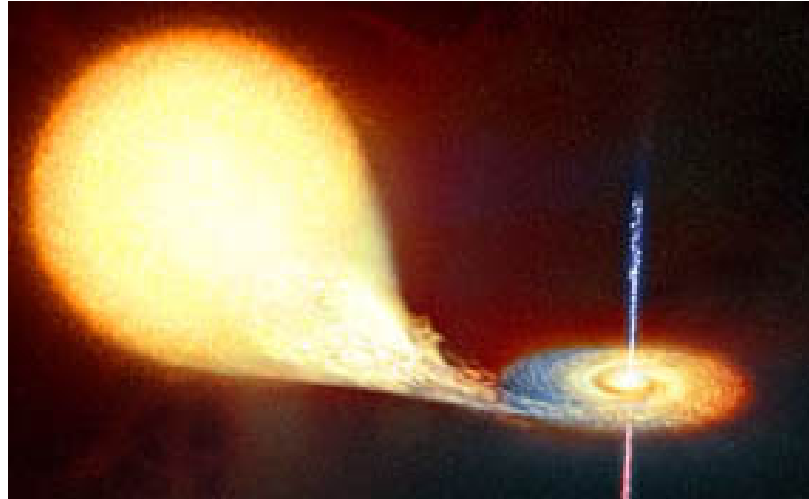


Figure 1.6: Artistic view of a microquasar. Taken from <http://www.daviddarling.info/encyclopedia/M/microquasar.html>.

### Diffuse $\gamma$ -rays

They are supposed to stem from the interaction between the cosmic rays and the molecular and dusty clouds in the galactic plane. The hadronic interactions would result in the creation of  $\pi^0$  particles which later decay in  $\gamma$ -rays.

---

<sup>1</sup>Even if historically the Crab Nebula has always shown a steady flux and could be used as *candle*, recently, flares have been detected in  $\gamma$ -rays (Tavani et al., 2011; Abdo et al., 2011). Nevertheless, the variability has not been detected in the VHE range so that the preferred *Cherenkov telescope candle* is still usable (Mariotti, 2010c; Ong, 2010b).

### 1.3.2 Extragalactic sources

#### Active Galactic Nuclei (AGNs)

An AGN is a compact region at the centre of a galaxy that has a much higher luminosity than the rest of the galaxy over at least some portion, and possibly all, of the electromagnetic spectrum. The radiation from AGNs is believed to be a result of the accretion of mass by a supermassive Black Hole. AGNs are the most luminous persistent sources of electromagnetic radiation in the Universe. Since this work is a dedicated study of AGNs, a modelling of this type of sources can be found in Chapter 2.

#### Starburst Galaxies

The main feature of a starburst galaxy is the exceptionally high rate of star formation, compared to the usual star formation rate seen in most galaxies. The rate of supernova explosions is very high there, making it the main candidate for the acceleration of cosmic rays. The observed VHE  $\gamma$ -rays are most probably the secondary products of decaying pions, created by the collisions of cosmic rays with interstellar medium nucleons.

#### Gamma-ray bursts (GRBs)

Gamma-ray bursts are flashes of gamma rays associated with extremely energetic explosions that have been observed in distant galaxies. They are randomly distributed in the sky and can not be predicted in advance. They are the most luminous electromagnetic events known to occur in the universe. The initial burst in  $\gamma$ - and X-rays is usually followed by a longer-lived *afterglow* emitted at longer wavelengths. These sources have not been detected so far in the VHE range even if the models predict VHE  $\gamma$ -ray emission. They are difficult to catch mainly due to two reasons:

- The durations of the bursts are very short, they can vary from milliseconds to several minutes (Horváth, 2002). Typically they are divided into short and long bursts. Since the VHE range can only be observed by infrastructures on Earth and usually these are heavy instruments due to the needed large collection area (see Chapter 3) the repositioning time of the instruments is of the order of the explosion event lifetime. Nevertheless, even during the *afterglow* emission part of the VHE  $\gamma$ -ray emission is expected. For that reason a special telescope design is needed as in the case of the MAGIC telescopes (see Sec. 4.9).
- The expected energy release by the models, in the VHE range is just at the edge of the ground based instruments capabilities. An important requirement is the low energy threshold of the experiment, especially important is the energy range below 100 GeV (Aleksić et al., 2010a).

The origin of gamma-ray bursts is still unknown, the long duration bursts are thought to be produced by the core collapse of massive stars, while the short ones could be associated to merger events between two neutron stars.

### **1.3.3 Dark Matter (DM) search**

Some DM models predict VHE gamma-ray emission due to the self-annihilation of DM particles (eg. neutralino predicted by the Super-Symmetric (SUSY) theories). As the universe consists to about one third of up-to-now invisible dark matter, it is believed that these particles form giant clumps, associated with the accumulation of ordinary baryonic matter. The most promising candidates are the dwarf spheroidal galaxies and clusters of galaxies. Despite important efforts have been made, the VHE  $\gamma$ -ray emission remains undetected. Anyhow, the predicted fluxes by SUSY are so low that most of the possible models cannot be ruled out by the non-detection, since the sensitivity of the current generation of Cherenkov and space-born telescopes is not good enough yet.



---

# 2

---

## Active Galactic Nuclei

Some galaxies have very luminous nuclei, which typically produce more radiation than the entire rest of the galaxy in the full or a large part of the electromagnetic spectrum, from radio to  $\gamma$ -rays. These compact regions at the center of galaxies are called Active Galactic Nuclei (AGNs). The radiation from AGNs is believed to be a result of the accretion of mass by a super-massive Black Hole (SMBH) at the centre of the host galaxy. There are correlations between the Black Holes (BH) masses and some quantities of the host galaxies as their luminosity, their velocity dispersion, light concentration, the size of their dark matter haloes or the core radio emission (Ferrarese and Ford, 2005). These evidences point to a common evolution of the central BH (typical masses are  $\sim 10^6\text{-}10^9 M_\odot$ ) and their host galaxies.

In the standard picture, it is assumed that every galaxy center hosts a BH which can be in quiescent status, not showing any activity (this applies to 99% of the galaxies). On the contrary, 1% of the galaxies have an active BH in their center. According to the best estimations, AGNs remain active for up to  $\sim 10^7$  years, which means that an enormous amount of material must be consumed in order to maintain their luminosities. Nevertheless, they are very variable, increasing quite often their luminosities, so-called *flares*, which can last from minutes to days or weeks in the entire or in a part of the electromagnetic spectrum. AGNs are important in the understanding of the evolution of the Universe since they are the most luminous persistent sources of electromagnetic radiation, hence together with GRBs they can be used for studies of distant objects and the behaviour of their distant representatives provide powerful tests for the understanding of the evolution of the Universe.

All AGNs share three main characteristics: they are extremely compact, emit in the whole electromagnetic range and they are very massive. Apart from that, usually the different kinds of AGNs present spectral differences. As represented in Fig. 2.1, usually AGNs are classified in two groups according to their radio emission. Only few AGNs shows important radio emission, the so-called *radio-loud* AGNs, otherwise, they are named *radio-quiet*. This first classification is performed using the *radio-loudness* parameter ( $R$ ) which is defined as  $R = F_5/F_B$  where  $F_5$  represents the radio flux at 5 GHz and  $F_B$  the optical flux in the B band. The R distribution for a sample of AGNs show a clear bimodal distribution (Kellermann et al., 1989), the two peaks are located at  $R \sim 1$ , where most of the

galaxies are concentrated, and  $R \sim 100$  populated with not more than 10-20% of the sample.

As shown in Fig. 2.1, the next divisions are based on the appearance of the galaxy and later on the flux and the features of the optical spectra. *Radio-quiet* galaxies are divided depending on the optical spectral line widths. Blazars are very compact sources which emit throughout the whole electromagnetic spectrum with highly variable fluxes. They are divided into Flat Spectrum Radio Quasars (FSRQs), which present an optical spectrum with clear emission lines, while the optical spectrum of BL Lac objects typically display weak lines (if any) and is dominated mainly by continuum emission. Typically, the Spectral Energy Distribution (SED) from Blazars is composed of two bumps: one at low energies (UV to X-ray) and a second one at high energies (X-ray to  $\gamma$ -ray range). According to the peak frequencies, BL Lacs can be further divided into High, Intermediate and Low-peaked (HBL, IBL and LBL) BL Lacs which take into account the peak frequency of the synchrotron part. Despite of this apparent great variety, it is believed that all AGNs represent the same basic scenario changing the angle at which they are observed, the mass of the BH, the accretion rate and the interstellar medium, among other characteristics. This scenario is called the *Unified model* and will be discussed later in Sec. 2.1. Since this thesis is based on the study of the Flat Spectrum Radio Quasar PKS 1222+216 and the BL Lac objects 1ES 1215+303 and 1ES 1218+304, all of which belong to the Blazar type, I will concentrate on these two types of objects from here on.

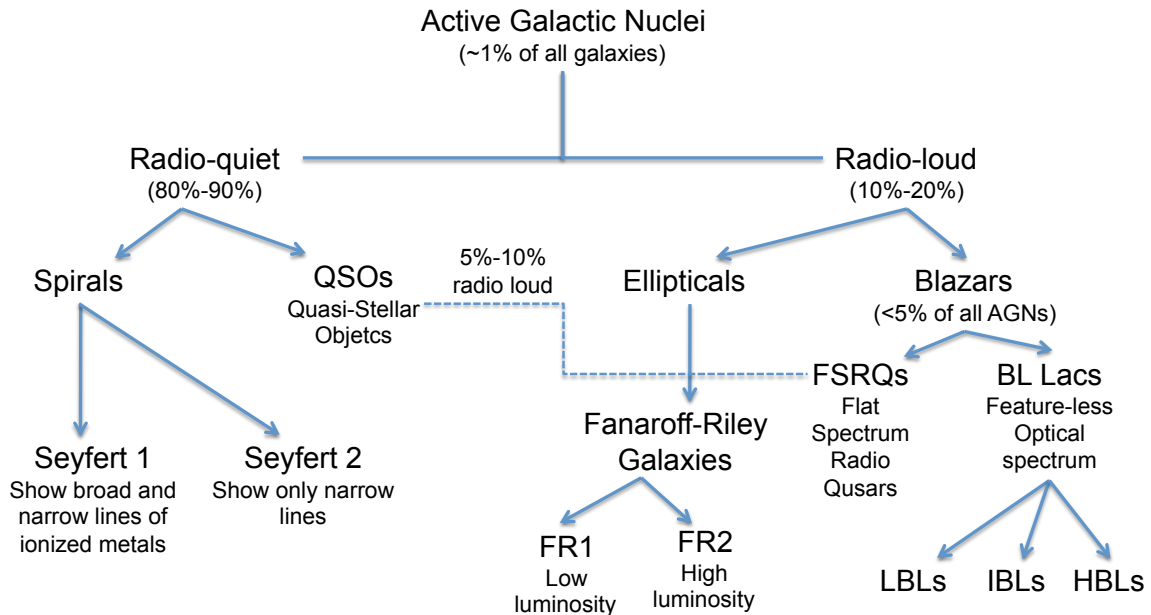


Figure 2.1: AGN classification scheme.

In 1992, the first BL Lac was detected in VHE  $\gamma$ -rays, namely Markarian 421 (Punch et al., 1992), their number has constantly increased since then, due to the new generation of sensitive Cherenkov telescopes collaborating with  $\gamma$ -ray satellites like *Fermi*. Up to now, 46 VHE  $\gamma$ -ray AGNs have been discovered, a chronologically ordered catalogue is shown

in Table 2.1 and their distribution on the sky in Fig. 2.2. Most of them are of type HBL, which is not surprising since, due to their nature, LBL and FSRQ are more difficult to observe in the VHE band, given that their fluxes at these energies are much lower.

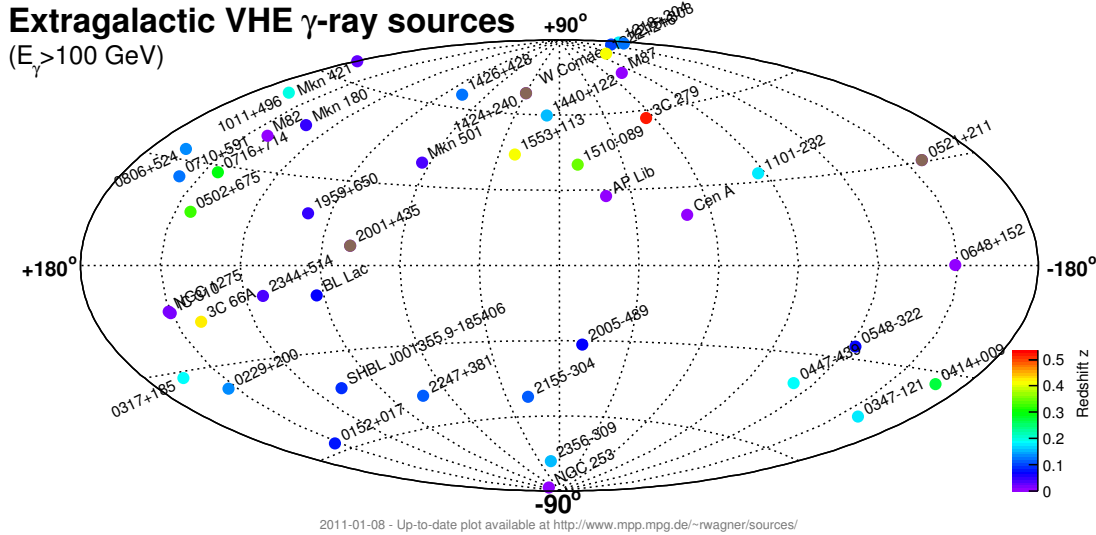


Figure 2.2: Skymap of the extragalactic VHE  $\gamma$ -ray emitters, taken from <http://www.mpp.mpg.de/~rwagner/sources/index.html>.

## 2.1 The Unified Model and the structure of AGNs

The *Unified Model* (Antonucci, 1993; Urry and Padovani, 1995) is based on a common AGN structure which, depending on the orientation to the observer, presents some characteristics or others which lead to the different classes of AGNs.

The AGN structure of the *Unified Model* is formed by a BH or a SMBH in its center which accretes gas from a surrounding disk. From the center of radio loud AGNs, two jets extend to large distances perpendicularly to the disk. These two components compose the emitting regions and furthermore, there are two radiation-absorbing parts: a gas cloud region which can absorb and re-emit the radiation from the disk and the jet, located at  $\sim 0.1\text{-}1$  pc from the central BH, and a dusty torus further away which also can absorb and re-emit the disk radiation (see Fig. 2.3). Depending on the orientation towards the observer, this rather simple structure can be observed as different shapes, as displayed in Fig. 2.4.

In the following, each of the components of the Unified model is explained in more detail:

- **Accretion of the matter:** The central BH accretes matter, distributed into a rotating disk around the BH. The rotation velocity increases as matter approaches the BH, there is thus a velocity structure of the disk which correlates with temperature. The disk emits thermal emission, due to the high density this emission can be assumed as black body, for a each given temperature, and so the total emission from the disk

Source	Redshift	AGN type
Mkn 421 (Punch et al., 1992)	0.030	HBL
Mkn 501 (Quinn et al., 1996)	0.034	HBL
1ES 2344+514 (Catanese et al., 1998)	0.044	HBL
1ES 1959+650 (Nishiyama, 1999)	0.047	HBL
PKS 2155-304 (Chadwick et al., 1999)	0.116	HBL
1H 1426+428 (Horan et al., 2002)	0.129	HBL
M87 (Aharonian et al., 2004)	0.0044	RG
PKS 2005-489 (Aharonian et al., 2005)	0.071	HBL
1ES 1218+304 (Albert et al., 2006a)	0.182	HBL
H 2356-309 (Aharonian et al., 2006b)	0.165	HBL
1ES 1101-232 (Aharonian et al., 2006b)	0.186	HBL
PG 1553+113 (Aharonian et al., 2006a; Albert et al., 2007b)	0.40-0.47 <sup>a</sup>	HBL
Mkn 180 (Albert et al., 2006b)	0.045	HBL
PKS 0548-322 (Superina et al., 2008)	0.069	HBL
BL Lacertae (Albert et al., 2007c)	0.069	LBL
1ES 0229+200 (Aharonian et al., 2007a)	0.140	HBL
1ES 0347-121 (Aharonian et al., 2007b)	0.185	HBL
1ES 1011+496 (Albert et al., 2007d)	0.212	HBL
3C 279 (Albert et al., 2008a)	0.536	FSRQ
RGB J0152+017 (Aharonian et al., 2008)	0.080	HBL
1ES 0806+524 (Acciari et al., 2009a)	0.138	HBL
W Comae (Acciari et al., 2008)	0.102	IBL
S5 0716+71 (Teshima et al., 2008)	0.31 <sup>a</sup>	LBL
3C 66A (Acciari et al., 2009b)	0.444 <sup>a</sup>	IBL
MAGIC J0223+430 (Aliu et al., 2009a)	-	Uni
Centaurus A (Aharonian et al., 2009b)	-	RG
RGB J0710+591 (Ong, 2009a)	0.125	HBL
PKS 1424+240 (Ong, 2009c; Teshima, 2009)	-	IBL
NGC 253 (Acero et al., 2009)	0.0008	Starb.
M82 (VERITAS Collaboration et al., 2009)	0.0007	Starb.
VER J0521+211 (Ong, 2009d)	-	Other
RBS 0413 (Ong and Fortin, 2009)	0.19	HBL
1ES 0414+009 (Hofmann and Fegan, 2009)	0.287	HBL
1ES 0502+675 (Ong, 2009b)	0.341	HBL
PKS 0447-439 (Raue et al., 2009)	0.2	HBL
PKS 1510-089 (Wagner and HESS collaboration, )	0.36	FSRQ
RGB 0648+152 (Ong et al., 2010)	-	Uni
IC 310 (Mariotti, 2010b)	0.019	Uni
4C +21.35 (Mose Mariotti, 2010)	0.432	FSRQ
AP Lib (Hofmann, 2010a)	0.049	LBL
MAGIC J2001+435 (Mariotti, 2010a)	-	HBL
1ES 1440+122 (Ong, 2010a)	0.162	HBL
B3 2247+381 (Mariotti and MAGIC Collaboration, 2010a)	0.12	HBL
NGC 1275 (Mariotti and MAGIC Collaboration, 2010b)	0.01755	Other
SHBL J001355.9-185406 (Hofmann, 2010b)	0.09485	HBL
ON 325 (Mariotti, 2011)	0.13-0.237 <sup>b</sup>	LHL

Table 2.1: List of AGNs detected in VHE  $\gamma$ -rays, ordered by date of discovery. LBL, IBL and HBL are Low, Intermediate and High-peaked BL Lacs respectively, FSRQ denotes Flat Spectrum Radio Quasar, RG is a Radio Galaxy and Starb. are Starburst galaxies. Those redshifts denoted by <sup>a</sup> have large uncertainties in their measurement or ambiguities in the identification of the optical absorption lines, while <sup>b</sup> means that two values for the redshift have been published.

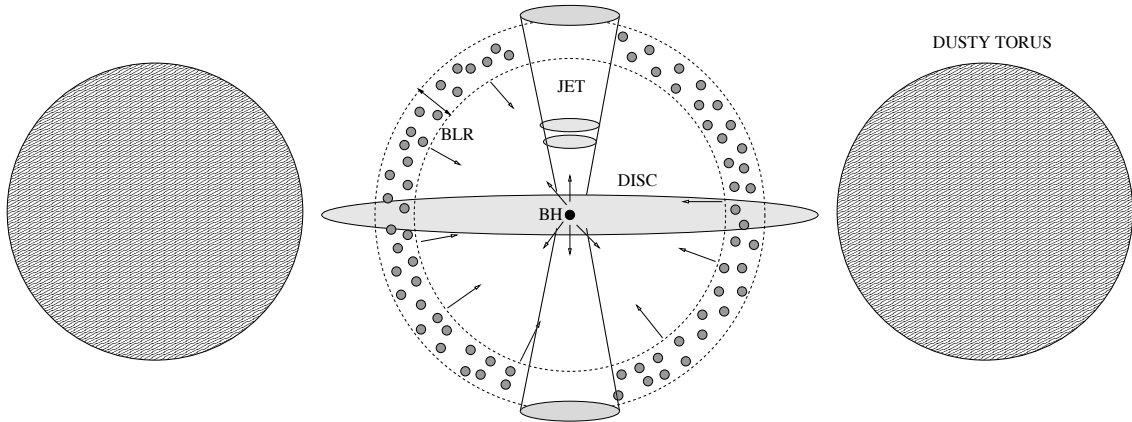


Figure 2.3: A cartoon of the AGN structure: the dusty torus has to be thought of as donut-like around the inner most region and is displayed here as cross section.

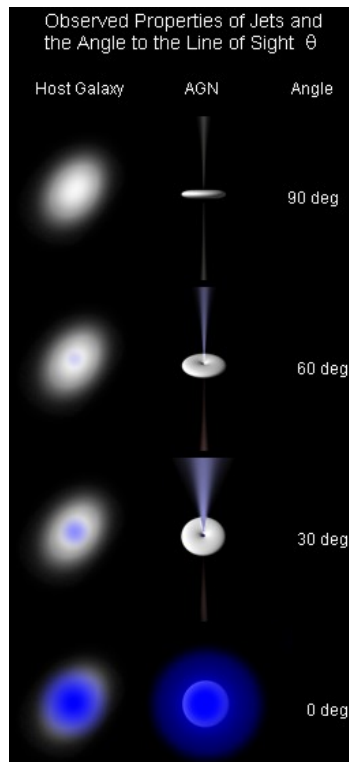


Figure 2.4: Simulated views of AGNs and their host galaxies for different orientations. Taken from [http://en.wikipedia.org/wiki/Active\\_galactic\\_nucleus](http://en.wikipedia.org/wiki/Active_galactic_nucleus).

will be the superposition of different back body spectra. During the accreting process, a loss of angular momentum, due to viscosity and turbulence, will take place as well. The entire emission from the disk is emitted in the optical and UV band, the so-called “*blue bump*”. The process depends strongly on the BH mass and the accretion rate. The disk emission is limited by the *Eddington limit*, which is reached when the outward force exerted by the pressure radiation exceeds the inward gravitational force driving the accretion.

- **Corona:** An extremely hot electron population surrounds the disk and interacts via inverse Compton scattering with the UV photons from the disk leading to X-ray emission.
- **Broad Line Region (BLR):** A cloudy gas shell, located at  $\sim$ 0.1-1 pc from the center, where the primary continuum emission from the disk is reprocessed photo-ionizing the gas clouds. The clouds are moving fast what produces the widening of the lines and therefore is responsible for the broad lines present in the optical spectrum of some types of AGNs like quasars.
- **Torus:** This component is a dusty region with toroidal shape located at  $\sim$ 1-10 pc from the center. Due to its absorption properties, the absence of broad emission lines can be explained for those AGN types, where our line of sight crosses this structure. The torus emits mainly in IR wavelengths.
- **Narrow Line Region (NLR):** In this region, the presence of ionized matter moving slowly (can be infer from the line widths) emits narrow lines in the optical spectrum. It is located at  $\sim$ 100 pc from the center (not shown in Fig. 2.3).
- **Jets:** In case of radio-loud AGNs, a pair of twin jets, pointing in opposite directions and perpendicular to the disk plane, appears. These extend from the vicinity of the central BH up to large distances from the nucleus ( $>100$  kpc). This component presents relativistic behavior, especially close to the BH. Electro-magnetic emission is produced over the whole spectrum, and it is the only component able to produce  $\gamma$ -rays. Hereafter, we will concentrate on the jets in order to study how  $\gamma$ -rays and particularly VHE  $\gamma$ -rays are produced.

## 2.2 Jets

The jet formation process is still under debate, but mostly it is believed that jets are born in disk regions very close to the BH. Thus, jet evolution is strongly correlated with the central engine. One of the favourite theories is the Blandford-Snajek mechanics (Blandford and Znajek, 1977) which explains an electromagnetic extraction of energy and angular momentum from a BH and its surrounding disk. Jets are thought to be mainly composed of electrons, with some smaller portion of protons and their interaction products entangled in magnetic fields.

The emission from the jet is assumed to come from these electrically charged particles moving at relativistic velocities along the jet. Due to the high velocities, the physically measured values are affected by the so-called *beaming* effect. This effect is responsible for

an apparent brightening of the relativistically moving sources. The Lorentz factor ( $\Gamma$ ) is defined as  $\Gamma = (1 - \beta^2)^{-1/2}$  where  $\beta = v/c$  and  $v$  is the velocity of the jet w.r.t. the reference frame of the observer. For a source moving at velocities close to the light speed, that is say  $\Gamma \gg 1$ , three main effects appear (Ghisellini, 2000):

- Light aberration: For a source emitting isotropically in its rest frame, the emission is seen collimated in a cone of angle  $\sin(\theta) = 1/\Gamma$ . Thus, the higher the speed of the emitting object, more collimated will be seen its radiation. About 75% of total emitted power is observed in this cone.
- Arrival time contraction: Observed time differences ( $\Delta t_{obs}$ ) are not equal to the ones in the rest frame of the emitter ( $\Delta t_{em}$ ). Their relation depends on the velocity and the angle between the velocity vector and the line-of-sight to the observer, as follows:

$$\Delta t_{obs} = \Gamma(1 - \beta \cos(\theta))\Delta t_{em} \equiv \frac{\Delta t_{em}}{\delta} \quad (2.1)$$

where the relativistic Doppler factor is defined as  $\delta = [\Gamma(1 - \beta \cos(\theta))]^{-1}$ , see Fig. 2.5.

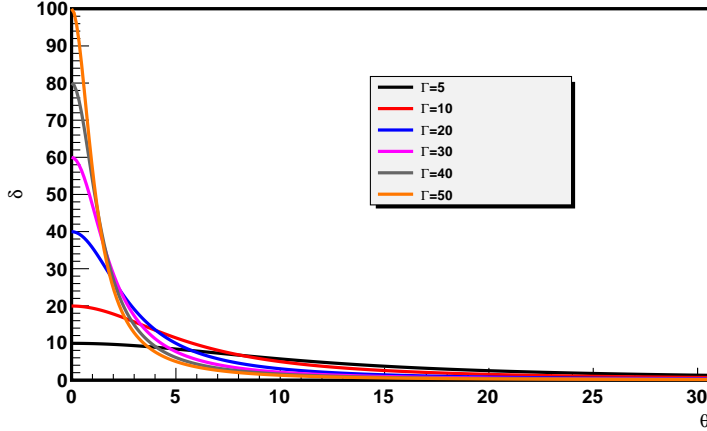


Figure 2.5: Doppler factor as a function of the angle between the velocity vector and the line-of-sight to the observer for different values of the Lorentz factor.

- Relativistic Doppler effect on the frequency: The frequency of the emitted photons from the moving source will be observed blue-shifted or red-shifted depending on the direction of the movement. In case of Blazars, where we are looking into the jet, and the emission region is coming to us the spectrum will be shifted to higher energies following the relation:

$$\nu_{obs} = \delta\nu_{em} \quad (2.2)$$

Moreover, the cosmological redshift produces a shift on the frequencies, which in this case appear red-shifted depending on the distance of the source, expressed as the redshift  $z$ . The total change in frequency results in:

$$\nu_{obs} = \frac{\delta}{z+1} \nu_{em} \quad (2.3)$$

From now on all the calculations will be performed in the rest-frame of the source and thus, the cosmological doppler effect will not be present in the formulation.

### 2.2.1 Jet emission models

There are two different approaches to model the jet emission, the so-called *Leptonic* and the *Hadronic* models, which differ in the used type of emitting particle. While in leptonic models, the two main interaction partners are electrons, or positrons, and photons, the hadronic models are based on the emission from protons and their interaction products. From these two approaches, a third category called lepto-hadronic models have been built. As reference, the Lecture notes for the National School of Astrophysics “F. Lucchin” - Gamma Astrophysics and Galaxy Formation - September 21-27 2008 have been used in this section.

#### Leptonic models

Four different processes are involved to model the emission from electrons and positrons (hereafter referred to as electrons):

- **Synchrotron emission:** Due to the presence of magnetic fields in the jet, the relativistic electrons are accelerated by the Lorentz force:

$$\vec{F} = \frac{e}{c}(\vec{E} + \vec{v} \times \vec{B}) = \frac{d}{dt}(\gamma m \vec{v}) \quad (2.4)$$

where  $\gamma$  denotes the Lorentz factor of the electrons.

The parallel and perpendicular components to the magnetic field are:

$$F_{\parallel} = \gamma m a_{\parallel} = \frac{e}{c}(E_{\parallel} + v_{\parallel} B \sin(0^\circ)) \rightarrow a_{\parallel} = \frac{e}{\gamma mc} E_{\parallel} \quad (2.5)$$

$$F_{\perp} = \gamma m a_{\perp} = \frac{e}{c}(E_{\perp} + v_{\perp} B \sin(90^\circ)) = \frac{e}{c}(E_{\perp} + v_{\perp} B) \rightarrow a_{\perp} = \frac{e(E_{\perp} + v_{\perp} B)}{\gamma mc} \quad (2.6)$$

One can see that the parallel acceleration component does not depend on the magnetic field, but only its perpendicular component. This means that the absolute value of the velocity does not change in the presence of magnetic fields, only the direction of the particle, originating a rotation movement around the magnetic field lines. Typically, the high conductivity of the fully ionized plasma ensures that there are no large-scale

electric fields present in the jet, only local electric fields from charged particles which can produce Bremsstrahlung. Therefore, I will neglect the electric field in the further calculations.

The gyration radius, called *Larmor radius* can be derived as:

$$r_L = \frac{v^2}{a} = \frac{\gamma mc^2 \beta \sin(\theta)}{eB} \quad (2.7)$$

where  $\theta$  is the angle between the velocity vector of the particle, and the magnetic field lines, called *pitch angle*, and  $\beta$  is the velocity of the charged particle in units of the speed of light.

The fundamental frequency (gyration frequency) is the inverse of the time needed to complete one orbit:

$$\nu = \frac{eB}{2\pi\gamma mc} = \frac{\nu_L}{\gamma} \quad (2.8)$$

where  $\nu_L$  is the gyration frequency for sub-relativistic particles, called the *Larmor frequency*.

The stronger the magnetic field, the smaller  $r_L$  and the higher  $\nu_L$  while, on the contrary, the greater the particle velocity, the larger  $r_L$  and the lower  $\nu_L$ .

The emitted power by a single electron due to synchrotron radiation is given by the *Larmor formula*:

$$P(\theta) = \frac{2e^4}{3m^2c^3} B^2 \gamma^2 \beta^2 \sin^2(\theta) \quad (2.9)$$

In case of an isotropic distribution of pitch angles we can average the term, resulting in:

$$\langle P \rangle = \frac{4}{3} \sigma_T c \gamma^2 \beta^2 U_B \quad (2.10)$$

where  $U_B$  is the magnetic energy density ( $U_B = B^2/8\pi$ ) and  $\sigma_T$  the Thomson scattering cross section for electrons,  $\sigma_T \approx 6.65 \cdot 10^{-25} \text{ cm}^2$ .

The electrons in a plasma emitting synchrotron radiation cool down due to the energy losses. This characteristic synchrotron cooling time can be estimated as:

$$t_{syn} = \frac{E}{\langle P \rangle} = \frac{\gamma m_e c^2}{4/3 \sigma_T c U_B \gamma^2 \beta^2} \approx \frac{7.75 \cdot 10^8}{B^2 \gamma} \text{ s} = \frac{24.58}{B^2 \gamma} \text{ yr} \quad (2.11)$$

Thus, the cooling time scale depends strongly on the magnetic field such that a same electron can be cooled in seconds or years, depending on the environment.

The typical wavelength (or frequency) associated to the syncrotron process for sub-relativistic particles is related to the inverse of the typical time scale. Nevertheless, in the relativistic case, due to the beaming effects, most of the energy is emitted

in a cone (due to light aberration). Thus, the typical frequency is related to the fraction of the time, for each orbit, during which the observer receives radiation:

$$\nu_s = \gamma^3 \nu = \frac{\gamma^2 e B}{2\pi m_e c} \quad (2.12)$$

The spectrum emitted by a single electron can be described as:

$$P(\nu, \gamma, \theta) = \frac{\sqrt{3} e^3 B \sin(\theta)}{m_e c^2} F(\nu/\nu_c), \quad (2.13)$$

$$F(\nu/\nu_c) \equiv \frac{\nu}{\nu_c} \int_{\nu/\nu_c}^{\infty} K_{5/3}(y) dy, \quad (2.14)$$

$$\nu_c \equiv \frac{3}{2} \nu_s \sin(\theta), \quad (2.15)$$

where  $K_{5/3}(y)$  is the modified Bessel function of order 5/3. The frequency dependence is contained in the function  $F$  which peaks at  $\nu \approx 0.29 \nu_c$ , as can be seen in Fig. 2.6. It presents a power-law shape for low frequencies and an exponential decay for high ones. These relations hold for relativistic particles in a magnetic field smaller than:

$$B \lesssim \frac{7.22 \cdot 10^{14}}{\gamma \sin^2(\theta)} \text{ Gauss}, \quad (2.16)$$

that is to say if during one orbit the emitted energy is smaller than the electron energy.

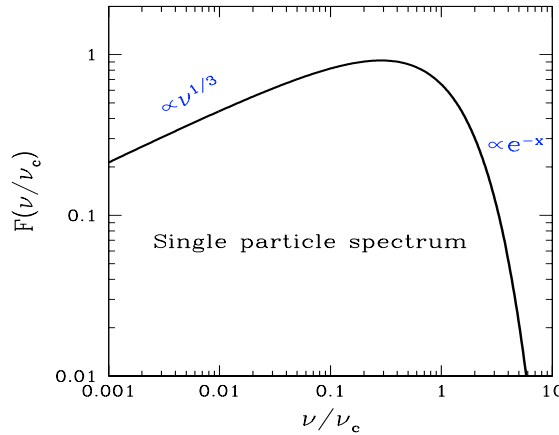


Figure 2.6: Single particle spectrum due to synchrotron radiation.

However, we will observe not the spectrum from a single electron, but the superposition of the emission of all implicated electrons. Typically in high energy astrophysics, the particle energy distribution is assumed to be a power-law:

$$N(\gamma) = K\gamma^{-p} = N(E)\frac{dE}{d\gamma}; \quad \gamma_{min} < \gamma < \gamma_{max}, \quad (2.17)$$

where  $K$  is a constant,  $p$  the so-called spectral index,  $\gamma$  the individual particle Lorentz factor w.r.t. the jet,  $\gamma_{min}$  and  $\gamma_{max}$  are maximal and minimal particle  $\gamma$  factors, defined by physical conditions and  $E$  is the single particle energy.

The total emissivity, defined as the power unit solid angle produced within a unit volume, can be calculated integrating the power produced by a single electron times the density of particles,  $N(\gamma)$ . Assuming an isotropic emission, that the distribution of pitch angles is isotropic and that these assumptions hold for low and high values of  $\gamma$ , then:

$$\epsilon(\nu, \theta) \propto KB^{(\alpha+1)}\nu^{-\alpha} \quad (2.18)$$

A power-law electron distribution produces a power-law spectrum with a spectral index of radiation  $\alpha$  which is related to the slope of the distribution of electrons as  $\alpha = (p - 1)/2$ .

The absorption counterpart of this process is called synchrotron absorption and the cross section of the process can be mathematically described as:

$$\sigma(\nu, \gamma, \theta) = \frac{16\pi^2}{3\sqrt{3}} \frac{e}{B} \frac{1}{\gamma^5 \sin(\theta)} K_{5/3} \left( \frac{\nu}{\nu_c \sin(\theta)} \right) \quad (2.19)$$

Ghisellini and Svensson (1991) point out that the synchrotron absorption cross-section is larger than the Thomson cross-section at frequencies

$$\nu < 1.7 \cdot 10^{15} \frac{(B \sin(\theta))^{2/5}}{\gamma} \text{Hz} \quad (2.20)$$

This means that the relativistic electrons can be accelerated if they are illuminated by a low frequency radiation and, given the large cross-section at low energies, the process will be efficient even if the photon field is not very dense.

The synchrotron emission from an AGN is typically emitted from radio to X-rays and presents a high degree of polarization.

- **Inverse Compton scattering:**

Compton scattering is a scattering process which results from the interaction between electrons in the jet and photons which can be emitted by an external source or by the same electron population due to the synchrotron emission process. The cross-section of this process depends strongly on the energy of the electron, resulting in two different regimes. The so-called *Thomson* scattering regime where the energy of the incoming photon is small with respect to the electron rest mass-energy, and the *Klein-Nishina regime* (KN) where the energy of the incoming photon is comparable or greater than  $m_e c^2$ . The *direct Compton* process implies a transfer of energy from the photons to

the electrons, as a heating mechanism and usually takes place in the Thomson regime while the inverse process, called *inverse Compton* scattering, is produced in case of very energetic electrons where the electron transfers part of its energy to the photon. The  $\gamma$ -ray emission in the VHE band is produced by relativistic electrons in the jet and so it occurs in the KN regime.

The *Thomson* scattering cross section,  $\sigma_T$  is independent of the photon frequency:

$$\sigma_T = \frac{8\pi}{3} r_e^2 \approx 6.65 \cdot 10^{-25} \text{ cm}^2 \quad (2.21)$$

where  $r_e$  is the classical electron radius.

This  $\sigma_T$  is the classical limit of the more general *Klein-Nishina* cross-section formula defines as:

$$\sigma_{KN} = \frac{3}{4} \sigma_T \left\{ \frac{1+x}{x^3} \left[ \frac{2x(1+x)}{1+2x} - \ln(1+2x) \right] + \frac{1}{2x} \ln(1+2x) - \frac{1+3x}{(1+2x)^2} \right\} \quad (2.22)$$

where  $x$  denotes the energy of the photon, expressed in units of the electron rest mass, 512 keV.

The process is less efficient at high energies, due to its lower cross-section as shown in Fig. 2.7, thus the high energy photons will be scattered less than those of lower energies. I will focus further on *inverse Compton* scattering since this is the process responsible for VHE  $\gamma$ -rays.

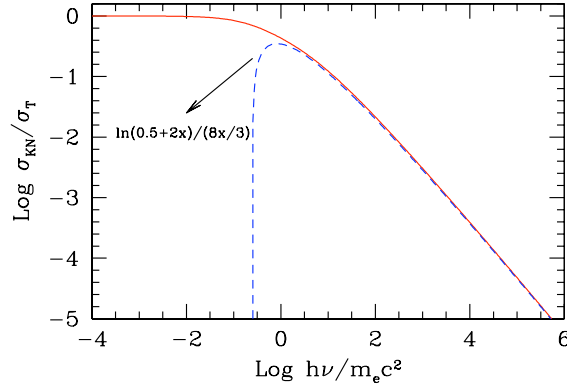


Figure 2.7: The total Klein-Nishina cross section as a function of energy. The dashed line is an approximation at high energies.

Assuming an isotropic distribution of incident photons and relativistic electrons, the average photon energy after one scattering process ( $x_1$ ) can be estimated as:

$$\langle x_1 \rangle = \frac{4}{3} \gamma^2 x \quad (2.23)$$

The energy loss rate of the electron is given by

$$P_e(\Gamma) = \frac{dE_e}{dt} = \frac{4}{3} \sigma_T c \gamma^2 \beta^2 U_r \quad (2.24)$$

where  $U_r$  is the radiation energy density and  $\beta = v/c$ .

Compared with the energy loss rate due to synchrotron emission (Eq. 2.10), the only difference comes from the term  $U_r$  which in case of *synchrotron* radiation is the magnetic energy density ( $U_B$ ), instead of the radiation energy density. Therefore, if relativistic electrons are in presence of radiation and magnetic fields, they will emit by both processes, and their ratio will be directly connected to the ratio of the energy densities.

$$\frac{L_{syn}}{L_{IC}} = \frac{P_{syn}}{P_c} = \frac{U_B}{U_r} \quad (2.25)$$

This relation fails at the extremes of the energy range. In case of low energies, electrons can emit and absorb synchrotron radiation quite efficiently so that the synchrotron cooling is compensated by the heating due to the absorption process. In the other extreme, at high energies, the electrons are mainly scattered into the KN regime, where the cross-section is smaller and a lower number of scatterings occur and hence the electrons cool less efficiently.

The cooling time for the *inverse Compton* process, if the photon energy is smaller than the electron energy at rest, is:

$$t_{IC} = \frac{E_e}{dE_e/dt} = \frac{3m_e c}{4\sigma_T c \gamma^2 \beta^2 U_r} \quad (2.26)$$

The spectrum from a single particle in a monochromatic and isotropic photon field can be described by the IC emissivity,  $\epsilon_{IC}$

$$\epsilon_{IC}(x_1) = \frac{\sigma_T n I_0 (1 + \beta)}{4\gamma^2 \beta^2 x_0} F_{IC}(x_1) \quad (2.27)$$

where  $I_0$  is the specific intensity for electrons which do not change their energy in the scattering,  $n$  is the number of electrons per unit volume, and the function  $F_{IC}$  is defined as (see Fig. 2.8)

$$F_{IC}(x_1) = \frac{x_1}{x} \left[ \frac{x_1}{x} - \frac{1}{(1 + \beta)^2 \gamma^2} \right]; \quad \text{if } \frac{1}{(1 + \beta)^2 \gamma^2} < \frac{x_1}{x} < 1 \quad (2.28)$$

corresponding to *downscattering*, if the photon loses energy in the scattering or, for the contrary case, for *upscattering*:

$$F_{IC}(x_1) = \frac{x_1}{x} \left[ 1 - \frac{x_1}{x} \frac{1}{(1 + \beta)^2 \gamma^2} \right]; \quad \text{if } 1 < \frac{x_1}{x} < (1 + \beta)^2 \gamma^2 \quad (2.29)$$

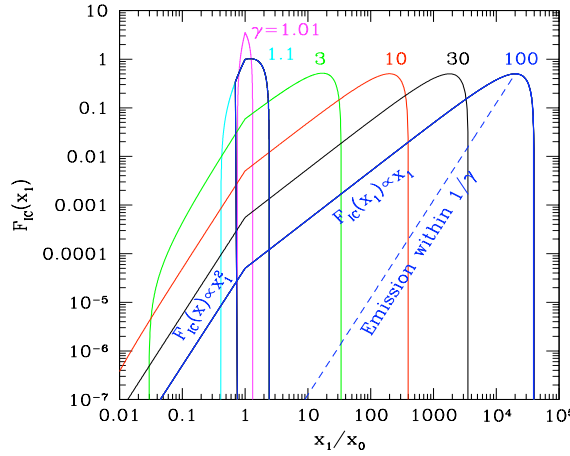


Figure 2.8: Spectrum shape of a single electron spectrum due to *inverse Compton* scattering. The different color lines represent different  $\gamma$  values (denoted on the top) in an isotropic and monochromatic radiation field.

As in the case of synchrotron emission, the spectrum emitted from many electrons, can be derived assuming a power-law energy distribution for the relativistic electrons (Eq. 2.17) and an isotropic and monochromatic photon field, and can also be described by a power-law:

$$\epsilon_c(h\nu_c) = \frac{1}{4\pi} \frac{(4/3)^\alpha}{2} \frac{\tau_c}{R/c} \frac{U_r}{h\nu_0} \left(\frac{\nu_c}{\nu_0}\right)^{-\alpha} \quad (2.30)$$

where  $\tau_c$  represents the scattering optical depth of relativistic electrons and  $R$  the radius of the source. As in the case of synchrotron emission, the relation between the spectral index of the electron distribution and the index of the emitted spectrum is  $\alpha = \frac{p-1}{2}$ .

As, one photon can suffer multiple scatterings, a *Comptonization parameter*,  $y$ , is defined as the average number of scatterings times the average fractional energy gain per scattering. The number of scatterings can be estimated taking into account the optical depth and the size of the source. If  $y > 1$  the *Comptonization* process is important since the resulting spectrum is more energetic than the primary photon field.

The *inverse Compton* scattering process can be divided into two different types depending on the seed photons origin:

- **External Compton:** this process takes place in the AGN jets as result of the interaction between the relativistic electrons in the jets and the two main external photon fields, the optical-UV emission from the accretion disk and the IR radiation field produced by the torus. Of course, the importance of these two processes will depend strongly on the position of the emitting electrons w.r.t. these two radiation fields.

- **Synchrotron-Self Compton (SSC, Maraschi et al., 1992)**: this process is a mixture of the two previous emission mechanisms, the relativistic electrons moving in a magnetized medium will produce synchrotron emission and will interact with the same population of synchrotron photons via the *inverse Compton* process. It can be described by the same equations as the external *Compton* case, but instead of using an external energy density,  $U_r$ , we can use the energy density created by the synchrotron emission and of course, depending on the energy of the particles, this can occur in the *Thomson* or the KN regime. Given the strong connection between both processes, it can be used to constrain physical quantities of the jet (Tavecchio et al., 1998).
- The Mirror model (Ghisellini and Madau, 1996): This model consists of the reflection of part of the synchrotron emission by the BLR which travels back to the jet. Nevertheless, the contribution to the spectrum emitted by the jet is typically small.

Taken into account all these processes, it is possible to model the emission from blazars and FSRQs. As an example, the emitted spectrum by the FSRQ PKS1222+21 will be modelled in Chapter 7.

### Hadronic models

The *proton blazar model* (Mannheim, 1993) assumes that the emission at low energies is from synchrotron radiation from electrons and the high energy component mainly comes from the interaction between energetic protons in the jet. This process is able to produce  $\gamma$ -ray emission at much higher energies than leptonic processes do, but it needs extreme conditions, as very high densities and strong magnetic fields. Moreover, the processes are typically slower than in the leptonic models, and it is difficult to reconcile them with fast variability, typical for AGNs. Moreover, it is difficult to explain correlations between X-rays and  $\gamma$ -ray emissions. A possible alternative at high energies, is to have a mixture of hadronic and leptonic models, the hadronic component can be responsible for the base luminosity and the variability can come from an electron population.

In this thesis I will focus on leptonic models.

## 2.3 Spectral Energy Distribution

The Spectral Energy Distribution (SED) from Blazars typically shows a double-peaked structure where the total energetic output is dominated by the high energy component. Usually the emission at low energies is highly polarized which is a hint that it is mainly produced by synchrotron radiation while the higher energies are produced through *inverse Compton* scattering (IC) of photons by the same electron population responsible for the synchrotron emission (SSC) or due to an external photon field (EC).

There are three important features of the SED: the flux level, the peak frequencies and the spectral slopes. They can change with time or be stable, in case of blazars they are typically very variable. During a flare state, the flux can change several orders of magnitude and the duration of the flare can vary in time scales from minutes to years. Thanks to the variability time scale, important constraints on the size and the localization of the emission

region can be set. In case of short variability, for instance, the size ( $R$ ) of the emitting region can be constrained using the causality relation:

$$R < ct \frac{\delta}{1+z} \quad (2.31)$$

where  $t$  is the characteristic variability time scale,  $\delta$  the Doppler factor and  $z$  the redshift of the source.

Another important point is the time correlation between different energy ranges which, if present, points to a common origin in a single emitting region. Time correlations have been found in TeV and X-rays for some sources, but they are not always observed e.g. the so-called “orphan TeV flare” (Krawczynski, 2004).

Finally, the spectral variations associated to the flare states are interesting for particle acceleration physics, since jets are one of the most powerful particle accelerators in the Universe and, given the extreme conditions, such environments cannot be reproduced on Earth. Therefore, jets can be used as a particle laboratory. Especially interesting in this context is the production processes of heating and cooling of particles. Typically, the spectra become harder when the fluxes increase during a flare state.

After the discovery of the *gamma*-ray spectral range, thanks to the  $\gamma$ -ray telescope EGRET, a systematic study on the blazar average SEDs was performed by Fossati et al. (1998). This work yielded a distribution, called the *blazar sequence*. It establishes different types of blazars, depending on the peak frequencies of the typical two bumps, the integral fluxes and the radio emission. The low energy component extends from  $\sim 10^{13}$  to  $10^{17}$  Hz, and the high energy component from  $\sim 10^{21}$  to  $10^{24}$  Hz. There is a typical relation between the luminosity and the frequencies: objects with high luminosities have both peaks at lower frequencies as for example the FSRQs, and the luminosities are lower as the peaks move to higher frequencies and the spectral slopes typically are harder. Following these trends, blazars are thus divided into three groups: HBL, IBL and LBL, see Fig. 2.9.

In recent studies, this classification according to the blazar sequence, appears not to be correct in some particular cases, where the classification is not in agreement with the physical properties. Ghisellini et al. (2011) have proposed a new classification based on the luminosity of the broad-line region, measured in Eddington units.

## 2.4 Gamma-ray absorption

The most efficient process of  $\gamma$ -ray absorption is the pair production due to the interaction between two photons ( $\gamma + \gamma \rightarrow e^- + e^+$ ). The cross-section of the process is given by the following relation

$$\sigma(s) = \frac{3}{16} \sigma_T (1 - s^2) [(3 - s^4) \ln \frac{1+s}{1-s} - 2s(2 - s^2)], \quad (2.32)$$

where  $\sigma_T$  is the Thomson cross-section and  $s$  represents the velocity of the pairs in the center of mass reference frame, which is defined as:

$$s = [1 - \frac{2}{x_1 x_2 (1 - \mu)}]^{1/2}, \quad (2.33)$$

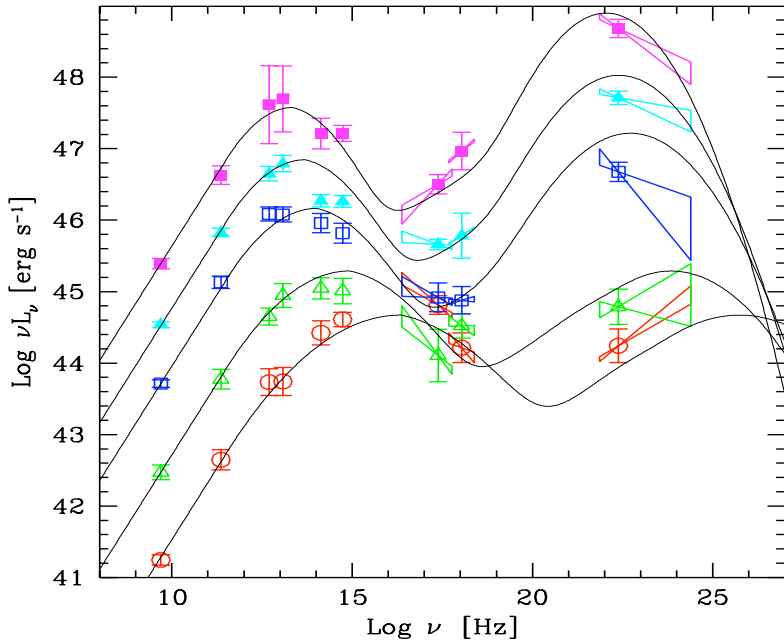


Figure 2.9: Average SEDs from Fossati et al. (1998), showing the blazar sequence. The different colors denote different types of blazars.

where  $x_1$  and  $x_2$  are the ratios between the photon energy and the energy of the electron at rest ( $x_a = h\nu_a/m_ec^2$ ) and  $\mu$  denotes the collision angle between the two photons ( $\mu = \cos\theta$ ).

This process can only occur if the energies of the photons are high enough, i.e. the sum of the photon energies in the center of mass rest frame has to be at least equal the sum of the electron-positron pair energy at rest. Taken into account the collision angle, the energy threshold of the process can be then written as:

$$x_1x_2(1 - \mu) > 2 \quad (2.34)$$

The maximum cross-section is reached at  $x_1x_2(1 - \mu) \approx 4$ , as can be seen in Fig. 2.10. From there, we can derive the photon wavelength for which the absorption is maximal, when interacting with a  $\gamma$ -ray:

$$E_{max} = \frac{2(m_ec^2)^2}{E_\gamma} = \frac{hc}{\lambda_{max}}, \quad (2.35)$$

$$\lambda_{max} = 1.24(E_\gamma[TeV]) \quad [\mu m] \quad (2.36)$$

Thus, depending on the  $\gamma$ -ray energy, the absorption will be mainly due to a given energy range of photons (see Table 2.2).

Nevertheless, due to the beaming effect, the absorption can be reduced. In case of relativistic movement of the jet towards the observer, the biggest part of the emission from a relativistic particle is emitted into a small angle due to relativistic aberration, thus the

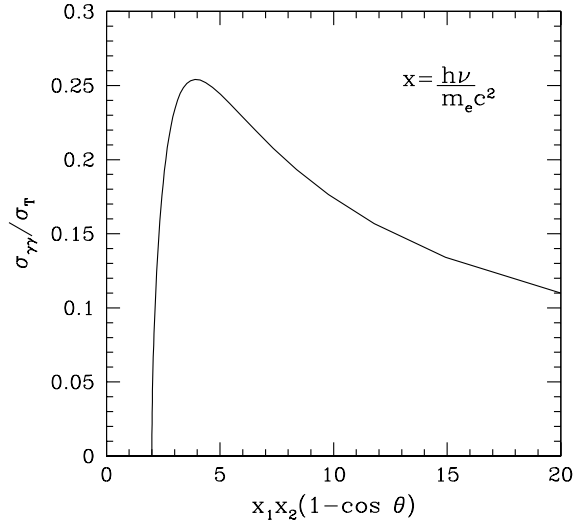


Figure 2.10: Cross-section for pair creation process as a function of the energy of the photons.

number of photons available for possible interactions is restricted. Moreover, the observed energy is boosted by the beaming so that the emitted energy would be lower by factor ( $E/\delta$ ), and hence the target photon energies needed to reach the energy threshold for pair creation will be higher. Assuming a typical power-law spectrum, where the flux decreases when going to higher energies, the number of target photons is also reduced. The absence of absorption features on the VHE spectrum sets therefore a lower limit on the Doppler factor.

The  $\gamma$ -ray absorption process takes place inside the source (self-absorption), since the medium is filled with target photons from different energy ranges and also outside of the source on the way to Earth, due to different background radiation components present in the Universe, as described in Sec. 2.4.1.

The self-absorption process will affect the *intrinsic*<sup>1</sup> source spectrum. The effect of the absorption will depend strongly on the location of the emission zone inside the inhomogeneous AGN structure. If the  $\gamma$ -rays are produced close to the central BH, they can suffer absorption due to the presence of UV and optical emission from the accretion disk and X-rays from the corona. Furthermore, the presence of the dust torus will produce absorption due to the IR photons emitted from it.

#### 2.4.1 Background Radiation

Background radiation not only is due to the diffuse radiation from sources but also fills the Universe. This background covers almost the whole electromagnetic spectrum as one can see in Fig. 2.11. Depending on the energy band (wavelength range), its origins will be different:

<sup>1</sup>*intrinsic* spectrum is typically used to refer to the total emitted spectrum by the source, while the observed one will be also affected by absorption due to intergalactic backgrounds.

$\gamma$ -ray photon energy	Target photon energy range
<80 GeV	X-Rays
80-300 GeV	UV
300-600 GeV	Optical
600 GeV-80 TeV	Infrared
>80 TeV	Microwaves

Table 2.2: Energy range photon target for the maximum absorption due to pair creation process during the interaction with  $\gamma$ -rays.

- **CGB (Cosmic Gamma-ray Background):** The CGB is constituted by the unresolved extragalactic  $\gamma$ -ray sources and photons generated in the interaction between Cosmics rays and the interstellar medium.
- **CXB (Cosmic X-ray Background):** The CXB is a combination of emission from nearby hot gas and contributions from resolved and unresolved X-ray sources distributed over the sky like AGNs.
- **CUVOB (Cosmic Ultra-Violet and Optical Background):** This component is mainly due to stellar emission and is strongly correlated with the evolution of the Universe. Also the *zodiacal* light<sup>2</sup> contributes to this diffuse background.
- **CIB (Cosmic Infrared Background):** The main contribution to the CIB comes from the re-emission of the stellar light by dust. Also *zodiacal* light has a thermal emission component which is comprised in this range.
- **CMB (Cosmic Microwave Background):** This background stems from the decoupling of matter and radiation after the Big Bang and shows a blackbody spectrum with a temperature of  $\sim 2.7$  K.
- **CRB (Cosmic Radio Background):** The CRB is due to diffuse extragalactic light.

The  $\gamma$ -ray absorption is mainly due to photons from X-rays to microwaves. Nevertheless, as can be observed in Fig. 2.11, the principal contribution to the background level is the CMB followed by CUVOB and CIB whose fluxes are comparable. Since the CXB is almost two orders of magnitude lower than the CUVOB and the CIB, its effect on the absorption of  $\gamma$ -rays needs not to be taken into account. Due to its larger flux, the CMB will produce the main absorption effect at photon energies higher than  $\sim 80$  TeV. The principal contribution to the absorption of VHE  $\gamma$ -rays comes therefore from the CUVOB and the CIB, usually called Extragalactic Background Light (EBL). Of course, the absorption due to the EBL will depend strongly on the distance of the source since as longer the photons travel, the larger becomes the probability of interaction. Moreover, the EBL evolves with the evolution of the Universe, thus  $\gamma$ -rays from very far sources were confronted with a different EBL at the beginning of their voyage.

<sup>2</sup>*Zodiacal* light is produced due to the dispersion of solar radiation by the dust in the Solar System.

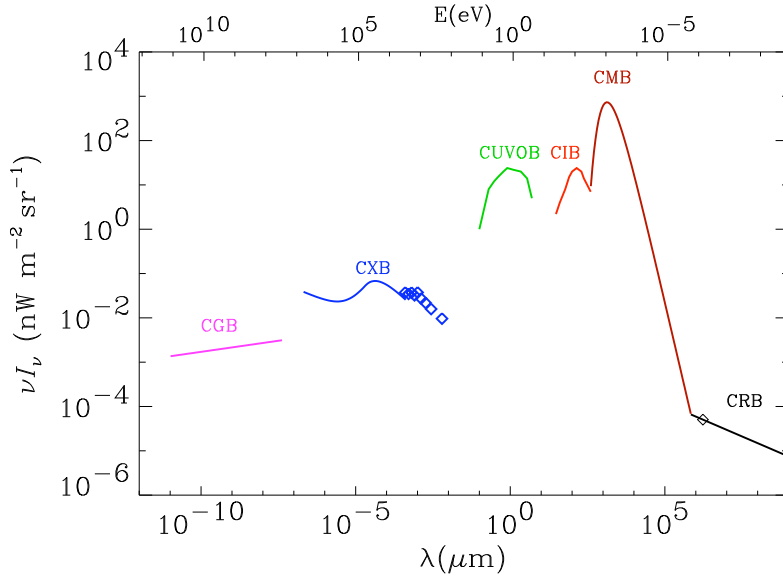


Figure 2.11: Spectrum of the cosmic background radiation(Hauser and Dwek, 2001).

The EBL presents a two peak structure as can be seen in Fig. 2.11, one peak in the optical range, due to starlight, while the second peak at  $\sim 100 \mu\text{m}$  is due to the re-emission of starlight by dust.

The study of the EBL is not only very interesting in terms of AGN studies, but has also cosmological consequences since EBL accumulates the emission from all epochs of the evolution of the Universe. Nevertheless, the measurement of the EBL is a difficult task since the foregrounds are much brighter than the background. For this reason, not only direct measurements have been used in order to estimate the EBL but also indirect ones. Mainly there are three indirect methods which provide lower and upper limits, which together with the direct measurements have constrained considerably the uncertainties for the estimation of the EBL in the past years. The indirect methods are:

- Source number counts give a lower EBL limit. It is based on the assumption that the resolved sources are only part of the total emitters, yielding thus a lower limit on the EBL.
- The VHE spectra from far sources, as AGNs or GRBs, are deformed due to the interaction with the EBL as function of their redshift. Assuming basic properties of the intrinsic spectra of the sources, upper limits on the EBL can be inferred.
- There are two further methods based on statistical analysis. The first one, named *stacking technique* consists of a pile-up of infrared sky maps which allow to detect sources which are not visible in a single image and set lower limits to the EBL. The second method, called *fluctuation technique*, can derive upper limits from fluctuations of the background estimation from different regions of the sky.

### 2.4.2 EBL Models

Based on direct and indirect methods, different approaches have been used in order to model the EBL. The main objective of these models is the estimation of the luminosity density as a function of the distance. The models can be grouped in three subgroups according to the way in which the problem is addressed:

- Forward evolution: This method is based on galaxy evolution, assuming several cosmological conditions. It simulates how the Universe has evolved up to nowadays, integrating the stellar emission from the epoch of the very first stars till today, using stellar evolution models (Gilmore et al., 2009; Somerville et al., 2008; Kneiske and Dole, 2010; Finke et al., 2010; Somerville et al., 2008). In this type of EBL models, different research fields are involved like stellar physics, stellar evolution, inter-stellar medium (ISM) physics and cosmology, and the comparison with data is possible at each step.
- Backward evolution: In this case, the method starts from the present Universe and develops back in time, starting from galaxy observations of the local universe and extrapolating them to higher redshifts. In this kind of models, unlike forward evolution models, no assumptions about stellar physics, ISM, etc are used. For the stellar emission, average templates for the observed spectral energy distribution are used (Stecker et al., 2006; Franceschini et al., 2008).
- Observed galaxy evolution: Only direct observations of the evolution of the galaxies are used in this kind of models. Domínguez et al. (2011) calculated the changing fractions of quiescent galaxies, star-forming galaxies, starburst galaxies and active galactic nuclei (AGN) from redshifts 0.2 to 1, and then they extrapolated the results for higher redshifts.

Even if the observed galaxy evolution models have the advantage that they stem from direct observations and therefore are expected to be the most reliable models, the forward and backward evolution models offer the great advantage that they can set constraints in different fields. For example, new EBL limits from VHE spectra can constrain the stellar emission models, stellar evolution, ISM physics, etc.

Taken into account the most recent developed models, despite the use different approaches, these are in good agreement. The current status of EBL research is summed up in Fig. 2.12. By now, the EBL measurements still remain uncertain to a factor of about 2-3 and, as we will see in the next section, the study of far VHE emitters is a good method to constrain them further.

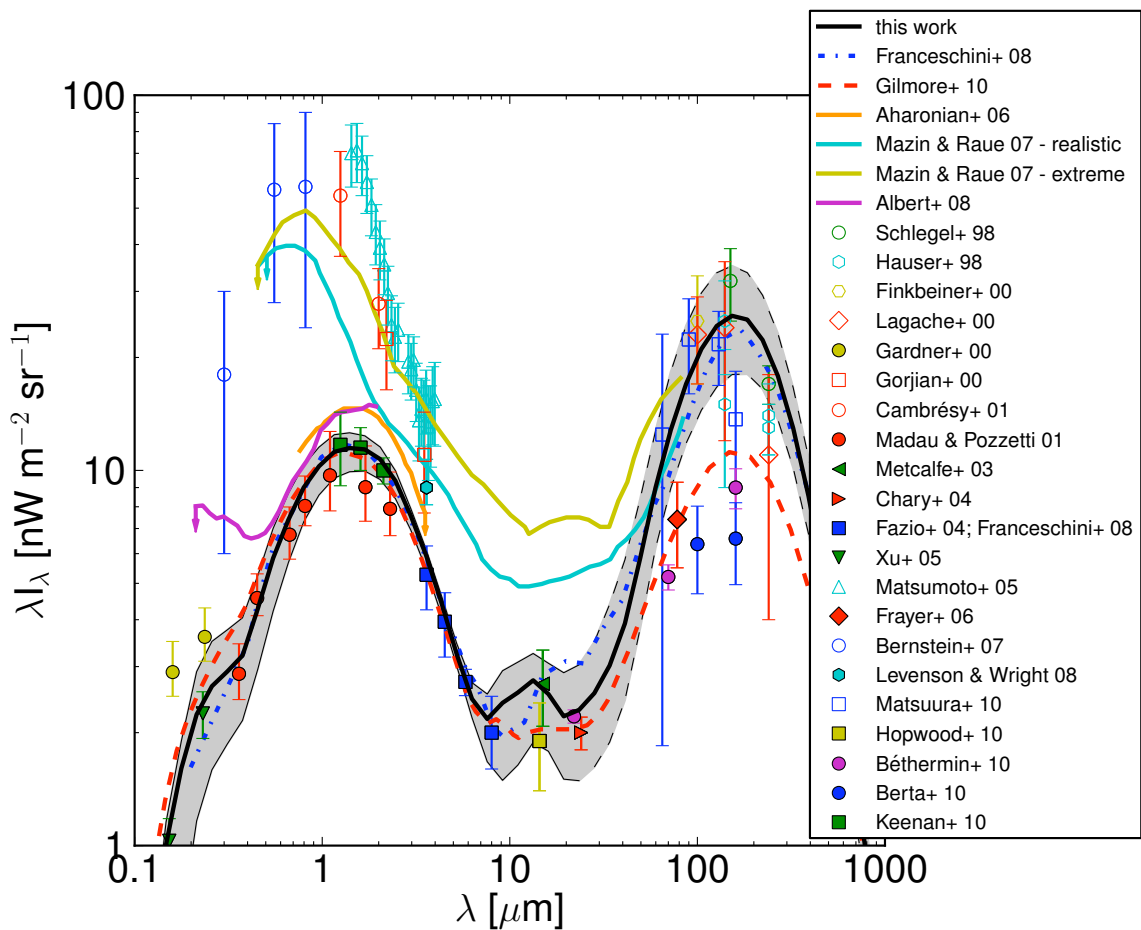


Figure 2.12: A comparison of recent EBL models, adopted from Domínguez et al. (2011).

### 2.4.3 Effects on the VHE spectra

Due to the absorption effects from the interaction between  $\gamma$ -rays and the EBL photons, the VHE spectra from far sources are distorted:

$$F_{obs}(E) = F_{int}(E) \cdot e^{-\tau(E,z)} \quad (2.37)$$

where  $F_{obs}(E)$  is the observed flux,  $F_{int}(E)$  is the intrinsic emitted spectrum by the source and  $\tau(E, z)$  the optical depth.

The optical depth strongly depends on the distance and the energy range covered by the intrinsic source spectrum. For energies lower than  $\sim 80$  GeV, the absorption is almost negligible since the density of the background photons is low, while for energies greater than 80 TeV, the photons suffer a quasi-total absorption due to the high density of CMB photons. For a given gamma ray energy, the gamma-ray horizon is defined as the source redshift for which the optical depth is  $\tau(E, z) = 1$ .

Since VHE spectra from AGNs typically cover an energy range from few tens of GeV to few TeV, the spectra are affected by EBL absorption. Since the EBL density distribution over frequency presents a double peak structure (Fig. 2.12) and not a constant flux, the absorption of  $\gamma$  photons will depend also on their energies.

In order to find the intrinsic source spectrum, we have to make use of EBL models to obtain the de-absorbed spectrum. This can only be done if the redshift of the source is known. Nevertheless, we can proceed the other way around: assuming basic characteristics of the intrinsic spectrum, the distance of the source can be inferred using EBL models.

The AGN VHE  $\gamma$ -ray spectra can be used as probes of the EBL using characteristics of the de-absorbed spectra. A limit on the maximally physically allowed spectral slope of the intrinsic spectrum can be set to  $\Gamma < 1.5$ , from the standard modelled acceleration and emission processes, which allow to set upper limits on the EBL models, as in case of the FSRQ 3c279 (Albert et al., 2008a) at redshift  $z = 0.536$ . There, it was discovered that the Universe was more transparent than expected by some EBL models, constraining the  $\gamma$ -ray horizon (see Fig. 2.13). However, this method becomes ineffective for sources which present an important self-absorption process since the assumed maximally allowed spectral slope would not be valid anymore in that case. Nevertheless, for realistic assumptions on the intrinsic spectra of AGNs, the self-absorption may not affect the derived EBL limits (Tavecchio and Mazin, 2009).

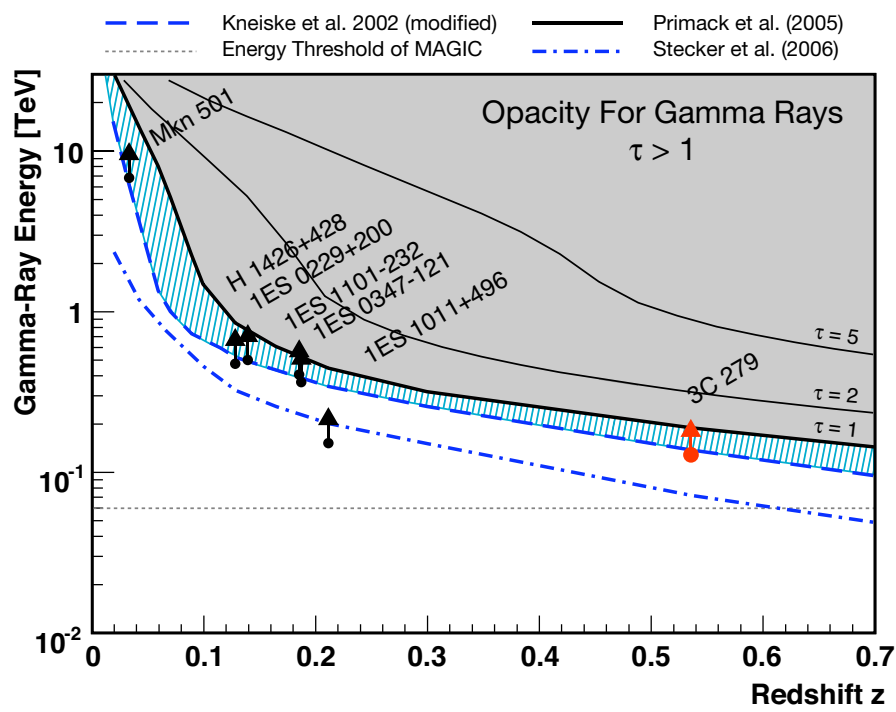


Figure 2.13: Gamma-ray energy as a function of the redshift for some models and data from different sources. The detection from 3c279 in 2006 constrained the  $\gamma$ -ray horizon (Albert et al., 2008a).

---

# 3

---

## Cherenkov Technique

Cosmic rays are mostly atomic nuclei, electrons, gamma rays and neutrinos. These cosmic rays interact with the atmosphere and produce cascades of particles<sup>1</sup>. Therefore, due to the opacity of the atmosphere,  $\gamma$ -rays cannot be measured from ground-based instruments as the case of optical light, for example (see Fig. 3.1). Nevertheless, the atmospheric absorption can be circumvent using satellites as e.g. *Fermi* for  $\gamma$ -rays observations. However, in the case of Very High Energy (VHE)  $\gamma$ -rays the required collection area is very big, due to the low fluxes, and instruments with the required sizes cannot yet be sent into Space. Thus, the only way to measure VHE  $\gamma$ -rays is using indirect methods from ground, based on the  $\gamma$ -ray induced air showers which produce Cherenkov radiation. A general overview about Air Showers will be given in this chapter, more detailed explanations can be found e.g. in Longair (1992) and Longair (1994).

### 3.1 Air showers

The Air showers (AS) are mainly produced in the troposphere, because that layer (located between the surface of the Earth till 10-12 km above sea level) concentrates 99% of the atmospheric mass. Different types of cosmic rays can produce air showers and the characteristics of the produced cascade depends directly on their progenitor particle. The primary particles interact with air molecules producing new particles, and these in turn interact again with air molecules and so on. This kind of interactions requires a given energy threshold (the critical energy), so that the shower will be growing while the secondary particles have enough energy to create new particles, then a maximum will be reached and the shower will decrease due to losses by ionization and Compton scattering. The typical height of this maximum depends directly on the energy of the primary particle.

According to their origins, AS can be classified into two main groups; on the one hand those produced by a nucleon called hadronic showers and on the other hand, those arising from an electron or a  $\gamma$ -ray in which case they are known as electromagnetic cascades. Henceforth, I will address both types of air showers to establish the main differences based

---

<sup>1</sup>except low energy neutrinos due to its low level of interaction which are capable to cross the Earth without interaction.

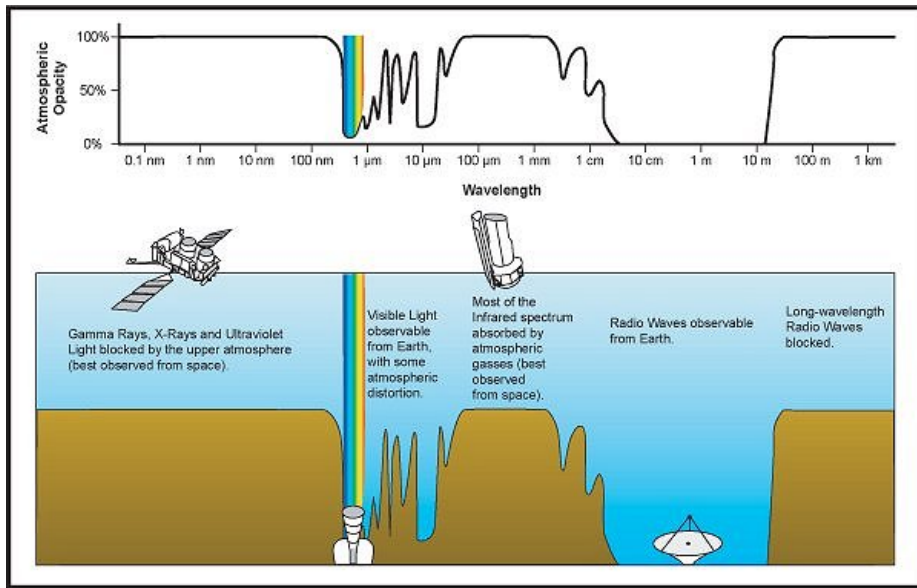


Figure 3.1: Atmospheric transmission at different energy ranges. Adopted from <http://www.astro.queensu.ca/~hanes/PHYS015-2010/Notes/T05-Pt04-Full-Spectrum.html>.

on which a possible  $\gamma$ -ray can be distinguished from a nucleon.

### 3.1.1 Electromagnetic air showers

The electromagnetic air showers induced by a  $\gamma$ -ray start with an electron-positron pair ( $e^- - e^+$ ) creation (Fig. 3.2). The two particles are slowed due to the presence of an electric field generated by a nucleus in the atmosphere, and a photon is emitted via *Bremsstrahlung*. The average energy lost due to this process of deceleration is proportional to both the energy of the particle and the mean free path that depends on the characteristics of the medium, in this case the atmosphere.

$$-\frac{dE_e}{dX} = \frac{E_e}{X_e} \quad (3.1)$$

where  $E_e$  is the particle energy,  $X$  the traveled distance and  $X_e$  the mean free path which in case of an electron in the Earth atmosphere is  $X_e = 37 \text{ g cm}^{-2}$ .

The critical kinetic energy of a  $\gamma$ -ray in order to be able to produce an  $e^- e^+$  pair is about 1 MeV. If the kinetic energy of these electrons and positrons is higher than 81 MeV, *Bremsstrahlung* will be dominant in the energy loss process. In case of lower energies only the ionization process will take place and no cascade can develop. Thanks to the pair production process and *Bremsstrahlung*, new particles are created up to the point at which the particles reach the critical energy. The number of created particles grows exponentially with the length of the cascade until it reaches a maximum (when the average energy of particles in the cascade is equal to the critical energy), from there on the cascade decays. Because of the Earth's magnetic field, the charged particles are deflected slightly from the

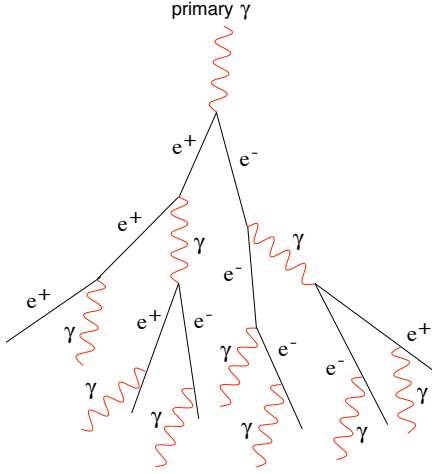


Figure 3.2: Sketch of an electromagnetic shower.

incidence direction of the primary photon or electron.

The longitudinal evolution of the air shower depends on the energy of the incident particle and the traveled path in the atmosphere (directly correlated with time). A widely used analytic approximation is called Rossi's Approximation B (Rossi, 1952; Greisen, 1956):

$$N_e(t, E_0) \simeq \frac{0.31}{\sqrt{\ln(E_0/E_c)}} \cdot \exp[t \cdot (1 - 1.5 \ln s)], \quad (3.2)$$

where  $E_0$  is the energy of the progenitor photon,  $E_c$  the critical energy for the *Bremsstrahlung* process, and  $s$  is the age parameter which combines the time and the incident  $\gamma$ -ray energy  $E_0$  as follows:

$$s = \frac{3t}{t + 2 \ln(E_0/E_c)}, \quad (3.3)$$

where the time  $t$  is defined in terms of traveled path units of  $X_e$  which depend on the atmospheric characteristics and the incidence angle of the progenitor  $\gamma$ -ray.

In Fig. 3.3, the dependence between the initial energy of the  $\gamma$ -ray and the average longitudinal development of the shower is sketched. The showers generated by low energy  $\gamma$  photons die out before they reach the ground (i.e. in the case of the MAGIC telescopes at a height of 2200 m above sea level, this happens for energies lower than approx. 200 GeV).

Together with a longitudinal evolution, a transversal development takes place in the shower. It is due to the multiple scattering affecting electrons and positrons which translates into a dispersion from the cascade's central axis. The transversal development can be parametrized by the *Molière* radius (Eq. 3.4),  $R_M$ , in a cylinder of which cylinder is contained 90% of the shower. 99% of the particles are contained in a cylinder with radius of radius  $3.5 M_R$ .

$$R_M = 21.1 \text{ MeV} \cdot \frac{X_0}{E_c} \approx 9.3 \text{ g cm}^{-2}, \quad (3.4)$$

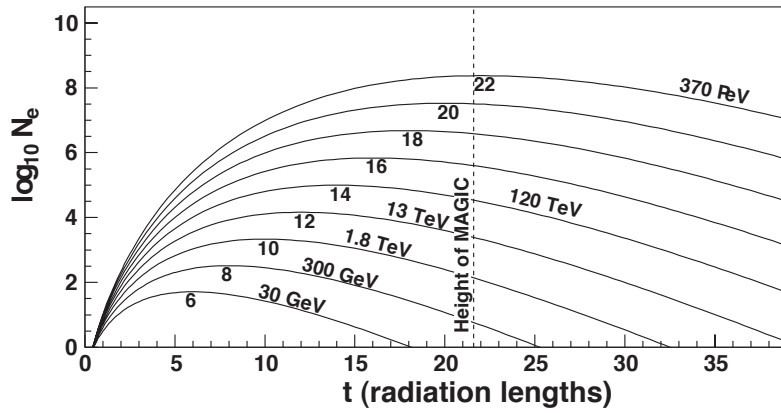


Figure 3.3: Longitudinal development of an electromagnetic shower for different values of  $\ln(E_0/E_c)$ . The X-axis represents the radiation length ( $t$ ) while in the Y-axis the number of electrons (and positrons) is represented in logarithmic values. Taken from Gaug (2006).

where  $X_0$  is the radiation length and  $E_c$  is the critical energy.

The lateral evolution of the electromagnetic shower is modeled by the Nishimura-Kamata-Greisen (NKG) formula:

$$\rho(r, t, E_0) = K \cdot \frac{N_e(t, E_0)}{R_M^2} \cdot \left(\frac{r}{R_M}\right)^{s-2} \cdot \left(1 + \frac{r}{R_M}\right)^{s-4.5}, \quad (3.5)$$

where  $\rho(r, t, E_0)$  is the electrons' and positrons' density as a function of the distance to the cascade axis ( $r$ ) and the time, expressed in units of radiation lengths and the energy of the incident  $\gamma$ -ray.  $K$  is the normalization constant. This formula however is valid only in the range  $1.0 < s < 1.4$ .

Moreover, there are important fluctuations in the development of the showers even if they have been produced by  $\gamma$  photons of the same energy since the process is very sensitive to random processes.

### 3.1.2 Hadronic air showers

Hadronic showers (see Fig. 3.4) are created by the collision between two nuclei, that is a nucleon coming from Space with an atom in the Earth's atmosphere. In this process, mainly muons, pions, kaons, photons and neutrinos are created, which together with fragments from the primary nucleon form the particle cascade. These particles will continue to interact with atmospheric particles, until the energies of the particles reach the threshold energy needed for pion creation (approx. 1 GeV). In these showers, components of three different kinds can be found hadronic, electromagnetic and muonic ones.

- **Hadronic component:** The hadronic shower core is composed of nucleons, mesons, kaons, neutrinos, etc. Some sub-atomic particles are heavy, thus the transfer of transverse moments can be important and is passed onto the decay products of the heavy particle.

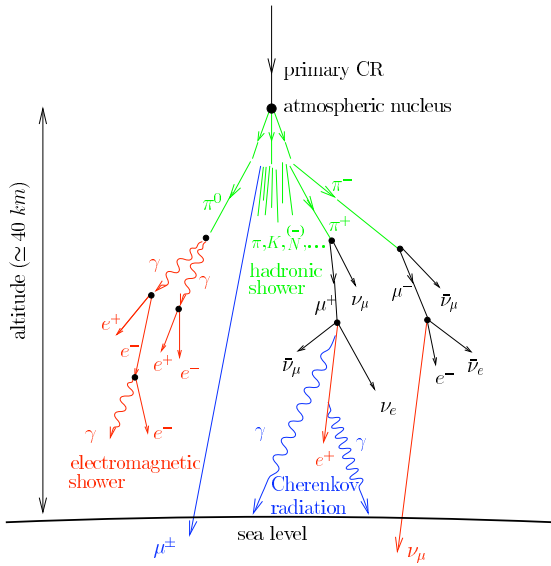


Figure 3.4: Sketch of a hadronic shower.

- **Electromagnetic component:** This component consists of electrons, positrons and photons produced in secondary electromagnetic showers. This part of the shower is created by the decay of neutral mesons, mainly neutral pions which decay almost instantly into two photons. There is a continuous energy transfer from the hadronic component to the electromagnetic one which is the dominant process of the evolution. The electromagnetic component can become completely separated from the hadronic part. This electromagnetic part could be later confused with a pure electromagnetic shower. It forms part of the Cherenkov telescope background which cannot be subtracted.
- **Muonic component:** Charged pions and kaons decay in muons and neutrinos. The neutrinos cannot be detected by the Cherenkov telescopes, but the muons can be seen and are usually distinguishable due to their ring shape (Fig. 3.5).

In summary, the principal secondary particles created in a hadron air shower are protons, neutrons, electrons, positrons, charged pions, muons and neutrinos. The overall flux measured from these particles can be found in Fig. 3.6. One can see that the flux of all particles decreases rapidly as they penetrate the atmosphere with the exception of muons and neutrinos which show a flat flux dependency with height. The Cherenkov light emitted by muons create a distinct signature which can be later used in the analysis.

The mean free path for a hadronic shower can be defined as in the case of electromagnetic showers (Eq. 3.1), with  $X_h = 83 \text{ g cm}^{-2}$  and  $X_p = 107 \text{ g cm}^{-2}$  for pions. Comparing these number with the mean free path for electrons ( $X_e = 37 \text{ g cm}^{-2}$ ), one can see that protons and pions are much more penetrating in the atmosphere than electrons, thus hadronic

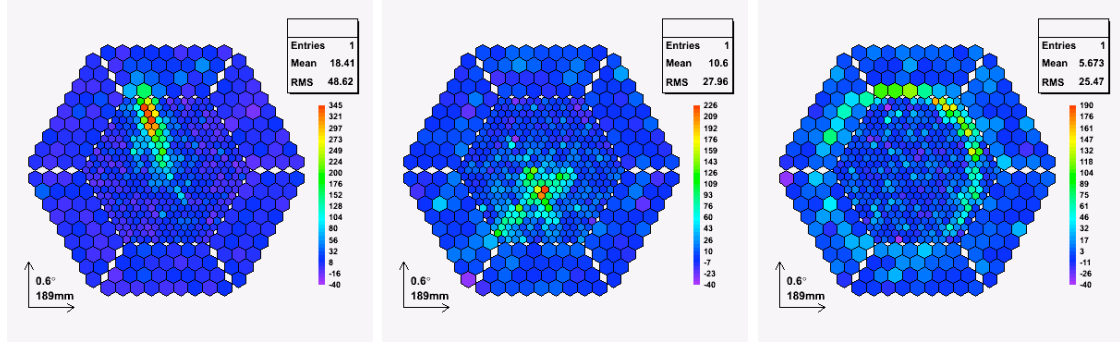


Figure 3.5: Projection in the camera plane of showers from different progenitor particles. From left to right: an electromagnetic shower, a hadronic shower and a muon ring. Taken from Gaug (2006).

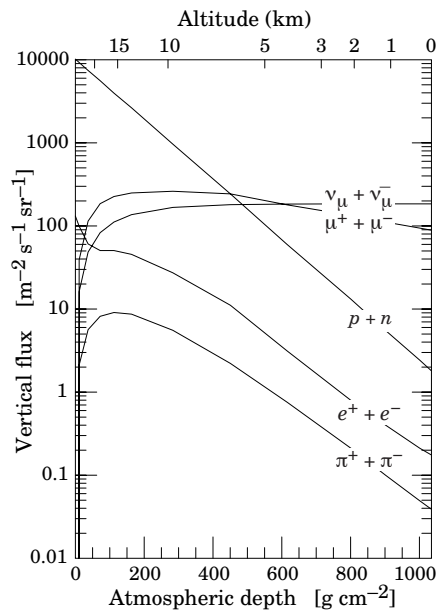


Figure 3.6: Vertical flux of different particles as a function of atmospheric depth.

showers have a larger development in the atmosphere than electromagnetic ones.

The electromagnetic showers are quite simple, compact and symmetric with respect to the main axis of the shower, while the hadronic ones are spread further out and appear more asymmetric.

## 3.2 Emission from Air Showers

### 3.2.1 Cherenkov radiation

Most of the particles generated in the air showers are relativistic and produce Cherenkov emission in the atmosphere. The Cherenkov radiation is produced as response of a medium when a charged relativistic particle travels through it at a speed higher than the speed of light in that medium. The atoms and molecules of the medium which are close to the relativistic particle path are polarized due to the electric field created by the particle (Fig. 3.7), and, once the particle is far from the region, they turn back to their original configuration. During the polarization state the atoms behave as dipoles which more coherently when the traveling particle is close. If the particle is not relativistic the dipoles are organized in a symmetric configuration but if the speed of the particle is higher than the speed of light in the medium, the distribution of the dipoles is not symmetric anymore and produces a net polarization field (Fig. 3.7).

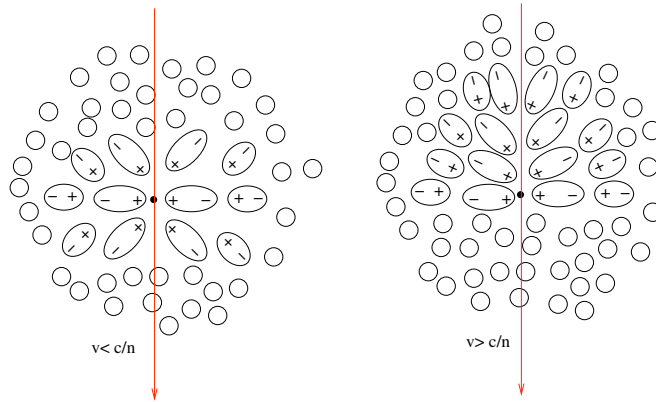


Figure 3.7: Polarization sketch of a dielectric medium through which a charged particle moves. On the left, the effect produced by a particle travelling with a velocity lower than the speed of light in the medium and on the right, by a particle travelling faster than the speed of light in the medium.

Therefore, charged relativistic particles travelling through the Earth's atmosphere, which is the case of air showers, produce Cherenkov radiation. This radiation is generated whenever the threshold condition is met:

$$E > m_0 c^2 \cdot \frac{n(\lambda)}{\sqrt{n(\lambda)^2 - 1}}, \quad (3.6)$$

where  $m_0$  and  $E$  are the rest mass and the energy of the relativistic particle, respectively,

and  $n(\lambda)$  the refraction index of the medium as a function of the wavelength. Since the refraction index of the atmosphere depends on the altitude, the condition will depend not only on the energy of the particle, but also on the height in the atmosphere, so that the energy threshold will change as the particle moves downwards.

Cherenkov radiation is emitted in a small cone centered around the particle trajectory, which aperture angle is called Cherenkov angle ( $\theta_c$ ) and is defined as:

$$\cos(\theta_c, \lambda) = \frac{1}{\beta n(\lambda)}, \quad (3.7)$$

where  $\beta$  is the velocity of the particle in units of the speed of light and  $n(\lambda)$  the refraction index as a function of the wavelength.

The Cherenkov angle will depend on the altitude, as the refraction index. During the development of the air shower, several particles emit at the same time, thus the resulting emission spectrum is a superposition of the emitting cones, the so-called *Cherenkov light pool* (Fig. 3.8), with a typical radius of  $\sim 120$  m, depending on the observation zenith angle.

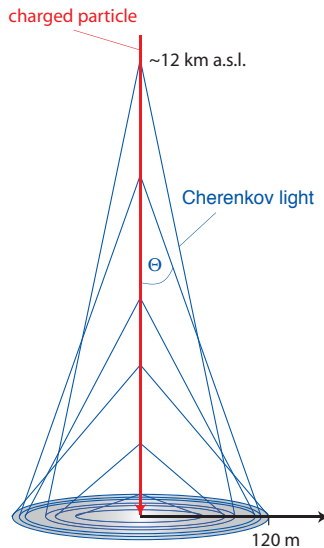


Figure 3.8: *Cherenkov light pool* produced as the overlap of different Cherenkov emission cones.

Cherenkov light is seen as very fast flashes, its duration depends on the type of AS. In case of electromagnetic showers, it lasts typically  $\sim 3\text{-}10$  ns while in case of a hadronic ones, the durations of the light flashes can be longer.

The Cherenkov spectrum can be described as:

$$\frac{d^2N}{dxd\lambda} = \frac{2\pi\alpha}{\lambda^2} \cdot \left(1 - \frac{1}{\beta^2 n^2(\lambda)}\right), \quad (3.8)$$

$$\frac{d^2N}{dEdx} \approx 370 \sin^2 \theta_c(E) \text{ eV}^{-1} \text{cm}^{-1}, \quad (3.9)$$

where  $\beta = v/c$  and  $\alpha \sim 1/137$ , the fine structure constant,  $\lambda$  the wavelength of the emitted Cherenkov photon and  $x$  is the unit path length of the particle.

In case of an electromagnetic shower, around 500 Cherenkov photons are produced in total per each GeV of energy coming from the progenitor photon. The Cherenkov spectrum covers the UV-optical range from less than 300 nm down to radio wavelengths. Nevertheless, not all these photons can reach the telescope detector, due to the interaction with the atmosphere (Fig. 3.9). There are several factors which have to be taken into account:

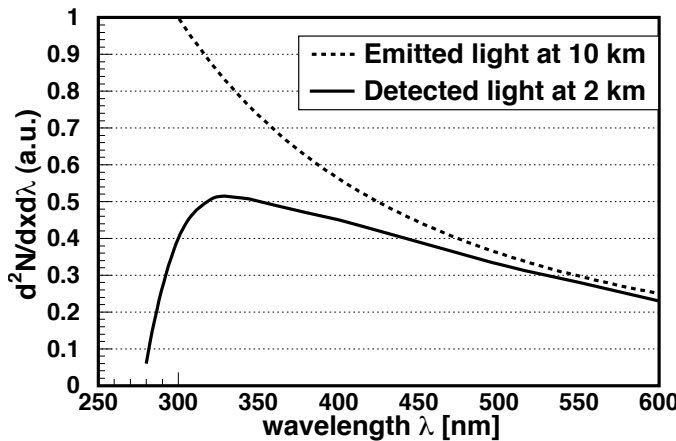


Figure 3.9: Part of the Cherenkov spectrum emitted from an AS (dotted line) and the detected one (solid line). The difference is due to atmospheric effects (see the text for more information).

- Observation zenith angle: The Cherenkov photons interact with the atmospheric components while travelling to the ground, thus they can be absorbed and scattered. The longer the path in the atmosphere, more likely becomes an interaction with other particles. Then, the zenith angle plays a key role in this process, since Cherenkov light stemming from showers with low energy, may not reach the telescopes at all, depending on the zenith angle of observation.
- Scattering:
  - **Rayleigh scattering:** It is due to the interaction with atmospheric molecules. The cross-section of this process depends on the wavelength as  $\lambda^{-4}$  and is typically the most important effect during observation in good weather conditions observations.
  - **Mie scattering:** This process is due to the interaction between the photon and particles whose sizes are larger than the photon wavelength (e.g. water drops, dust grains, small icy crystals). This scattering process will be the dominant one in case of not optimal observation conditions, such as under the presence of clouds or *calima*<sup>2</sup>. The effective cross section depends on the wavelength as  $\lambda^{-a}$  where  $1 \leq a \leq 1.5$ .

<sup>2</sup>Presence of Saharian dust in suspension in the atmosphere.

- **Multiple scattering:** The secondary particles created in the air shower can move away from the central axis due to multiple interactions. The Cherenkov photons produced by these scattered particles will produce a halo around the Cherenkov light pool. The radius of the Cherenkov light pool and the halo dimensions depend on the zenith angle of the observation.

### 3.2.2 Fluorescence

Like the Cherenkov radiation, the fluorescence emission is produced by a charged particle traversing the atmosphere. The air atoms not only are ionized due to the charged particle's movement but also get excited to meta-stable electron levels. The mean life time of these excited states is short, they decay to the ground level and emit characteristic UV fluorescence light. Fluorescence light comes mainly from Nitrogen atoms since it is the most important component of the Earth's atmosphere, peaking at wavelengths from 300 nm up to 430 nm (The Pierre AUGER Collaboration et al., 2010). Its emission is isotropic and depends on the shower size so it can also be used for indirect measurements of cosmic rays. The energy threshold for fluorescence emission is  $\sim 10^{18}$  eV, thus this technique can only be used for UHECR studies e.g. the AUGER experiment.

## 3.3 The Cherenkov imaging technique

Imaging Atmospheric Cherenkov Telescopes (IACTs) use the Cherenkov radiation emitted by air showers for indirect measurements of  $\gamma$ -rays from the ground. As can be seen in Fig. 3.9, most of the *Cherenkov* emission from air showers is detected in the optical range. Nevertheless, standard optical telescopes cannot be used for this technique, due to the rapid evolution of this kind of emission. In order to capture an image of the air showers, several important factors have to be taken care of in the telescope design: fast response of the photo-detectors, large collection areas are needed in order to collect as much light as possible from the Cherenkov light pool, etc. These design requirements not only depend on the nature of the Cherenkov emission, but also on the desired targets, for example most of the galactic sources emit from medium to high energies ( $E > 250$  GeV) while GRBs or AGNs typically emit at lower energies ( $E < 100$  GeV). So the energy threshold of the instrument is an important parameter for the physical studies to be achieved.

A very sophisticated analysis method is needed for two main reasons: On one hand the projection of the shower onto the camera plane has to be carefully studied, typically using image parameters (e.g. Hillas, 1985), which allow us to derive information about the AS development (more details can be found in Sec. 5.5). On the other hand, air showers are not only produced by  $\gamma$ -rays but also from other sources of cosmic rays. This translates into a very small relative  $\gamma$ -ray rate ( $\sim 10^{-4}$  for the strongest steady sources). The discrimination procedure therefore needs to be powerful. A first step to achieve this goal is already implemented as part of the telescope hardware (the trigger, see Sec 4.5) which performs a first background rejection, but afterwards a sophisticated offline processing of the data is necessary. There are different background types and, depending on their nature, the rejection will be more or less complicated:

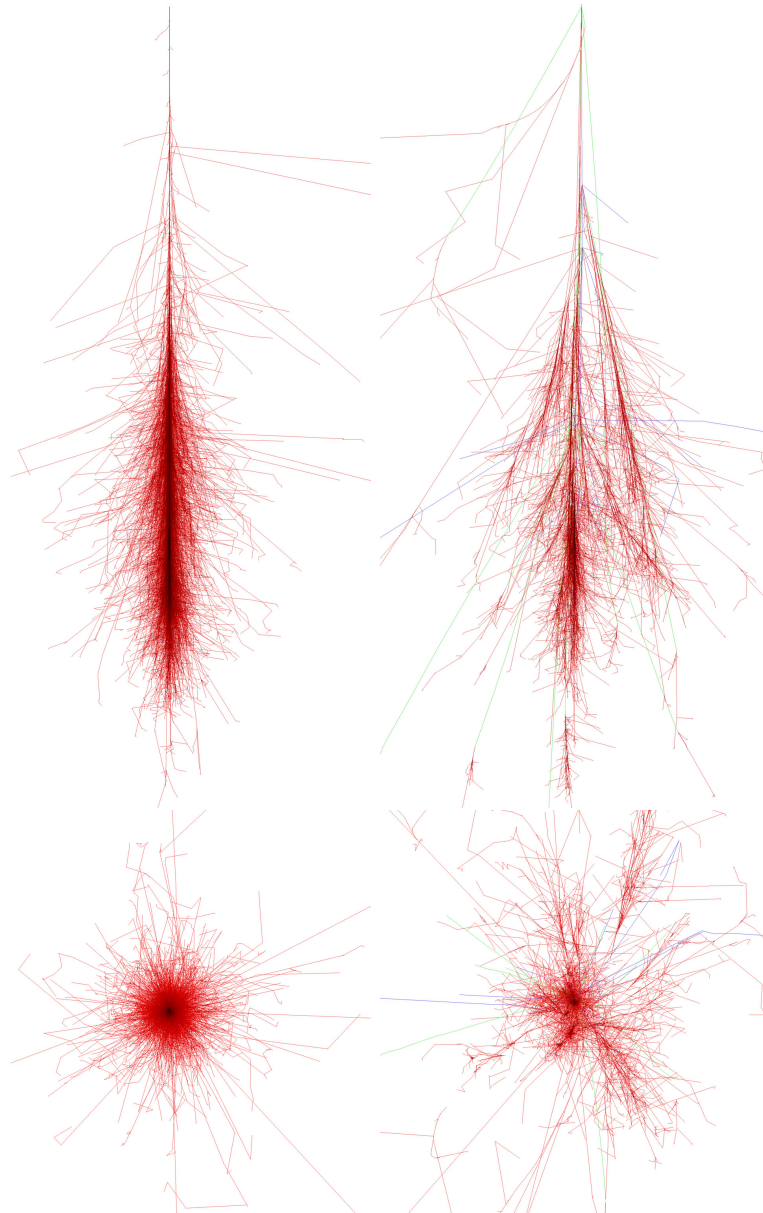


Figure 3.10: Simulations for a photon (left) and proton (right) generated AS, assuming an energy of 100 GeV and observed at zenith. The upper plots represent the shower evolution while the bottom ones are the projected view at ground (taken from F. Schmidt, ‘CORSIKA Shower Images’, <http://www.ast.leeds.ac.uk/~fs/showerimages.html>).

- **Night Sky Background (NSB):** The NSB is due to the emitted light from stars, galaxies, the moon, human light pollution, etc. It depends strongly on the observations conditions, the presence of bright stars in the FoV of the telescope, the observed part of the sky, the presence of clouds, zodiacal light, etc.
- **Hadrons:** The hadronic showers constitute a very important source of background. Their rejection can be achieved due to geometrical differences. While electromagnetic showers are more compact and simple, the hadronic ones present a much more complex structure which translates into more compact images for  $\gamma$ 's and more dispersed ones for hadrons. These, moreover, present a higher number of unconnected clusters (called number of islands), as can be seen in Fig. 3.10. Finally, the arrival time structure for different parts of the shower is different (Aliu et al., 2009b).
- **Cosmic electrons:** The electromagnetic air showers are not only produced by  $\gamma$ -rays, but are also due to electrons. The developed showers cannot be distinguished from  $\gamma$ -ray-induced air showers and, thus, they cannot be rejected. They constitute a source of irreducible background, however they are isotropically distributed.
- **Muons:** Typically, the projection of the emitting cone is a ring shape which is easy to be differentiated from  $\gamma$  showers, but at low energies ( $E < 100$  GeV) only parts of the ring can be seen which can be then confounded with a  $\gamma$ -like image shape. Another difference from gamma-like shower is that the muonic showers are produced more closer to the ground than the gamma-like ones.
- **Diffuse  $\gamma$ -rays:** There are  $\gamma$ -rays generated by unresolved sources which result in identical AS but without a privileged direction. In principle, this kind of events cannot be avoided and produces an irreducible background such as the cosmic electrons.

The background events are distributed isotropically while the showers produced by  $\gamma$ -rays which come from the observed source have a privileged incident direction. Therefore, a large amount of background events can be rejected selecting the incident direction in which the  $\gamma$ -ray source is expected to be.

The use of more than one telescope operating in stereoscopic configuration (see Fig. 3.11) can achieve better rejection of these backgrounds, in addition to a better angular resolution and energy estimation.

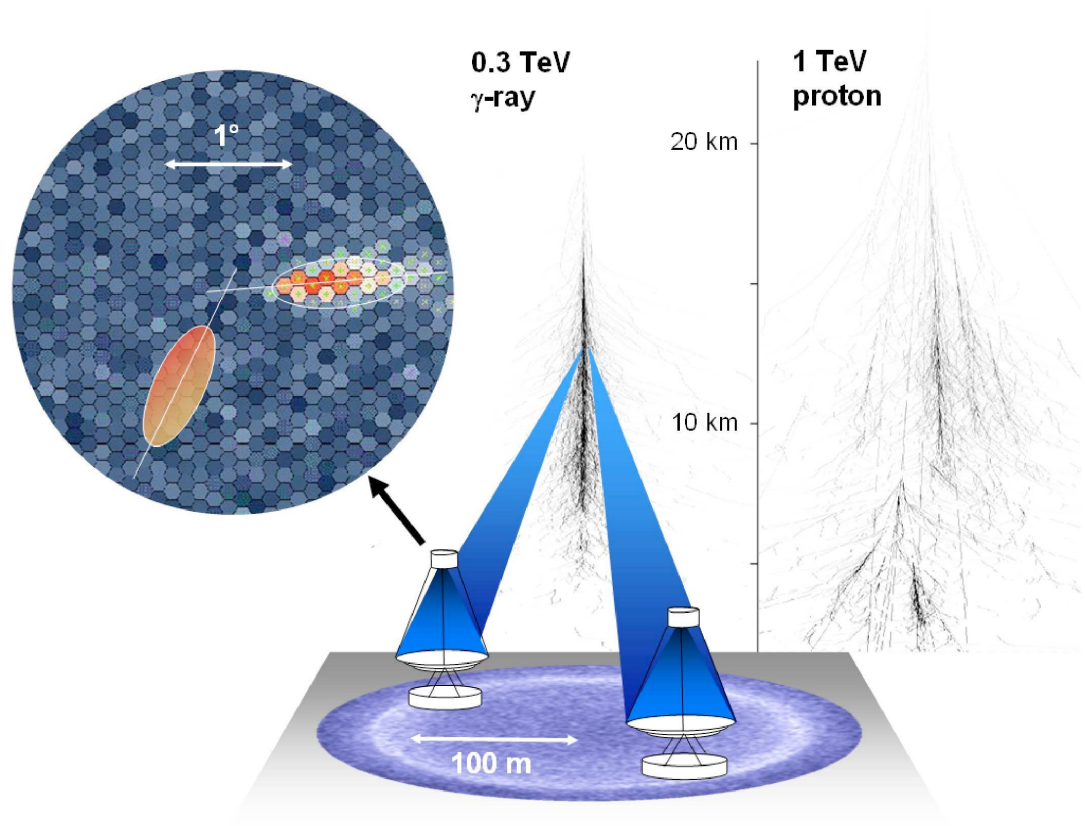


Figure 3.11: Schematic view of *Cherenkov telescopes*, taken from Hinton and Hofmann (2009).



---

# 4

---

## The MAGIC telescopes

The MAGIC (Major Atmospheric Gamma Imaging Cherenkov) stereo system is composed of two Imaging Atmospheric Cherenkov Telescopes (IACTs). Fig 4.1 shows a photo of them. The first phase of the project started on August 2004, operating only one telescope, called MAGIC-I, later in November 2009, it became a stereoscopic system after the construction of the second telescope, placed at approximately 85 m from the first and dubbed MAGIC-II. The MAGIC telescopes are currently the largest stand-alone operative telescopes of their kind in the world, with a diameter of 17 m each. They are situated at 2200 m altitude at the Observatorio del Roque de los Muchachos, on the Canary island of La Palma, Spain (N 28.45°, W 17.53°).

MAGIC-I and MAGIC-II follow the same design concepts and most of the MAGIC-II components are a copy of MAGIC-I, except for some technological improvements that have been included in MAGIC-II. As a matter of fact, an upgrade for the MAGIC-I telescope will be carried out during summer 2011 adopting several design improvements introduced for MAGIC-II.

The MAGIC telescopes are optimized to measure VHE  $\gamma$ -rays in the energy range from 50 GeV to few tens of TeV. Nevertheless, in certain observation configurations (mainly using the so-called “Sum Trigger”), the energy threshold can reach down to 25 GeV (Aliu et al., 2008).

### 4.1 The telescope structure and drive system

The telescope structure has been designed in view of two main aspects: on one hand, since there is no protection from a dome, it has to be very resistant to the inclemencies of the weather and robust to be able to support its large 17 m reflector. On the other hand, since the observation of GRBs is one of the physical objectives and this kind of phenomena is very fast, the structure had to be light enough in order to be able to turn to different sky positions as fast as ever possible. A three-layer structure made of low-weight carbon fiber-epoxy tubes joined by aluminum knots was selected combining small weight with high rigidity. The camera is held on a metallic arch supported also by thin steel cables. It is mounted in an alt-azimuth configuration and placed on a circular rail of 18 m diameter,



Figure 4.1: The MAGIC telescopes. Taken from <http://magic.mppmu.mpg.de/gallery/index.html>.

which allows to point the telescope slightly below the horizon.

The total weight of the frame is less than 60 tons and the weight of all moving components amounts to 72 tons (Bretz et al., 2009). Thanks to its powerful drive system and light weight, the telescope is able to point to a given position in the sky within less than 20 seconds.

## 4.2 The mirrors

Both telescopes' reflectors consist of a 17 m diameter tessellated parabola, holding 247 individual panels of  $1 \text{ m}^2$  with a focal length of 17 m. The reflector is parabolic in order to maintain the timing information of the recorded photons. The panels can be heated to prevent icing and dew accumulation. In the case of MAGIC-I, each individual panel is composed of 4 mirrors while in the case of MAGIC-II, the panels are one single mirror (see Fig. 4.2). Three types of mirrors have been used for the telescopes. The reflector of MAGIC-I is mainly formed of  $0.25 \text{ m}^2$  aluminum mirrors with exception of a couple of  $1 \text{ m}^2$  aluminum mirrors which were installed for test purposes. Out of the 247 mirror tiles of MAGIC-II, 143 are aluminum mirrors, while the remaining 104 are made of glass. The total area of the reflecting surface is  $234 \text{ m}^2$ . More details can be found in Tescaro (2010).

The movement of the reflector structure can produce a misalignment of the mirrors, especially when the telescope moves in elevation due to the weight of the mirrors and the structure. In order to correct for this effect, the mirrors are adjusted by an Active Mirror Control (AMC) system, depending on the orientation of the telescope. The alignment of the panels is corrected online, using a laser situated in the middle of each panel. These lasers point to the camera so that the position of each panel can be checked. Moreover, look-up tables (LUTs) are created from the reflection of individual stars onto the camera by each mirror panel. The radius of curvature of each mirror is adequate for its position on the

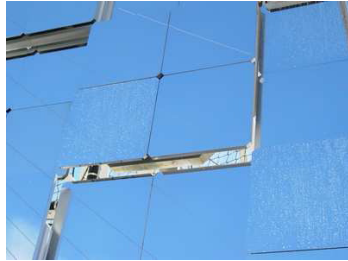


Figure 4.2: A MAGIC-I reflector panel composed of four mirrors is shown.

paraboloid.

The reflector is usually focused to 10 km, because this corresponds to the typical height of the shower maximum for a 100 GeV gamma-ray induced shower at low zenith angle observations.

### 4.3 The camera

The camera works in the optical range. However, the typical optical cameras cannot be used for IACTs since a very fast response is needed due to the intrinsic nature of the Cherenkov light flashes from air showers and for the gamma/background separation. For this reason, photomultipliers (PMTs) are used for *Cherenkov telescopes*. The PMTs of both cameras have an enhanced Quantum Efficiency (QE). Apart from that, the two cameras of MAGIC-I and MAGIC-II differ, so I will describe them independently.

The MAGIC-I camera has a hexagonal shape and consists of 577 hemispherical PMTs. In order to maximize the light collection, each PMT is equipped with a hexagonal light guide, approaching the form of a Winston cone. There are two types of phototubes, the inner part of the camera uses smaller PMTs (1 inch diameter), while the outer ring consists of larger PMTs (1.5 inch diameter). This difference is due to economic reasons. The choice does not affect much the sensitivity of the instrument, since small pixels are mostly needed for small  $\gamma$ -ray showers, which are detected at proximity to the camera center, while large showers spread out into the outer ring, where spatial resolution is not so critical anymore, due to the larger number of hit pixels. However, this applies only if the  $\gamma$ -ray source is observed in the centre of the camera or close to it and for point-like sources. The total FoV of the MAGIC-I camera is about  $3.5^\circ$ . Only pixels of the inner camera are included in the majority trigger, which has a FoV of  $\sim 2$  degrees. In Fig. 4.3 a picture and sketch of the both cameras can be found.

The MAGIC-II camera has a circular shape and is composed of 1039 pixels. This difference with respect to the MAGIC-I camera is due to the fact that only small PMTs of 1 inch diameter have been used, in order to achieve a more uniform response (Borla-Tridon et al., 2009). The quantum efficiency of the PMTs is higher than in the case of MAGIC-I. Nevertheless, the camera FoV is almost the same as that of the MAGIC-I camera, about  $3.5^\circ$  whereas the trigger FoV has increased to  $2.5^\circ$ . The pixels are grouped in seven PMTs packed in a cluster of hexagonal configuration. Also approximated Winston cones have

been used in order to guide the light to the PMTs.

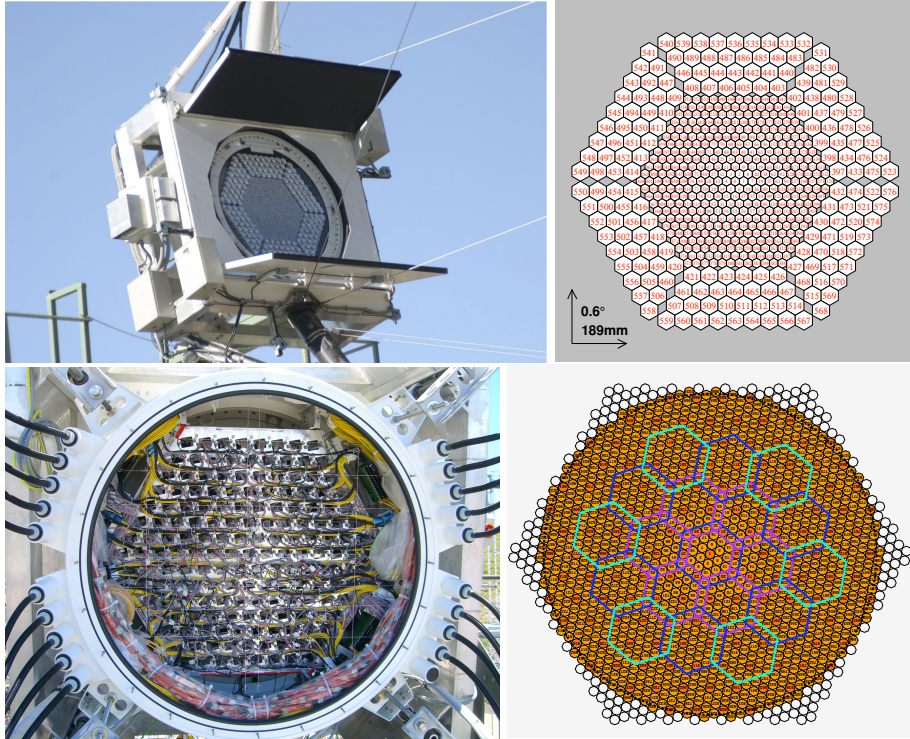


Figure 4.3: Pictures and schemes of the cameras of MAGIC-I and MAGIC-II. Taken from Tescaro (2010).

#### 4.4 The starguider

In addition to the PMT camera, there is a CCD camera installed in the center of the mirror dish, in order to monitor the tracking system and correct for a possible mispointing. This camera has a field of view of  $4.6^\circ$  in which it can see part of the telescope camera and a part of the sky. The starguider system compares the observed star positions with a catalogue of stars and measures the mispointing. This system is not only useful in order to check the pointing, but also for the data analysis since information about the atmospheric transparency can be derived from the number and apparent brightness of identified stars.

#### 4.5 The trigger

The trigger allows to reject background events which do not need to be recorded. Each telescope has its own trigger system and an additional stereo trigger connects both. This stereo trigger system allows to suppress the background much more efficiently.

The analogue signals from the PMTs are transferred via optical fibres to the receiver boards which are placed inside the control house. The reasons to have the receiver boards

outside of the camera are mainly two: reduced camera weight and the possibility to implement sophisticated trigger systems, as the so-called Sum Trigger, for example. Once the signal arrives at the receiver boards, it is split into two different paths which will travel through different systems. One part feeds into the trigger system and the other one goes to the readout system.

In case of MAGIC-I, only 325 inner camera pixels are used as trigger region, while for MAGIC-II 559 pixels are used (see Fig. 4.3), with a smaller overlap between each trigger patch, extending the trigger FoV. First, the signal goes to a discriminator which rejects fluctuations of the night sky background (NSB) or bright stars in the FoV adjusting different thresholds, the so-called Discriminator Thresholds (DTs), for each single pixel in the camera. This is done automatically by the *Individual Pixel Rate Control* (IPRC), called the *Level 0 Trigger*. The next step, the *Level 1 Trigger*, evaluates the topology of the signal. In this step, only signals above of a given threshold (*Level 0 Trigger*) and in coincidence with  $N$  neighbour pixels within a given short time  $\sim 3$  ns (typically  $N = 4$  or  $N = 3$ ), are selected. If at least one such cluster is discovered, a global event trigger signal is issued.

In addition to this trigger, the so-called *Level-3 (L3)* or stereo trigger imposes the condition to have a triggered event from both telescopes in a narrow time window  $\sim 100$  ns. There is a missing *Level 2 Trigger*, based on different topological criteria, which was constructed, but not used for standard data taking.

There is also a different trigger system used, called the Sum Trigger, which allows to decrease the energy threshold down to 25 GeV (Aliu et al., 2008). Until now, it has been only installed in MAGIC-I, but the MAGIC-II trigger system will be upgraded with a Sum Trigger next year. In this case, instead of analyzing patterns in clusters of pixels, the Sum Trigger divides the camera in patches (see Fig. 4.4) and adds the signal of all the PMTs of the patch. If the sum of the signals lies above a certain threshold the event will be saved. This method allows to detect smaller showers than the standard trigger, and hence to go down to lower energies.

There are two additional trigger configurations called calibration trigger and random trigger which are used to trigger the interleaved calibration and the interleaved pedestal events during the observation.

## 4.6 The readout system

The events which finally pass the trigger selection are saved using the readout system for the subsequent analysis. The  $\gamma$ -ray signals are very short in time and therefore fast readout electronics are required. Both telescopes digitize the signal at the same sampling speed but using very different electronics.

For MAGIC-I the Flash Analog to Digital Converters (FADCs) readout system (a scheme can be seen in Fig. 4.5), working at 2 GSamples/s, is used, installed in 2006 (Bartko et al., 2005). This system uses a fiber-optic multiplexing technique and commercial FADCs.

In case of MAGIC-II, the Domino Ring Sampler (DRS) is used (Pegna et al., 2006), working also at 2 GSamples/s. The analog signals are stored in a multi-capacitor bank that is organized as a ring buffer. In Fig. 4.6, one of the receiver boards is shown.

The signals are stored using a tree structure in the raw data, creating the files directly which will be processed later by the analysis chain.

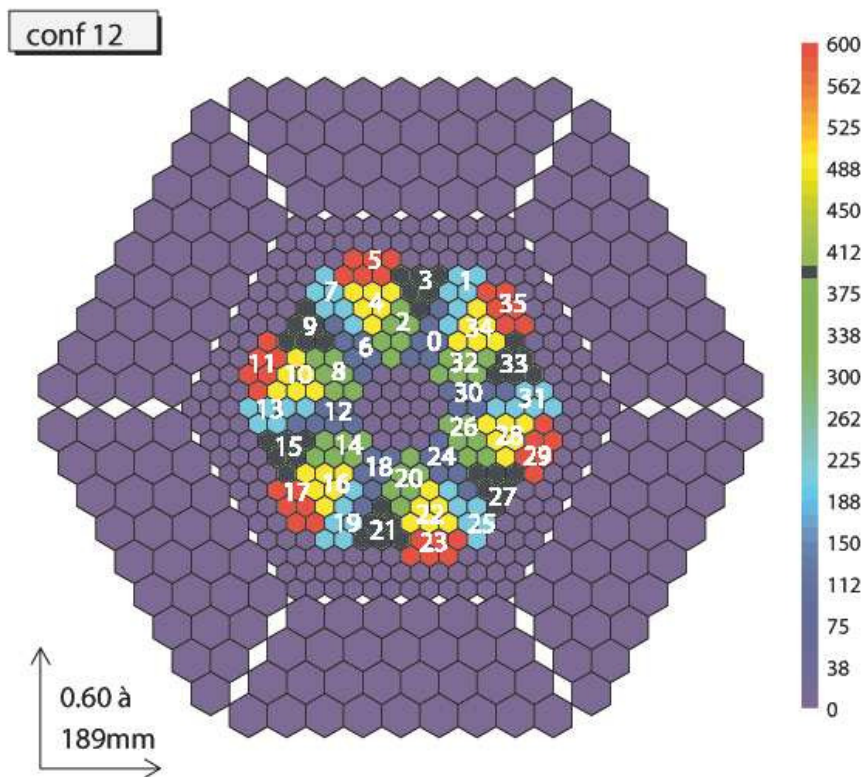


Figure 4.4: MAGIC-I camera sketch, where the colored regions represent different Sum Trigger patches.

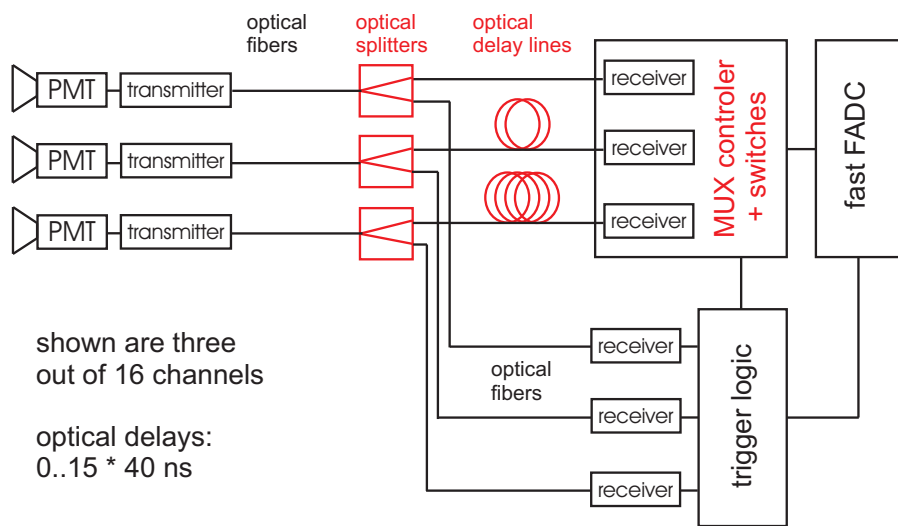


Figure 4.5: MAGIC-I readout system (Goebel et al., 2007).



Figure 4.6: Domino board.

## 4.7 The calibration system

The signals coming from the readout system have to be converted back into Cherenkov light fluxes impinging onto the camera. For this purpose, the calibration system is used, which calculates the relation between the number of FADC counts from the readout system, and the number of photo-electrons collected by the corresponding camera pixel. In order to do so, controlled light-pulses are sent to the camera and the response of the system is measured such that corresponding conversion factors can be estimated. Since the quantum efficiency can change from pixel to pixel, two different calibrations are needed, first a relative calibration between the PMTs and then, an absolute one which adjusts the response of the camera to the observed flux.

For MAGIC-I, the calibration system is composed of 64 LEDs emitting at three different wavelengths: 370 nm (UV LEDs), 460 nm (blue LEDs) and 520 nm (green LEDs), which emit fast light pulses at different intensities. It is located in a box in the center of the mirror dish, just in front of the camera (see Fig. 4.7).

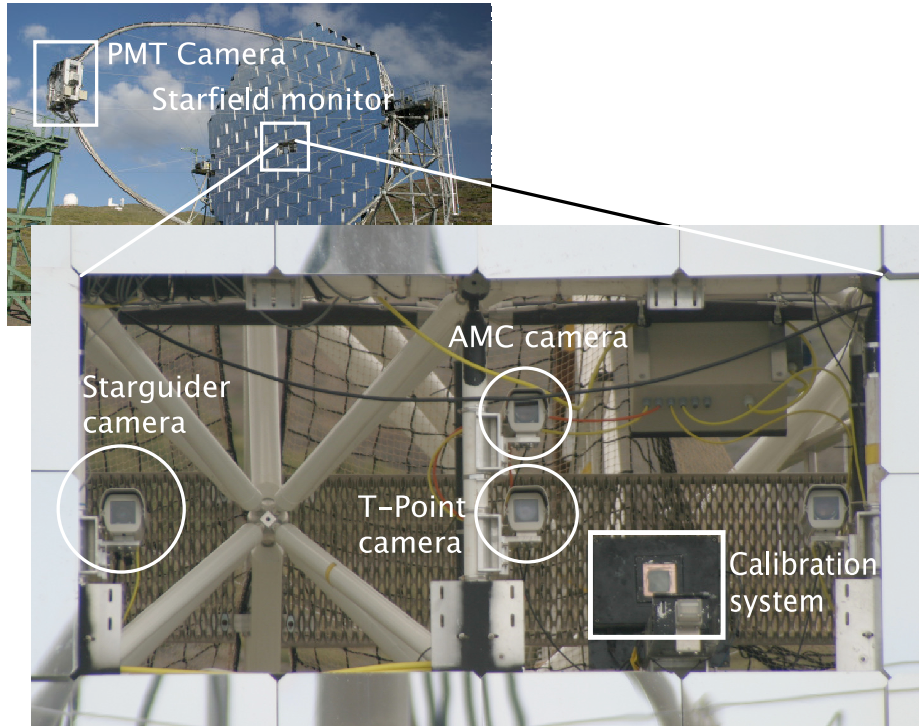


Figure 4.7: A photo of the Calibration box. Taken from Mazin (2007)

In the case of MAGIC-II, instead of LEDs, the solution adopted is a Nd-YAG laser, operating at its third harmonic at 355 nm. In order to provide a large dynamic range, two rotating filter wheels are situated between the laser and the camera and provide different intensities. The laser box is located at the central region of the mirror dish as in the case of the MAGIC-I telescope.

## 4.8 Observation modes

Basically there are two different observing modes. The so-called On-Off mode, where the telescope points directly to the observed source, while in the so-called Wobble mode the source is observed 0.4 degrees off-center.

**On-Off mode:** The telescope tracks the source in the center of the camera, creating the so-called On data. Additionally, Off data have to be taken with no known  $\gamma$ -ray source in the FoV and where the observed sky region has similar characteristics with respect to NSB, zenith distance, weather conditions, etc. as the On data. The normalized Off data will be subtracted in the analysis from the On data, to obtain the signal from the source.

Since the sensitivity drops with the distance from the camera center, this kind of observation is more sensitive, but one needs to take dedicated Off data at the cost of additional observation time. Sometimes, the On and Off observations do not match properly, since the observation conditions may have changed when the corresponding Off data are taken.

**Wobble mode:** In this types of observation, the source is observed displaced by typically 0.4 degrees from the center of the camera and the camera swaps the offset position by  $180^\circ$  every 20 minutes. If we assume that the response of the camera is homogeneous, we would record On and Off data at the same time, because when the source is at one position, the opposite one (called anti-source) can be used as Off data, see Fig. 4.8. The advantages of this method is to save observation time since no dedicated Off data has to be taken. Moreover, Off data are taken under similar conditions, so a better match between On and Off data is achieved. However, this method has also two points against: first, the assumption of the camera homogeneity is not completely true and second, since the sensitivity of the camera at 0.4 degrees from the center is lower than in the camera center, this observation mode is less sensitive. Taking into account the gain of observation time, the overall sensitivity is better in Wobble mode, however.

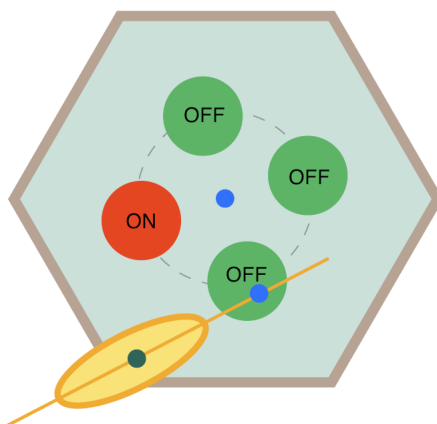


Figure 4.8: Sketch of the denition of the signal (On) and background (Off) regions in wobble observations. The red circle represents the On position while the anti-source is located at  $180^\circ$ . Taken from Mazin (2007)

## 4.9 The GRB alert system

In order to speed up the GRB observation as much as possible, all the observation process has been adapted for an automatic program, which guarantees minimal human interaction. This program is called *gspot* (Gamma Sources POinting Trigger). MAGIC receives automatic alerts from the GRB Coordinates Network (GCN)<sup>1</sup> which issues GRB observation alerts from satellites and their coordinates, often available within tens of seconds from the start of the burst, making possible a great multi-wavelength coverage. The MAGIC program *gspot* is working in two steps: it continuously filters out alert packages from selected satellites which fulfil pre-defined MAGIC observation criteria. If the alert fulfils the requirements, *gspot* will send the coordinates to the central control and will activate the fast movement of the telescope to point to the GRB coordinates.

## 4.10 The KVA telescope

In collaboration with MAGIC, the Kungliga Vetenskapsakademien (KVA) telescope is used for long term optical monitoring as part of the Tuorla blazar monitoring program<sup>2</sup>. KVA is a 35 cm telescope placed close to the MAGIC telescope and can be controlled remotely. It consists of two telescopes, the larger one being a 60 cm (f/15) Cassegrain telescope equipped with a CCD polarimeter capable of polarimetric measurements in the BVRI-bands, using a plane-parallel calcite plate and a super-achromatic lambda/2 retarder. The 35 cm telescope is used for photometric measurements in the B, V and R-bands. The photometric measurements are made in differential mode, i.e. by obtaining CCD images of the target and calibrated comparison stars in the same field of view.

---

<sup>1</sup><http://gcn.gsfc.nasa.gov>

<sup>2</sup><http://users.utu.fi/kani/1m>

---

# 5

---

## The Analysis Chain

In this chapter, I will give an overview about the analysis process. As usually, the aim of the observation from telescopes is to measure fluxes, in the case of Cherenkov telescopes the objective is to estimate the flux of cosmic  $\gamma$ -rays from a given sky position. From the emission of these  $\gamma$ -rays onwards, these suffer a lot of interactions, first with the surrounding medium, later on their travel through space and finally with the atmosphere and with the different components of the telescope. The final data we get from the telescope are affected by all these processes and have to be corrected. We could say, the analysis chain should invert the whole path traveled by the  $\gamma$ -rays from their birth to our readout system. All this process is performed using the standard MAGIC software, called MARS (MAGIC Analysis and Reconstruction Software, Moralejo et al., 2009) which has been developed by the MAGIC collaboration and is based on the C++ data analysis software ROOT<sup>1</sup>. The analysis of the data taken with only one telescope and the stereo analysis follow the same scheme, but in the stereo analysis more parameters can be used.

First of all, I will present the kind of data which are necessary for the analysis. Later, I will draft a scheme of the whole analysis and a detailed sequence of the used programs. This chapter of my thesis pretends to be a detailed review of the analysis chain since nothing of this kind has yet been published for the MAGIC stereo analysis, and I hope to facilitate this way the task of the data analyzers in the collaboration. For this purpose, the stereo data analysis will be carefully explained, the more technical parts of which can be found in Appendix A.

### 5.1 Data types

There are three main data types needed in order to perform MAGIC data analysis. These are the source data (and Off data in case of On/Off observations) taken by the telescopes, Monte Carlo (MC)  $\gamma$ -ray simulations and auxiliary data coming from individual subsystems of the instrument.

---

<sup>1</sup><http://root.cern.ch/drupal>.

- **Source data:** The source data can be wobble data in which the signal and background data can be extracted from the same files. Or it can be On/Off observations in which case On and Off data would be necessary. In any case, for the stereo data analysis dedicated Off data are necessary independent of the observation mode for the gamma-hadron separation, due to the reduction of the background in stereoscopic observation (more details in Sec. 5.9).
- **Monte Carlo simulations:** Typically in particle physics experiments, the calibration of the instruments is performed using a controlled incident light beam. Unfortunately, for Cherenkov telescopes, the response of the whole instrument cannot be tested in such a way (a complete particle accelerator would need to be placed in Space for this purpose), instead MC simulations are used. Mainly  $\gamma$ -ray simulations are produced, which are the ones used in the standard analysis, additionally other MC simulations are made for special studies simulating protons or helium for example. Several studies have been performed by the MAGIC collaboration in order to obtain a Monte Carlo data base as accurate as possible. Simulated gamma images have to resemble the images from real gamma-rays to a very high degree of precision in order to obtain the correct image parameters to be compared with real data. Although a single real  $\gamma$ -ray induced image can never be identified with 100% confidence, the comparison of the main parameters between real and simulated gamma images is possible and gave satisfactory results (Albert et al., 2008c).

The production of simulated MAGIC events goes through three steps. In a first step, the atmospheric showers are produced using the CORSIKA package (Heck et al., 1998). Next, the absorption and scattering of the Cherenkov photons from the shower, together with the reflection of these photons by the MAGIC mirrors, are simulated. As last step, the response of the MAGIC camera, trigger system and data acquisition electronics is simulated. These two last steps are done using the programs *reflector* and *camera* from MARS, more details can be found in Majumdar et al. (2005) and Carmona et al. (2008).

- **Auxiliary data:** This run type contains information from the subsystems which take care of the weather conditions, general status of the telescope, technical information, information from misbehaving parts of the instrument, etc.

The data are stored in three different run types whose format is basically the same (tree structure) but the contents are different.

- **Pedestal Run:** This run type contains events, only taken with the random trigger, which are used to calculate the pedestal offset for the calibration run. It is taken at the beginning of each the observation of each source.
- **Calibration Run:** This run type is taken with the standard calibration light pulses using the calibration trigger. These data are used to calculate initial conversion factors between FADC counts and photo-electrons in the camera, and to calibrate the arrival times of each readout channel. It is taken at the beginning of each new observed source every night.

- **Data Runs:** These are the files in which the source observation (in case of On or Wobble observations) or the background (in case of Off observations) have been saved. The observation rate is typically  $\sim 200$  Hz ( $\sim 800$  Hz in case of Sum Trigger observations), although it depends also on the observing conditions (galactic or extragalactic source, presence of the moon, weather conditions, etc.). Additionally, interlaced random triggers and calibration light pulses pulses are fired at a rate of 50 Hz, getting triggered by the pedestal and the calibration trigger.

These files are getting merged with the auxiliary data, storing the information from each subsystem in a different ROOT-tree.

Also the MC files have a similar structure, except for the auxiliary data which are not present in the case of MC simulations.

The raw data are converted in a ROOT-compatible format and are getting calibrated on-site and then transferred to the MAGIC data center PIC<sup>2</sup> (Barcelona) where they are stored. These data are made available at PIC through the GRID or also via a web interface. There is another automatic analysis chain running at La Palma, the online analysis which is performed quasi-simultaneously with the observation. It is very useful in case of sources showing a fast variability of their  $\gamma$ -ray emission, especially in case of GRB observations and  $\gamma$ -ray flaring sources like AGNs. The online analysis is only working for MAGIC-I data for the moment, but will be upgraded for the stereo system.

## 5.2 Analysis scheme

The MAGIC analysis scheme consists of the following steps:

- Extraction and calibration of the Cherenkov light pulses in each channel.
- Image cleaning.
- Image parametrization.
- Data quality selection.
- Calculation of separation parameters between  $\gamma$  and hadrons events.
- Application of quality cuts.
- Energy reconstruction.
- Reconstruction of the  $\gamma$ -ray direction.
- Signal search.
- Spectrum calculation.
- Light curve estimation.

---

<sup>2</sup><http://magic.pic.es>

### 5.3 The signal extraction and calibration

The first step of the analysis chain is the extraction and calibration of the Cherenkov light pulses in each channel of the camera. This is done by the so-called *callisto*<sup>3</sup> program. This task integrates the signal saved in form of counts per FADC time slice, converts the integral into equivalent photo-electrons and reconstructs the relative arrival time of each reconstructed light pulse.

First, the FADC voltage offset (the so-called “pedestal offset”) is subtracted from the integrated signal. For the signal integration, a sliding window algorithm is used which maximizes the summed integral of a fixed number of adjacent FADC slice contents. In the case of MAGIC-I data, the slice contents are additionally interpolated using a cubic spline.

The calculation of the pedestal offsets is done using pedestal runs and the interlaced pedestal events, triggered by the random trigger. The FADC contents of these events get summed up at the same place and with the same number of slices as in the signal reconstruction. Additionally to the pedestal offset, the pedestal fluctuations are calculated as the RMS of the distribution of FADC sums. These values will be later used to estimate the level of background light in each channel. The last step of the conversion of the extracted signal to photo-electrons uses the conversion factors obtained from the calibration runs and subsequent interlaced calibration pulses. These conversion factors are calculated assuming a perfectly homogeneous illumination of the camera by the calibration light source. A detailed explanation of the calibration process can be found in Gaug (2006).

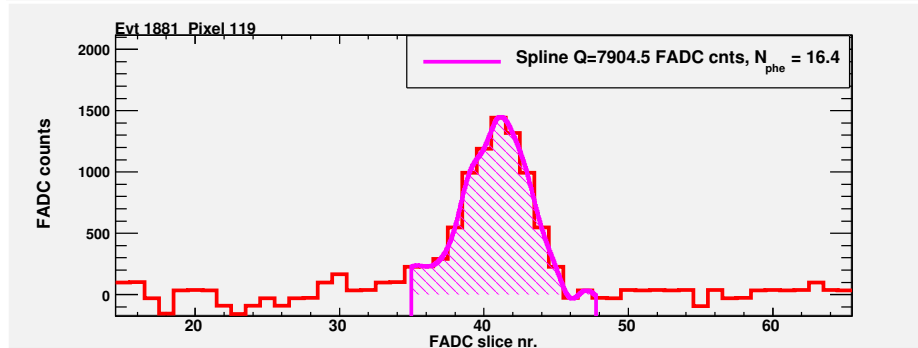


Figure 5.1: Signal pulse time windows. Courtesy of Markus Gaug.

Few pixels (typically no more than 10-15) cannot be calibrated due to technical problems, the signal from these pixels cannot be used. In order to minimize the impact of these so-called *bad pixels*, the signal from their neighbour channels are linearly interpolated, such that there are no holes left in the camera.

### 5.4 The image cleaning

The signals detected by each pixels are not only produced by photons from air showers, but there is also background light present, which can mimick Cherenkov light pulses. As

---

<sup>3</sup>callisto is one of the Jupiter’s moons and stands for “CALibrated Light Signals and Time Offsets”.

discussed in Chapter 3, one of the most important differences between the gamma and the hadron-like showers is the spread of the image: whereas the gamma-like events typically generate only one compact signal region, the hadron-like ones produce a larger number of signal clusters, called *islands*. Thus, the many small islands produced by noise, stars, etc. have to be removed in order to be able to classify the events properly. On the other side, any unnecessarily removed pixel will affect the energy threshold, since the shower size is related to the energy of the incident gamma-ray. So, the image cleaning level is a crucial number for the energy threshold.

The cleaning process uses fixed thresholds for the signal content of each channel and time coincidences of the calibrated light pulses with those of neighboring pixels. Two different algorithms are used for the cleaning: the standard (also called time cleaning) and the sum cleaning, which allows to reach better sensitivity at low energies. The final aim of this task is to select only those pixels which contain the air shower information and delete the rest. This is one of the tasks done by the program *star*.

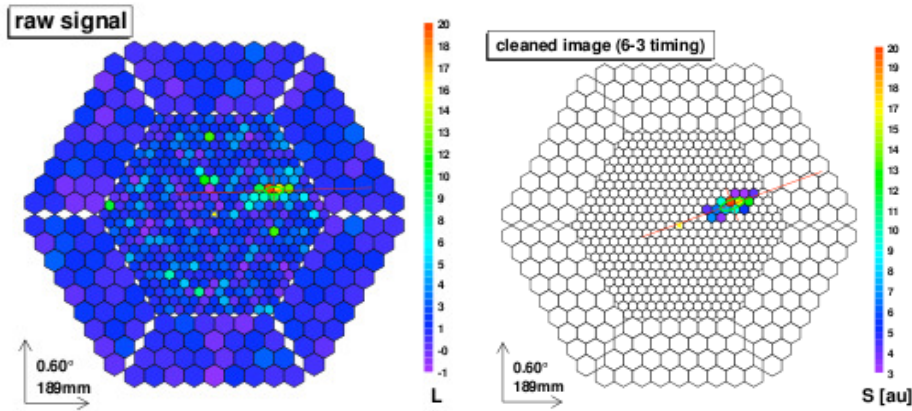


Figure 5.2: Left: Air shower image before cleaning. Right: Image after cleaning where the background light has been removed and the shower image parametrized.

#### 5.4.1 The standard cleaning

This method is divided in two steps, first the shower core is searched and in a second loop the rest of the shower pixels is found. The definition of a core pixel is a pixel whose signal is above a pre-defined threshold  $N_1$  and at least one pixel neighbour is also above that threshold inside a pre-defined time window  $T_1$ . In order to find the core pixels, the routine *star* scans the whole camera searching for the pixels which fulfil this condition. Once the core pixels have been identified, the boundary pixels are searched. The definition of a boundary pixel is the following: the charge of the pixel should be higher than a second threshold  $N_2$ , and at least one of the neighbors should be a core pixel with a maximal signal arrival time difference  $T_2$ . Under typical observation conditions without strong moon light, the values  $N_1 = 6$  phe,  $N_2 = 3$  phe,  $T_1 = 4.5$  ns,  $T_2 = 1.5$  ns for MAGIC-I are used. In the case of MAGIC-II, higher values  $N_1 = 9$  phe and  $N_2 = 4.5$  phe are used since the Domino

readout produces higher intrinsic noise. In case of strong moon light, the values  $N_1$  and  $N_2$  have to be raised for both telescopes.

#### 5.4.2 The Sum cleaning

This cleaning algorithm resembles the principles of the Sum Trigger. First, all combinations of 2 next-neighbors, w/o bad pixels (2NN), 3 next-neighbors (3NN) and finally 4 next-neighbors (4NN) in the camera are searched, always summing pixel contents whenever a very tight time coincidence criterion is met. The used thresholds, in units of sum/number of neighbors, are higher for the 2NN case, than for the 3NN, than for the 4NN case. This algorithm allows to go down to lower energies. Nevertheless, it represents an improvement in sensitivity with respect to the standard cleaning of about 10% at lower energies (mainly at energies lower than 100 GeV).

### 5.5 Shower parametrization

After the cleaning, only the Cherenkov light signals from pixels involved in the cascade image survive. These cleaned images typically have an elliptical shape, if an electromagnetic shower is involved, which will be parametrized using different parameters, such as Hillas parameters (Hillas, 1985) and some additional image and timing parameters which will be described below. The routine *star* takes care also of this task.

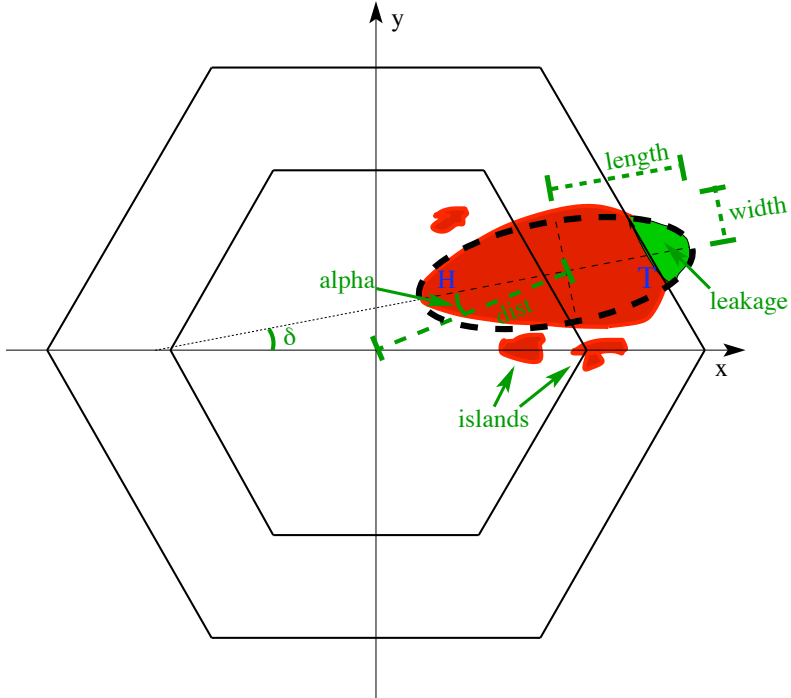


Figure 5.3: Sketch of the Hillas parameters.

### 5.5.1 The image parameters

- **Size:** This parameter represents the total amount of Cherenkov light captured by the camera for a given event. It is calculated summing up all the charge from the surviving pixels, measured in photo-electrons. This parameter is directly related to the shower energy since the number of created electron-positron pairs in an atmospheric  $\gamma$ -ray shower is proportional to the energy of the shower and the emitted number of Cherenkov photons per unit path length of an electron is almost constant (see Eq. 3.8).
- **Length:** This parameter is a measurement of the longitudinal development of the cascade and is parameterized by the length of the major axis of the ellipse.
- **Width:** This parameter *width* is a measurement of the lateral development of the cascade and is calculated as the length of the minor axis of the ellipse.
- **Dist:** The angular distance from the centroid of the image to the expected source position in the camera is named *dist*. While the previous parameters were independent from the expected position of the source, this parameter requires an assumption about the localization of the source.
- **Alpha ( $\alpha$ ):** The angle between the major axis of the image and the line joining the image centroid with the expected source position in the camera. This parameter measures the direction of the shower. In case of gamma-ray showers coming from the observed source, the shower axis should point to the expected source position in the camera, which means that the *alpha* parameter should be close to zero. In case of hadronic showers, the *alpha* parameter distribution should be plane. The *alpha*-parameter has been used as a powerful signal searcher for the MAGIC-I stand-alone data analysis. However, in case of stereoscopic data, the azimuth homogeneity is broken due to the L3 trigger and thus the *alpha*-parameter cannot be used for signal search purposes anymore.
- **Conc(N):** The fraction between the sum of photo-electrons contained in the  $N$  brightest pixels of the image and the total charge of the image (*size*). This parameter gives an idea of the compactness of the image which is expected to be greater for gamma-ray induced showers. Typically for the standard analysis  $N=2$ , is used.
- **Leakage:** The fraction between the sum of photo-electrons contained in the outermost ring of pixels in the camera and the total charge of the image (*size*). This parameter is important in case of very high energy showers which “leak out” of the camera and appear truncated. The *leakage* parameter takes into account the missing part of the shower in order to estimate the primary  $\gamma$ -ray energy. This effect starts play a role for incident  $\gamma$ -rays above 2 TeV in case of standard MAGIC observations, but for sources observed far from the camera center, the effect is stronger and becomes visible at lower energies.
- **Number of islands:** Number of spacially separated clusters of pixels after the cleaning. Usually, electro-magnetic showers produce one single connected image, while the hadronic ones tend to appear separated in several islands.

- **M3long:** M3long is calculated as the third moment along to the major axis of the ellipse and accounts for the asymmetry in the light distribution along the longitudinal shower development. For a gamma event the head of the shower should be closer to the expected source position in the camera while its tail is in the outer part of the camera. For low energy showers it is not useful since the images are quite small and concentrated.
- **Impact:** The impact parameter is defined as the distance of closest approach of the prolonged shower axis to the center of the telescope. This parameter is approximated by the *dist* parameter in single telescope data.

### 5.5.2 The timing parameters

- **Time RMS:** The width of the arrival times' distribution of all pixels after the cleaning. For  $\gamma$ -ray images the time distribution is typically narrower than for hadronic shower images.
- **Time Gradient:** Velocity of the temporal evolution along the major axis of the ellipse. This parameter measures how fast the arrival times change along the image major axis. Typically the arrival time differences become larger when moving away from the location of the source in the camera. This parameter depends strongly on the distance of the shower axis from the camera (parameterized by the *dist* parameter).

## 5.6 Quality selection

After the image cleaning, a first data quality selection is applied in order to reject bad quality data which would cause a posterior wrong flux estimation. Mainly, there are three kinds of problems which can affect the data quality: effects derived from hardware problems, bad weather and the moon light conditions.

**Hardware problems:** Several technical issues, which appear from time to time in the data, have to be checked, e.g. the number of well focused mirrors or the camera inhomogeneity.

**Bad weather:** Since the atmosphere plays an important role in this *Cherenkov technique*, the state of the weather conditions during the observation has a strong impact on the quality of the data. There are two main effects: the presence of clouds and the so-called calima (the presence of Saharian dust in the atmosphere). Both of them can absorb part of the *Cherenkov* light produced by the shower so that the incident  $\gamma$ -ray energy and the image parameters will be not properly reconstructed. Proper corrections for these atmospheric processes require a precise knowledge of the density profiles of the Mie-scattering particles, which can only be measured correctly with the use of a LIDAR. The MAGIC collaboration has such a device installed at the telescope site, however it was not yet fully operational at the time when the data for this thesis were taken. Therefore, only data from clear nights were used and the rest rejected.

**Moon light conditions or twilight:** If the observations were performed in presence of the moon, careful checks are needed about how much the intensity of the moon light

affects the data and especially if the cleaning levels have been high enough, such that no background light fluctuations create spurious islands in the image.

In Appendix A one can check how to select the good quality data from a list of standard parameters and plots.

### 5.7 Calculation of stereoscopic parameters

Until now, only independent parameters for each telescope have been introduced, and the stereoscopic ones remain to be calculated. This is done using the routine *superstar*. This program is only run for stereoscopic data and not for mono data analysis. *Superstar* performs the reconstruction of the stereoscopic shower parameters (direction, ground impact, height of the shower maximum, etc,) and can also reconstruct the energy. For this purpose, matching pairs of images are identified which belong to the same event from the two data streams (one per telescope), based on the L3 trigger number. These stereoscopic parameters are reconstructed as the crossing points of the two image major axes.

Out of these parameters, the so-called *MaxHeight* is especially important: it is the height at which the shower reaches its maximum calculated. This parameter results to be the most powerful stereoscopic shower parameters for the gamma/hadron separation.

### 5.8 The stereo DISP reconstruction

The DISP parameter is used to reconstruct the distance of the shower origin from the center of gravity along the major axis of the image, as was originally defined:

$$DISP = \xi \left( 1 - \frac{w}{l} \right) \quad (5.1)$$

where  $\xi$  is a free coefficient which can depend on the energy and zenith angle,  $w$  and  $l$  are the width and length of the image, respectively.

As this parameter can be affected by a possible truncation of the shower, additionally the *leakage parameter* has to be taken into account. Including this parameters in the calculation method, the precision of the DISP parameter can be improved (Domingo-Santamaria and Torres, 2005). Random Forest is a very efficient method to evaluate the common behaviour of data samples in the presence of correlated variables, thus a new method using Random Forest has been developed by the MAGIC collaboration (Aleksić et al., 2010b). This method is based on the training of the Random Forests to select the data correctly into given (small) bins of the true distance of the shower center from the source position in the camera using gamma-ray simulation data (MC). In a typical current implementation of this method, the following image parameters are used: *dist*, *length*, *width*, *size*, *impact*, *time gradient* and *maxheight*. It was observed that additional image parameters from the other telescope can improve the reconstruction precision of the *DISP* parameter from the original telescope, namely: *size<sub>o</sub>*, *impact<sub>o</sub>*, *time gradient<sub>o</sub>*, where the subscript “o” denotes the opposite telescope. Moreover, external parameters can be handed over to the algorithm, in this case the zenith angle of the observation.

Using this Random Forest method (hereafter *RF Disp*), an improvement of the angular resolution of  $\sim 25\%$  at 300 GeV and  $\sim 45\%$  at 1 TeV is found what means a sensitivity improvement of  $\sim 30\%$  (Saito and Sitarek, 2009).

The single telescope DISP method can be also used for stereoscopic analyses taking the major axes crossing point to improve the shower parameter reconstruction. However, this method cannot always resolve a left-right ambiguity of the source position w.r.t. the shower center. Especially single telescope DISP parameters, low-energy events and stereoscopic events with almost parallel images in their cameras are affected by this ambiguity. To resolve the ambiguity between the true arrival direction of the shower and the opposite one (the so-called “ghost”), ghost busting methods have been introduced and are sketched in Fig. 5.4 and Fig. 5.5.  $\Delta\delta$  stands here for the angular distance between the reconstructed shower direction in the MAGIC-I and MAGIC-II cameras and, depending on its value, different combinations of single telescope and stereo DISP parameters are used.

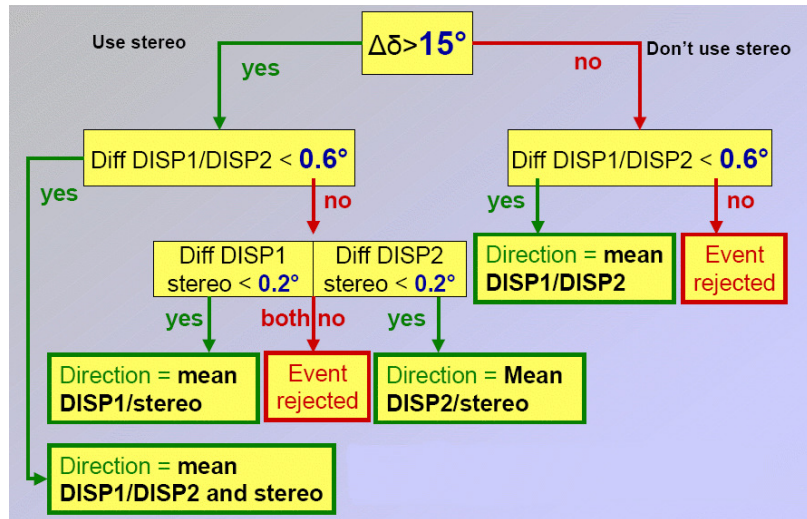


Figure 5.4: The ghost busting method scheme.

The turbo-buster method, in turn, evaluates all four possible pairs of direction combinations (see Fig. 5.5). The closest pair in distance is chosen and further checked whether its distance is less than a given value of  $0.05 \text{ deg}^2$ , otherwise the event is rejected.

These two methods allow an improvement of the angular resolution at low energies. Both of them give similar performance values, but the turbo buster method has become standard since it is a more stable algorithm.

The results of the calculation of the stereo DISP will be applied to the source data and MC test files using the program *melibea*. Appendix A shows how this is done step-by-step in the analysis.

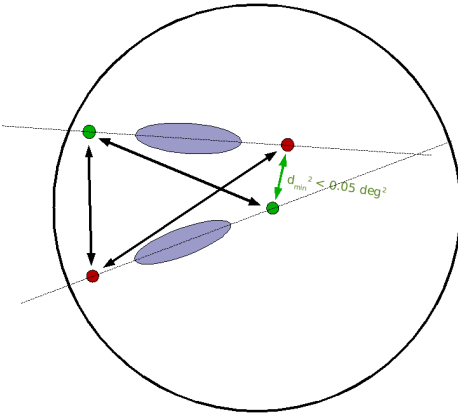


Figure 5.5: Sketch of the turbo buster method.

## 5.9 Gamma-hadron separation

The fraction of recorded events from gamma rays is of the order of 1 out of 1000, even for strong gamma-ray sources like the Crab Nebula. Therefore, a very good background rejection is needed. Using the image parameters that have already been calculated for each event, typical differences between hadronic and electromagnetic showers have to be recognised and corresponding cuts applied in order to select the gamma-like showers. For this task, the *Random Forest (RF)* method is used (Breiman, 2001), slightly adapted for the MAGIC analysis (see Albert et al., 2008b, for details). *Random Forest* is a multivariate classification method, able to work with several variables which are in general correlated. The method is based on the construction of decision trees. As input, one gives the program two data samples: one sample which contains  $\gamma$ -ray induced shower image parameters (which may contain a small contribution of hadronic events, but usually a “pure” sample of MC generated  $\gamma$ -ray images is used), and a background data sample which contains hadronic shower parameters (and only a small contribution of  $\gamma$ -induced showers). *RF* will build a new variable called *hadronness* which optimizes the separation between electromagnetic and hadronic shower parameters. In case of wobble MAGIC-I stand-alone data, the image parameters, calculated w.r.t. the anti-source position, can be used as Off data for the training because even in case of a strong source, the rate of  $\gamma$  images leaking into the anti-wobble region is very low, and the *RF* method still works with a small contamination of  $\gamma$ -ray images in the background sample. A different situation occurs in the stereoscopic wobble data, where the L3 trigger reduces much more the background and a dedicated observation with no  $\gamma$ -ray source in the field of view is needed. As a consequence, for stereo data analysis, an Off data sample is always needed no matter in which mode the source has been observed. Typically, Off data are taken from the data-base with zenith angle range matching the source data sample.

I will briefly describe how the *RF* classification method works. Usually, a large number (typically 100) of decision trees is generated. A list of the following image parameters is handed over to the *RF* matrices:

- 1: Size\_1
- 2: Size\_2
- 3: Width\_1
- 4: Width\_2
- 5: Length\_1
- 6: Length\_2
- 7: Impact\_1
- 8: Impact\_2
- 9: MaxHeight
- 10: TimeGradient\_1
- 11: TimeGradient\_2

where the subscripts “ $_1$ ” and “ $_2$ ” refer to the individual telescopes, i.e.  $Size\_1$  refers to the  $size$  parameter obtained from the MAGIC-I camera image,  $Size\_2$  from the MAGIC-II camera of the same event.

We hand over to the program simulated gamma showers and hadronic showers. Each tree will start to apply a cut in a randomly chosen parameter, such that the Gini index between the two samples becomes biggest. Then, a cut in another randomly chosen parameter is applied, again maximizing the Gini index, after having applied the first cut. This procedure will be repeated until only hadrons or gammas are contained in the sub-samples left. The outcome of this single decision tree is called leafes (see Fig 5.6). The outcome of one decision tree can be gamma-like or hadron-like, attributing it the value 0 or 1, respectively. After the application of all decision trees, the average of the decision trees’ outcome is made, creating new variable called *hadronness*. As one can see in Fig. 5.7, for low values of hadronness, the contamination of hadrons is small. This means that even if background events are present, their number is small compared to the number of retained gamma image. The new parameter *hadronness* is applied as a cut parameter to the source data and to a test MC sample using the MARS program *melibea*<sup>4</sup>.

## 5.10 The energy reconstruction

In this step, the image parameters, containing especially the  $size$  parameter, are converted into energy units. This conversion not only depends on the number of collected photo-electrons, but also on other parameters as the zenith angle of the observation, the image leakage, etc. In case of stand-alone MAGIC-I data, the energy estimation is performed using the Random Forest method, in case of stereoscopic data, it is reconstructed

---

<sup>4</sup>She is one of the protagonists of the *Celestina* novel.

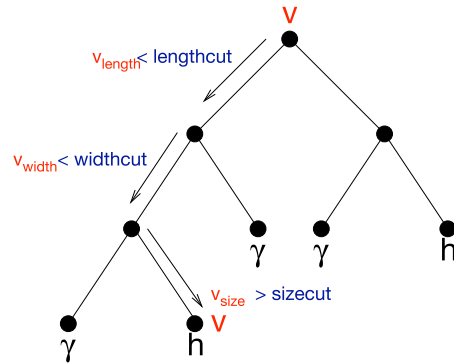


Figure 5.6: Sketch of decision trees.

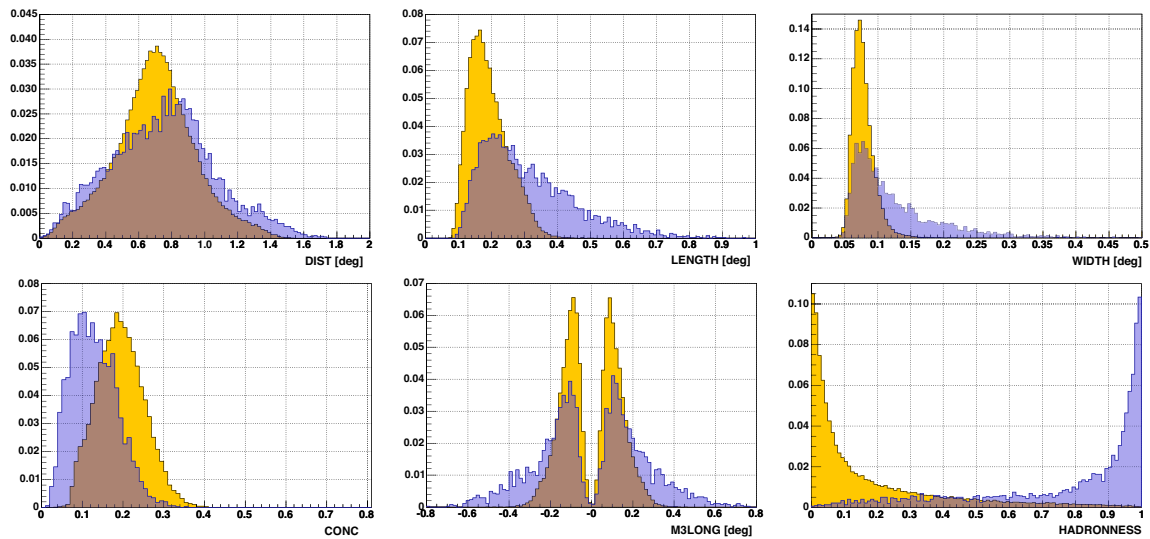


Figure 5.7: Distribution of the Hillas parameters and hadronness for gamma-like showers represented by the yellow shaded area and hadron-like showers in blue shaded area.

using lookup-tables based on the values of some selected image parameters: *size*, *Impact/CherenkovRadius*, *Ereal/Size/CherenkovDensity*, where the parameters *CherenkovRadius* and *CherenkovDensity* have been calculated based on the *MaxHeight* parameter and the observation zenith angle, assuming a toy atmospheric model. The lookup-tables have been created from MC  $\gamma$ -ray simulation data for a sufficiently large range of zenith angles.

The reconstruction is performed for each telescope independently and finally the reconstructed energy ( $E_{\text{est}}$ ) is a weighted average of the energy estimated for each telescope.

The *melibea* program takes care of the energy reconstruction process.

## 5.11 The signal search

The signal search is based on a parameter space where  $\gamma$ -ray induced showers can be differentiated from the hadronic ones. For this purpose, one has to apply first cuts which allow a background suppression, as in the case of the *hadronness* variable. Some standard set of cuts for different energy bins have been defined as explained in Appendix A.11.1.

There are three different approaches to look for a signal: the alpha ( $\alpha$ ) and theta<sup>2</sup> ( $\theta^2$ ) plots, and the skymaps. In all these methods, an excess in the distribution between the events reconstructed as stemming from the source position in a pre-defined parameter window (the so-called “signal region”) from On data and from Off data) is searched. The significance of this excess is calculated by Li-Ma formula (Li and Ma, 1983):

$$S = \sqrt{2} \cdot [N_{ON} \cdot \ln\left(\frac{1+\nu}{\nu} \cdot \frac{N_{ON}}{N_{ON} + N_{OFF}}\right) + N_{OFF} \cdot \ln\left((1+\nu) \cdot \frac{N_{OFF}}{N_{ON} + N_{OFF}}\right)]^{1/2} \quad (5.2)$$

where  $N_{ON}$  and  $N_{OFF}$  are the number of events in the signal region from On data and Off data, respectively and  $\nu$  is the normalization factor between the On and Off distribution. This normalization factor is obtained from outside the signal region where the events for On and Off data are supposed to be equally distributed. Usually in astroparticle physics, the significance limit is set by convention to  $5\sigma$ , prior to claim a discovery of a new source.

### 5.11.1 The *alpha* plot

The alpha parameter concentrates around small values for  $\gamma$ -ray induced shower images, while the hadronic ones are isotropically distributed, if the gamma-ray stems from the observed source. If we plot the alpha distribution of the gamma images against the hadron distribution, we will see a clear peak close to the value zero from the gamma-rays (see Fig. 5.8), if they come from a single source and this source is not extended, as is always the case for extra-galactic sources. This method is powerful for mono-data analysis but in case of stereo data the azimuth homogeneity is broken and thus this method cannot be used.

### 5.11.2 The *theta<sup>2</sup>* ( $\theta^2$ ) plot

In this case, instead of the *alpha* parameter, the  $\theta^2$  parameter is used.  $\theta^2$  is defined as the square of the distance between the expected and the reconstructed source position in the camera. As in the case of the *alpha* plot, if we plot On data against Off data, we will obtain a peak at zero, if  $\gamma$ -ray images from the observed source are contained in the data, since the

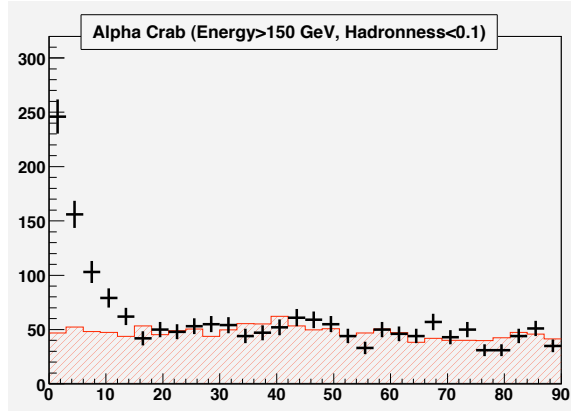


Figure 5.8: Alpha distribution from a Crab Nebula data sample. Taken from Becerra-González (2008).

gamma-like showers are expected to be reconstructed close to the expected source position in the camera, while the hadrons arrive from random directions.

$\theta^2$  plots can be produced using a standard MARS program, called *odie*.

### 5.11.3 The skymap

Until now, all calculations have been performed in camera coordinates. In order to create a skymap, the reconstructed arrival directions of all shower images are transformed into sky coordinates. Whereas in the cases of *alpha* and  $\theta^2$  distributions, only one assumed source position is used, performing a skymap, one can estimate the On/Off ratio in the whole FoV of the telescopes. For this purpose, a background model is created in camera coordinates and then this model is projected into sky coordinates and compared to the skymap from the source data.

Two standard programs in MARS create skymaps, named *caspar* and *zinc*. They both use the test statistic (TS) from Li and Ma (1983) Eq. 17, applied on a smoothed and modeled background estimation. Its null hypothesis distribution mostly resembles a Gaussian function, but in general can have a somewhat different shape or width, if the statistics is low. The distribution of TS values is compared to a corresponding distribution of the null hypothesis, which is calculated on-the-fly using MC simulations from the actual background map.

## 5.12 Flux estimation

The differential energy spectrum of a  $\gamma$ -ray source is defined as:

$$\frac{dF(E)}{dE} = \frac{N_\gamma}{dE \cdot dA \cdot dt} \quad (5.3)$$

and the observed spectrum is given by the following equation:

$$\frac{\Delta F_{obs}(\Delta E)}{\Delta E} = \frac{N_\gamma(\Delta E)}{\Delta E \cdot A_{\text{eff}}(\Delta E) \cdot \Delta t_{\text{eff}}} \quad (5.4)$$

where  $N_\gamma$  is the number of observed  $\gamma$ -rays after the applied cuts,  $A_{\text{eff}}$  is the Cherenkov telescope effective collection area and  $t_{\text{eff}}$  the effective observation time which is calculated as the observation time minus the dead time of the analysis chain. The number of  $\gamma$ -rays is calculated based on a  $\theta^2$  distribution (or an *alpha* plot in case of mono data) for each energy bin and using an optimized set of cuts per energy bin.  $A_{\text{eff}}$  is defined as the area in which the gamma-ray telescope can detect an air shower folded with the trigger efficiency and the efficiency cuts applied in the analysis. This effective area is calculated using MC  $\gamma$ -ray simulations and depends on the incident  $\gamma$ -ray energy, the zenith angle ( $\theta$ ), the azimuth angle ( $\psi$ ) (especially for stereoscopic data where the homogeneity of the azimuth is broken), the applied cuts and the atmospheric conditions. It is defined as:

$$A_{\text{eff}}(E, \theta, \psi) = \lim_{N_{sim}(E, \theta, \psi) \rightarrow \infty, A_{sim}(E, \theta, \psi) \rightarrow \infty} A_{sim}(E, \theta, \psi) \cdot \frac{N_{\text{analysis}}(E, \theta, \psi)}{N_{sim}(E, \theta, \psi)} \quad (5.5)$$

where  $N_{sim}(E, \theta, \psi)$  is the number of simulated  $\gamma$ -rays with an energy  $E$  in a given zenith and azimuth angle bin  $(\theta, \psi)$ ,  $A_{sim}(E, \theta, \psi)$  is the incident simulated area which has to be much bigger than the typical Cherenkov light pool, and  $N_{\text{analysis}}(E, \theta, \psi)$  is the number of remaining events after correct simulation of the telescope trigger and the application of all analysis cuts. In practice, the limit is replaced by a sufficiently large numbers  $N_{sim}(E, \theta, \psi)$  and  $A_{sim}(E, \theta, \psi)$ .

In case a signal is not found, an upper limit on the  $\gamma$ -ray flux from the observed source can be derived.

This task is performed by the program *fluxlc* where one can derive the differential energy spectrum, the integral flux and select time bins to produce a light curve (see Appendix A for details).

### 5.13 The unfolding

The obtained spectrum using *fluxlc* is based on bins of reconstructed energy, which are affected by instrumental biases and finite resolution and threshold effects. These effects typically depend on the assumed initial spectrum. In order to calculate the spectrum as a function of true  $\gamma$ -ray energy, an unfolding procedure has to be applied to the reconstructed spectrum. To do so, the energy of an initial spectrum-guess of simulated  $\gamma$ -rays is reconstructed and filled into the bins of reconstructed energy. The outcome is saved in the *migration matrix*. Mathematically, the distortion can be written as:

$$Y(E_{rec}) = \int M(E_{true}, E_{rec}) S(E_{true}) dx \quad (5.6)$$

where  $E_{rec}$  is the reconstructed energy,  $E_{true}$  the true energy,  $S$  represents the measured distribution (measured spectrum) while  $Y$  represents the emitted spectrum from the source, as a function of the  $\gamma$ -ray energies. The kernel  $M$  becomes the *migration matrix*, if a finite number of bins is used.

A rough estimation of the true spectrum can be obtained by just inverting the *migration matrix*. However the migration matrix itself depends on an assumption of the initial spectrum, therefore an iterative procedure has to be chosen which is made such that it converges at the true  $\gamma$ -ray spectrum. The following methods have been implemented in the MAGIC software and typically yield compatible results: *Bertero, Schmelling, Tikhonov* and a forward unfolding method (Albert et al., 2007a).

The unfolding is done by a *ROOT* macro in MARS called *CombUnfold.C*.

### 5.14 Spectral de-absorption

The EBL affects the  $\gamma$ -rays, absorbing part of them, as presented in Sec. 2.4.1. This means that the source energy spectrum measured on Earth is not the intrinsic one emitted by the source, due to this EBL effect. The process of correction for the EBL effect is called de-absorption. Different EBL models describe how the extragalactic background light affects the light. Taking into account these EBL models, we can de-absorb the observed spectrum. The intrinsic spectrum of the source can be expressed as:

$$F_{\text{em}}(E) = F_{\text{obs}} \cdot e^{\tau(E,z)}, \quad (5.7)$$

where  $F_{\text{em}}$  and  $F_{\text{obs}}$  denote the emitted and observed fluxes while  $\tau$  represent the optical depth which are given by the EBL models.

This task is a step beyond the MAGIC analysis chain since the EBL effect does not depend on the instrumentation, but rather on the physics scenario. Nevertheless, I am including it in the analysis chain, because it can also be computed using the corresponding attenuation factors from EBL models in the unfolding macro *CombUnfold.C*.

### 5.15 The telescopes performance

The sensitivity of ground-based gamma-ray telescopes is usually defined as the flux of a source which reaches a  $5\sigma$  significance detection in 50 hours of observation. Mathematically, it can be express as follows:

$$S(50 \text{ hr}) = \frac{N_{\text{ex}}}{\sqrt{N_{\text{off}}}} \cdot \sqrt{\frac{50}{T}} \quad (5.8)$$

where  $T$  is the observation time,  $N_{\text{ex}}$  the number of excess and  $N_{\text{off}}$  the number of estimated background events in the signal region.

After the operation of the telescopes in stereoscopic mode, the sensitivity has improved a factor of  $\sim 2$  with respect to the stand-alone MAGIC-I sensitivity, reaching an integral sensitivity of  $0.76 \pm 0.03\%$  of the Crab Nebula flux in 50 hours of effective observation time in the medium energy range ( $> 250$  GeV). Taking into account Eq. 5.8, as the sensitivity depends on the squared root of the observation time, this improvement on the sensitivity translate into a reduction of the observation time of 4 times approx. with respect to MAGIC-I mono-observations. Furthermore, the angular and energy resolution have been improved as well, with an angular resolution of  $\sim 0.07^\circ$  at 300 GeV and  $\sim 15\%$  of energy resolution in the medium energy range.

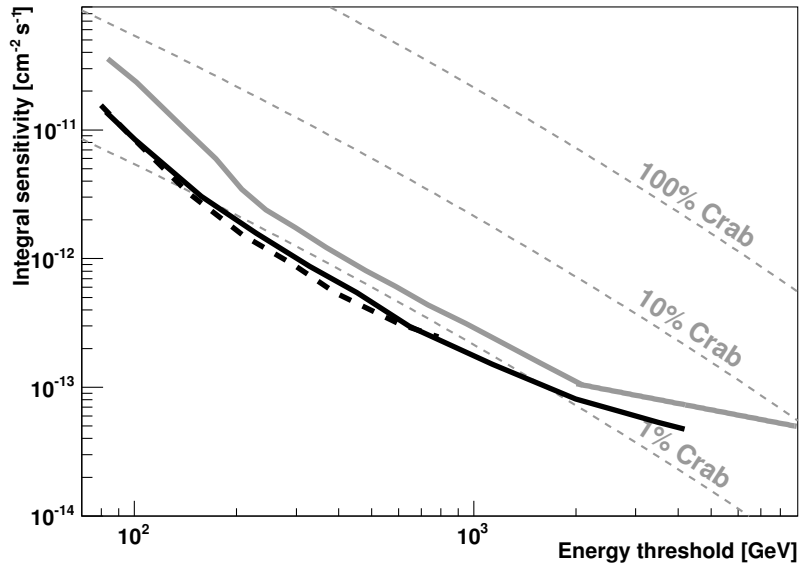


Figure 5.9: Integral MAGIC stereo system sensitivity. The grey solid line represents the integral sensitivity achieved by MAGIC-I while the black lines accounts for the integral sensitivity reached by the stereo system: the dashed line has been calculated using MC simulations and the solid one is the result from a Crab Nebula data sample analysis.

## 5.16 Systematic uncertainties

The uncertainty of in the measured fluxes can be divided in two different groups: statistical uncertainties and systematic errors. There are many factors which contribute to the systematic errors, the most important of which are:

- **The atmosphere:** The particles produced in the air showers interact with the atmospheric molecules assuming standard atmospheric profiles, which may vary with time. Moreover, the atmospheric transmission is not perfectly known at every moment. The contribution of dust and clouds is sometimes not visible by eye, but nevertheless affects the transmission of the Cherenkov light. Only one Mie-scattering model is simulated by the MC, which however may change from night to night or even on smaller time scales.
- **The mirrors:** The reflectivity of the mirrors change due to the presence of dust and a general degradation with time, affecting each mirror differently and also the pointing of the mirrors can vary within small errors from night to night due to problems in the mirrors focusing.
- **Cameras and readouts:** An additional source of uncertainty comes from the calculation of the calibration conversion factors. Especially the contribution of the photo-electron collection efficiency of each PMT and the degradation with time of the quantum efficiency of the coated PMTs may introduce uncertainties.

- **Signal extraction:** Small errors may be introduced by differences in the pulse shapes between simulated and real data.
- **Mispointing:** The mispointing affects the distribution of the events in the camera, which will produce a small error in the stereo parameter reconstruction.
- **Analysis:** Small differences between the real events and the gamma simulations may affect the precision of the reconstructed parameters and the cut efficiencies.

A detailed description of the systematic uncertainties can be found in Albert et al. (2008c). There, an overall systematic uncertainty of 16% on the reconstructed energy, with a systematic error of 11% on the flux normalization and a systematic slope error of  $\pm 0.2$  was found.



---

# 6

---

## Discovery of the Blazar PKS 1222+21 in VHE $\gamma$ -Rays

### 6.1 Introduction

The blazar PKS 1222+21 (also known as 4C 21.35) located at R.A. 12h24m54.45s and Dec. +21d22m46.48s, belongs to the class of Flat Spectrum Radio Quasars (FSRQs) and is located at a redshift of  $z = 0.432$  (Osterbrock and Pogge, 1987). FSRQs display luminous broad emission lines, often accompanied by a “blue bump” in the optical-UV region which is associated with the direct emission from the accretion disk. This optical-UV emission is believed to be re-processed by the Broad Line Region (BLR) clouds, filling the BLR with a dense optical-UV radiation field which can interact with VHE  $\gamma$ -rays causing internal absorption in the VHE domain (Donea and Protheroe, 2003). PKS 1222+21 is the third FSRQ detected in VHE  $\gamma$ -rays after PKS 1510-08 (Wagner, 2010) and 3C 279 (Albert et al., 2008a; Aleksić et al., 2011b) at the redshifts of  $z = 0.36$  and  $z = 0.536$ , respectively. It is thus the second most distant VHE source after 3C 279 with well measured redshift (the BL Lac 3C 66A with an estimated redshift  $z = 0.444$  would occupy this position of the ranking, but the redshift measures by Bramel et al., 2005, has a large uncertainty).

The satellite EGRET working in the energy range from 30 MeV to 30 GeV detected PKS 1222+21 for the first time as the most likely counterpart of 3EG J1224+2118 (Hartman et al., 1999). It has also been detected by the LAT detector of *Fermi* and appears in the First LAT Catalog (Abdo et al., 2010). There, it is included in the list of sources emitting at  $E > 100$  GeV (Neronov et al., 2011) whose photons have been detected during a flare state. VHE upper limits have been derived by the Cherenkov telescope Whipple at the level of  $12 \cdot 10^{-12} \text{ cm}^{-2}\text{s}^{-1}$  for  $E > 300$  GeV (Kerrick et al., 1995).

PKS 1222+21 is characterized by highly superluminal jet knots observed in radio with apparent velocity up to  $21c$  (Lister et al., 2009) which indicates relativistic beaming effects. This source presents a large-scale structure in radio which is more luminous than the core (Kharb and Shastri, 2004; Wang et al., 2004), a quite surprising fact for a blazar source. The detection of VHE emission from a such distant blazar has two important implications: it can be used in order to understand better the emission mechanisms of FSRQs

as well as tester for EBL models.

In this chapter, I will start describing the observations carried out by the MAGIC telescopes and presenting the discovery of the source in VHE, then I will present the spectrum and the light curve. Finally, the implications of both EBL models and jet emission models will be discussed. A new model to explain the findings is developed in the next chapter.

## 6.2 The observations

PKS 1222+21 has been observed by the MAGIC telescopes from the 3<sup>rd</sup> of May (triggered by a high state in *Fermi* data) to the 19<sup>th</sup> of June of 2010 (MJD 55319 to MJD 55366) for a total of  $\sim$ 16.5 hours of good quality data. On June 17<sup>th</sup> (MJD 55366), the source was detected in VHE  $\gamma$ -rays during a flare state in close coincidence with its brightest flare observed by the *Fermi* Large Area Telescope (LAT) (Tanaka et al., 2011) as can be seen in Fig. 6.6. Up to June 17<sup>th</sup> only hints of a signal have been detected by the MAGIC telescopes. The previous non-detection of the source, even during flare states in the GeV band, while the same source was detected by *Fermi*, is not only due to signal characteristics, but also due to bad weather at the MAGIC site together with the presence of the moon during the more promising emission states of the source.

The observation on June 17<sup>th</sup> lasted 30 minutes, starting at 21:50 UT and ending at 22:20 UT (MJD 55364.908 to MJD 55364.931) and was performed under moderate moon light conditions. The data were taken at zenith angles between 26° and 35° in wobble mode. During the following two nights, the source was followed-up by MAGIC, but due to stronger moon light conditions (which raises the energy threshold) and probably due to changes in the spectral photon index, which became softer, the detection of the source at high energies was no longer possible. The covered observation times and zenith angle ranges can be found in Table 6.1.

## 6.3 Data analysis and results

The data have been analyzed in the MARS analysis framework, as wobble data. For all days the standard cleaning was applied except in case of the flare detection from June 17<sup>th</sup>. In that case, due to the presence of the moon, the background was much higher and had to be treated using a higher cleaning level:  $N_1 = 7$  ph.e.,  $N_2 = 4$  ph.e. for the MAGIC-I camera and  $N_1 = 10$  ph.e.,  $N_2 = 5$  ph.e. for the MAGIC-II camera, while the default values are  $N_1 = 6$  ph.e.,  $N_2 = 3$  ph.e. and  $N_1 = 9$  ph.e.,  $N_2 = 4.5$  ph.e., respectively. As a result, the energy threshold of the analysis is  $\sim$ 60 GeV for standard cleaning levels and  $\sim$ 70 GeV for these higher cleaning levels, determined by Monte Carlo events and assuming a spectral photon index of  $\Gamma = 3.5$ . The strength of the signal has been calculated applying standard cuts.

The signal search was performed using the  $\theta^2$  distribution. In case of the flare data, an excess of 190  $\gamma$ -like events (6  $\gamma$ /min.) above a background of 86 events was obtained, which corresponds to a statistical significance of  $10.2\sigma$  using Eq. 17 in Li and Ma (1983) (see the Fig. 6.1). In the skymap, Fig. 6.2, the position of the excess is compatible with the location of PKS1222+21 and a point-like source.

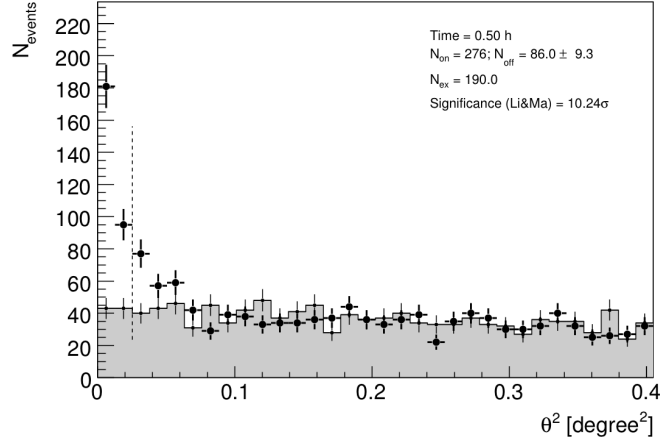


Figure 6.1: Distribution of the squared angular distance ( $\theta^2$ ) for events in the direction of PKS 1222+21 (black points) and normalized off-source events (grey histogram) for data taken on June 17<sup>th</sup>. The signal is extracted in the  $\theta^2$ -region denoted by the vertical dashed line.

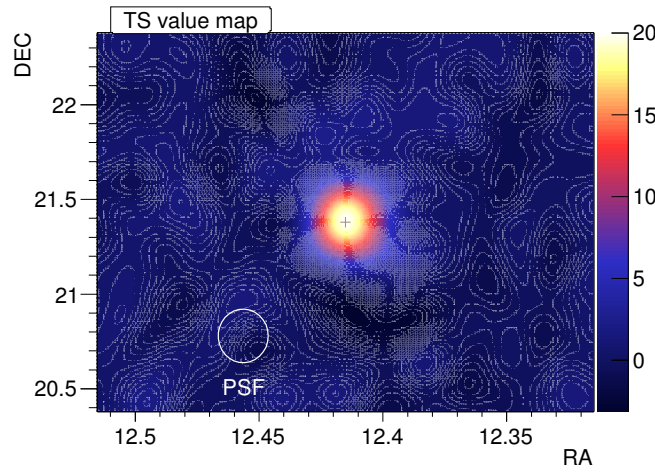


Figure 6.2: Skymap from PKS1222+21 during a flare state on the 17<sup>th</sup> of June 2010.

Night	MJD	Observation time [h]	Zenith angle
03/05/2010	55319	2.24	7°-27°
04/05/2010	55320	0.56	7°-27°
05/05/2010	55321	0.79	14°-30°
06/05/2010	55322	0.91	7°-17°
07/05/2010	55323	1.36	7°-31°
29/05/2010	55345	0.82	7°-25°
30/05/2010	55346	0.98	7°-36°
31/05/2010	55347	1.07	15°-32°
01/06/2010	55348	0.97	20°-38°
02/06/2010	55349	1.11	18°-37°
03/06/2010	55350	1.09	19°-36°
05/06/2010	55352	0.99	18°-36°
06/06/2010	55353	0.55	28°-36°
07/06/2010	55354	0.67	24°-36°
08/06/2010	55355	0.80	23°-35°
11/06/2010	55358	0.55	25°-35°
12/06/2010	55359	0.56	26°-36°
17/06/2010	55364	0.50	26°-35°

Table 6.1: Nights with good quality data taken by MAGIC from PKS 1222+21. The dates refer to the beginning of each night.

From the rest of the observation, only a detection is obtained on the 3<sup>rd</sup> of May (MJD 55319), with a significance of 4.63  $\sigma$  ( $N_{excess}=77$ ,  $N_{on}=278$  and  $N_{bg}=201$ ) giving a rate of  $\sim 0.6 \gamma/\text{min}$ . which is one order of magnitude lower than the rate detected in the flare state. In Table 6.2 the significances and flux upper limits for the whole campaign are shown, where no signal has been detected.

### 6.3.1 The VHE spectrum

During the flare state of the source, observed by MAGIC on June 17<sup>th</sup>, the observed differential energy spectrum extends from  $\sim 70$  GeV up to 400 GeV. For energies higher than 400 GeV, no significant excess has been found, instead upper limits corresponding to 95% confidence level (C.L.) have been calculated. The energy spectrum has been reconstructed using different unfolding algorithms to take into account the finite energy resolution of the instrument and the biases in the energy reconstruction, as explained in Sec. 5.13. All these unfolded spectra are compatible within uncertainties, *Tikhonov*'s unfolding algorithm has been selected because it gives the lowest  $\chi^2$ -value.

The VHE observed spectrum can be well-described by a simple power-law of the form:

$$\frac{dN}{dE} = N \left( \frac{E}{200 \text{ GeV}} \right)^{-\Gamma} \quad (6.1)$$

with photon index  $\Gamma = 3.75 \pm 0.27_{\text{stat}} \pm 0.2_{\text{sys}}$  and a normalization constant at 200 GeV

Night	MJD	Significance [ $\sigma$ ]	U.L. [ $\text{TeV}^{-1} \cdot \text{cm}^{-2} \cdot \text{s}^{-1}$ ]	U.L. [% Crab Flux]
03/05/2010	55319	4.63	-	-
04/05/2010	55320	-0.58	$1.195 \cdot 10^{-11}$	3.70
05/05/2010	55321	-0.70	$1.056 \cdot 10^{-11}$	3.27
06/05/2010	55322	1.35	$1.773 \cdot 10^{-11}$	5.49
07/05/2010	55323	1.34	$1.734 \cdot 10^{-11}$	5.37
29/05/2010	55345	-1.77	$4.613 \cdot 10^{-12}$	1.43
30/05/2010	55346	0.37	$2.604 \cdot 10^{-11}$	8.07
31/05/2010	55347	-0.53	$5.073 \cdot 10^{-12}$	1.57
01/06/2010	55348	-1.40	$1.202 \cdot 10^{-11}$	3.73
02/06/2010	55349	-0.42	$8.394 \cdot 10^{-12}$	2.60
03/06/2010	55350	0.23	$7.958 \cdot 10^{-12}$	2.47
05/06/2010	55352	-0.91	$1.370 \cdot 10^{-11}$	4.26
06/06/2010	55353	-1.37	$2.058 \cdot 10^{-11}$	6.38
07/06/2010	55354	0.67	$1.274 \cdot 10^{-11}$	3.95
08/06/2010	55355	-0.67	$2.363 \cdot 10^{-11}$	7.32
11/06/2010	55358	-0.44	$4.106 \cdot 10^{-11}$	12.72
12/06/2010	55359	-1.32	$2.506 \cdot 10^{-11}$	7.77
17/06/2010	55364	10.24	-	-

Table 6.2: Nightly significance of PKS 1222+21 calculated from the  $\theta^2$  distribution, and U.L. for  $E > 100$  GeV in case of significance  $\sigma < 4$ .

of  $N = (7.8 \pm 1.2_{\text{stat}} \pm 3.5_{\text{sys}}) \cdot 10^{-10} \text{ cm}^{-2} \text{ s}^{-1} \text{ TeV}^{-1}$ ). The integral flux at  $E > 100$  GeV is  $F_{100} = (4.6 \pm 0.5_{\text{stat}} \pm 1.4_{\text{sys}}) \cdot 10^{-10} \text{ cm}^{-2} \text{ s}^{-1}$  which corresponds to  $\sim 1$  Crab Nebula flux. In order to compare with the previous Whipple flux upper limit, the flux at  $E > 300$  GeV has been calculated, yielding  $F_{300} = (9.0 \pm 3.6) \cdot 10^{-12} \text{ cm}^{-2} \text{ s}^{-1}$  (corresponds to  $\sim 7\%$  of the Crab Nebula flux), a compatible result with the limit. The unfolded spectrum is shown in Fig. 6.3, where the black points represent the spectrum and the grey shaded area takes into account the systematic uncertainty of the analysis, calculated from the use of different sets of cuts and different unfolding methods.

As discussed in Sec. 2.4, the VHE  $\gamma$ -rays spectra suffer absorption due to the interaction by pair-production with the EBL. Consequently, the spectra have to be de-absorbed in order to get rid of this effect and be able to infer the intrinsic source spectra. In case of PKS 1222+21, different EBL models have been used to obtain the de-absorbed spectrum: Domínguez et al. (2011), Kneiske and Dole (2010), Gilmore et al. (2009), Franceschini et al. (2008) and Albert et al. (2008a). The de-absorbed spectrum is compatible with a simple power-law fit, independently of the used EBL model. In Fig. 6.3, the de-absorbed spectrum, using the current most precise EBL model of Domínguez et al. (2011), is shown well-fitted by a power-law with an intrinsic photon index of  $\Gamma = 2.72 \pm 0.34$ , represented by blue points while the blue shaded area represents the uncertainties due to the differences between EBL models.

Both the observed spectrum and the de-absorbed one can be well-described by a power-law, but the existence of a possible spectral cut-off has been studied by fitting different

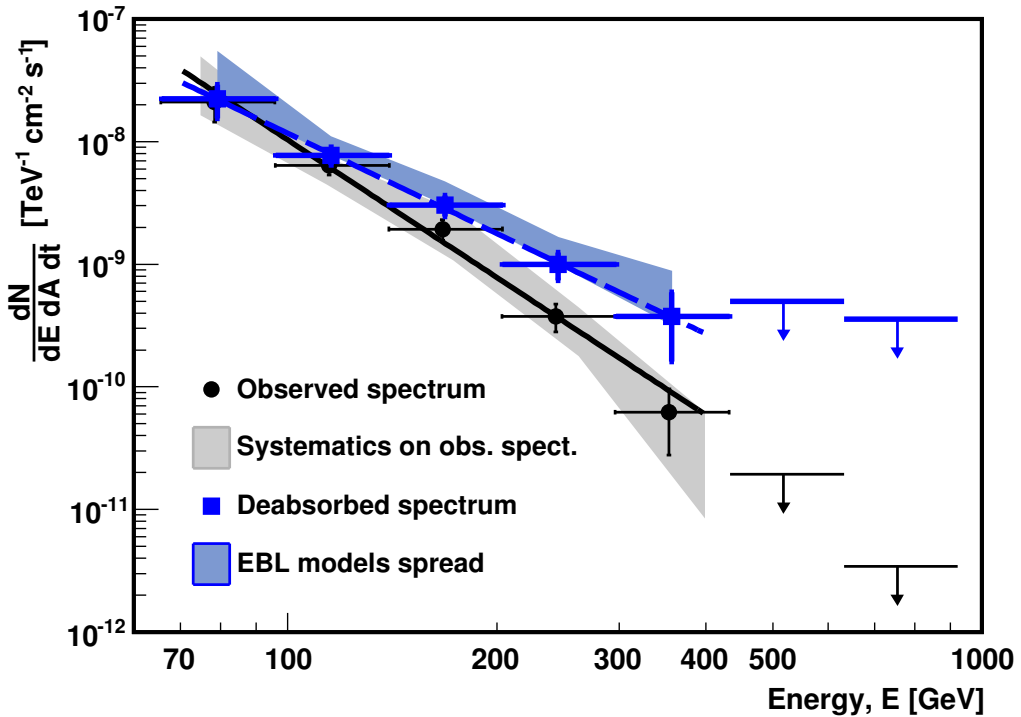


Figure 6.3: Differential energy spectrum of PKS 1222+21, as measured by MAGIC on June 17<sup>th</sup>, 2010. Differential fluxes are shown as black points, upper limits (95% C.L.) as black arrows. The black line is the best fit to a power-law. The grey shaded area represents the systematic uncertainties of the analysis. The absorption-corrected spectrum and upper limits, using the EBL model by Domínguez et al. (2011), are shown by the blue squares and arrows; the dashed blue line is the best fit power-law. The blue area illustrates the uncertainties due to differences in the EBL models, cited in the text, by Kneiske and Dole (2010); Gilmore et al. (2009); Franceschini et al. (2008) and Albert et al. (2008a).

power-laws with different photon indices and different values of the cut-off. The discrimination between the fits has been based on the resulting  $\chi^2$ -values (Lampton et al., 1976). The result is limited by the statistics, and one has to conclude that a cut-off cannot be excluded at 95% C.L. The value of the cut-off depends on the assumed photon index. Using the de-absorbed photon index obtained from the de-absorption with the model of Domínguez et al. (2011),  $\Gamma = 2.7$ , almost the hardest photon index, a cut-off above 180 GeV cannot be excluded. Considering the softest photon index compatible with Fermi data (see Sec. 6.4),  $\Gamma = 2.4$ , a cut-off for energies higher than 130 GeV could be possible. Nevertheless, even if the cut-off cannot be excluded for energies higher than 130 GeV, the spectrum is compatible with a simple power-law. As a result, in order to exclude the possibility of a cut-off in the de-absorbed spectrum, higher statistics are needed and hopefully more observations in the future will be able to constrain its position.

Regarding the quiescence state of the source, only on the 3<sup>rd</sup> of May, a detection was possible, but given its low statistical significance of just  $4.63\sigma$  a determination of the spectrum was not possible. The flux at  $E > 100$  GeV is obtained as  $(3.7 \pm 0.8_{\text{stat}} \pm 1.1_{\text{sys}}) \cdot 10^{-11} \text{ cm}^{-2}\text{s}^{-1}$  which corresponds to  $\sim 7\%$  of the Crab Nebula flux in the same energy band. In order to have an estimation of the spectral behavior, the hardness ratio has been calculated as  $H = F_{130-250}/F_{90-130}$  where  $F_{90-130}$  is the flux in the energy bin 90-130 GeV and  $F_{130-250}$  in the 130-250 GeV band, yielding  $H = 0.7 \pm 0.3$  while the same value during the flare state yields  $H=1.1 \pm 0.3$ , which is compatible within the statistical uncertainties. So, no limits on the spectral changes during flare states can be derived from that part of the data.

No detection has been found in VHE  $\gamma$ -rays for the rest of the data, only flux upper limits at 95% C.L. have been derived (see Table 6.2).

### 6.3.2 Source variability

In Fig. 6.4, a light curve of the whole observation campaign is shown, the black points correspond to the two detections, while the arrows represent the U.L.s at 95% CL assuming a spectral index of  $\Gamma = 3.75$ . This choice corresponds to the measurement during flare state, since we have no reasonable assumptions about the spectral shape during quiescent state.

PKS 1222+21 not only presents variability at nightly timescales (as shown in Fig. 6.4), but also a very fast intra-night variability during the flare on June 17<sup>th</sup>. Despite its short observation time, a variability study could be performed based on measured integral fluxes above 100 GeV. The minimum time bin in order to obtain a significance greater than  $3\sigma$  per bin results to be  $\sim 6$  minutes. The corresponding light curve of that night is shown in Fig. 6.5, where the black points represent the flux from the source, while the grey points show the flux calculated only from the background events. The background flux during the observation remains constant, thus instrumental variations of the performance during the observation can be excluded, as well as a measurable influence of the moon. The constancy hypothesis of the source flux can be rejected with high confidence since its probability is lower than  $1.1 \cdot 10^{-5}$  ( $\chi^2/\text{NDF}^1=28.3/4$ ). In order to quantify the variability time scale, different fits have been tested: the black dashed line in Fig 6.5 represents a linear fit, while

---

<sup>1</sup>NDF=Number of Degree of Freedom

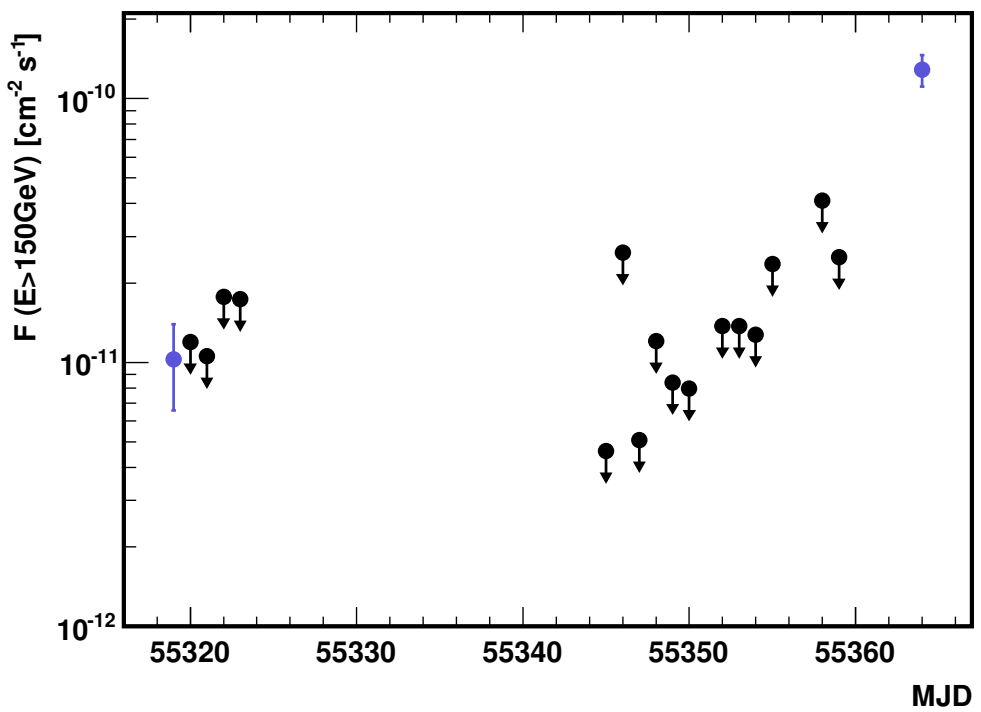


Figure 6.4: PKS 1222+21 light curve above 150 GeV for the whole observation campaign in nightly time bins. The blue points represent the flux calculated from the two detections of VHE  $\gamma$ -rays by MAGIC, while the black arrows indicate flux U.L.s at 95% C.L., calculated from the non-detection of the source.

the black solid line and exponential fit. The linear fit with slope  $(3.7 \pm 0.8) \cdot 10^{-13} \text{ cm}^{-2} \text{s}^{-2}$  can account properly for the flux changes, but does not allow to define an unambiguous time scale. For the exponential fit with characteristic time of  $(1.30 \pm 0.15) \cdot 10^{-3} \text{ s}^{-1}$  the doubling time of the flare is estimated as  $8.9_{-0.8}^{+1.3}$  minutes. Both fits are compatible with the data points, yielding  $\chi^2/\text{NDF}=5.68/3$  (corresponding to a probability of  $\sim 13\%$ ) and  $\chi^2/\text{NDF}=4.45/3$  (corresponding to a probability of  $\sim 22\%$ ), respectively. This short time scale is the fastest time variation ever observed in a FSRQ in the VHE  $\gamma$ -rays range and in any other energy range (Foschini et al., 2011) and is among the shortest time scales ever measured on VHE  $\gamma$ -rays emitting sources. It is only compatible with the source PKS 2155-304 and Mrk501, which present flux variations on a timescale of  $\sim 4$  minutes (HESS Collaboration et al., 2010; MAGIC Collaboration et al., 2008).

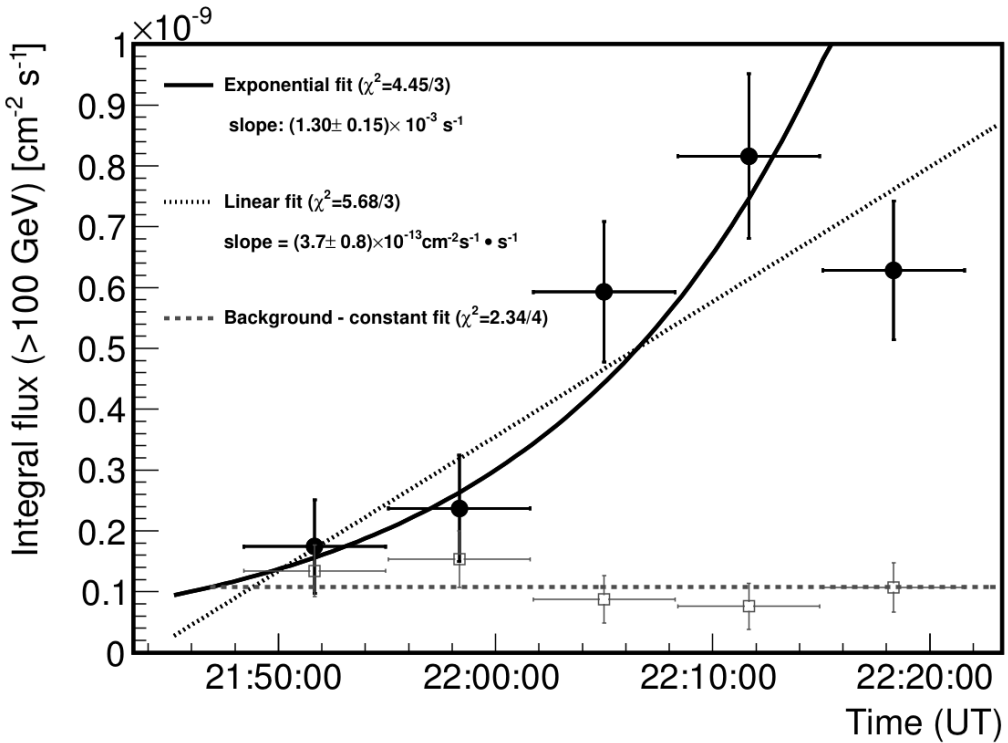


Figure 6.5: PKS 1222+21 light curve above 100 GeV during the VHE flare state on June 17<sup>th</sup>, in 6 minutes time bins (black filled circles). The black solid line is a fit with an exponential function and the black dotted line a fit with a linear function. The grey open squares denote the equivalent fluxes from the background events and the grey dashed line is a fit with a constant function to these points.

## 6.4 Fermi data

The LAT instrument onboard the *Fermi* satellite covers an energy range from 20 MeV to  $\sim 300$  GeV, observing the entire sky every 3 hours, when operated in survey mode. In Tanaka et al. (2011), a study of PKS 1222+21 from data collected from August 4, 2008

to August 4, 2010 is presented. According to these data, the source clearly shows three different states, in a first period, starting on August 4<sup>th</sup>, 2008 (MJD 54682), till September 26<sup>th</sup>, 2009 (MJD 55100), the source is in a quiescent state, where only upper limits can be derived. The source gradually increases its flux with minor flares superimposed, until April 24<sup>th</sup>, 2010 (MJD 55310), when a general flare period starts. During this flare period, two strong flares are detected: a first one on April 29<sup>th</sup>, 2010 (MJD 55315), few days before its first detection in VHE  $\gamma$ -rays by MAGIC, and the second one on June 18<sup>th</sup>, 2010 (MJD 55365), coinciding with the flare in the VHE band. In Fig. 6.6, the daily light curve for the flare period for  $E > 100$  MeV, measured by *Fermi* together with the variation of the photon index is shown. The red arrow and the two red circles respresents the MAGIC detection. Both detections in the VHE range by MAGIC correspond with a hard spectral index measured by *Fermi*,  $\Gamma \sim 2$ . In case of May 3<sup>rd</sup> detection the flux in *Fermi* was already low while in case of June 17<sup>th</sup> the flare was still going on. Unfortunately, the coverage by MAGIC is not good enough in order to draw conclusions from the long term correlation.

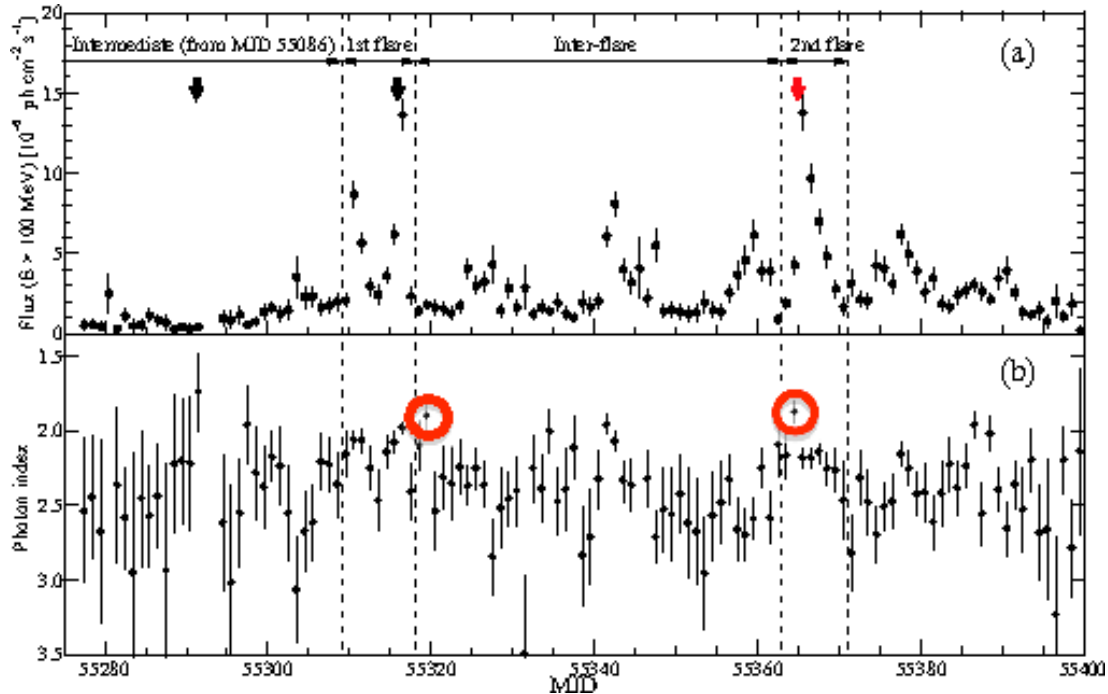


Figure 6.6: Fermi daily light curve of PKS 1222+21 for  $E > 100$  MeV in the upper panel. The lower panel represents the photon index derived from a single power-law fitted to the LAT data. The red arrow represents the detection in VHE  $\gamma$ -rays by MAGIC on 17<sup>th</sup> June 2010, while the black arrows represent the epochs when two very high energy photons with energies above 100 GeV were detected by *Fermi*. Figure taken from Tanaka et al. (2011). The two red circles denote the detection of VHE  $\gamma$ -rays by MAGIC.

Spectra from different epochs are presented in Fig. 6.7. The combined spectrum from all active periods is harder than that from quiescent states, where the spectrum is well described by a single power-law with a photon index  $\Gamma = 2.57 \pm 0.07$ . The spectral differences between different active epochs are not significant and compatible within uncertainties (see Table 6.3), all of them are compatible with a broken power-law with a cut-off from 1 to 3

GeV, depending on the state.

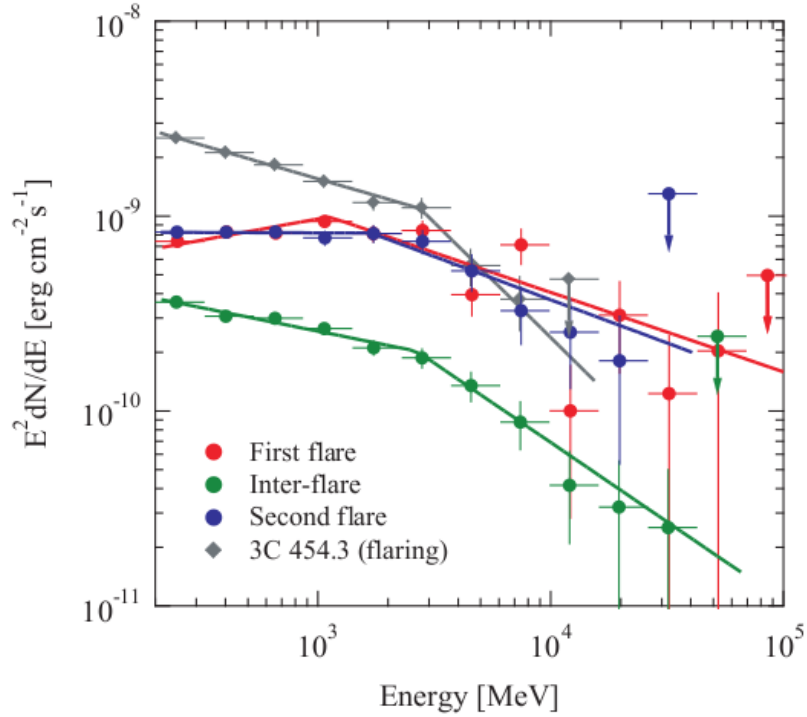


Figure 6.7: The three different spectral energy distributions of PKS 1222+21, measured by *Fermi* corresponding to different periods of activity (red, blue and green filled circles). In grey diamonds, the spectrum of 3C 454.3 (one of the brightest sources detected in the  $\gamma$ -rays band) is shown in flare state for comparison. Solid lines show the best-fit broken power-law models, while arrows indicate 95% upper limits. Figure taken from (Tanaka et al., 2011).

#### 6.4.1 Spectral energy distribution of PKS 1222+21

In order to build the high energy SED, covering the MeV/GeV energy range, a combination of almost simultaneous *Fermi*/LAT and MAGIC data is needed. Unfortunately, during the 30 minutes flare observation by MAGIC, there is a gap in the observation of PKS 1222+21 in the LAT sky survey data. Thus, an analysis of LAT data for a period of 2.5 h (MJD 55364.867 to 55364.973), encompassing the MAGIC observation, has been performed, using the same procedure as in Tanaka et al. (2011). This dedicated LAT analysis results in an integral flux of  $(6.5 \pm 1.9) \cdot 10^{-6} \text{ cm}^{-2}\text{s}^{-1}$  at energies of  $E > 100 \text{ MeV}$ . Given the short selected observation time bin, the statistics in LAT data are rather low, resulting in a non-detection at  $E > 2 \text{ GeV}$ . Only two spectral points up to 2 GeV can be derived from LAT analysis and an upper limit at 95% C.L. in the range from 2 to 6.3 GeV. The resulting spectrum is shown as black square points in Fig. 6.8, which are best fitted by a single power-law with spectral index of  $1.95 \pm 0.21$ . The red bow tie at low energies accounts for the uncertainties associated to the spectral fits. Comparing this value with the typical spectral index shown in Table 6.3 one can see the result is in agreement with the spectral

State	$\Gamma_{LE}$	$\Gamma_{HE}$	$E_{br}$ [GeV]
Intermediate+Active	$2.18 \pm 0.02$	$2.64 \pm 0.06$	$2.4^{+0.2}_{-0.2}$
Intermediate	$2.30 \pm 0.05$	$2.69 \pm 0.40$	$2.5^{+1.1}_{-0.4}$
First flare	$1.80 \pm 0.06$	$2.40 \pm 0.07$	$1.1^{+0.3}_{-0.2}$
Inter-flare	$2.24 \pm 0.03$	$2.81 \pm 0.14$	$2.7^{+0.6}_{-0.6}$
Second flare	$2.00 \pm 0.05$	$2.44 \pm 0.10$	$1.7^{+1.1}_{-0.4}$

Table 6.3: Spectral fits for PKS 1222+21, using broken power-law models, with low and high energy spectral indices  $\Gamma_{LE}$  and  $\Gamma_{HE}$ , respectively, and the break photon energies  $E_{br}$  (Tanaka et al., 2011).

index measured during flare states, where a wider time window has been used. Thus, a break in the MeV spectrum is also expected, as in the rest of flare data sample analysis. Regarding the VHE range, the observed spectral points by MAGIC are represented as black circles, while the de-absorbed spectrum using the EBL model by Domínguez et al. (2011), extrapolated to lower energies, is represented by the blue solid line. The bow tie accounts for the uncertainties due to different EBL models used in the spectral de-absorption process, as explained in Sec. 6.3.1. This extrapolation smoothly connects with Fermi data, assuming the typical break around 1-3 GeV, which is compatible with the specific LAT data analysis. Therefore, it is reasonable to assume that the high energy spectrum from PKS 1222+21 can be described by a broken power-law with  $\Gamma_{LE} = 1.9$  and  $\Gamma_{HE} = 2.7$  where the second component extends from a few GeV up to 400 GeV.

## 6.5 Discussion of the results

### 6.5.1 EBL limits

Extragalactic  $\gamma$ -rays are absorbed by pair production due to the interaction with photons, as discussed in Sec. 2.4. Only VHE  $\gamma$ -rays satisfy the energy threshold to interact with low energy photons. Depending on the nature of these low energy target photons, the interaction can lead to internal absorption, if the low energy photons have been produced by the source itself, or otherwise, the absorption can be due to EBL photons. The spectra only affected by EBL absorption could thus be used for indirect derivations of EBL limits. Even in case of self-absorbed sources, for realistic spectral distributions of the internal photons fields, the self-absorption should not change significantly the inferred EBL limits (Tavecchio and Mazin, 2009). In case of PKS 1222+21, where the VHE spectrum extends from 70 GeV to 400 GeV, those EBL photons which play an important role in the absorption process, are the ones in the optical and UV range.

Since *Fermi* data are mainly not affected, neither by the EBL, nor by self-absorption, the EBL optical depth can be derived from the VHE spectrum, assuming the spectral index of the intrinsic spectrum of the source cannot be smaller than the *Fermi*/LAT index. This in the case of PKS 1222+21 is the softer spectrum with spectral index  $\Gamma_{HE} = 2.4$  (Aleksić et al., 2011c). The maximally allowed optical depth,  $\tau$ , is obtained from a one-side upper limit at 95% C.L. of the observed flux and can be calculated from:

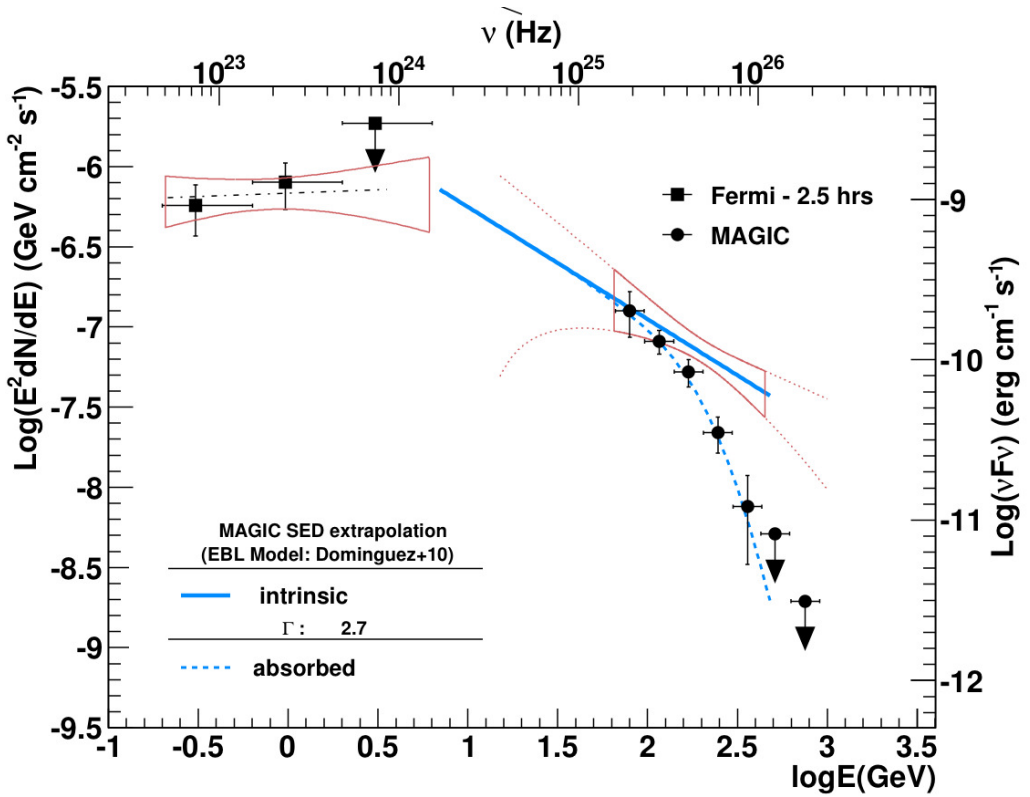


Figure 6.8: High energy SED of PKS 1222+21 during the flare of June 17<sup>th</sup>, 2010 (MJD 55364.9), showing *Fermi*/LAT (squares) and MAGIC (circles) differential fluxes. A red bow tie in the MeV/GeV range represents the uncertainty of the likelihood fit to the *Fermi*/LAT data. The unfolded and deabsorbed spectral fit to the MAGIC data is shown as a red bow tie, extrapolated to lower and higher energies (dotted lines). A thick solid line (photon index  $\Gamma = 2.7$ ) indicates a possible extrapolation of the MAGIC deabsorbed data to lower energies. The thick dashed line represents the EBL absorbed spectrum, obtained from the extrapolated intrinsic spectrum using the model of Domínguez et al. (2011).

$$F_{obs}(E) = F_{int}(E) \cdot e^{-\tau(E,z)}, \quad (6.2)$$

$$\tau_{max}(E) = \ln \left[ \frac{F_{int}(E)}{F_{obs}(E) - 1.64 \cdot \Delta F(E)} \right], \quad (6.3)$$

where  $F_{int}(E)$  is the maximally allowed intrinsic flux at energy  $E$ ,  $F_{obs}(E)$  and  $\Delta F(E)$  are the measured flux and its uncertainty, respectively. These derived values can be compared with the predicted optical depth by EBL models at  $z = 0.432$ , as shown in Fig. 6.9. From there, one can see that our measurement is compatible with EBL model predictions and no new constraints can be set. It is worth to note that most of the present EBL models are well in agreement in this energy range (except for Albert+08, which has been calculated as a maximum EBL in the UV range), in contrast to the situation some years ago, where a similar observation by MAGIC could severely constrain the existing models (Albert et al., 2008a). This observation can also be found in Fig. 6.3, where uncertainties in the VHE spectrum calculation (grey shaded area) are larger than the differences between different EBL models (blue area).

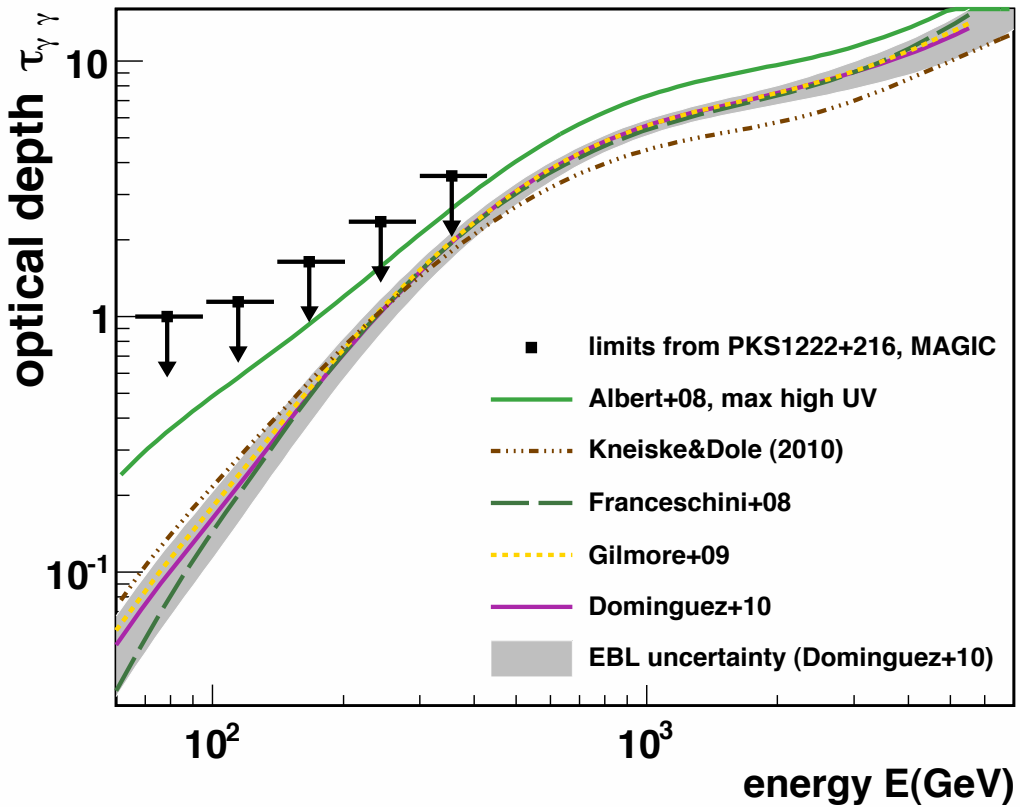


Figure 6.9: Optical depth upper limits at 95% C.L. along the line of sight to PKS 1222+21 ( $z=0.432$ ) assuming the limiting intrinsic photon index  $\Gamma_{VHE} = 2.4$  compared with optical depths predicted for the same redshift by different EBL models. Adapted from Aleksić et al. (2011c).

### 6.5.2 Implications for jet emission models

As discussed in Sec. 6.4.1, the quasi-simultaneous detection in the VHE and GeV energy bands on June 17<sup>th</sup> 2010 can be fitted by a simple power-law with spectral index  $\sim 2.7 \pm 0.3$  from few GeV up to 400 GeV without a strong cut-off, at least for energies higher than 130 GeV, in the framework of the currently accepted EBL models. This evidence suggests that the 100 MeV-400 GeV emission, peaking at  $\sim 1\text{-}3$  GeV (corresponding to the spectral break), belongs to a unique component produced in a single region of the jet. How can these spectral features be explained in the standard AGN picture? The spectral break at few GeV can be explained based on the model by Poutanen and Stern (2010) for 3C 454.3, which predicts the same kind of broken power-law for the spectra. In that work, the principal  $\gamma$ -ray absorption is due to pair production from the interaction of the jet photons with the HeII Lyman recombination continuum and line emission from BLR clouds, as calculated in Tanaka et al. (2011). The case of VHE emission is more complicated: commonly assumed by standard jet emission models, the VHE  $\gamma$ -ray emission is produced by inverse Compton (IC) scattering of relativistic electrons in the jet, interacting with the external photon field of the BLR. This mechanism is able to produce VHE photons, but in such a scenario, the decrease of efficiency of the IC scattering and the absorption of VHE  $\gamma$ -rays have to be taken into account. The change of the IC efficiency, due to the Klein-Nishina regime, leads to a lower cross section of the process (Ghisellini and Tavecchio, 2009) at high energies of roughly  $E_{KN} \simeq 22.5 \nu^{-1}$  GeV, where  $\nu$  is the frequency of the target photons in units of  $10^{15}\text{Hz}$  (Aleksić et al., 2011c). The absorption of VHE  $\gamma$ -rays is due to pair production (Reimer, 2007; Tavecchio and Mazin, 2009; Liu and Bai, 2006), the threshold energy of which can be expressed as  $E_{\gamma\gamma} = 60 \nu^{-1}$  GeV Aleksić et al. (2011c). Since the BLR is filled with optical-UV photons, both effects become important at similar energies, that is a few tens of GeV, where thus a cut-off is expected. However, no cut-off has been found at such energies. The lack of this spectral signature cannot be explained in the EBL frame arguing an inconsistency in the EBL models, since a possible effect from the EBL is negligible at such energies. The absorption is calculated based on H L $\alpha$  absorption in the BLR. However, if we consider instead, as proposed by Poutanen and Stern (2010), HeII Lyman absorption, the energy threshold would be even lower, thus the VHE  $\gamma$ -photons could escape even less from the BLR and never be detected. The canonical scenario, where the VHE emission is supposed to be produced inside the BLR, can thus not reproduce the observed spectrum of PKS 1222+21.

In order to avoid that strong absorption, we can consider a scenario in which the VHE emission is produced beyond the BLR, the so-called far dissipation scenario (Sikora et al., 2008), within the IR photon field of the dusty torus, emitting at a typical frequency of  $\nu_{\text{IR}} = 10^{13}$  Hz. In this case, the cut-off is expected at much higher energies  $\geq 1$  TeV, in agreement with the observed VHE spectrum. Moreover, since the MeV-GeV emission seems to be co-spatial according to observed SED, the model proposed by Poutanen and Stern (2010) as a general scenario can be rejected in case of PKS 1222+12.

Another important result is the variability of the source not only on nightly time-scales, but also on time-scales down to  $\sim 10$  minutes, measured at VHE  $\gamma$ -ray energies. The fact that these very short time-scales cannot be detected by *Fermi* is not in contradiction with the co-spatial assumption, because due to their small collection area, not enough photon

counting statistics can be obtained in such a small time window by *Fermi*. Taking into account the causality relation (Eq. 2.31),  $R < ct\delta/(1+z) \sim 1.3 \cdot 10^{13}\delta$  cm, a upper limit on the section of the jet can be set since the emitting region should be at least at a distance  $d > R_{BLR}$  from the BH. The radius of the BLR however can be derived from the relation  $R_{BLR} = 10^{17}L_{disk,45}^{1/2}$  cm (Ghisellini and Tavecchio, 2009), where the accretion disk luminosity is  $L_{disk} = 5 \cdot 10^{45}$  ergs $^{-1}$  (Fan et al., 2006), resulting in  $R_{BLR} \approx 2.2 \cdot 10^{17}$  cm which is a reasonable value within the typical values of  $R_{BLR} = 10^{17-18}$  cm (Kaspi et al., 2007; Bentz et al., 2009). Then, assuming a conical jet with constant semi-aperture angle,  $\theta$ , the trigonometric relation with the jet radius at BLR distances is expressed as  $R \sim \sin(\theta) \cdot d$ .

From radio observations, super-luminal motion on the jet has been measured with a bulk Lorentz factor of  $\Gamma \approx 20$  and the jet axis pointing to  $\phi = 3^\circ$  to of our line of sight (Jorstad et al., 2001; Malmrose et al., 2011). Since this source is a FSRQ and not a BL Lac, as maximum the semi-aperture angle of the jet has to be smaller than  $3^\circ$ . Thus, assuming  $\theta = 3^\circ$ ,  $R > \sin(\theta)R_{BLR} \sim 1.15 \cdot 10^{16}$  cm. Therefore, a Doppler factor of the order of at least  $\delta \approx 900$  would be needed in order to obtain this short variability in a canonical scenario, in which the emitting region is the whole section of the jet. However, the Doppler factor is defined as  $\delta = 1/[\Gamma \cdot (1 - \beta \cos \phi)]$  yielding  $\delta \approx 19$ , which is far from the needed Doppler factor in order to reconcile the observational facts with the canonical scenario.

There are some suggested scenarios which allow a reconciliation between spectral data and time scale: a strong re-collimation of the jet could avoid the constraint by the time variability, as proposed by Nalewajko and Sikora (2009) or a model involving two-zone emission scenarios, as will be explained in Chapter 7. Other options are hadronic models describing proton interactions, but up to now there are no predictions for this source in that framework. However, also hadronic models are confronted with the causality relation in a same manner.

Finally, Tanaka et al. (2011) demonstrate that during the flare from June 17<sup>th</sup>, the jet carried a total power comparable to the total accretion luminosity which means that the two major flares detected by the *Fermi* LAT should be considered being saturated at the maximum level, and we should not expect to detect any flares from PKS 1222+21 more luminous. Considering that the VHE emission is coming from the same region, we can conclude that it is not likely to detect a stronger flare in VHE, either.

Concluding, the VHE detection of PKS 1222+21 strongly challenges the standard present emission models: a scenario like Poutanen and Stern (2010) is completely excluded for this source, and the localization of the emission region w.r.t. the BLR must be reconsidered. One possible solution to reconcile models with data can be found in the next chapter.

---

# 7

---

## Emission Model for PKS 1222+21

### 7.1 Introduction

The detection of the Flat Spectrum Radio Quasar PKS 1222+21 in the VHE domain from  $\sim 70$  GeV to 400 GeV, together with the fast variability detected in that energy range, heavily challenges the canonical emission models. FSRQs show broad emission lines in their optical-UV spectra which are thought to originate from the Broad Line Region (BLR), due to the presence of dense clouds of gas ( $n \sim 10^9\text{-}10^{10}$  cm $^{-3}$ ) which move at typical velocities of thousands of km/s, and which get photo-ionized by the UV emission of the accretion disk. This region is thought to have a spherical shape with radius  $R_{\text{BLR}} \sim 10^{17}\text{-}10^{18}$  cm from the central black hole (Kaspi et al., 2007; Bentz et al., 2009). Therefore, inside the BLR, the environment is rich of optical-UV photons from the reprocessed light of the emission disk by the BLR clouds, due to scattering or due to absorption and re-emission by the clouds. The optical-UV photons can interact with VHE  $\gamma$  photons and produce  $e^- e^+$  pairs.

Unlike BL Lac objects, where the optical spectrum does not show features and the spectral energy distribution can be explained by a *Synchrotron-Self Compton (SSC)* model, in case of FSRQs, the emission mechanism responsible for the  $\gamma$ -ray production is inverse *Compton* scattering from an external photon field (EC) such as that of the BLR. In this scenario, a pronounced softening of the VHE spectrum is expected at few tens of GeV, due to the reduction of the efficiency of the process in the Klein-Nishina (KN) regime, and due to the strong absorption of photons via pair-production in the optical-UV photon field of the BLR. Nevertheless, the quasi-simultaneous SED from Fermi and MAGIC data during the flare from June 17, 2010 (see Fig. 6.8) shows clearly the absence of a cut-off at the expected energies. The absorption problem can only be circumvented, if the VHE emission is not produced within the dense UV-optical photon field, but instead outside the BLR, where the absorption would be due to IR photons emitted by the dusty torus. In this case, the combined effects from the KN regime and the absorption due to the external IR photons would produce a cut-off at much higher energies around 1 TeV, in agreement with the observed SED where the maximum detected energy lies at 400 GeV. However, this far-dissipation scenario is not compatible either with the data, due to the detected fast variability time scale of  $\sim 10$  minutes, as discussed in Sec 6.5.2. In this chapter, I

will focus on the modelling of the SED in the context of a two-zone emission scenario, which has been previously proposed to explain the ultra-fast variability of two BL Lacs, namely PKS 2155+304 and Mkn 501 (Ghisellini and Tavecchio, 2008; Giannios et al., 2010). The two-zone scenario consists of a compact region, a small “*blob*”, mainly responsible for the  $\gamma$ -ray emission which causes the fast variability, while the low energy emission comes from a standard emission region, corresponding to the whole section of the jet, as typically assumed in the canonical model. The difference between the case of PKS1222+21 and the two previously proposed ones comes from the physical characteristics of the environment, since in FSRQs, the external photon field plays a key role, which is not the case for BL Lacs.

Blobs inside jets are commonly observed in radio and in particular have been detected in this source by Jorstad et al. (2001). In that respect, the proposed assumption of such an internal jet structure is supported by observational findings.

## 7.2 A scheme of the model

The typical spectral energy distribution of blazars shows two bumps, which can be described, in a first approximation, as a two peak distribution, shown in Fig. 7.1. It is characterized by two peak frequencies,  $\nu_s$  and  $\nu_c$ , which correspond to the synchrotron and inverse Compton processes, respectively, with the corresponding peak luminosities  $L_s$  and  $L_c$ , and the spectral indices.

Assuming that the synchrotron and inverse Compton emission belong to the same electron population, and taking into account that a power-law distribution of electrons produces a power-law photon spectrum in both processes, in order to explain the SED model, one can start with a power-law distribution of electrons (Fig. 7.2), mathematically expressed as:

$$N(\gamma) = \begin{cases} K\gamma^{-n_1} & \text{if } \gamma_{\min} < \gamma < \gamma_b \\ K\gamma^{-n_2} & \text{if } \gamma_b < \gamma < \gamma_{\max}, \end{cases} \quad (7.1)$$

where  $\gamma$  represents the Lorentz factors of the electrons in the rest frame of the jet,  $\gamma_{\min}$ ,  $\gamma_{\max}$  and  $\gamma_b$  are their minimum, maximum and break values, respectively;  $n_1$  and  $n_2$  are the two power-law spectral indices before and after the break. The spectral indices of the emitted spectrum,  $\alpha$ , and those of the electron distribution,  $n$ , are related, both in the synchrotron and inverse Compton case, as:

$$\alpha = \frac{n - 1}{2} \quad (7.2)$$

In standard one-zone models, the emitting region is assumed to be a sphere with size comparable to that of the jet cross section which contains the relativistic electrons tangled within a magnetic field of intensity  $B$ , moving with a bulk Lorentz factor  $\Gamma$  at an angle  $\theta$  with respect to the line of sight to the observer. Typically, the standard models can account for the emission from IR to gamma-rays, while the radio emission is believed to stem from different parts of the jet. In the particular case of PKS 1222+21, different emission regions with different velocities can be detected at radio frequencies (Jorstad et al., 2001).

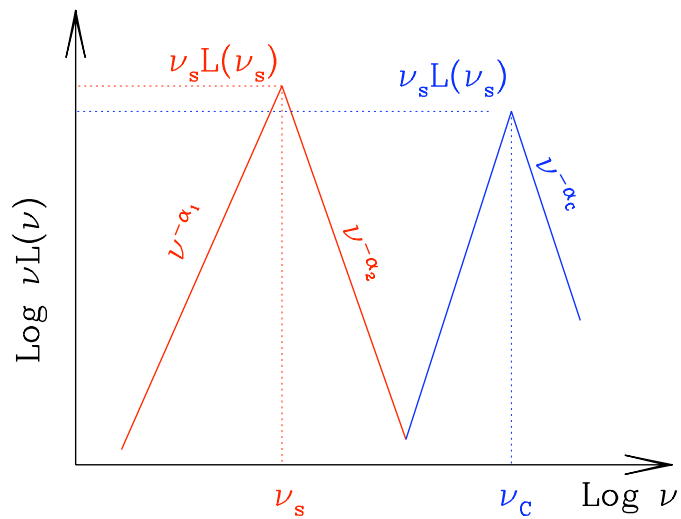


Figure 7.1: A sketch of the most simple model for an SSC spectral energy distribution.

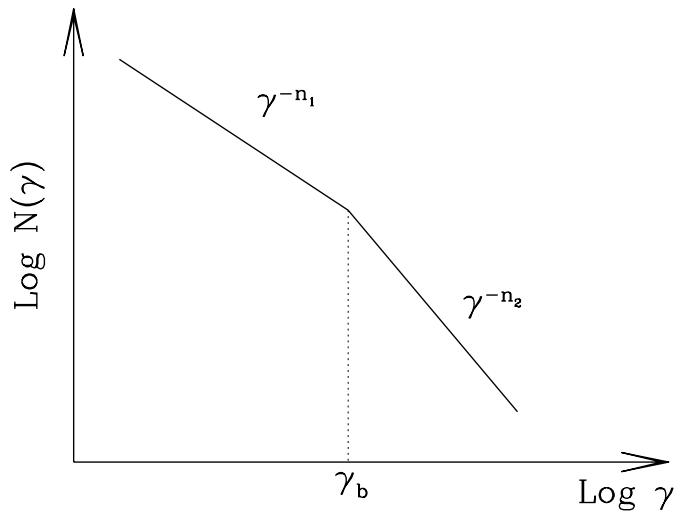


Figure 7.2: Broken power-law distribution for electrons.

The emission from inverse Compton scattering can be produced either by SSC or external Compton. The importance of each mechanism depends strongly on the type of source. In FSRQs, where there is an important external photon field, external Compton emission dominates while for BL Lacs, the environment does not play a key role and therefore, the SSC mechanism prevails against the external Compton one. Depending on the localization of the emitting region, the external Compton field will be dominated by optical-UV or IR photons. In the modelling, I will assume an isotropic radiation field, which can be modeled as a black-body spectrum. In addition, relativistic effects have to be taken into account, since they introduce important features:

- In the emitting region rest frame, the energy density of the external field is seen as relativistically boosted by a factor  $\Gamma^2$ .
- The probability of interaction between electrons and photons inside the jet increases, due to the aberration of light which produces a photon field appearing more concentrated and, in the rest frame of the emitting region, seen as blue-shifted. This enhances the inverse Compton scattering probability and can even decelerate the emitting region (Ghisellini, 2000).

For the numerical calculations, a code from Maraschi and Tavecchio (2003) has been adapted.

### 7.3 The spectral energy distribution

The known parts of the SED of PKS 1222+21 from radio frequencies up to the VHE range are shown in Fig. 7.3. The red points at VHE  $\gamma$ -ray frequencies represent the MAGIC spectral points, measured during the flare of June 17, 2010. These data have been corrected for the EBL absorption using the recent model of Domínguez et al. (2011). The pink triangle points come from the *Fermi*/LAT quasi-simultaneous observation of 2.5 hours encompassing the MAGIC detection, from where two spectral points and one upper limit at 95% C.L. have been calculated, as well as the bow-tie which represents the uncertainty derived from the fit. The black line at high frequencies depicts the Fermi spectrum in quiescent state (Tanaka et al., 2011) of the source, for comparison. The X-ray, plotted in blue squares, and optical-UV data points have been obtained from *Swift* observations (Tavecchio et al., 2011). *Swift* observed PKS 1222+21 during May-June 2010 in correspondence with the high state of activity of the source in the *Fermi* energy band. Unfortunately, there are no observations available from June 17. The closest day of observation to the VHE flare is June 20 where the daily average LAT flux was similar to that of June 17 (see Fig. 6.6), plotted in blue squares. The UVOT data points cover the optical-UV energy band, shown in red circles. The red star points represent SDSS data taken on January 2008.

Comparing UVOT and SDSS data, UVOT fluxes are a factor two higher which can be related to different emission states of the source. Moreover, in both cases, the hard optical-UV spectrum suggests the presence of direct thermal emission from the accretion disk (Ghisellini and Tavecchio, 2009). Therefore, this brightening can be interpreted as an increase of the accretion luminosity.

The IR data, shown in pink squares, come from the Spitzer Space Telescope (Malmrose et al., 2011) and can be fitted to a black body with a temperature of  $T = 1200$  K and another thinner part as a black body of  $T = 600$  K, most probably related to the dusty torus emission. The archival radio data have been taken from NED, shown in green circles, and from Jorstad et al. (2001), shown in green squares. These points represent measurements from different regions of the jet.

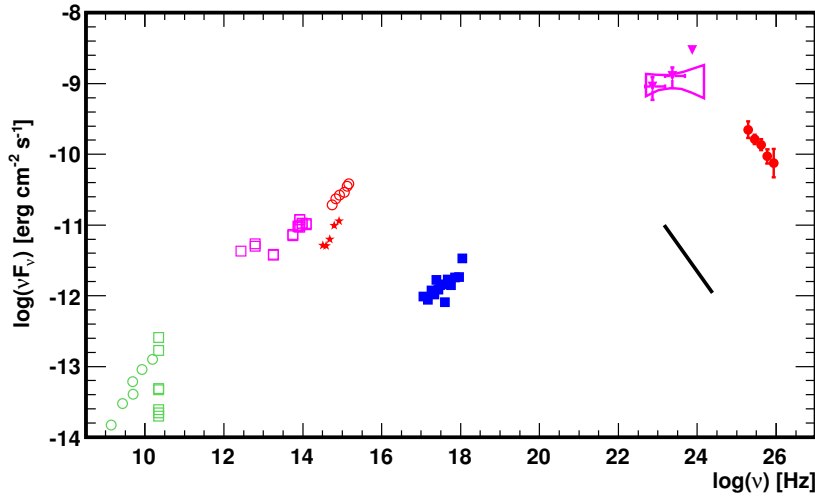


Figure 7.3: Spectral energy distribution for PKS 1222+21, see text for explanations.

## 7.4 Modelling of the spectral energy distribution

As typical for the spectral energy distribution of blazars, the one from PKS 1222+21 shows a two bump shape. The leading  $\gamma$ -ray emission mechanism for the second bump should be due to the external Compton scattering with the IR photons emitted by the torus. However, a canonical model cannot explain the high variability detected in VHE  $\gamma$ -rays of the order of  $\sim 10$  minutes which is also supported by the detection of fast variability of  $\lesssim 2$  hours detected in the MeV-GeV band from *Fermi* observations during the high states (Foschini et al., 2011). Measurements of a shorter variability time-scale by *Fermi* are limited due to the lack of sufficient photon statistics. The fast variability in both energy bands, together with the spectral connection between the MeV and GeV band which can be well-described by a simple power-law from 1 GeV to 400 GeV, strongly suggest that the emission belongs to a unique region. Also a hint of variability of X-rays during the flare has been found from the analysis of *Swift* data before and after the flare (Tavecchio et al., 2011). Taking into account these observational facts, a scenario composed of two co-spatial emitting zones inside the jet, both located outside the BLR can be thought of (see Fig. 7.4): a small and compact emitting region, a spherical “blob” with radius  $R_b$  moving at a Lorentz factor  $\Gamma_b$  w.r.t. the

observer and a bigger emitting region assumed to be a sphere with radius,  $R_j$ , similar to the cross section of the jet which moves at a Lorentz factor  $\Gamma < \Gamma_b$ . I will assume further  $\Gamma \sim 20$ , as found by Jorstad et al. (2001) from radio data. The “blob” will account mainly for the gamma-ray emission while the whole section of the jet will domain the emission at lower frequencies. Different processes will take place in both emitting regions: Synchrotron, SSC and EC. In case of the “blob”, the EC emission will be due to two different photon fields: on one hand, the IR photon field from the torus and on the other hand, the photon field created by the jet. I assume a conical jet with a semi-aperture angle of  $\phi \sim 3^\circ$ , which is compatible with the radio measurements as has been discussed in Sec. 6.5.2.

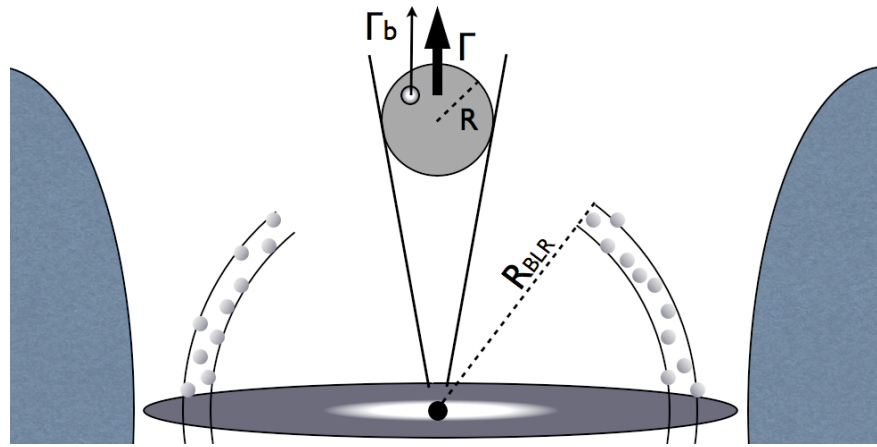


Figure 7.4: Sketch of the geometrical arrangement assumed in the model.

In the model, the BLR is simulated as a spherical shell located at  $R_{\text{BLR}}$  from the central BH which is illuminated by the accretion disk with luminosity  $L_d$ . The relation between  $R_{\text{BLR}}$  and  $L_d$  is given by  $R_{\text{BLR}} = 10^{17} \cdot L_{d,45}^{1/2}$  (Ghisellini and Tavecchio, 2009), where  $L_{d,45}$  stands for the luminosity in units of  $10^{45} \text{ erg s}^{-1}$ . A fraction,  $\xi$ , of the disk emission is reprocessed by the BLR clouds, which is typically  $\xi = 0.1$ . The disk emission is modeled as a black body, as suggested by Tavecchio and Ghisellini (2008). The hard optical-UV spectrum suggests that it probably comes from the direct disk emission. Thus, the black body is defined as fitting the optical-UV data resulting in a temperature of  $T_d = 2.5 \cdot 10^4 \text{ K}$ . The IR emission from the torus is modeled as a black body with a temperature  $T_{\text{torus}} = 1.8 \cdot 10^3 \text{ K}$  which defines properly the IR data, but disagrees with the assumed model by Malmrose et al. (2011), since there, two IR emission components are assumed. However, in the paper they cannot completely reproduce the observed data.

Absorption of gamma-rays by the IR radiation field is neglected for simplicity since it is expected to become important only at around 1 TeV and PKS 1222+21 has been detected only up to 400 GeV. Assuming the parameters shown in the first row of Table 7.1, the corresponding fit is shown in Fig 7.5 where the blue dashed line represents the emission from the “blob”, the red dashed line denotes the emission from the whole section of the jet. The solid black line is the sum of these emission components. The radio emission cannot

be well-fitted by this model, but since the data are not simultaneous and radio emission is detected from different emission zones along the jet, no constraint can be set in this scenario. Also a faster “blob” with a  $\Gamma_b = 70$  can be assumed, as shown in Fig. 7.6.

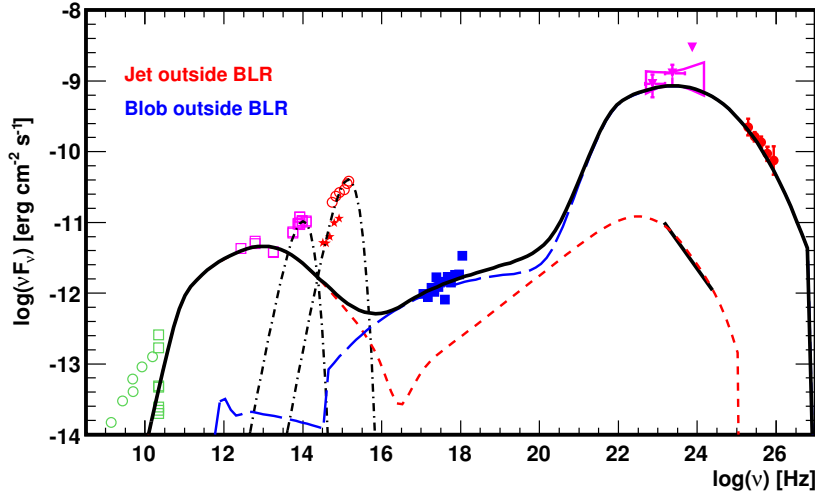


Figure 7.5: Spectral energy distribution fit by the model considering two emitting regions outside the BLR with a  $\Gamma = 20$  for the jet and  $\Gamma_b = 50$ .

As result of the two-zone emission modelling, the interplay between the whole section of the jet and the small “blob” is not important, as shown in Fig. 7.7, that is to say the EC emission in the “blob” due to the photon field produced by the whole section of the jet is negligible, when compared with the EC emission by the “blob” as interaction with the IR photons from the torus. Thus, the two emitting regions could be spatially separated. In this scenario, the “blob” has to remain outside the BLR in order to avoid the absorption of the VHE  $\gamma$ -rays but the larger emitting region can be located both inside or outside the BLR. These two cases are shown in Fig. 7.8 and Fig. 7.9. In the latter case, the absorption due to the BLR suffered by the whole section of the jet has been neglected since it affects mainly the  $\gamma$ -rays and by construction, this energy range is dominated by the “blob” emission, which remains outside the BLR.

Since in this two-emission zone model, the number of free parameters is twice that of the one-zone model, it is difficult to give exact numbers for the fit results, but the fits can give an idea of a revised understanding of this object which clearly can account for the observations. As shown in Table 7.1, a low magnetic field is needed in the compact “blob” which could originate from reconnection events which could naturally produce compact regions of fast moving plasma inside the jet, the so-called “jet in jet” scenarios proposed by Giannios et al. (2009, 2010).

As has been shown, the proposed scenario can describe the observed SED for PKS 1222+21 during the flare state detected on June 17, 2010. However, an extensive study of the variability in different energy bands is needed in order to understand the emission processes

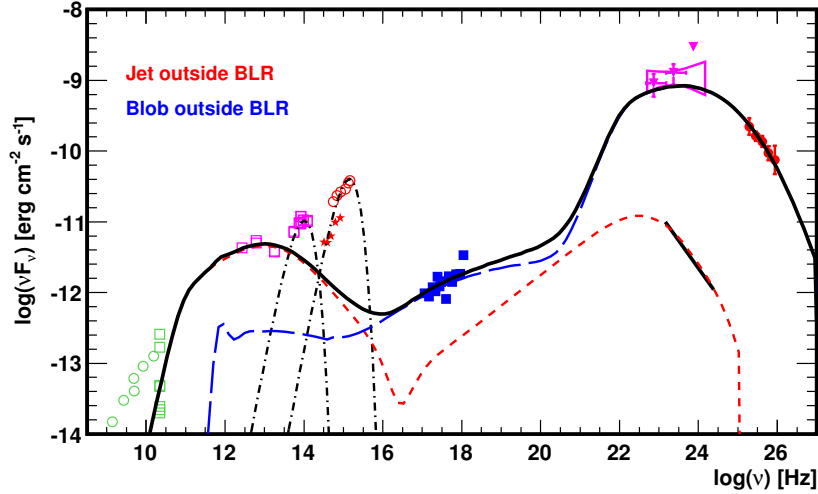


Figure 7.6: Spectral energy distribution fit to the model considering two emitting regions outside the BLR with  $\Gamma = 20$  for the jet and  $\Gamma_b = 70$ .

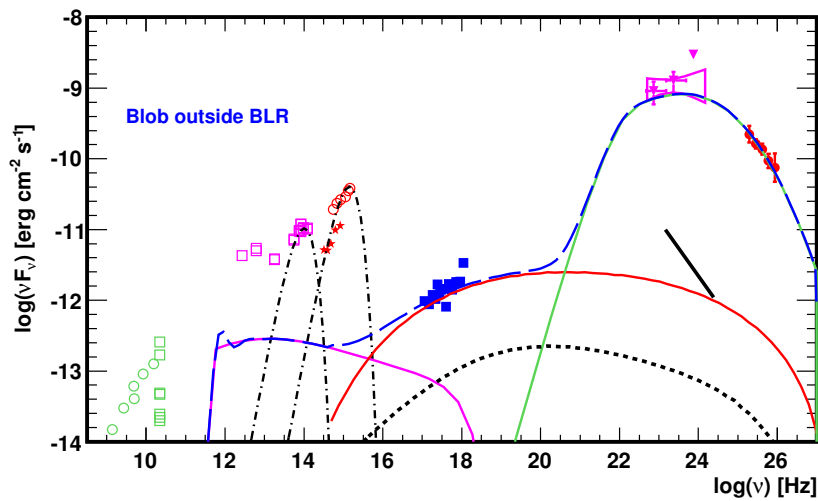


Figure 7.7: Spectral energy distribution fit to the model considering two emitting regions outside the BLR with  $\Gamma = 20$  for the jet and  $\Gamma_b = 70$ . Only the “blob” emission is represented by colored lines: the solid pink line represents the synchrotron emission part, the red line denotes the SSC, the green line is the EC emission due to the IR photon field and the dotted black line represents the EC emission due to the photon field of the jet.

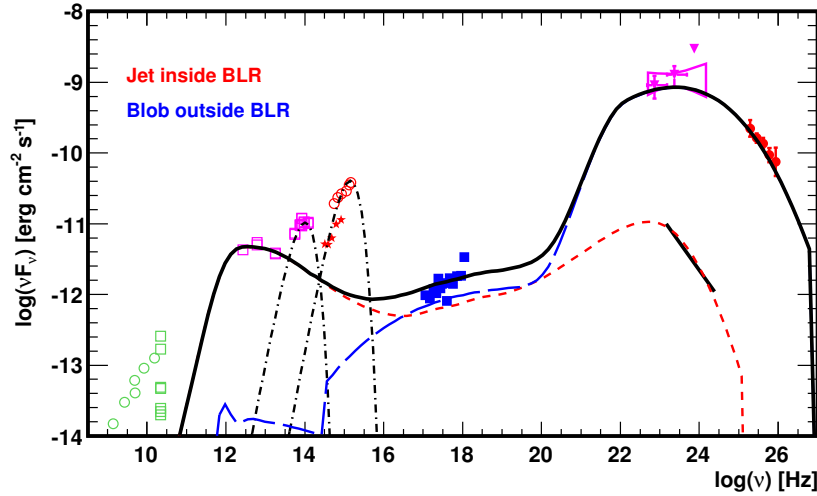


Figure 7.8: Spectral energy distribution fit to the model considering the “blob” emitting outside the BLR with  $\Gamma_b = 50$  and the jet inside the BLR with  $\Gamma = 20$ .

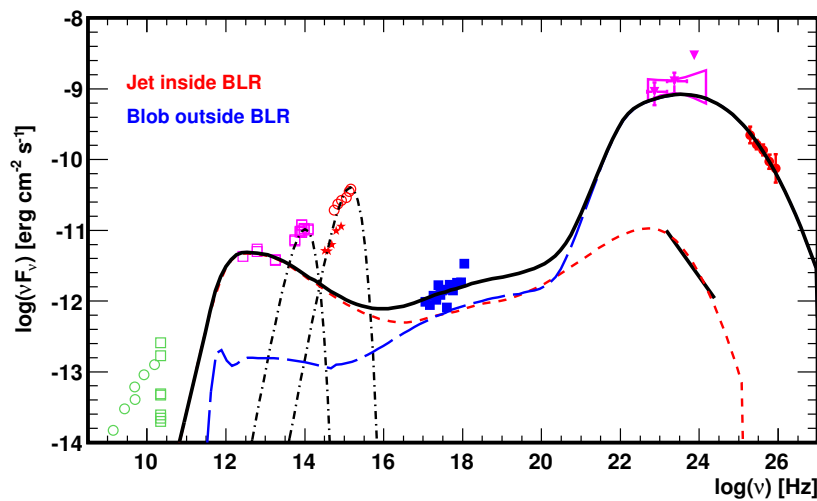


Figure 7.9: Spectral energy distribution fit to the model considering the “blob” emitting outside the BLR with a  $\Gamma_b = 70$  and the jet inside the BLR with  $\Gamma = 20$ .

in the source. For example, a correlation study between optical and  $\gamma$ -rays would be very important. If a correlation between optical and  $\gamma$ -rays is found, depending on the characteristics of the optical brightening, different conclusions could be derived:

- If the optical spectrum does not change its spectral index, this would indicate that there is a change in the disk emission, since one would expect an enhancement of its luminosity, but still compatible with a black body spectrum. From there, an important question arises, how much time would be needed that a change in the disk can affect the jet emission at long distances from the central black hole? The difference in the time-of-flight can be approximated as:

$$t_{\text{var}} \sim \frac{R_{\text{em}}}{2\Gamma^2 c} \quad (7.3)$$

where  $R_{\text{em}}$  denotes the distance from the central BH to the emitting region and  $\Gamma$  is the bulk Lorentz factor of the jet. This formula is only valid for very small angles w.r.t. line-of-sight to the observer, which is the case for PKS 1222+21. Assuming that the distance to the BH has to be at least the BLR radius, in order to be consistent with the observations, and  $\Gamma \approx 20$  which is a realistic value from the radio observations,  $t_{\text{var}} \approx 3.5$  hours is obtained. Thus, a time delay between the optical and  $\gamma$ -ray emission activity is expected in that case, with the optical flare photons arriving earlier. Otherwise, if a time delay is found the other way around, arriving first the  $\gamma$ -ray emission and only then the optical one, we could reject this hypothesis. Therefore, additional simultaneous multi-wavelength data are mandatory in order to confirm or reject this prediction of the two-zone emission model.

- In case the optical spectral index changes, it would indicate that the synchrotron emission is much higher than the disk emission and thus the change does not come from the disk but rather from the jet.

	$\gamma_{\min}$	$\gamma_b$	$\gamma_{\max}$	$n_1$	$n_2$	$B$ [G]	$K$ [ $\text{cm}^{-3}$ ]	$R$ [cm]	$\Gamma$	$P_{p,45}$	$P_{e,45}$	$P_{B,45}$
Jet out	1	950	$2 \cdot 10^4$	2.1	4.35	0.3	$3.1 \cdot 10^2$	$1 \cdot 10^{17}$	20	240	0.9	1.8
Blob out	100	750	$4 \cdot 10^5$	2.2	3.35	$5.5 \cdot 10^{-3}$	$8 \cdot 10^8$	$6.4 \cdot 10^{14}$	50	316	60	$1.6 \cdot 10^{-7}$
Jet out	1	950	$2 \cdot 10^4$	2.1	4.35	0.3	$3.1 \cdot 10^2$	$1 \cdot 10^{17}$	20	240	0.9	1.8
Blob out	100	750	$4 \cdot 10^5$	2.2	3.35	$2.7 \cdot 10^{-2}$	$9 \cdot 10^7$	$7.1 \cdot 10^{14}$	70	84	16	$9 \cdot 10^{-6}$
Jet in	1	400	$2 \cdot 10^4$	2.1	4.0	0.55	$1.5 \cdot 10^5$	$1.1 \cdot 10^{16}$	20	$1.5 \cdot 10^3$	5.1	$7.3 \cdot 10^{-2}$
Blob out	100	750	$4 \cdot 10^5$	2.2	3.35	$5 \cdot 10^{-3}$	$8 \cdot 10^8$	$6.5 \cdot 10^{14}$	50	320	60	$1.3 \cdot 10^{-7}$
Jet in	1	400	$2 \cdot 10^4$	2.1	4.0	0.55	$1.5 \cdot 10^5$	$1.1 \cdot 10^{16}$	20	$1.5 \cdot 10^3$	5.1	$7.3 \cdot 10^{-2}$
Blob out	100	750	$4 \cdot 10^5$	2.2	3.35	$2 \cdot 10^{-2}$	$9 \cdot 10^7$	$7.1 \cdot 10^{14}$	70	84	16	$4.9 \cdot 10^{-6}$

Table 7.1: Input parameters for the emission models shown in the figures. Out and in denotes the localization of the emitting region, belonging outside the BLR or inside, respectively.  $\gamma_{\min}$ ,  $\gamma_b$  and  $\gamma_{\max}$  are the minimum, break and maximum Lorentz factor of the electron population while  $n_1$  and  $n_2$  denote the low and high energy slopes of the broken power-law of the electron distribution. The magnetic field is represented by  $B$ , the normalization of the electron distribution by  $K$  and the radius of the emission region by  $R$ . The last three columns show the power carried by cold protons (assuming one proton per emitting electron), relativistic electrons and the magnetic field in units of  $10^{45}$  erg s $^{-2}$ .



---

# 8

---

## Discovery of VHE $\gamma$ -Ray Emission from 1ES 1215+303

### 8.1 Introduction

1ES 1215+303 (also known as ON 325), is a blazar located at R.A. 12h17m52.08s and Dec. +30d07m0.64s, belonging to the BL Lac type and classified as intermediate-frequency peaked (IBL). Its redshift is uncertain, as there are two different values available in the literature:  $z = 0.130$  (Browne, 1971) and  $z = 0.237$  (Murphy et al., 1993), both of them often cited. Since its optical spectrum has not yet been published, it is difficult to judge which value of both is the correct one. In Nilsson et al. (2003), the magnitude of the host galaxy was measured as  $R = 16.24$ , and from there, following the methodology of Nilsson et al. (2008), the derived redshift is  $z = 0.13 \pm 0.04$  (K. Nilsson, priv. communication), clearly in favor of the first value by Browne.

This source had been observed before in VHE  $\gamma$ -rays by Wipple, yielding only flux upper limits (U.L.) at 95% C. L. for  $E > 300$  GeV:  $F_{300} < 8.23 \cdot 10^{-11}$  cm $^{-2}$ s $^{-1}$  for a 1999 observation campaign and  $F_{300} < 1.89 \cdot 10^{-11}$  cm $^{-2}$ s $^{-1}$  for 2000 observations (Horan et al., 2004). Also from previous MAGIC observations during a 2007-2008 campaign, an U.L. at 95% C.L. for  $E > 120$  GeV:  $F_{120} < 3.5 \cdot 10^{-11}$  cm $^{-2}$ s $^{-1}$  has been obtained Aleksić et al. (2011a). 1ES 1215+303 was included as promising candidate TeV blazar by Costamante and Ghisellini (2002) and is also part of the Fermi bright AGN catalog, showing a hard spectrum with spectral slope  $\Gamma = 1.89 \pm 0.06$  (Abdo et al., 2009).

The source was observed again by MAGIC, this time with the stereoscopic system, during 2010, resulting in a hint of a signal, and later during 2011, MAGIC followed-up the source another time, triggered by a high optical state, which was reported by the Tuorla monitoring program<sup>1</sup>. Based on these observations, its discovery in the VHE range was possible (Mariotti, 2011). In this chapter, data analysis of both 2010 and 2011 campaigns will be presented.

Inside the MAGIC FoV, when pointing to 1ES 1215+303, another TeV blazar can be found: the high-frequency peaked 1ES 1218+304 (Albert et al., 2006a) at redshift  $z = 0.182$ ,

---

<sup>1</sup><http://users.utu.fi/kani/1m>.

situated  $\sim 0.8$  degrees from 1ES 1215+303. From MAGIC 2010 and 2011 observations, the detection of 1ES 1218+304 in both observation campaigns is possible with high significance and therefore, a detailed study can be performed also on that source, presented in Chapter 9.

## 8.2 The observations

The MAGIC telescopes followed-up the source during two different observation campaigns for a total of  $\sim 42$  hours. The first campaign consisted in observations from January–February to May–June 2010, while the second observation period covers January and February 2011, and was triggered by a high optical state of the source from the Tuorla monitoring program (see Fig. 8.7).

During the first campaign,  $\sim 21.2$  hours of good quality data were taken in wobble mode. From these,  $\sim 17.9$  hours were observed at the standard wobble distance at  $0.4^\circ$  from the source (wobble angles:  $0^\circ$  and  $180^\circ$ ), then the angles were changed to  $90^\circ$  and  $270^\circ$  ( $\sim 3.2$  hours) due to the presence of a strong source, 1ES 1218+30.4, at a distance of  $\sim 0.8^\circ$  and approx. the same declination as that of 1ES 1215+303, which makes the estimation of the background difficult. In Fig. 8.1, a FoV of the approx. size of the trigger region of the camera is shown, where the two sources are identified as yellow circles, while the different wobble pointings are represented by the red markers. The data sample from 2010 covers a zenith range from  $1^\circ$  to  $40^\circ$ , most of the data were taken at a zenith angle lower than  $35^\circ$ .

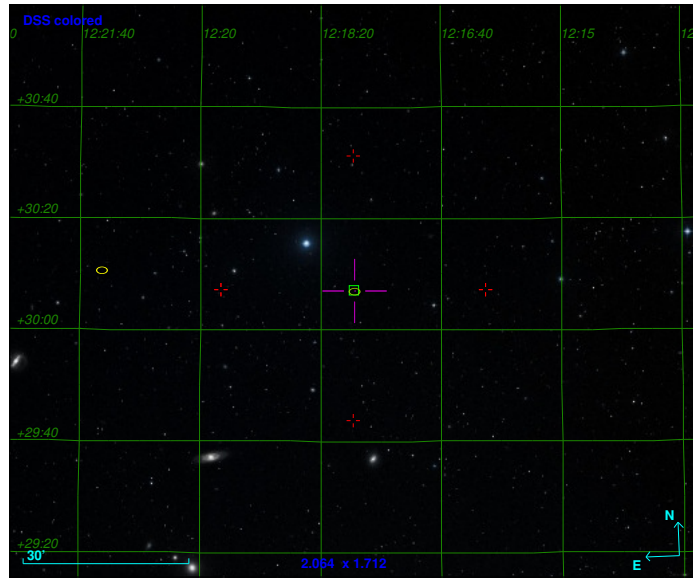


Figure 8.1: Sky region centered at the position of 1ES 1215+303 with approx. size of the trigger region of the MAGIC telescopes. By the yellow circle on the left side, the position in the sky of 1ES 1218+304 is represented. The red markers represent the wobble pointing positions.

Regarding the second observation campaign during 2011, a total of  $\sim 20.8$  hours of good quality data were collected. The observation was performed in wobble mode, using the

wobble angles  $90^\circ$  and  $270^\circ$ . The data were taken at zenith angles from  $\sim 0^\circ$  to  $27^\circ$ . Most of the data were taken in dark night conditions, but also a small amount of them were taken in moderate moon conditions. Table 8.1 gives a summary of the observations.

Day	MJD	Zenith angle	Observation time (h)	Significance ( $\sigma$ )
12/01/2010	55208	1-14	0.98	-0.38
15/01/2010	55211	1-12	1.11	0.97
19/01/2010	55215	2-16	0.86	3.31
20/01/2010	55216	1-16	1.74	1.03
22/01/2010	55218	1-19	1.97	1.23
23/01/2010	55219	1-40	3.38	2.36
24/01/2010	55220	1-24	1.44	0.45
25/01/2010	55221	1-20	1.08	-0.63
09/02/2010	55236	1-32	2.70	-1.64
12/02/2010	55239	6-34	1.72	1.41
14/05/2010 <sup>a</sup>	55330	1-31	1.57	0.41
15/05/2010 <sup>a</sup>	55331	12-35	0.62	1.07
16/05/2010	55332	18-35	0.95	-1.14
17/05/2010 <sup>a</sup>	55333	21-30	0.51	-0.73
10/06/2010 <sup>a</sup>	55357	27-37	0.53	1.12
01/01/2011	55562	1-21	1.20	4.01
02/01/2011	55563	1-20	1.26	1.61
04/01/2011	55565	0-16	1.41	2.76
05/01/2011	55566	2-17	1.18	1.60
06/01/2011	55567	1-15	1.55	2.98
07/01/2011	55568	1-24	1.86	1.16
08/01/2011	55569	1-26	2.02	3.72
09/01/2011	55570	0-26	2.14	2.75
10/01/2011	55571	1-9	0.58	0.03
11/01/2011	55572	0-10	1.04	2.09
12/01/2011	55573	0-11	1.00	4.60
13/01/2011	55574	0-12	1.07	3.83
14/01/2011	55575	1-14	1.04	2.52
15/01/2011	55576	1-15	1.74	1.48
16/01/2011	55577	2-7	0.28	0.99
27/01/2011	55588	14-23	0.49	0.88
02/02/2011	55594	16-27	0.64	-0.90
03/02/2011	55595	3-8	0.31	1.0

Table 8.1: Summary of the MAGIC observations of 1ES 1215+303. The first part of the table shows the data taken during the 2010 campaign, while the second part shows the 2011 observations. The 2010 data were taken in wobble mode at angles 0 and 180 degrees, except for the data indicated with <sup>a</sup> which were observed at  $90^\circ$  and  $270^\circ$ . In case of 2011, all data were taken at  $90^\circ$  and  $270^\circ$ . The dates refer to the beginning of each night. The significance in the last column has been estimated from the  $\theta^2$  distribution, using the standard full energy cuts ( $E > 250$  GeV).

### 8.3 Data analysis and results

The data analysis has been performed using the software package *MARS*. The main difficulty in this particular analysis stems from the presence of 1ES 1218+304 in the FoV. The corresponding region has to be excluded from the background estimation, in order to avoid an over-estimation of the background level. Due to the different observation positions in the camera, the analysis has been performed for the observation pairs:  $0^\circ$ - $180^\circ$  and  $90^\circ$ - $270^\circ$  separately, and then the results have been combined. The energy threshold of the analysis has been calculated from Monte Carlo simulations with the same characteristics as the source data, defined as the maximum in the energy distribution after applying the same cuts as for the source data, yielding  $\sim 70$  GeV.

The nightly significances can be found in Table 8.1 for the 2010 and 2011 data taking campaigns, calculated from the  $\theta^2$  distributions, and using standard cuts over the full energy range ( $E > 250$  GeV). These results show that the significance during 2011 is systematically higher than during 2010. In fact, the combined  $\theta^2$  distribution from 2010 results in a hint of a signal with a significance of  $\sim 2.7\sigma$  ( $N_{ON} = 125$ ,  $N_{OFF} = 93$  and  $N_{EX} = 32$ ), see Fig. 8.2. The skymap for those data is shown in Fig. 8.3, where the only source detected with enough statistics is 1ES 1218+304.

During the 2011 campaign, the source was finally detected for the first time in VHE  $\gamma$ -rays, with a high significance of  $9.3\sigma$  ( $N_{ON} = 155$ ,  $N_{OFF} = 59$  and  $N_{EX} = 96$ ), using the combination of the whole 2011 data sample and using the standard full range energy cuts (see Fig. 8.4). The skymap for the 2011 data is shown in Fig. 8.5, where both 1ES 1215+303 and 1ES 1218+304 are detected with high significance.

#### 8.3.1 The VHE spectrum of 1ES 1215+303

The VHE spectrum of 1ES 1215+303 can only be derived from the 2011 data, where the source was detected with high statistics. The total flux from 2010 for  $E > 200$  GeV results in  $F_{2010} = (2.16 \pm 0.9_{stat} \pm 0.6_{sys}) \cdot 10^{-12} \text{ cm}^{-2}\text{s}^{-1}$  (corresponding to  $\approx 1\%$  of the Crab Nebula flux) while the total flux from the 2011 campaign at the same energies is  $F_{2011} = (6.2 \pm 0.9_{stat} \pm 1.9_{sys}) \cdot 10^{-12} \text{ cm}^{-2}\text{s}^{-1}$  ( $\approx 3\%$  of the Crab Nebula flux). Therefore, the flux in 2011 is a factor  $\sim 3$  higher than in 2010. Nevertheless, taking into account the uncertainties, it would be also compatible with a constant flux.

The VHE spectrum covers the energy range from  $\sim 80$  GeV to 1.45 TeV and can be well described by a simple power-law of the form:

$$\frac{dN}{dE} = N_{200} \cdot \left( \frac{E}{200 \text{ GeV}} \right)^{-\Gamma}, \quad (8.1)$$

where  $N_{200}$  is the normalization constant at 200 GeV,  $N_{200} = (0.50 \pm 0.10_{stat} \pm 0.04_{sys}) \cdot 10^{-10} \text{ cm}^{-2}\text{s}^{-1}\text{TeV}^{-1}$  and the photon index  $\Gamma = (2.78 \pm 0.21_{stat} \pm 0.17_{sys})$ . The systematic uncertainties of the analysis have been estimated only from the use of different unfolding algorithms. All the unfolding algorithms are in very good agreement, as shown in Fig. 8.15, where the black points represent the unfolded observed spectrum using the Tikhonov algorithm and, the grey shaded area accounts for the use of other unfolding methods. Also the corresponding fits for the different unfolding algorithms can be found in Table 8.2. I will

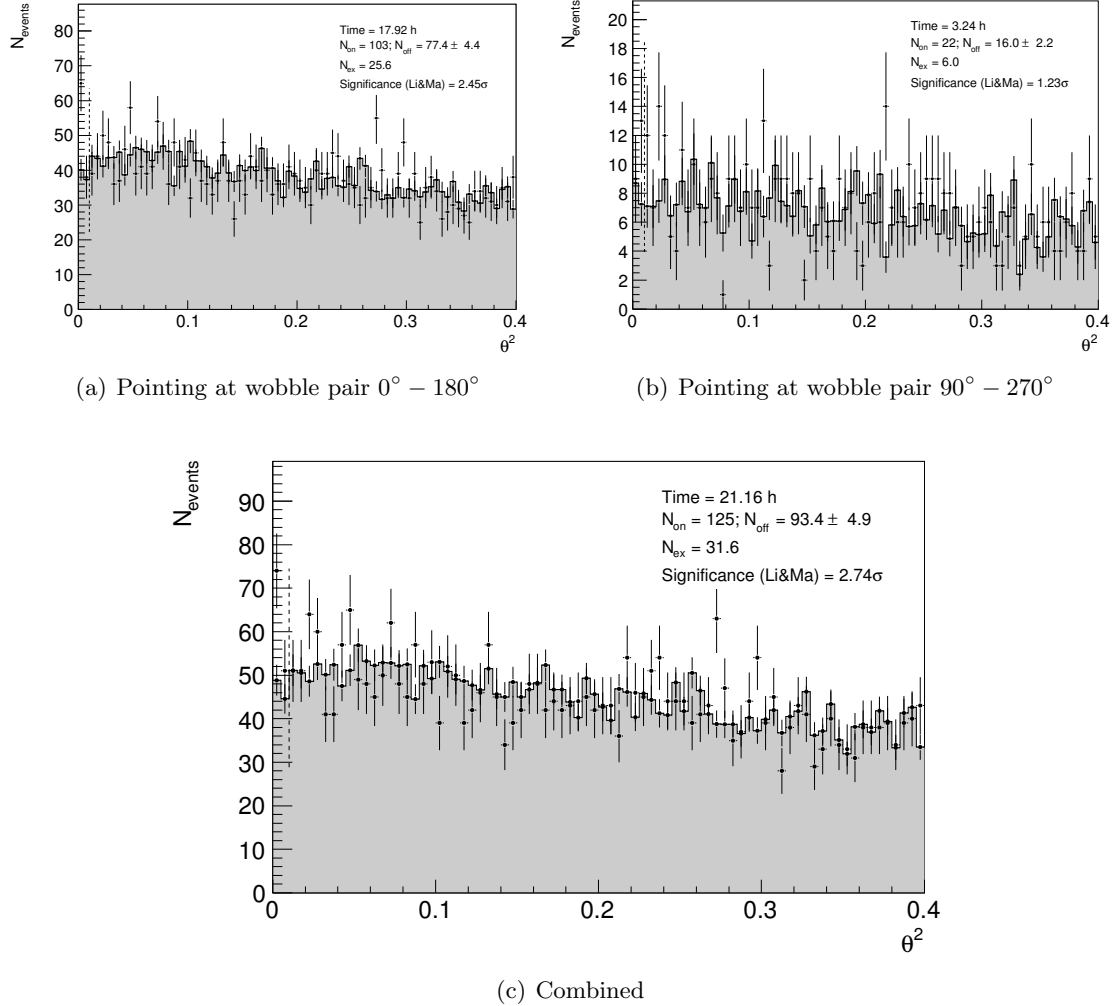


Figure 8.2:  $\theta^2$  distributions at the position of 1ES 1215+303 for the 2010 data. The top left plot shows the  $\theta^2$  distribution calculated with data taken at 0 and 180 degrees, while in the top right plot, only data observed at 90 and 270 degrees have been taken into account. The combined distribution for the entire 2010 observation period is plotted in the bottom figure.

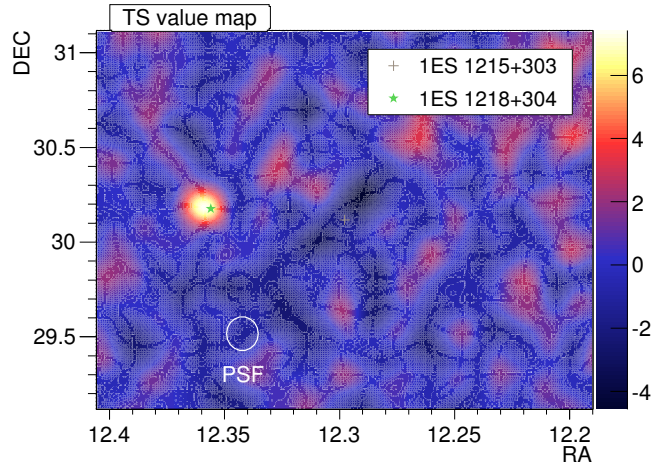


Figure 8.3: Skymap for the combined 2010 data, in which the source positions of 1ES 1218+304 and 1ES 1215+303 are not taken into account in the model background estimation. Only the bright source 1ES1218+304 is visible.

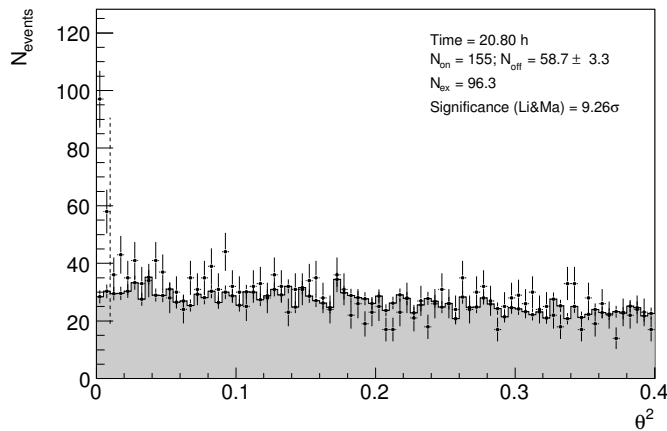


Figure 8.4:  $\theta^2$  distribution of 1ES 1215+304 from the combined 2011 data, using standard cuts over the full energy range.

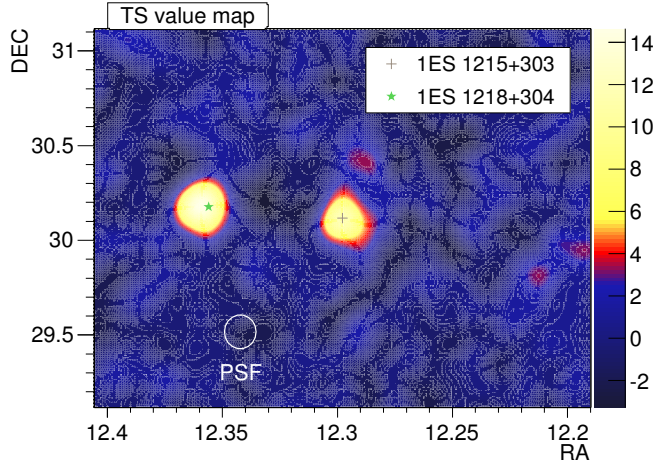


Figure 8.5: Skymap of the observed FoV of 1ES1215+303 from 2011 data, using standard cuts over the full energy range. One can see the presence of the bright second source 1ES 1218+304.

use the results from the Tikhonov algorithm from here on, since this is the method which gives the best probability of the fit.

Unfolding algorithm	$f_0$ [ $10^{-10}\text{cm}^{-2}\text{s}^{-1}\text{TeV}^{-1}$ ]	Spectral index	$\chi^2/\text{NDF}$	Probability
Schmelling	$0.53 \pm 0.07$	$-2.79 \pm 0.20$	2.95/5	71%
Tikhonov	$0.50 \pm 0.10$	$-2.78 \pm 0.21$	2.25/5	81%
Bertero	$0.52 \pm 0.08$	$-2.76 \pm 0.21$	3.95/5	57%
Schmelling (MINUIT)	$0.51 \pm 0.08$	$-2.80 \pm 0.21$	2.50/5	78%
BerteroW	$0.54 \pm 0.08$	$-2.78 \pm 0.21$	3.08/5	69%

Table 8.2: Measured spectrum of 1ES 1215+303 from 2011 data, best fit to a power law for different unfolding algorithms.

## 8.4 Study of variability from multi-frequency data

The VHE flux measured in 2011 is compatible with steady emission, as shown in Fig. 8.6, where the flux for energies higher than 200 GeV is represented as a function of time on a nightly time-scale. The light curve can be well-fitted by a constant yielding  $F = (6.5 \pm 0.9) \cdot 10^{-12} \text{cm}^{-2}\text{s}^{-1}$ , compatible with the total flux in 2011, and yielding a  $\chi^2/\text{NDF}=6.8/17$  corresponding to 99% probability. Also different time bins have been tested resulting always in a fit compatible with a steady flux.

Optical data was provided by the Tuorla monitoring group. The optical light curve in the R-band ( $\lambda = 6580 \text{\AA}$ ) is shown in Fig. 8.7, where the grey shaded areas represent the MAGIC observation campaigns in 2010 and 2011. Variability is found from these two periods, which are not compatible with a steady flux ( $\chi^2/\text{NDF}=3802/59$ ), showing a higher activity (20%-30%) during 2011 observations. Also in case of the MAGIC observations, the

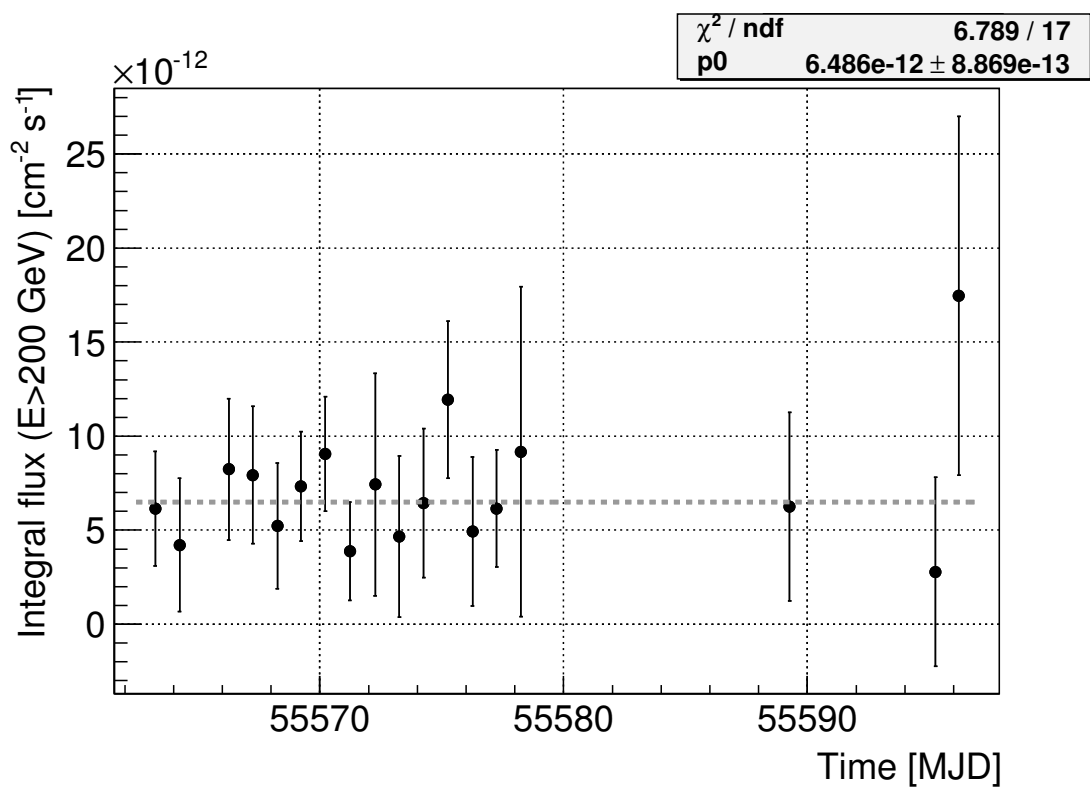


Figure 8.6: Light curve of 1ES 1215+303 from the data taken during the 2011 campaign for energies higher than 200 GeV.

source was more active during 2011, which suggests a correlation between optical and VHE  $\gamma$ -rays.

The optical light curves on nightly time-scales for both periods are plotted in more detail in Fig. 8.8 and Fig. 8.9. In both cases, the hypothesis of a constant flux can be rejected with a probability lower than  $6 \cdot 10^{-171}$  ( $\chi^2/\text{NDF}=939.6/40$ ) and  $9 \cdot 10^{-97}$  ( $\chi^2/\text{NDF}=509.9/18$ ), respectively. However, the nightly light curve in the VHE band does not show detectable variability, but due to the large uncertainty in the flux measurement by MAGIC, changes smaller than 30%, as in the case of the optical data on nightly time-scales, cannot be discarded.

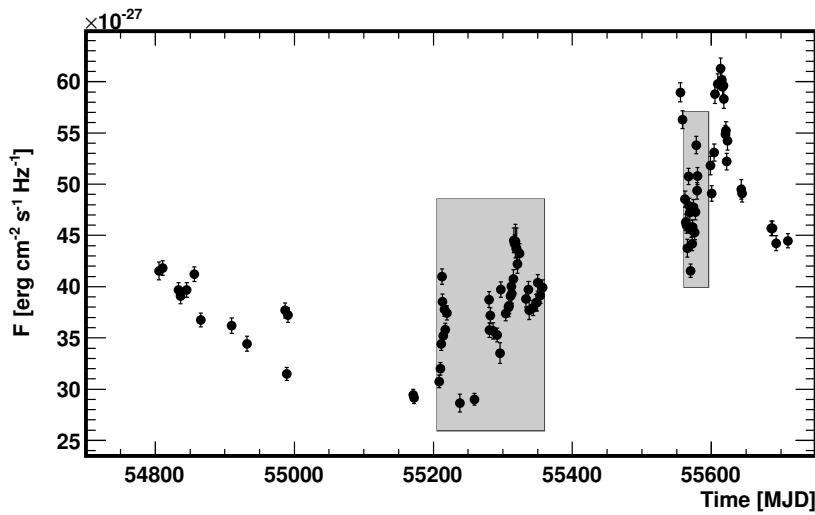


Figure 8.7: Optical light curve in the R-band of 1ES 1215+303. The grey shaded areas represent the time windows observed by MAGIC during the 2010 and 2011 campaigns.

In Fig. 8.10, the light curve for X-rays, from 2 to 10 keV, measured by *Swift* (A. Stamerra, priv. communication) can be found for the 2011 observation campaign. *Swift* only observed this source during five nights during the 2011 MAGIC campaign on 1ES 1215+303. The nightly flux is not compatible with a steady flux  $\chi^2/\text{NDF}=33.2/4$  (corresponding to a probability of  $10^{-6}$ ). Also two additional data sets have been analyzed in order to compare its emission state with before and after the MAGIC observations. The closest previous observations by *Swift* were performed almost one year before, on MJD 55168, showing a flux from 2 to 10 keV of  $F = (1.36 \pm 0.32) \cdot 10^{-12} \text{ cm}^{-2}\text{s}^{-1}$ . The posterior observation was carried out on MJD 55674, about 3 months after the MAGIC observations, resulting in  $F = (1.49 \pm 0.18) \cdot 10^{-12} \text{ cm}^{-2}\text{s}^{-1}$ . Therefore, during the detection in the VHE band by MAGIC, the source was also in a higher state in the X-ray band (of a factor 2 approx.) compared with previous and later observations. However, the spectral index measured in the X-ray band is compatible with the constancy hypothesis with a probability of  $\sim 55\%$  ( $\chi^2/\text{NDF}=3.05/4$ ), as shown in Fig. 8.11. For comparison, the spectral index measured on MJD 55168 in X-rays is  $\Gamma = 2.6 \pm 0.2$ , compatible with the measurements. Nevertheless,

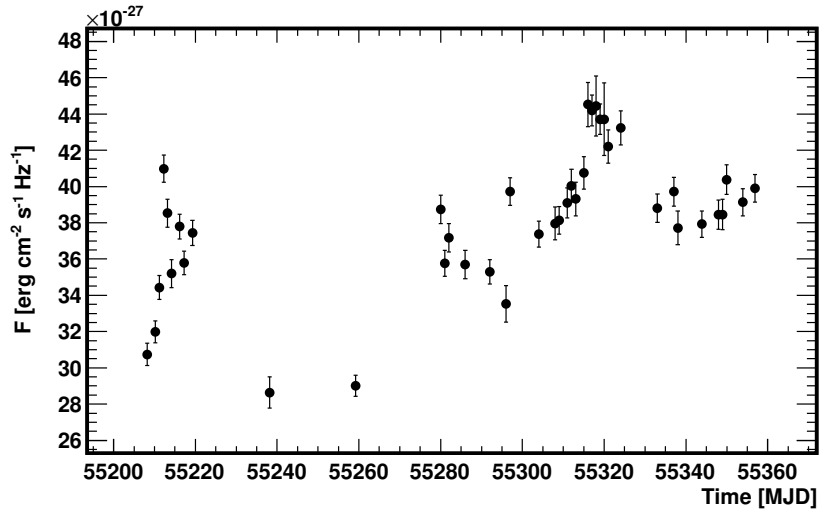


Figure 8.8: Optical light curve of 1ES 1215+303 in the R-band during the first MAGIC observation campaign in 2010.

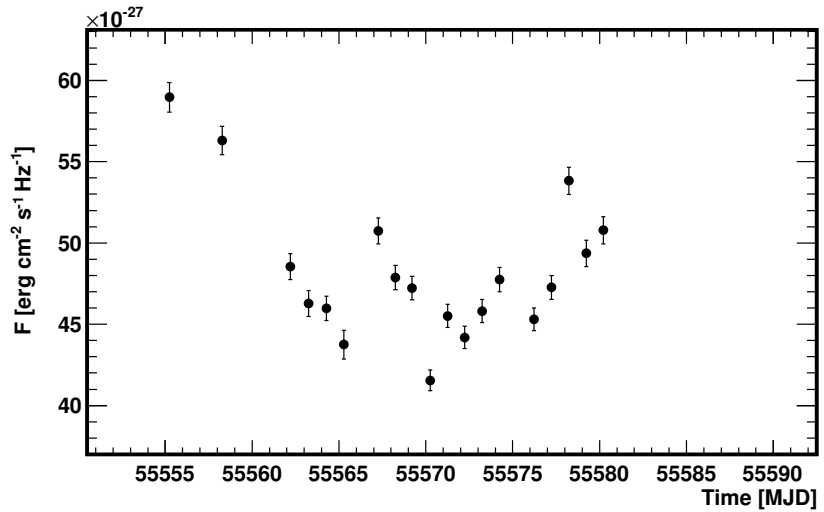


Figure 8.9: Optical light curve of 1ES 1215+303 in the R-band during the second MAGIC observation campaign in 2011.

the statistics is not good enough to draw strong conclusions.

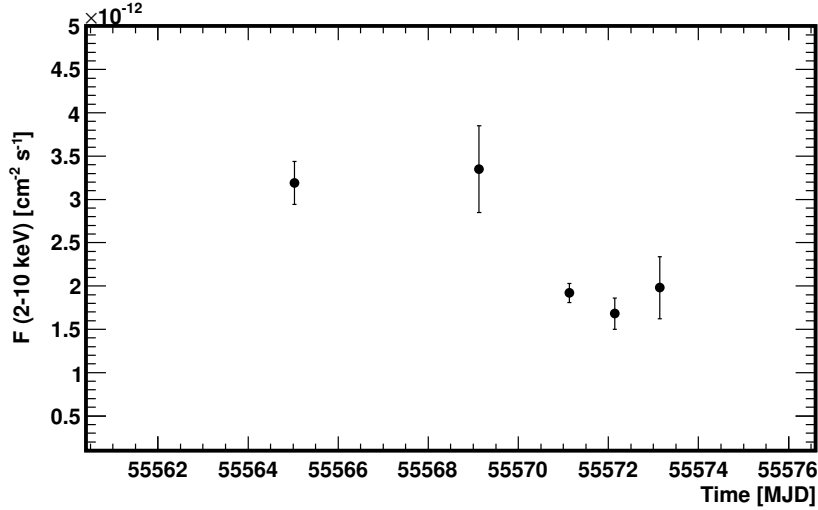


Figure 8.10: X-ray light curve of 1ES 1215+303 for the 2011 observation campaign, measured by *Swift* on a nightly time scale.

Also data from UVOT onboard of *Swift* have been analyzed. The light curves for the different wavelength bands from optical to UV are shown in Fig. 8.12 (the fluxes calculated on MJD 55168 are shown for comparison) and also in Table 8.3. Nevertheless, only four observations were carried out by UVOT in this period, the flux remained constant in all the bands, but due to the lack of statistics no strong conclusions can be drawn, as in the case of the X-ray data. During the period observed by MAGIC, the source was in a higher state in the UV and optical bands, when compared with the previous detection on MJD 55168.

Filter	$\lambda$ [ $\text{\AA}$ ]	Flux [ $10^{-11} \text{ cm}^{-2} \text{s}^{-1}$ ]	Uncertainty [ $\text{cm}^{-2} \text{s}^{-1}$ ]
V	5468	1.14	0.11
B	4392	1.17	0.11
U	3465	1.14	0.11
UVW1	2600	1.04	0.10
UVM2	2246	1.16	0.11
UVW2	1928	1.07	0.10

Table 8.3: Fluxes measured from 1ES 1215+303 by UVOT on MJD 55168.

The emission in  $\gamma$ -rays measured by *Fermi* for an energy range from 0.5 to 100 GeV, High Energy (HE)  $\gamma$ -rays, (G. Bonnoli, priv. communication) is marginally compatible with the constancy hypothesis of  $F = (1.56 \pm 0.32) \cdot 10^{-8} \text{ cm}^{-2} \text{s}^{-1}$  with a probability of  $\sim 8\%$  ( $\chi^2/\text{NDF}=8.19/4$ ), as shown in Fig. 8.13, where the fluxes are represented on a weekly time-

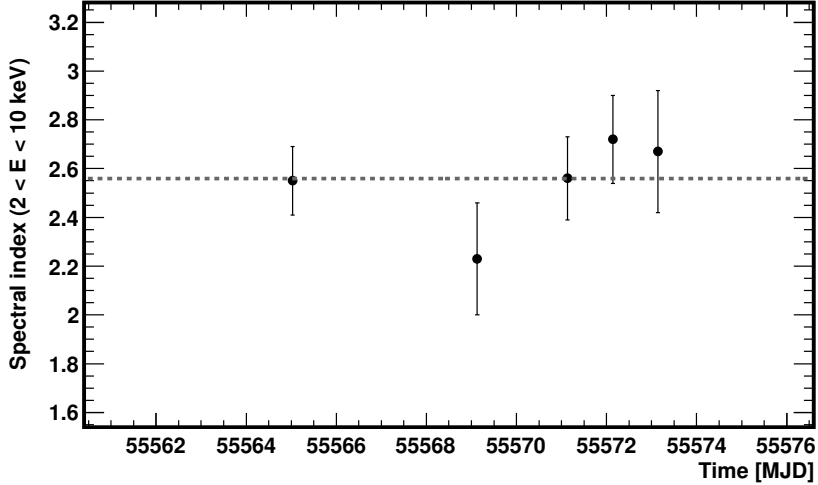


Figure 8.11: Time evolution of the spectral index for X-rays measured with *Swift* during the observation campaign of 1ES 1215+303 in 2011.

scale covering the same time period as the MAGIC observations during 2011. Interestingly, this light curve suggests a more active period during the third week of the observation.

The total flux measured by *Fermi* for the 2011 campaign for energies between 0.5 and 100 GeV is  $F = (1.65 \pm 0.28) \cdot 10^{-8} \text{ cm}^{-2}\text{s}^{-1}$ . For comparison, the fluxes from two periods in 2010 corresponding to the observations during the less active state have been analyzed: Jan-Feb 2010,  $F = (1.02 \pm 0.22) \cdot 10^{-8} \text{ cm}^{-2}\text{s}^{-1}$  and May-June 2010,  $F = (0.72 \pm 0.20) \cdot 10^{-8} \text{ cm}^{-2}\text{s}^{-1}$ . This means that 1ES 1215+303 was also in a marginally higher state in HE  $\gamma$ -rays during the 2011 campaign.

The spectral index for HE  $\gamma$ -rays measured by *Fermi* is compatible with a constant fit at  $\Gamma = 2.14 \pm 0.19$  with a probability of  $\sim 91\%$  ( $\chi^2/\text{NDF}=0.95/4$ ) for the entire 2011 campaign. For comparison, the two spectral indices calculated for the 2010 observations are  $\Gamma = 2.11 \pm 0.25$  and  $\Gamma = 2.07 \pm 0.07$  for Jan-Feb 2010 and May-June 2010, respectively. Thus, the spectral index is compatible, within uncertainties, for different periods and flux states of the source.

As a conclusion, the multi-frequency data suggest a correlation on large time scales between optical, UV, X-rays and  $\gamma$ -rays (both HE and VHE) during an enhancement of the overall flux during the 2011 observation campaign. This makes sense, since in the case of BL Lacs, the emission is modeled typically with a Synchrotron Self-Compton (SSC) model (see Sec. 8.6) which means more optical photons can produce more inverse Compton (IC) scatterings with the relativistic electrons in the jet, corresponding to a flux enhancement in the VHE range. However, due to the lack of statistics for the strictly simultaneous data at the different wavelengths, and the large uncertainties in the VHE band, compared with the flux changes observed on nightly time-scales in optical and X-rays, a correlation on shorter time-scales cannot be derived.

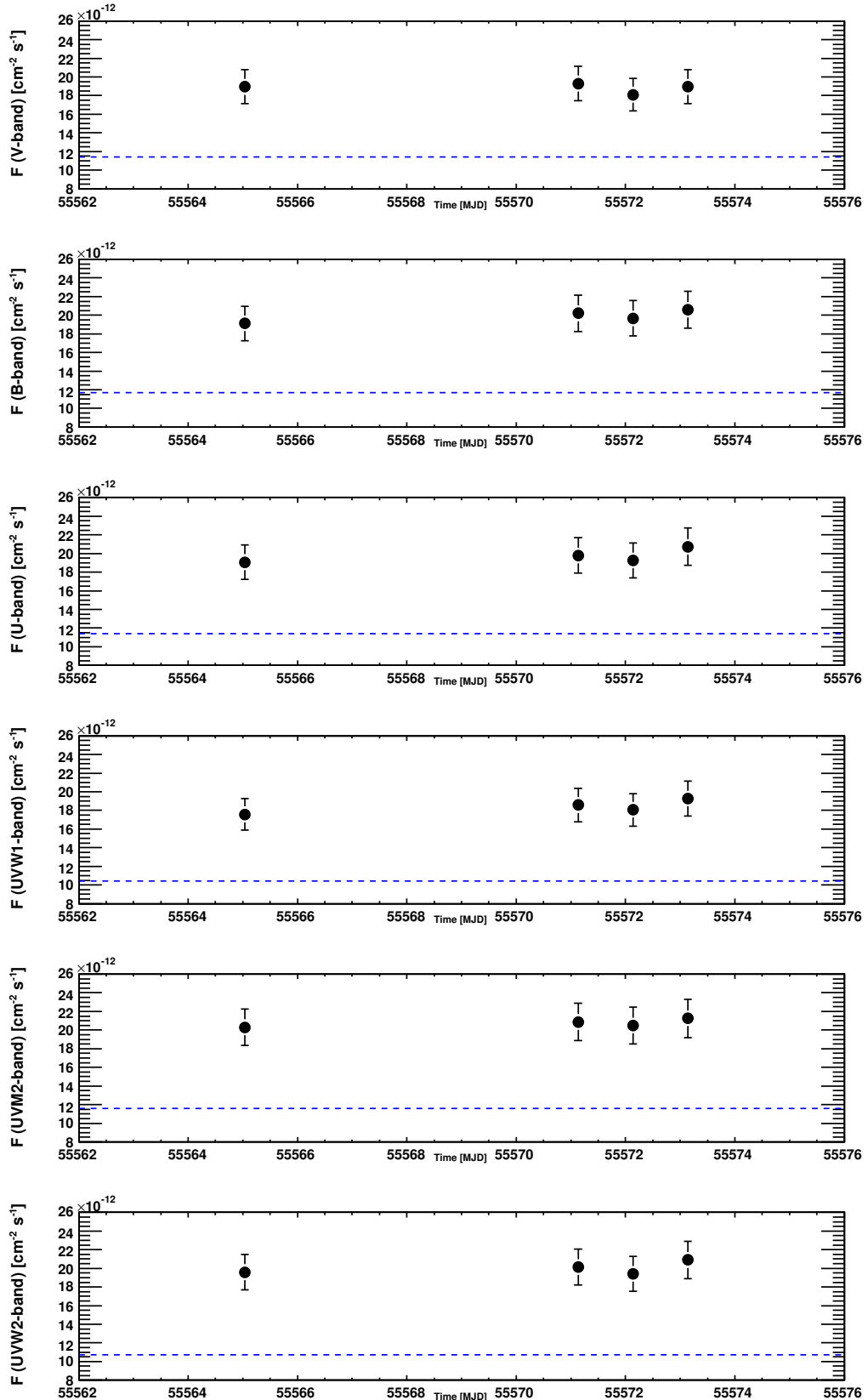


Figure 8.12: Light curves of 1ES 1215+303 on different bands observed by UVOT in 2011. The dashed blue line shows the reference value calculated for MJD 555168.

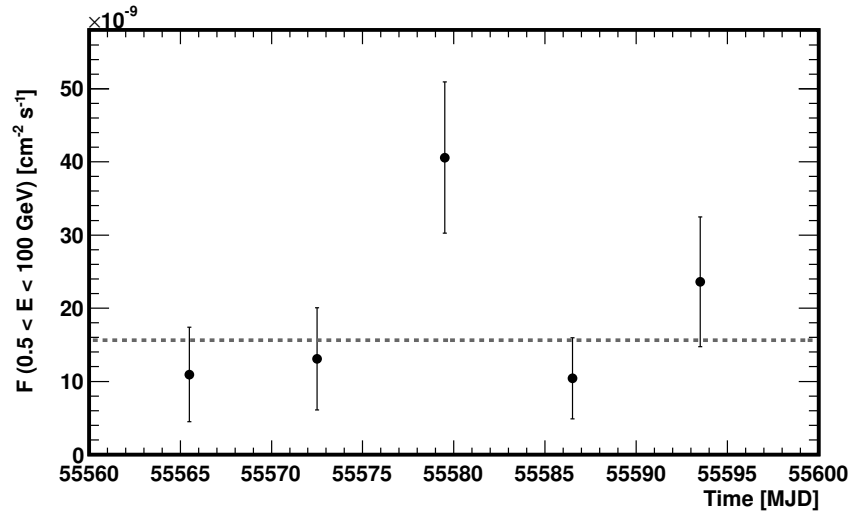


Figure 8.13: *Fermi* light curve for 1ES 1215+303 covering an energy range from 0.5 to 100 GeV during the 2011 MAGIC campaign in weekly time bins.

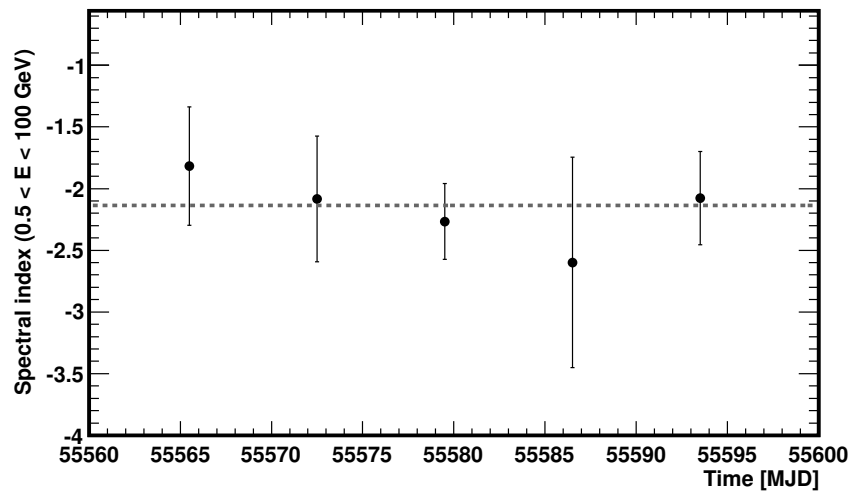


Figure 8.14: Time evolution of the spectral index measured by *Fermi* during the observation campaign of 1ES 1215+303 in 2011.

## 8.5 An EBL study from the observations of 1ES 1215+303

Due to the interaction between VHE  $\gamma$ -rays and the extragalactic background light via pair production, VHE  $\gamma$ -photons are absorbed. In order to infer the intrinsic spectrum emitted by the source, the spectrum needs to be de-absorbed. Thus, the characteristics of the EBL are imprinted onto the spectrum. Since that extends from  $\sim 80$  GeV to 1.45 TeV, the EBL from UV down to IR wavelengths can be tested. For this purpose, I will make use of different EBL models by Domínguez et al. (2011), Franceschini et al. (2008), the “max high UV” EBL model described in Albert et al. (2008a), Kneiske and Dole (2010), Kneiske et al. (2002), and Primack et al. (2005).

The probability of the interaction between the VHE photons and the EBL depends on the distance to the source. In this particular case, since there are two possible values for the redshift ( $z = 0.13$  and  $z = 0.237$ ). I will de-absorb the observed spectrum using both values and later check whether the results yield physically allowed spectra.

The results assuming a redshift of  $z = 0.13$  are shown in Fig 8.15, where the unfolded observed VHE spectrum is illustrated in the form of black points and the systematic uncertainties, due to the use of different unfolding algorithms, are accounted by the grey shaded area. The blue points are the de-absorbed spectral points and the blue area indicates their spread using different EBL models. As one can see, the last point at high energies shows a slight, but insignificant (see Table 8.4) enhancement for most of the EBL models: Domínguez et al. (2011), Franceschini et al. (2008), Albert et al. (2008a) and Kneiske et al. (2002). Nevertheless, the de-absorbed spectral points can be well fitted by a power law. Only spectra de-absorbed using the models from Kneiske and Dole (2010) and Primack et al. (2005) do not show this behavior. In Fig. 8.16, the observed spectrum in black points and the deabsorbed spectral point using Primack et al. (2005) is represented, the blue shaded area illustrates the different EBL models. In Table 8.4, the fits from the different EBL models can be found.

Assuming the redshift  $z = 0.237$ , the last spectral point at high energies is even higher for all the EBL models than the expected flux by the power law fit, as can be seen in Fig. 8.17. Also in Fig 8.18, where the blue shaded area represents the EBL models spread, this behavior is observed. However, the fit to the spectral points always results in acceptable probabilities (as shown in Table 8.5) and is therefore statistically not significant.

A priori, none of the values found in the literature for the redshift, can be rejected with this method, since it is compatible with the present generation of EBL models. Nevertheless, in case of  $z = 0.237$ , all models show an enhanced last point, even for the EBL model of Kneiske and Dole (2010), which has been calculated as a strict lower limit to the EBL. For this model, assuming  $z = 0.13$ , the point fits better to the power law. However, the probability of the fits are all good, such that no significant constraint on the redshift can be set in this way.

The last energy bin covers the energy range from  $\sim 960$  GeV to 1.45 TeV. The target photons for  $\gamma$ -rays of this energy bin interact with the IR photons of the EBL. The higher flux from the de-absorbed spectral point at high energies could suggest an over-estimation of the cosmological IR backgrounds. Also, this behavior has been found in case of the BL Lac 1ES 1218+303 (see Sec. 9.5) at redshift  $z = 0.182$ , but since the deviation is not significant either, we cannot set further new constraints on the EBL models. However, assuming that

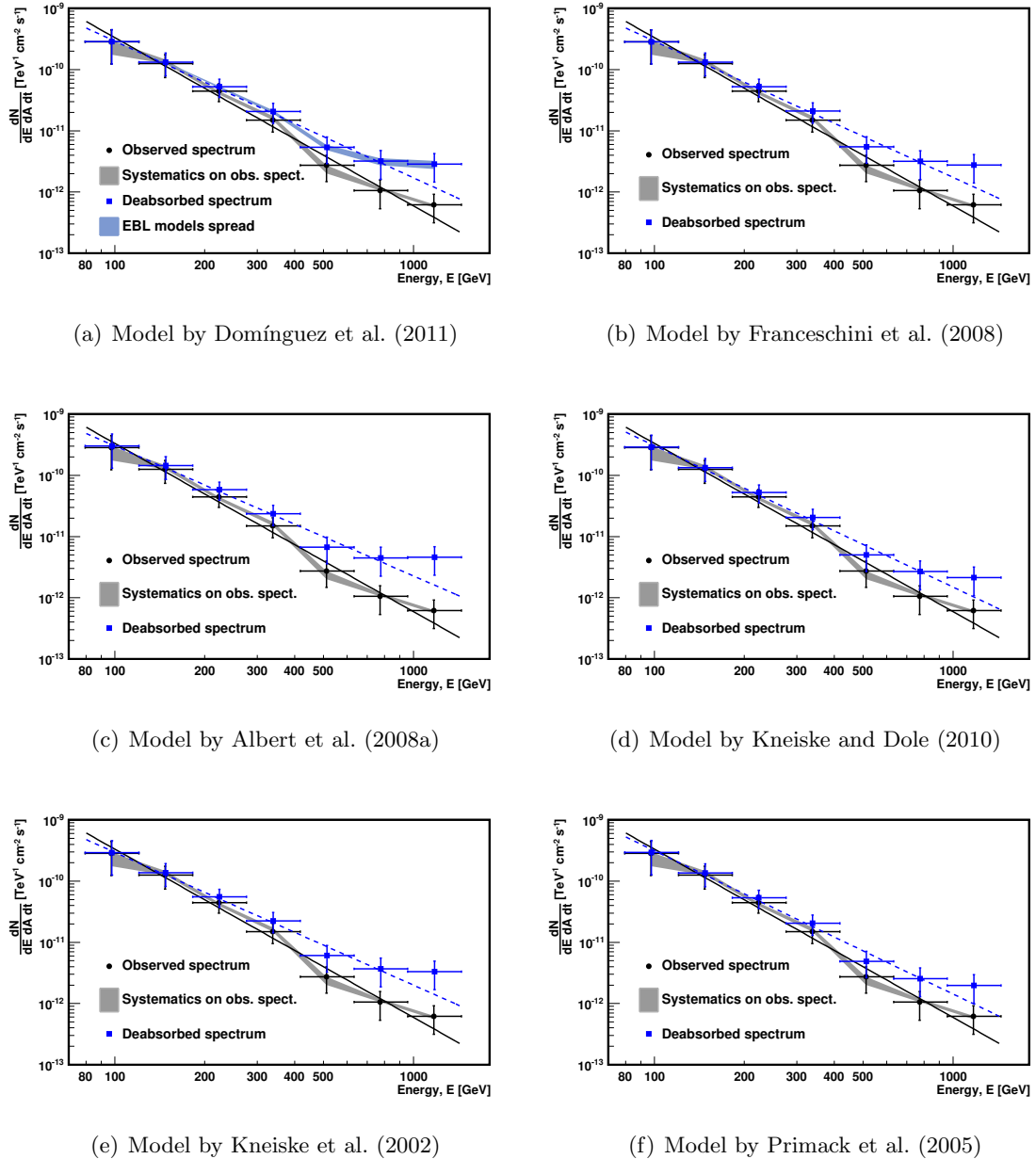


Figure 8.15: Differential energy spectrum from 1ES 1215+303 in 2011 assuming  $z = 0.13$ . The black points represent the measured differential fluxes unfolded by Tikhonov algorithm. The solid black line represents the best fit to a power law and the grey shaded area the systematic uncertainties of the analysis. The blue points are the absorption corrected spectrum using different EBL models (see figure subtitles). The stripped blue line represents the best fit power law for the de-absorbed spectrum. And the blue shaded area in the first figure represents the uncertainty of Domínguez et al. (2011).

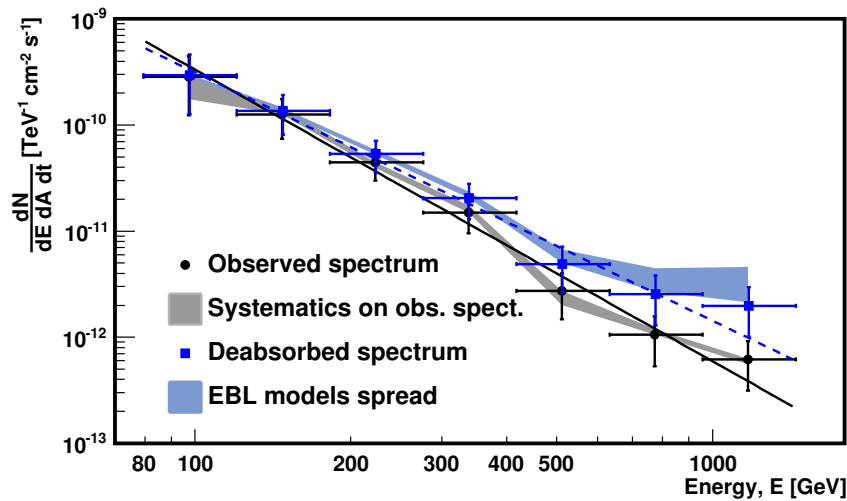


Figure 8.16: Differential energy spectrum from 1ES 1215+303 measured by MAGIC during the 2011 campaign assuming  $z = 0.13$ . The black points represent the measured differential fluxes unfolded by the Tikhonov algorithm. The solid black line represents the best fit to a power law and the grey shaded area the systematic uncertainties of the analysis. The blue points are the absorption corrected spectrum using the EBL models from Primack et al. (2005). The stripped blue line represents the best fit power law for the de-absorbed spectrum and the blue area the spread of EBL models Domínguez et al. (2011), Franceschini et al. (2008), the “max high UV” EBL model described in Albert et al. (2008a), Kneiske and Dole (2010), Kneiske et al. (2002) and Primack et al. (2005).

EBL model	$f_0$ [ $10^{-10} \text{ cm}^{-2} \text{s}^{-1} \text{TeV}^{-1}$ ]	Spectral index	$\chi^2/\text{NDF}$	Probability
Domínguez et al. (2011)	$0.61 \pm 0.12$	$-2.24 \pm 0.26$	$2.29/5$	81%
Domínguez et al. (2011) Low Limit	$0.58 \pm 0.11$	$-2.31 \pm 0.26$	$2.30/5$	81%
Domínguez et al. (2011) Upper Limit	$0.63 \pm 0.12$	$-2.18 \pm 0.26$	$2.27/5$	81%
Franceschini et al. (2008)	$0.61 \pm 0.12$	$-2.13 \pm 0.26$	$2.17/5$	83%
Albert et al. (2008a)	$0.68 \pm 0.13$	$-2.12 \pm 0.28$	$2.65/5$	75%
Kneiske and Dole (2010)	$0.61 \pm 0.12$	$-2.32 \pm 0.25$	$2.07/5$	84%
Kneiske et al. (2002)	$0.64 \pm 0.13$	$-2.17 \pm 0.26$	$2.24/5$	82%
Primack et al. (2005)	$0.61 \pm 0.12$	$-2.35 \pm 0.24$	$2.06/5$	84%

Table 8.4: De-absorbed spectrum of 1ES 1215+303 best fit to a power law for different EBL models assuming  $z = 0.13$ .

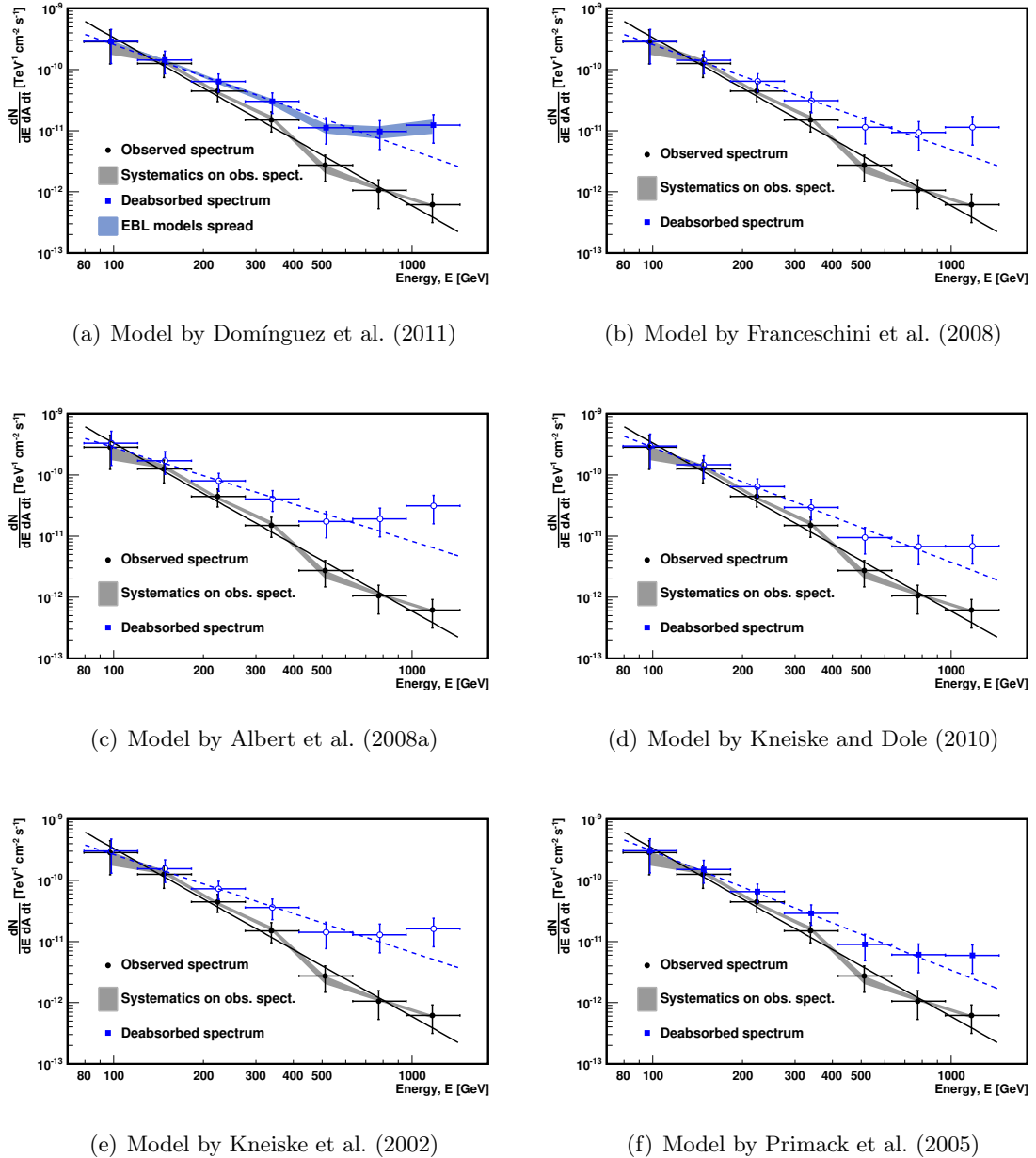


Figure 8.17: Differential energy spectrum from 1ES 1215+303 in 2011 assuming  $z = 0.237$ . The black points represent the measured differential fluxes unfolded by Tikhonov algorithm. The solid black line represents the best fit to a power law and the grey shaded area the systematic uncertainties of the analysis. The blue points are the absorption corrected spectrum using different EBL models (see figure subtitles). The stripped blue line represents the best fit power law for the de-absorbed spectrum. And the blue shaded area in the first figure represents the uncertainty of Domínguez et al. (2011).

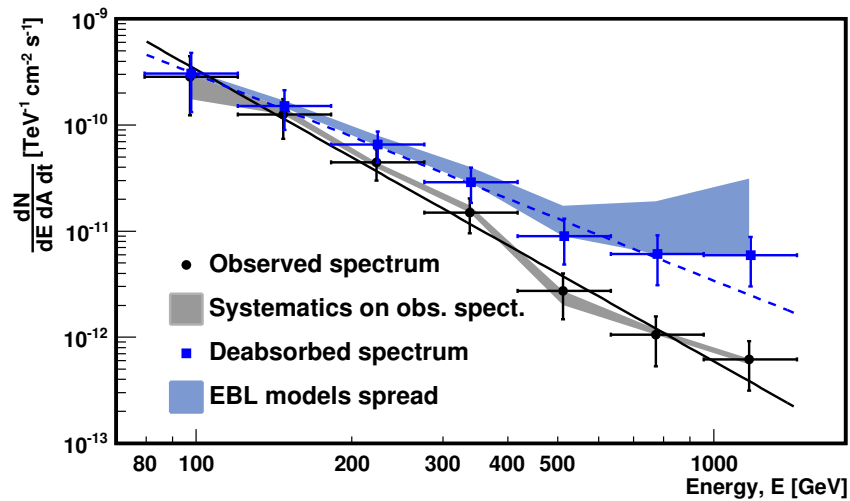


Figure 8.18: Differential energy spectrum from 1ES 1215+303 measured by MAGIC during the 2011 campaign assuming  $z = 0.237$ . The black points represent the measured differential fluxes unfolded by the Tikhonov algorithm. The solid black line represents the best fit to a power law and the grey shaded area the systematic uncertainties of the analysis. The blue points are the absorption corrected spectrum using the EBL models from Primack et al. (2005). The stripped blue line represents the best fit power law for the de-absorbed spectrum and the blue area the spread of EBL models Domínguez et al. (2011), Franceschini et al. (2008), the “max high UV” EBL model described in Albert et al. (2008a), Kneiske and Dole (2010), Kneiske et al. (2002) and Primack et al. (2005).

EBL model	$f_0$ [ $10^{-10} \text{ cm}^{-2} \text{s}^{-1} \text{TeV}^{-1}$ ]	Spectral index	$\chi^2/\text{NDF}$	Probability
Domínguez et al. (2011)	$0.74 \pm 0.15$	$-1.71 \pm 0.32$	$3.01/5$	70%
Domínguez et al. (2011) Low Limit	$0.69 \pm 0.14$	$-1.84 \pm 0.31$	$2.95/5$	71%
Domínguez et al. (2011) Upper Limit	$0.79 \pm 0.16$	$-1.62 \pm 0.32$	$3.01/5$	70%
Franceschini et al. (2008)	$0.75 \pm 0.15$	$-1.70 \pm 0.31$	$2.73/5$	74%
Albert et al. (2008a)	$0.91 \pm 0.19$	$-1.51 \pm 0.36$	$3.88/5$	57%
Kneiske and Dole (2010)	$0.75 \pm 0.15$	$-1.87 \pm 0.28$	$2.27/5$	81%
Kneiske et al. (2002)	$0.84 \pm 0.17$	$-1.59 \pm 0.32$	$2.89/5$	72%
Primack et al. (2005)	$0.76 \pm 0.15$	$-1.94 \pm 0.27$	$2.18/5$	82%

Table 8.5: De-absorbed spectrum of 1ES 1215+303 best fit to a power law for different EBL models assuming  $z = 0.237$ .

the last spectral point is only weakly correlated with the rest of the spectral points, in the sense that it probes a distinct part of the EBL spectrum, we can estimate the statistical significance for the hypothesis that the current EBL models overestimate the cosmic IR background. For this purpose, the significance has been calculated that the last spectral point is statistically not compatible with the power-law fit from the rest of the points. This procedure is reasonable, if no additional emission component at TeV energies is assumed, like in the case of leptonic emission models for BL Lacs of this kind. The result yields always between  $0.7\sigma$  and  $1\sigma$  for the different EBL models and the lower redshift case, and between  $0.8\sigma$  and  $1.1\sigma$  for the higher redshift case, if the statistical uncertainties from the fit and the data point are taken into account. Due to the pile-up problems in distant sources, axiom-like particles (ALPs) have been proposed as a possible solution instead of EBL models which are usually in good agreement even though different approaches have been used to estimate them. Photons are supposed to oscillate to ALPs (and vice-versa) in the presence of electric or magnetic fields which could yield a lower absorption by the EBL photons (Sánchez-Conde et al., 2009).

Under the hypothesis that the observed hint of a pile-up is not due to statistical fluctuations, how many additional excess events are needed in order to obtain a significance of at least  $3\sigma$ ? At such high energies, virtually no background is present anymore in the signal region, which means that the statistical uncertainties of the excess are entirely determined by the Poissonian fluctuations of the number of recorded  $\gamma$ -rays. Moreover, as can be seen from the small size of the grey band around 1 TeV in figure 8.18, the systematic uncertainty due to the use of different unfolding procedures, appears very small at that energy. Hence, a 9 or 7 times higher flux or observation time for the two redshift cases, respectively, are needed in order to start to delimit the EBL models under these assumptions. These numbers are little realistic from the point of view of the observational capabilities of the MAGIC telescopes since more than 150 hours would be needed. Even in an extreme high state with a flux enhancement of a factor 7 would be unrealistic to extend for  $\sim 20$  hours. Had this source been observed by CTA (CTA Consortium, 2010) under the same circumstances, with a sensitivity of a factor  $\sim 7$  better than the one of the current MAGIC stereo system at TeV energies, the answer could probably be given. Moreover, with such an improved sensitivity, and assuming an extrapolation of the unabsorbed spectrum, additional points at even higher energy should be found, which would demonstrate more clearly a possible pile-up of events in the de-absorbed spectrum.

## 8.6 Spectral energy distribution of 1ES 1215+303

The SED for 1ES 1215+303 covering from radio to VHE  $\gamma$ -rays is shown in Fig. 8.19 presenting the double bump structure typical for a BL Lac. The red and grey points represent the VHE  $\gamma$ -ray spectral points detected by MAGIC during the 2011 observation campaign, corrected by EBL absorption with the model from Primack et al. (2005) for the two redshifts available,  $z = 0.13$  and  $z = 0.237$ , respectively. The pink butterfly and points have been obtained from simultaneous *Fermi* data to the MAGIC observation campaign in 2011 (G. Bonnoli, priv. communication). The blue squares stem from the simultaneous X-rays observations from *Swift*, where the maximum and minimum flux has been estimated (A. Stamerra, priv. communication). The open red circles represent the UVOT data from

*Swift* which are also simultaneous to the MAGIC dataset. The IR points represent historical data of the source, taken from Fan and Lin (1999). The radio observations come from a historical database<sup>2</sup> and are presented by the green circles and squares.

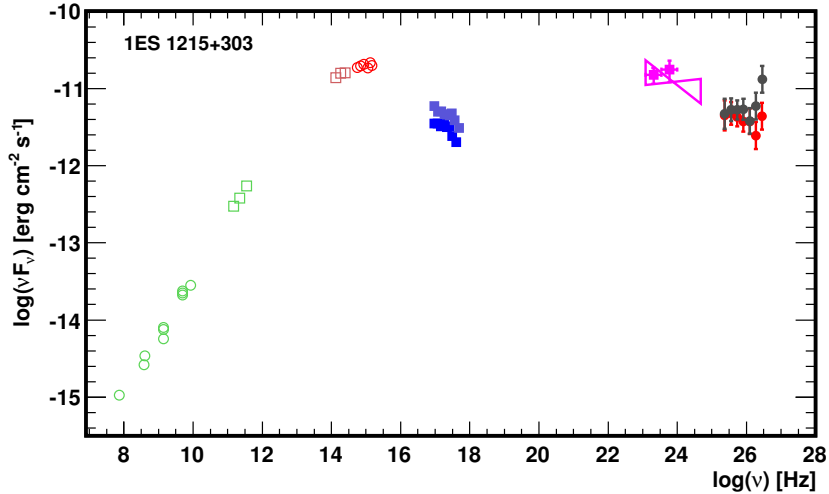


Figure 8.19: Spectral energy distribution for 1ES 1215+303.

As discussed previously in Sec. 7.2, a double peaked distribution can be reproduced with a broken power-law electron distribution in the framework of leptonic models. Thus, in order to model the emission from 1ES 1215+303, a broken power-law distribution of electrons will be assumed. Given the lack of features in the typical spectra of BL Lacs, it is generally assumed that the jet extends into a clearer environment and therefore, the external photon field can be assumed negligible. Thus, a Synchrotron Self-Compton (SSC) model is typically used to model the emission from BL Lacs. I will assume the canonical jet emission scenario, assuming an emitting region as a sphere whose radius is comparable to the section of the jet which travels with a Lorentz factor  $\Gamma$  (Ghisellini and Tavecchio, 2009). These electrons emit synchrotron radiation due to the interaction with the magnetic field producing the first peak of the SED. Then, the same relativistic electron population can interact with the synchrotron photons via inverse Compton scattering emitting the higher frequency peak of the SED. For the numerical calculations, the code from Maraschi and Tavecchio (2003) has been used.

Since the redshift of this source is uncertain, both values have been tested in order to fit the SED using a SSC model. Assuming  $z = 0.13$ , the SED can be well described by a SSC model, as shown in Fig. 8.20. This model can account for the simultaneous data of the source and is in agreement with the hint of correlations between different wavelengths found in Sec. 8.4. However, given the hard de-absorbed spectrum when the assumed redshift is  $z = 0.237$ , the SED cannot be fitted to an SSC model any more. As shown in Fig. 8.21,

<sup>2</sup><http://tools.asdc.asi.it/SED/sed.jsp?&ra=184.46708&dec=30.11667&q=ON325>.

the VHE slope is harder than the X-ray spectral index and thus, the fit of these two slopes is not possible with a single electron population, as assumed in the SSC model. Therefore, in the framework of the current EBL models and the standard leptonic models, this value of the redshift is disfavored. The parameters used for the fit of the model can be found in Table 8.6.

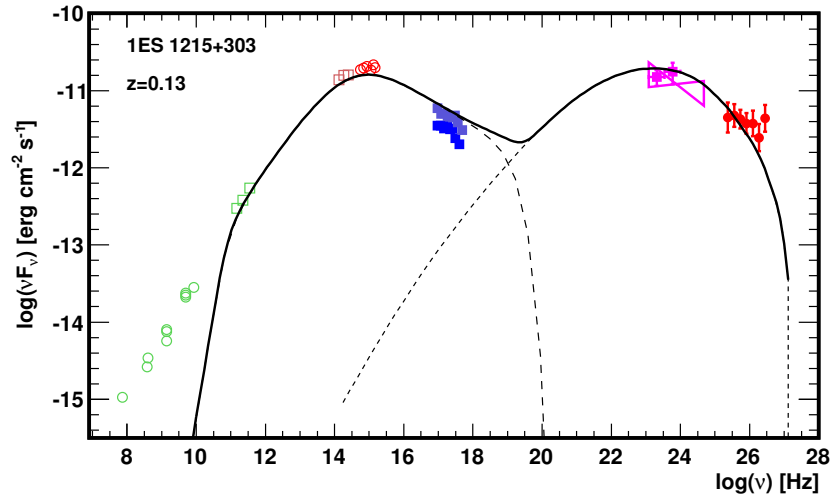


Figure 8.20: Spectral energy distribution for 1ES 1215+303 modeled by a SSC model assuming a redshift of  $z = 0.13$  and a Lorentz factor of  $\Gamma = 20$ .

The SED from 1ES 1215+303 shows two broad peaks which are similar to the emission from HBLs, although this source is classified as an IBL in the literature. Possibly, a revision of the classification is needed or a possible spectral change occurs during high activity states. However, the behavior of the spectral indices, shown in Sec. 8.4, suggests no big changes for different periods and flux states of the source.

$z$	$\gamma_{\min}$	$\gamma_b$	$\gamma_{\max}$	$n_1$	$n_2$	$B [\text{G}]$	$K [\text{cm}^{-3}]$	$R [\text{cm}]$	$\Gamma$	$P_{p,45}$	$P_{e,45}$	$P_{B,45}$
0.13	10	$4.8 \cdot 10^3$	$9 \cdot 10^5$	1.655	3.55	0.2	$6 \cdot 10^3$	$5 \cdot 10^{15}$	20	2.74	0.443	$2 \cdot 10^{-3}$
0.237	10	$4 \cdot 10^3$	$9 \cdot 10^5$	1.655	3.6	0.25	$2 \cdot 10^4$	$5 \cdot 10^{15}$	20	9.14	1.39	$3 \cdot 10^{-3}$

Table 8.6: Input parameters for the emission models shown in the figures. In the first column the redshifts are given.  $\gamma_{\min}$ ,  $\gamma_b$  and  $\gamma_{\max}$  are the minimum, break and maximum Lorentz factor of the electron population while  $n_1$  and  $n_2$  denote the low and high energy slopes of the broken power-law of the electron distribution. The magnetic field is represented by  $B$ , the normalization of the electron distribution by  $K$  and the radius of the emission region by  $R$ . The last three columns show the power carried by cold protons (assuming one proton per emitting electron), relativistic electrons and the magnetic field in units of  $10^{45} \text{ erg} \cdot \text{s}^{-2}$ .

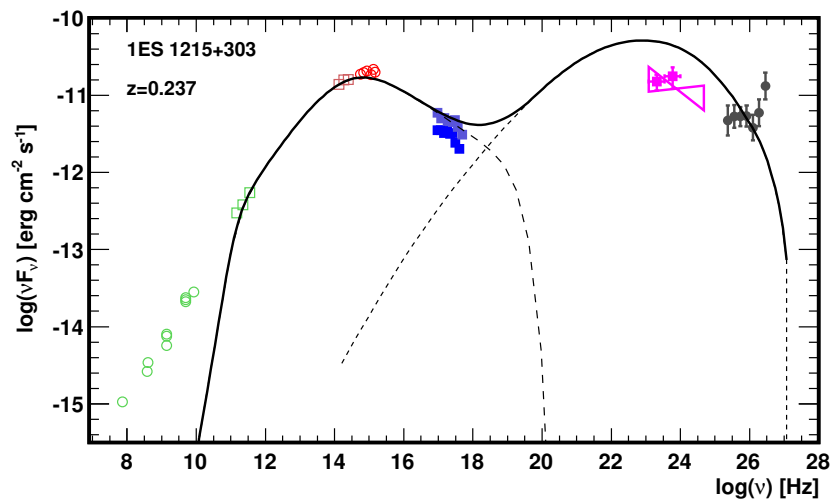


Figure 8.21: Spectral energy distribution for 1ES 1215+303 modeled by a SSC model assuming a redshift  $z = 0.237$  and a Lorentz factor of  $\Gamma = 20$ , which was obtained by the fit to the lower energy bump on the left side.

---

# 9

---

## Observation of the BL Lac 1ES 1218+304 at VHE $\gamma$ -Rays

### 9.1 Introduction

1ES 1218+304 is a BL Lac object located at R.A. 12h21m21.92s and Dec. +30d10m36.83s and classified as HBL (Padovani and Giommi, 1995). It is characterized by a synchrotron peak at X-rays energies and a second peak at high energy gamma-ray energies, whose spectral energy distribution (SED) can be usually well fitted by a synchrotron-self-Compton (SSC) model where the first peak is due to synchrotron radiation and for the the second peak inverse Compton process is the responsible mechanism (Rüger et al., 2010; Weidinger and Spanier, 2010) in the framework of leptonic models.

This source was observed in the VHE band by Whipple (Horan et al., 2004) from 1995 to 2000, yielding only flux upper limits for  $E > 300$  GeV, from 0.83 to 2.85 in units of  $10^{-11}\text{cm}^{-2}\text{s}^{-1}$  (8-36% of the Crab Nebula flux), depending on the observation period. Finally, in 2005, the source was discovered in VHE gamma-rays by MAGIC (Albert et al., 2006a), yielding a differential energy spectrum for an energy threshold of 120 GeV, which can be described by a simple power-law from 87 GeV to 630 GeV:  $F = (8.1 \pm 2.1) \cdot 10^{-11}(E/250\text{ GeV})^{-3.0 \pm 0.4} \text{ TeV}^{-1}\text{cm}^{-2}\text{s}^{-1}$  and a steady flux for  $E > 100$  GeV of  $F_{100} = (8.7 \pm 1.4) \cdot 10^{-11} \text{ cm}^{-2} \text{ s}^{-1}$ . Later in 2007, the Veritas Collaboration reported the detection of the source during 2007 (Acciari et al., 2009c) with results statistically consistent with the previous findings by MAGIC. Veritas found a spectrum from  $\sim 160$  GeV to  $\sim 1.8$  TeV, which can be described by a simple power-law of index  $\Gamma = (3.08 \pm 0.34_{\text{stat}} \pm 0.2_{\text{sys}})$  and an integral flux for  $E > 200$  GeV of  $F = (12.2 \pm 2.6) \cdot 10^{-12} \text{ cm}^{-2}\text{s}^{-1}$  ( $\sim 6\%$  of the Crab Nebula flux), also no variability was detected. A second detection by Veritas (Acciari et al., 2010), revealed a flare of the source from January 15<sup>th</sup> to February 5<sup>th</sup>, 2009, where the source reached  $\sim 20\%$  of the Crab Nebula flux. During this flare, no change in the spectral slope was found, just an enhancement of the flux.

This source is located at a redshift of  $z = 0.182$  and can be detected up to high energies  $> 1$  TeV, which makes this source a suitable object for EBL studies.

## 9.2 Observations

1ES 1218+304 is in the same FoV as 1ES 1215+303 and therefore, the MAGIC data set is exactly the same as the one described in Sec. 8.2. The observation of 1ES 1215+303 was performed in wobble mode with wobble distances of 0.4 degrees from the camera center, and at the different wobble angles:  $0^\circ$ ,  $90^\circ$ ,  $180^\circ$  and  $270^\circ$ , respectively. This results in not equidistant wobble positions wrt. the position of 1ES 1218+304 as shown in Table 9.1. However, the sensitivity of the MAGIC camera is almost constant up to  $\sim 0.3^\circ$  from the camera center. Further it drops quickly (see Fig. A.3 in the Appendix) especially due to the small trigger area in M1 camera which means smaller collection.

wobble angle w.r.t. 1ES 1215+303	Distance of 1ES 1218+304 to the camera center
$0^\circ$	$0.36^\circ$
$180^\circ$	$1.16^\circ$
$90^\circ$	$0.82^\circ$
$270^\circ$	$0.86^\circ$

Table 9.1: Distance of the observed position of 1ES 1218+304 to the camera center, measured in degrees, for the different wobble data samples.

## 9.3 Data analysis and results

Since the observation of 1ES 1218+304 was performed off-axis, and moreover at different positions with respect to the camera center, the analysis had to be carried out independently for each set of data. That means in case of 2010 data, that four different analyses had to be performed for the distinct distances to the camera center which were combined afterwards and in case of 2011 data, two different analyses were needed. Moreover, appropriate MC simulations had to be used in order to take into account the change in efficiency at different positions in the camera. This was performed selecting the proper bins in distance to the camera center from MC simulations of  $\gamma$ -rays from random directions (the so-called “diffuse MC simulations”).

A clear detection of the source is obtained from both observation campaigns. In case of the 2010 data, for a total of  $\sim 21$  hours of observations, the combined  $\theta^2$  distribution results in a significance of  $\sim 11.6 \sigma$  ( $N_{ON} = 4062$ ,  $N_{OFF} = 3224$  and  $N_{EX} = 838$ ). The combined  $\theta^2$  distribution using the standard low energy set of cuts as well as the individual distributions for each pointing, are shown in Fig. 9.1. This clear detection is in agreement with the skyplot presented in the previous chapter, where 1ES 1218+304 is detected compatible with a point-like source, see Fig. 8.3.

In case of 2011 data, the results of the signal search can be found in Fig. 9.2, where individual  $\theta^2$  plots for each pointing, as well the combined one, are shown using low energy standard cuts. As a result, a signal of  $\sim 13.9 \sigma$  ( $N_{ON} = 2677$ ,  $N_{OFF} = 1883$  and  $N_{EX} = 794$ ) has been found for a total of  $\sim 21$  hours of observation time.

In Fig. 9.3, the  $\theta^2$  distribution for the combined 2010 and 2011 data is shown, resulting in a strong detection of  $\sim 16.2 \sigma$  ( $N_{ON} = 6739$ ,  $N_{OFF} = 5151$  and  $N_{EX} = 1588$ ).

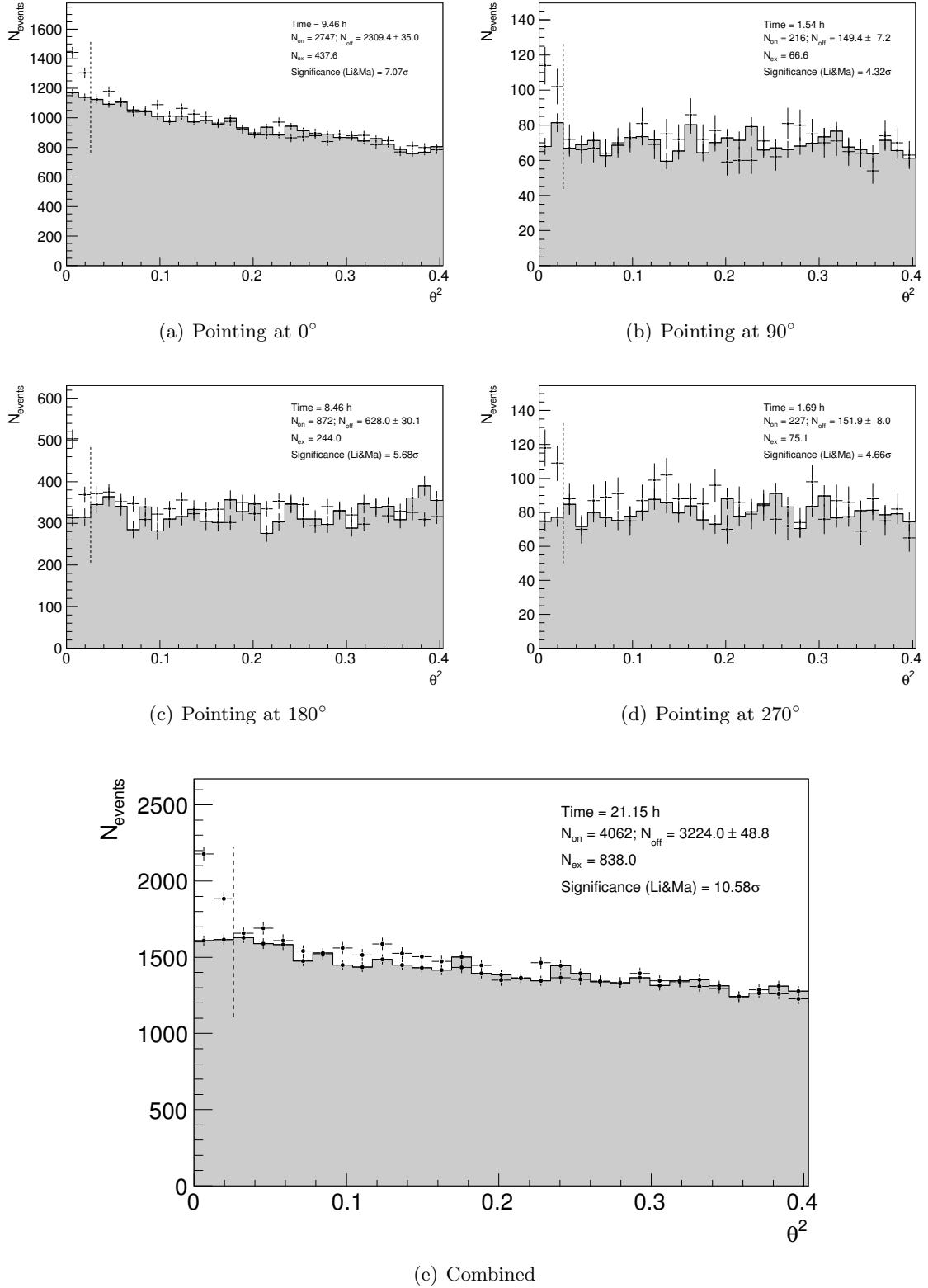


Figure 9.1:  $\theta^2$  distributions, obtained from the 2010 data at  $0^\circ$ ,  $90^\circ$ ,  $180^\circ$  and  $270^\circ$  wobble angles w.r.t. the position of 1ES 1215+303 and the combined distribution, respectively. Standard low energy cuts have been used.

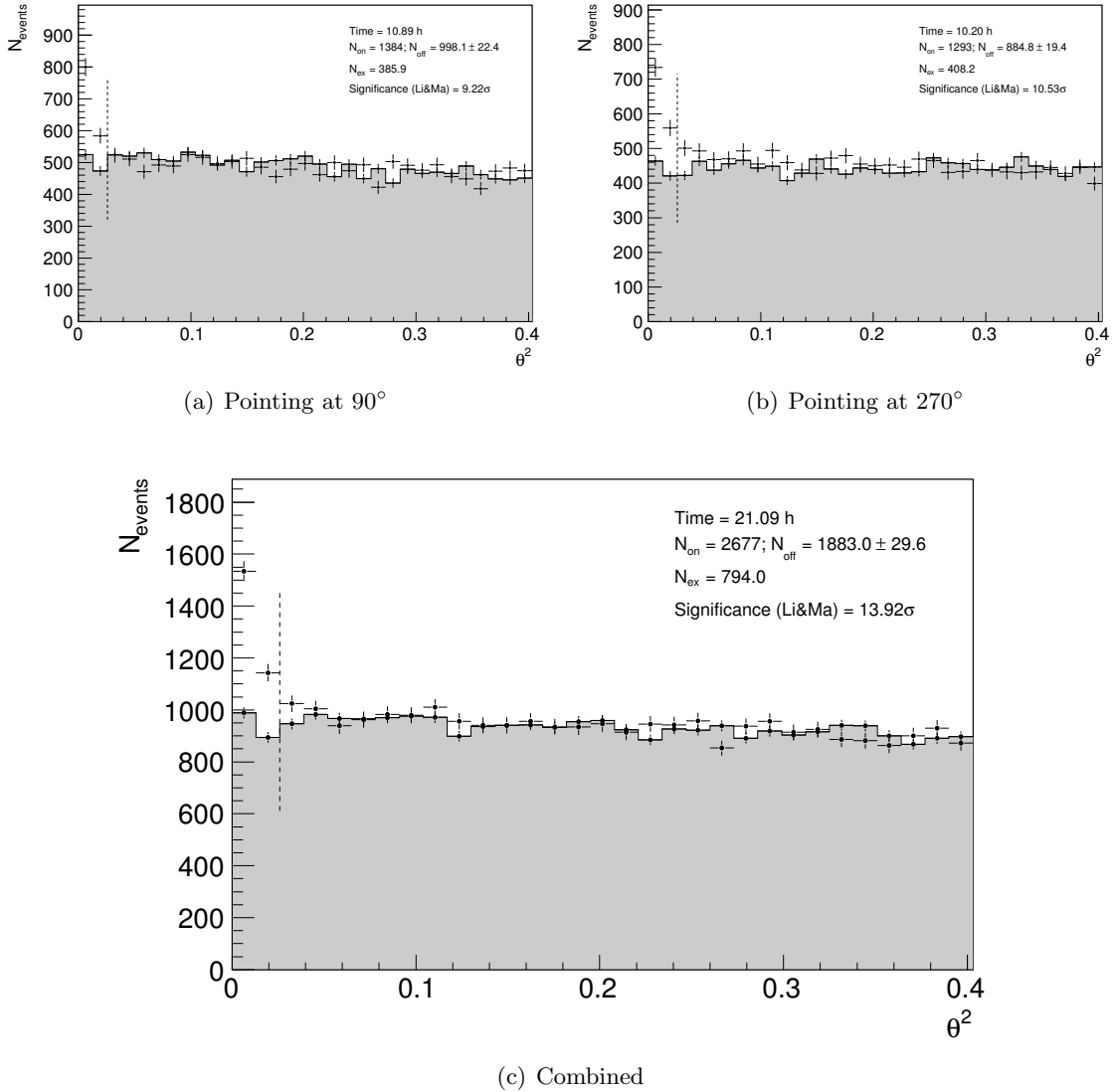


Figure 9.2:  $\theta^2$  distributions obtained from 2011 data at  $90^\circ$  and  $270^\circ$  wobble angles w.r.t. the position of 1ES 1218+304 and the combined distribution, respectively. Standard cuts for low energies have been used.

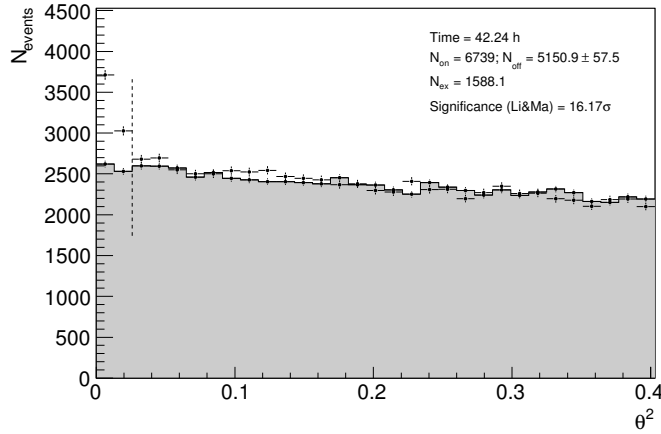


Figure 9.3:  $\theta^2$  distribution, obtained from combined 2010 and 2011 data, using standard cuts at low energies.

The skymap for the combined data from the two observation campaigns can be found in Fig. 9.4, where a clear detection of both 1ES 1218+304 and 1ES 1215+303 is observed. The detection is compatible with a point-like source.

The nightly significance per pointing and the combined ones can be found in Table 9.2.

### 9.3.1 The VHE spectrum of 1ES 1218+304

For the spectral analysis, loose cuts have been used. In this particular case, where the source is observed far from the camera center, at least in some of the pointings, an explicit cut in the *leakage* parameter (0.3 in case of MAGIC-I and 0.2 for MAGIC-II data, the difference is based on the size of the outer part of the camera which are larger in MAGIC-I) has been made in order to reject those showers which contain most of the signal outside the camera and which can thus cause a wrong calculation of the other image parameters.

The energy threshold of the analysis is different for each data set, due to the different efficiency and collection area, which change from one pointing to another. The energy threshold is calculated using Monte Carlo simulations with the same characteristics as the source data. The energy threshold is defined as the maximum in the energy distribution where the same set of cuts as for the analyzed data has been applied. This results range from  $\sim 60$  to  $80$  GeV depending on the source position in the camera. Therefore, as a global energy threshold of the analysis,  $\sim 80$  GeV can be assumed.

As in the case of the signal search, for spectrum calculation purposes, the different data sets had to be analyzed independently, for each source distance to the camera. The four spectra could be combined in the unfolding procedure, which gave stable results for different unfolding algorithms, as can be seen in Table 9.3. Therefore, the VHE differential energy spectrum, measured in 2010, can be described by a power-law of the form:

$$\frac{dN}{dE} = N_{200} \cdot \left( \frac{E}{200 \text{ GeV}} \right)^{-\Gamma} \quad (9.1)$$

Day	MJD	Zenith angle	Observation time (h)			Significance ( $\sigma$ )		
			P1	P2	Total	P1	P2	Total
12/01/2010	55208	1-14	0.40	0.57	0.97	1.59	3.57	3.24
15/01/2010	55211	1-12	0.61	0.50	1.11	4.24	2.93	5.25
19/01/2010	55215	2-16	0.57	0.29	0.86	1.99	1.18	2.29
20/01/2010	55216	1-16	0.91	0.83	1.74	3.07	1.15	3.26
22/01/2010	55218	1-19	1.14	0.82	1.96	2.68	3.68	3.99
23/01/2010	55219	1-40	1.55	1.83	3.38	4.68	3.67	5.90
24/01/2010	55220	1-24	0.86	0.58	1.44	0.61	1.47	1.15
25/01/2010	55221	1-20	0.51	0.57	1.08	2.55	2.35	3.38
09/02/2010	55236	1-32	1.49	1.21	2.70	1.68	3.40	3.04
12/02/2010	55239	6-34	0.85	0.86	1.71	-0.77	2.64	1.30
14/05/2010 <sup>a</sup>	55330	1-31	0.73	0.84	1.57	1.64	1.52	2.22
15/05/2010 <sup>a</sup>	55331	12-35	0.28	0.34	0.62	2.20	3.61	4.09
16/05/2010	55332	18-35	0.56	0.39	0.95	0.31	4.89	2.09
17/05/2010 <sup>a</sup>	55333	21-30	0.26	0.25	0.51	1.82	1.76	2.53
10/06/2010 <sup>a</sup>	55357	27-37	0.27	0.26	0.53	3.22	3.11	4.48
01/01/2011	55562	1-21	0.67	0.53	1.20	1.67	0.52	1.60
02/01/2011	55563	1-20	0.68	0.58	1.26	1.97	2.83	3.36
04/01/2011	55565	0-16	0.83	0.58	1.41	2.58	-0.48	1.86
05/01/2011	55566	2-17	0.87	0.60	1.47	1.73	1.19	2.09
06/01/2011	55567	1-15	0.68	0.87	1.55	1.12	3.59	3.40
07/01/2011	55568	1-24	0.87	0.99	1.86	1.17	1.87	2.18
08/01/2011	55569	1-26	0.87	1.15	2.02	3.23	4.47	5.45
09/01/2011	55570	0-26	1.16	0.98	2.14	4.51	4.95	5.82
10/01/2011	55571	1-9	0.29	0.29	0.58	1.44	1.43	2.03
11/01/2011	55572	0-10	0.58	0.46	1.04	2.18	2.35	3.05
12/01/2011	55573	0-11	0.55	0.44	0.99	2.41	2.37	2.77
13/01/2011	55574	0-12	0.59	0.48	1.07	2.69	2.46	3.63
14/01/2011	55575	1-14	0.62	0.42	1.04	1.98	2.56	3.15
15/01/2011	55576	1-15	0.87	0.86	1.73	3.99	4.84	5.60
16/01/2011	55577	2-7	-	0.28	0.28	-	2.22	2.22
27/01/2011	55588	14-23	0.20	0.29	0.49	0.59	2.12	1.99
02/02/2011	55594	16-27	0.29	0.35	0.64	0.93	0.64	1.11
03/02/2011	55595	3-8	0.25	0.06	0.31	0.96	1.02	1.52

Table 9.2: MAGIC good quality observation data of 1ES 1218+304. The first part of the table are the data from the 2010 campaign, while the second part accounts for the 2011 observations. The 2010 data were observed at wobble angles 0 and 180 degrees around the position of 1ES 1215+303, except for the nights with <sup>a</sup> which were observed at 90 and 270 degrees. In case of 2011, all data were taken at 90 and 270 degrees. The column named P1 and P2 refers to the observations taken at 0 or 180 degrees wobble angle, depending on the observation pointing and , and P2 stands for observations at 90 or 270 degrees wobble angle, while the column named “Total” refers to the combined observing time or significance from the two different pointings. The results are based on the  $\theta^2$  distributions, using the standard cuts at low energies.

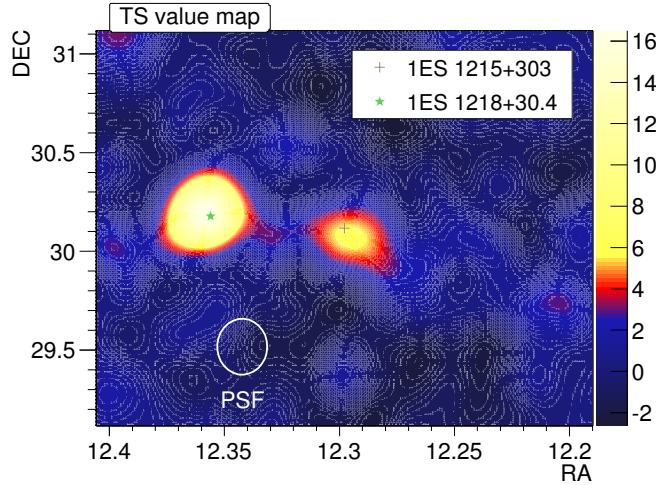


Figure 9.4: Skymap for the combined 2010 and 2011 data, using standard cuts at low energies. The BL Lac 1ES1215-303 is also present in this map, see chapter 8.

where  $N_{200}$  is the normalization constant at 200 GeV which was obtained as  $N_{200} = (0.98 \pm 0.09_{\text{stat}} \pm 0.05_{\text{sys}}) \cdot 10^{-10} \text{ cm}^{-2} \text{s}^{-1} \text{TeV}^{-1}$ . The photon index was calculated as  $\Gamma = 2.70 \pm 0.14_{\text{stat}} \pm 0.06_{\text{sys}}$ . A lower limit of the systematic uncertainties of the analysis has been derived from the comparison of different unfolding algorithms. In Fig. 9.6, the observed VHE spectrum with the MAGIC telescopes during 2010, unfolded using the Tikhonov algorithm, is represented as black points, while the uncertainties are depicted by the grey shaded area. The total flux for energies of  $E > 200$  GeV during the 2010 observation campaign is  $F_{2010} = (1.18 \pm 0.12_{\text{stat}} \pm 0.35_{\text{sys}}) \cdot 10^{-11} \text{ cm}^{-2} \text{s}^{-1}$  (corresponding to 6% of the Crab Nebula flux).

Unfolding algorithm	$f_0 [10^{-10} \text{cm}^{-2} \text{s}^{-1} \text{TeV}^{-1}]$	Spectral index	$\chi^2/\text{NDF}$	Probability
Schmelling	$0.98 \pm 0.06$	$-2.71 \pm 0.12$	0.48/4	98%
Tikhonov	$0.98 \pm 0.09$	$-2.70 \pm 0.14$	0.38/4	98%
Bertero	$1.00 \pm 0.01$	$-2.76 \pm 0.12$	2.26/4	69%
Schmelling (MINUIT)	$0.95 \pm 0.07$	$-2.71 \pm 0.13$	0.26/4	69%
BerteroW	$1.00 \pm 0.01$	$-2.73 \pm 0.13$	0.65/4	96%

Table 9.3: Measured spectrum of 1ES 1218+304 from 2010 data, best fit to a power-law for different unfolding algorithms.

Regarding the spectrum derived from the 2011 data set, since the data was taken with two different pointings, observing the source at 0.86 and 1.16 degrees from the camera center, respectively, and in both of the data sets the signal search resulted in a strong detection with significances higher than  $9\sigma$ , the spectrum from each data set can be unfolded independently. The measured VHE spectra from 2011 for each data set, unfolded by different unfolding algorithms, is shown in Fig. 9.5, where the blue and black points are

the differential energy spectral points from the analysis at 0.86 and 1.16 degrees from the camera center, respectively. The lower limit of the systematic uncertainties, due to the use of different unfolding algorithms, are represented by the blue and grey shaded areas. The measured spectrum of the source observed at 0.86 degrees from the camera center covers an energy range from  $\sim 80$  GeV to 1.15 TeV, while the spectral range from the data set taken at 1.16 degrees from the camera center, ranges from  $\sim 80$  GeV to 740 GeV. This is plausible, since the shower size is correlated with the energy of the progenitor  $\gamma$ -ray, such that the further the source is observed from the camera center, a bigger part of the shower image will be truncated, and these images have been rejected by the *leakage* cut. Thus, from the data taken at 1.16 degrees from the camera center, no significant points at energies from  $\sim 740$  GeV to 1.15 TeV have been found. Both spectra are in good agreement and compatible within the uncertainties, as shown in Fig. 9.5. Therefore, the spectra can be combined in a single spectrum. The result is shown in Table 9.4.

Unfolding algorithm	$f_0$ [ $10^{-10} \text{cm}^{-2}\text{s}^{-1}\text{TeV}^{-1}$ ]	Spectral index	$\chi^2/\text{NDF}$	Probability
Schmelling	$1.30 \pm 0.10$	$-2.94 \pm 0.10$	2.03/5	84%
Tikhonov	$1.20 \pm 0.10$	$-2.90 \pm 0.12$	0.69/5	98%
Bertero	$1.20 \pm 0.10$	$-2.85 \pm 0.10$	3.70/5	59%
Schmelling (MINUIT)	$1.30 \pm 0.10$	$-2.95 \pm 0.11$	1.38/5	93%
BerteroW	$1.20 \pm 0.10$	$-2.84 \pm 0.10$	3.96/5	56%

Table 9.4: Measured spectrum of 1ES 1218+304 from 2011 data, best fit to a power-law for different unfolding algorithms.

The total VHE spectrum from the entire 2011 campaign is obtained from the combination of the previous two spectra at different positions in the camera. It results in a differential energy spectrum which can be well-described by a single power-law of the form of Eq. 9.1 with the normalization constant at 200 GeV:  $N_{200} = (1.20 \pm 0.10_{\text{stat}} \pm 0.10_{\text{sys}}) \cdot 10^{-10} \text{ cm}^{-2}\text{s}^{-1}\text{TeV}^{-1}$ , and the spectral index  $\Gamma = 2.90 \pm 0.12_{\text{stat}} \pm 0.11_{\text{sys}}$ . In Table 9.4, the fit results for the different unfolding methods are shown.

The measured differential energy spectra from the 2010 and 2011 data sets are compatible within uncertainties (see Fig. 9.6), thus they can be combined. The combined spectrum obtained from the whole data set is fitted by a power-law, Eq. 9.1, resulting in a normalization constant:  $N_{200} = (1.10 \pm 0.10_{\text{stat}}) \cdot 10^{-10} \text{ cm}^{-2}\text{s}^{-1}\text{TeV}^{-1}$ , where the systematic uncertainty from the unfolding methods is negligible, and the spectral index  $\Gamma = 2.81 \pm 0.10_{\text{stat}} \pm 0.04_{\text{sys}}$ . In Table 9.5, the fit results for the different unfolding methods are given. The total integral flux from the 2011 data above  $E > 200$  GeV is  $F = (1.60 \pm 0.14_{\text{stat}} \pm 0.48_{\text{sys}}) \cdot 10^{-11} \text{ cm}^{-2}\text{s}^{-1}$  (corresponding to 8% of the Crab Nebula flux). These results are compatible with previous detections of the source but extends to lower energies.

#### 9.4 Variability study in optical and VHE band

The light curve obtained from the 2010 data set for energies above 200 GeV is shown in Fig. 9.7 in nightly time bins. It is compatible with a steady emission of flux  $F =$

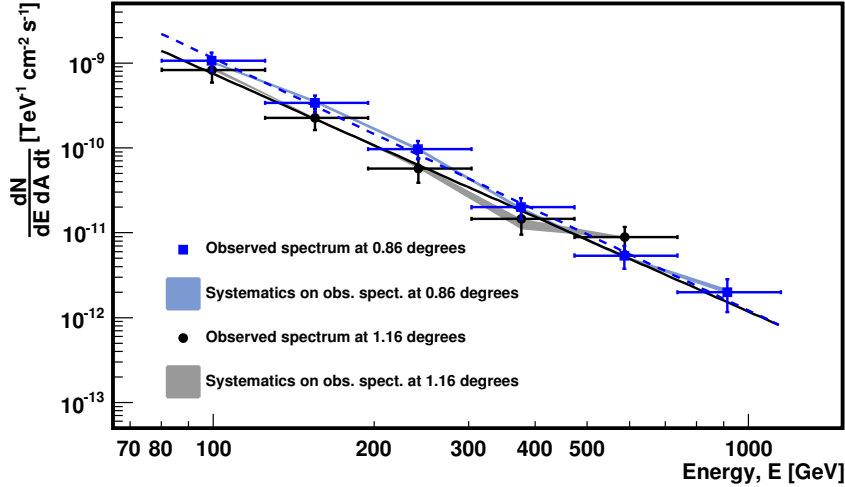


Figure 9.5: Measured VHE spectrum of 1ES 1218+304 from the 2011 data set from the two different pointings. In blue, the spectral points and the best fit of the spectrum measured in 2011 from data taken at 0.86 degrees form the camera center. The black points and fit are the ones derived from the analysis of the data set observed at 1.16 degrees from the camera center. Both shaded areas, blue and grey, account for the systematic uncertainties derived from the use of different unfolding methods.

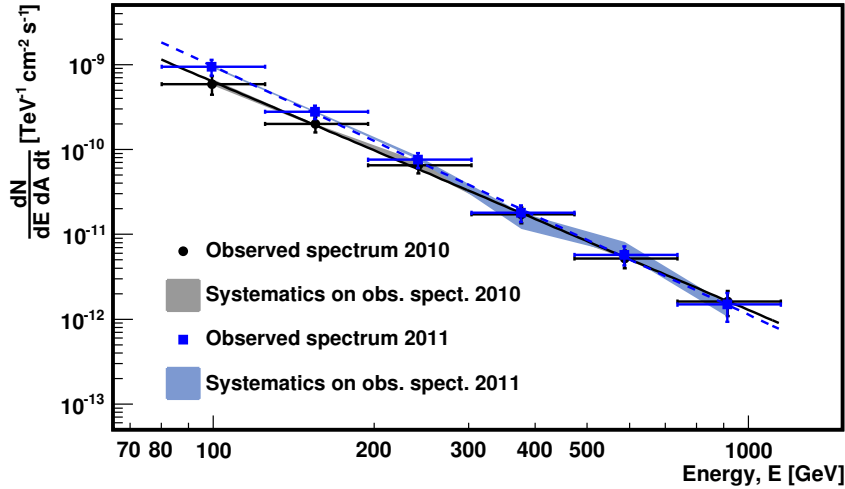
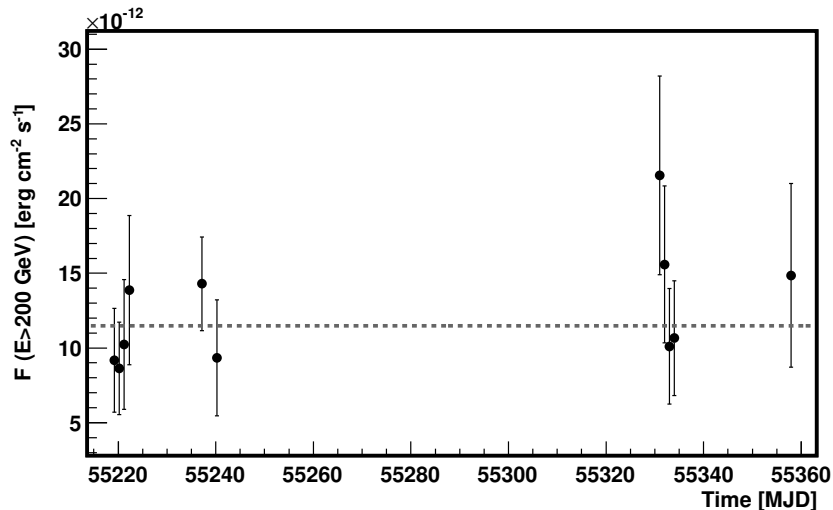


Figure 9.6: Comparison between the spectra of 1ES 1218+304 from 2010 and 2011. The black points represent the spectral points derived from the 2010 data set, and the solid black line is the best fit to the 2010 data. In blue points, the differential energy spectrum from 2011 is shown, and the dashed blue line is the best fit to the 2011 spectral points. The shaded areas, grey and blue, represent the systematic uncertainties for the 2010 and 2011 data analysis, derived from the use of different unfolding algorithms.

Unfolding algorithm	$f_0$ [ $10^{-10} \text{cm}^{-2}\text{s}^{-1}\text{TeV}^{-1}$ ]	Spectral index	$\chi^2/\text{NDF}$	Probability
Schmelling	$1.10 \pm 0.10$	$-2.84 \pm 0.09$	2.13/4	71%
Tikhonov	$1.10 \pm 0.10$	$-2.81 \pm 0.10$	0.60/4	96%
Bertero	$1.10 \pm 0.10$	$-2.85 \pm 0.09$	3.27/4	51%
Schmelling (MINUIT)	$1.10 \pm 0.10$	$-2.81 \pm 0.09$	1.26/4	87%
BerteroW	$1.10 \pm 0.10$	$-2.83 \pm 0.09$	1.85/4	76%

Table 9.5: Measured spectrum of 1ES 1218+304 from the combined data of 2010 and 2011, best fit to a power-law for different unfolding algorithms.

$(1.15 \pm 0.12) \cdot 10^{-11} \text{ cm}^{-2}\text{s}^{-1}$  with  $\chi^2/\text{NDF} = 6.08/10$  (probability  $\sim 81\%$ ).



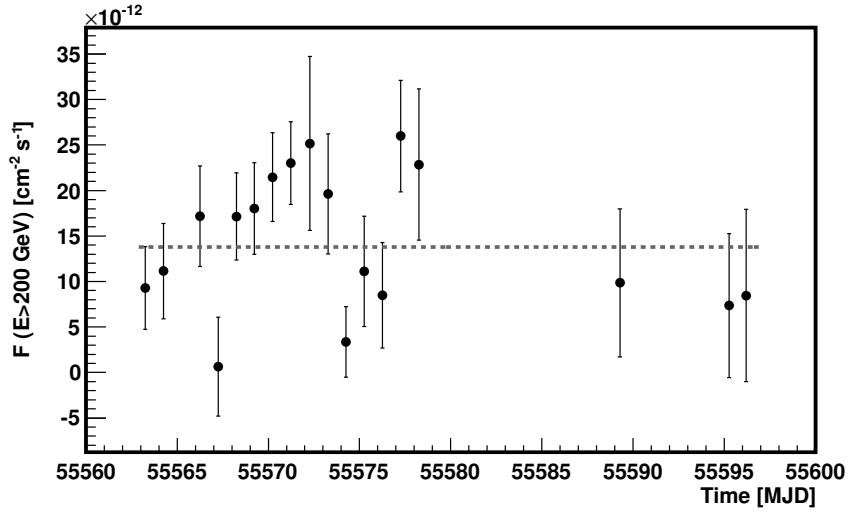


Figure 9.8: VHE  $\gamma$ -ray light curve from data taken in 2011.

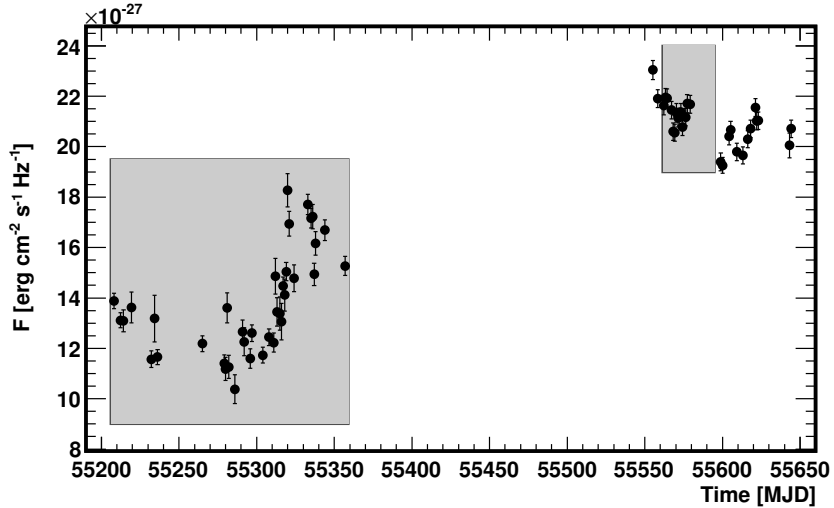


Figure 9.9: Optical light curve for 1ES 1218+303 on a nightly time-scale. The flux has been measured in the R band. The grey shaded area represents the observation windows by MAGIC during both observation campaigns.

time-scales, as shown in Fig. 9.10. The probability of a constant flux is lower than  $7 \cdot 10^{-150}$  ( $\chi^2/\text{NDF}=824/36$ ). However, the optical light curve for 2011 is compatible with a constant flux of  $F = (21 \pm 0.09) \cdot 10^{-27} \text{ erg cm}^{-2} \text{ s}^{-1} \text{ Hz}^{-1}$ , see Fig. 9.11. No correlation between optical and VHE  $\gamma$ -ray fluxes have been found neither in nightly time scales.

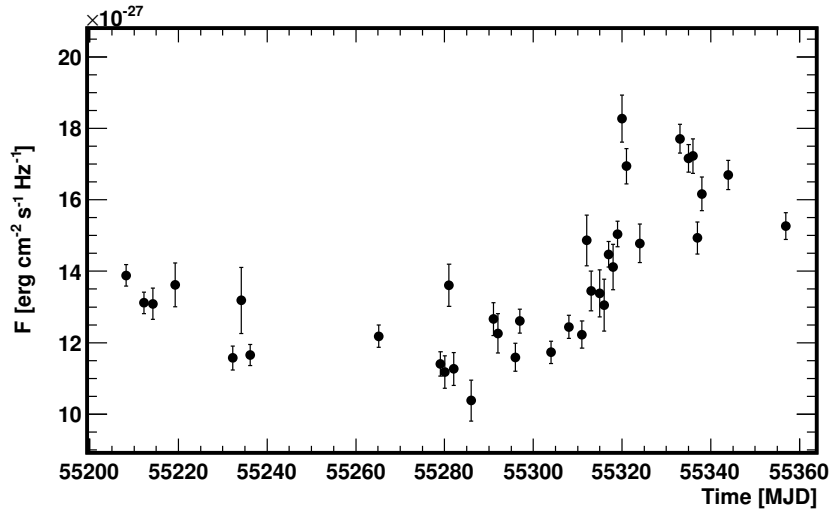


Figure 9.10: Optical light curve for 1ES 1218+303 for the 2010 observations on a nightly time-scale. The flux has been measured in the R band.

## 9.5 An EBL study from the observations of 1ES 1218+304

Following the same approach as in the previous source studies, the correction for the EBL absorption has to be applied. 1ES 1218+304 is located at  $z = 0.182$ , its VHE spectrum covers an energy range from  $\sim 80$  GeV to 1.15 TeV and can be used to test the EBL from IR to UV frequencies. Like in the previous chapter, the following different EBL models have been used: Domínguez et al. (2011), Franceschini et al. (2008), Albert et al. (2008a), Kneiske and Dole (2010), Kneiske et al. (2002), and Primack et al. (2005).

In Fig. 9.12, the observed unfolded differential energy spectrum by the Tikhonov algorithm, represented in black points and the best fit is shown by the solid black line while the grey shaded area accounts for those systematic uncertainties of the analysis derived from different unfolding algorithms. The de-absorbed spectrum, using the different EBL models, and theirs fits, are shown in blue. The de-absorbed spectral points can be well-fitted by a power-law for the used EBL models, from Kneiske and Dole (2010) and Primack et al. (2005). For the rest of the used EBL models, the last spectral point at higher energies, from  $\sim 740$  GeV to 1.15 TeV, cannot be well fitted by the power-law showing a higher flux, but still the fit parameters are acceptable. The values of the fits can be found in Table 9.6. At maximum, this pile-up effect is  $\sim 2\sigma$ . Therefore, in order to start to set new limits to the EBL of this hint is not due to fluctuations, it is needed at least a factor 2 higher

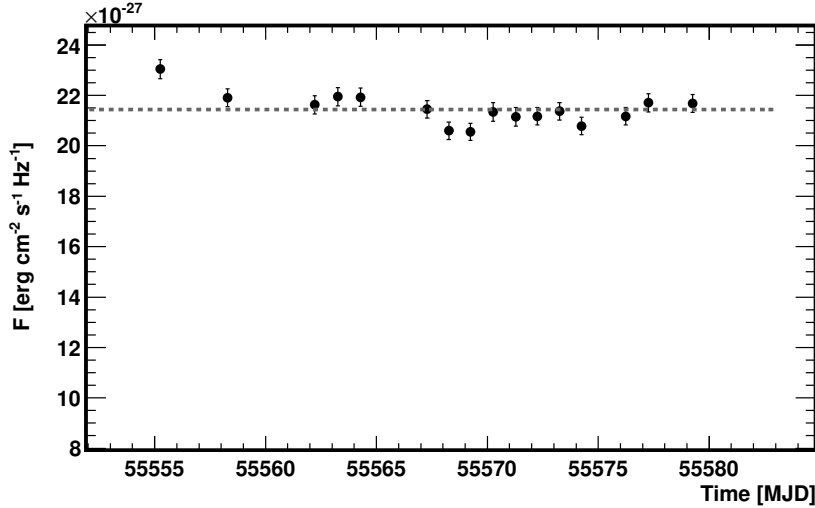


Figure 9.11: Optical light curve for 1ES 1218+303 for the 2011 observations on a nightly time-scale. The flux has been measured in the R band.

flux or observation time. This would mean an additional observation time of the order of  $\sim 85$  hours with the MAGIC telescopes. For further powerful instruments as CTA, which sensitivity at such energies will be about 7 times better, from 20 hours of observations the EBL models can start to be constrained. The advantage of CTA is not only the shorter observation time needed but also the possibility to get some spectral point for higher energies which are useful for EBL studies.

At high energies, the absorption of the VHE photons is mainly due to the IR photon field. This means that the EBL could be over-estimated at IR wavelengths, however this effect is not significant. This result was also obtained in the case of 1ES 1215+303 (see Sec. 8.5) but still the probability of the fit as a power-law cannot be discarded with the available statistics. 1ES 1218+303 is a very good candidate for further EBL studies since its base emission is well detected and stable over years. In fact, even during the flare state detected by Acciari et al. (2010), the spectral index didn't change, just the flux level increased. Therefore, this source is a good candidate to study EBL since it is detectable even in the quiescent state with high statistics.

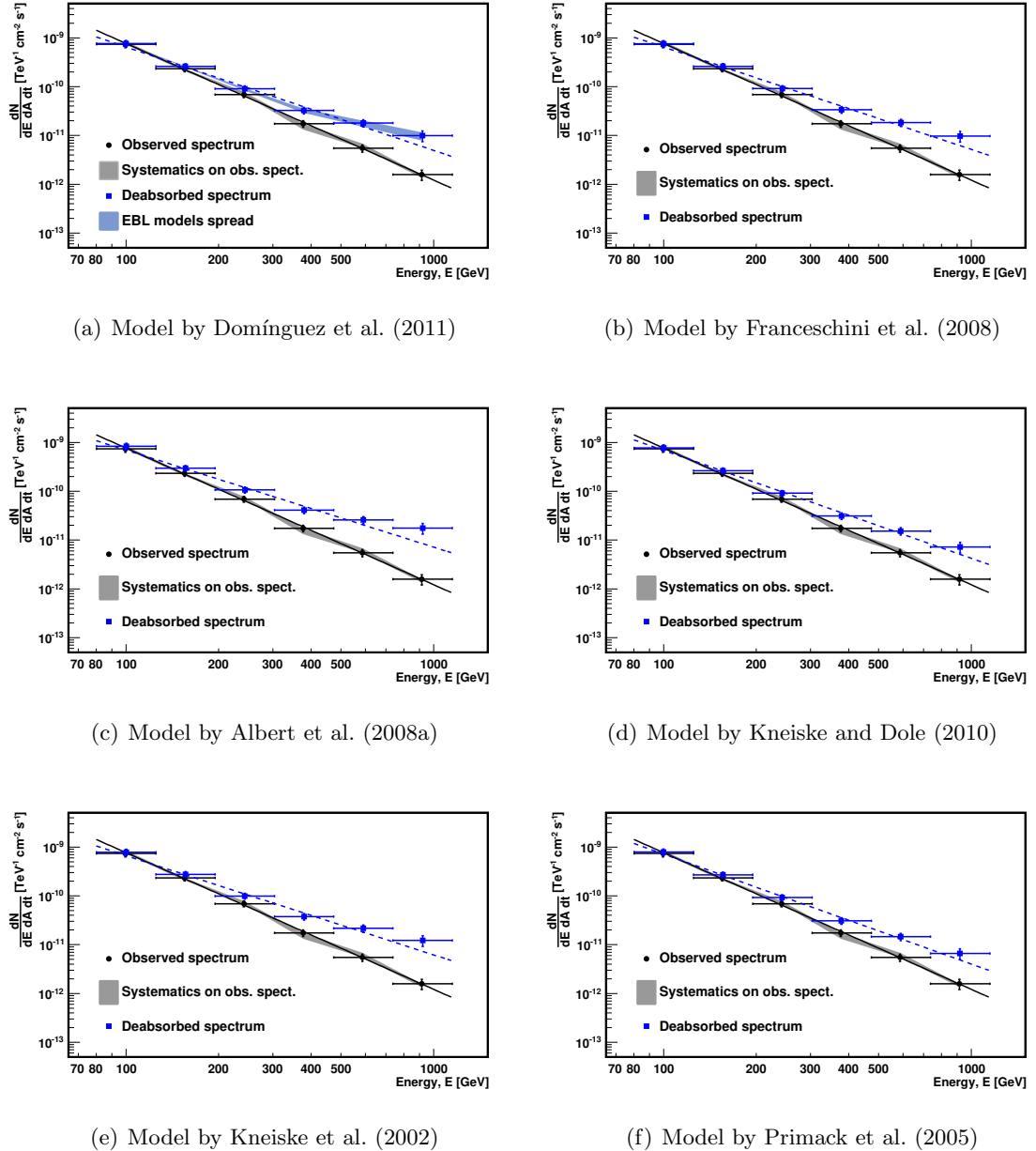


Figure 9.12: Differential energy spectrum from 1ES 1218+304 observed in 2010 and 2011. The black points represent the measured differential fluxes unfolded by the Tikhonov algorithm. The solid black line represents the best fit to a power-law and the grey shaded area represent the systematic uncertainties of the analysis. The blue points are the absorption corrected spectrum using different EBL models (see figure subtitles). The striped blue line represents the best fit power-law to the de-absorbed spectrum. And the blue shaded area in the first figure represents the uncertainty of Domínguez et al. (2011).

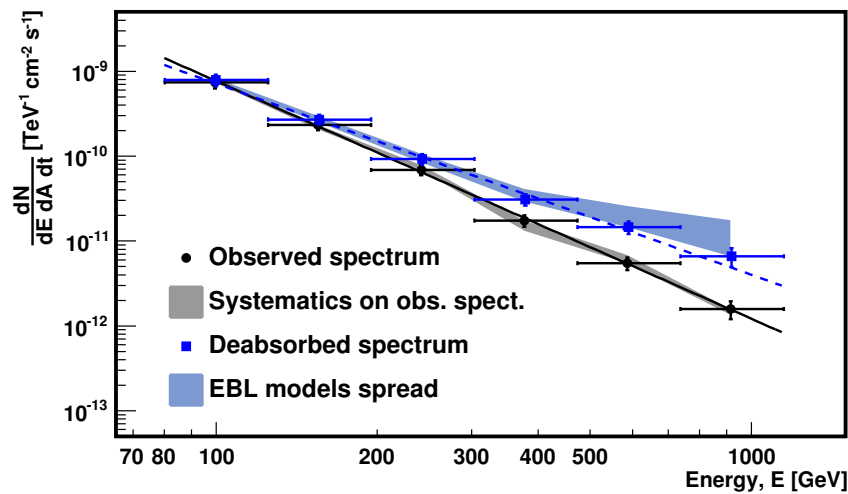


Figure 9.13: Differential energy spectrum from 1ES 1218+304 observed in 2010 and 2011. The black points represent the measured differential fluxes unfolded by the Tikhonov algorithm. The solid black line represents the best fit to a power-law and the grey shaded area represents the systematic uncertainties of the analysis. The blue points are the absorption corrected spectrum using the EBL models from Primack et al. (2005). The stripped blue line represents the best fit power-law for the de-absorbed spectrum and the blue area represents the spread of EBL models Domínguez et al. (2011), Franceschini et al. (2008), the “max high UV” EBL model described in Albert et al. (2008a), Kneiske and Dole (2010), Kneiske et al. (2002) and Primack et al. (2005).

EBL model	$f_0$ [ $10^{-9}\text{cm}^{-2}\text{s}^{-1}\text{TeV}^{-1}$ ]	Spectral index	$\chi^2/\text{NDF}$	Probability
Domínguez et al. (2011)	$0.15 \pm 0.01$	$-2.09 \pm 0.13$	$5.86/4$	21%
Domínguez et al. (2011) Low Limit	$0.14 \pm 0.01$	$-2.19 \pm 0.13$	$5.24/4$	26%
Domínguez et al. (2011) Upper Limit	$0.16 \pm 0.01$	$-2.03 \pm 0.13$	$6.19/4$	19%
Franceschini et al. (2008)	$0.15 \pm 0.01$	$-2.07 \pm 0.13$	$5.10/4$	28%
Albert et al. (2008a)	$0.18 \pm 0.01$	$-1.96 \pm 0.14$	$8.76/4$	7%
Kneiske and Dole (2010)	$0.15 \pm 0.01$	$-2.20 \pm 0.12$	$3.36/4$	50%
Kneiske et al. (2002)	$0.16 \pm 0.01$	$-2.01 \pm 0.13$	$6.00/4$	20%
Primack et al. (2005)	$0.15 \pm 0.01$	$-2.24 \pm 0.12$	$2.58/4$	63%

Table 9.6: De-absorbed spectrum of 1ES 1218+304 best fit to a power-law for different EBL models.

---

# 10

---

## Conclusions and Outlook

The MAGIC telescopes belong to the second generation of Imaging Atmospheric Cherenkov Telescopes, and are currently the largest of their kind with a single telescope mirror diameter of 17 m. They observe Very High Energy (VHE)  $\gamma$ -rays and operate in the energy range from  $\sim$ 50 GeV to few tens of TeV. The telescopes have been operated in stereoscopic mode since autumn 2009, and since that time, several new sources have been discovered. This work explains in detail the currently used concepts for the analysis of MAGIC stereoscopic data, applied to a large and diverse set of new data. Moreover, several non-standard analysis approaches have been applied in order to successfully recover source data from 2010 and 2011 which were not taken under optimal observation conditions. These include data taken under moderate moon light and sources found at non-standard positions inside the MAGIC camera.

On June 17<sup>th</sup> 2010, MAGIC discovered the second most distant VHE  $\gamma$ -ray source with well measured redshift  $z = 0.432$ , which belongs to the class of Flat Spectrum Radio Quasars (FSRQs). Only two additional objects of this type had been detected up to then in the VHE domain. MAGIC observed the fastest flare ever seen in FSRQs in VHE  $\gamma$ -rays, on a time scale of about 10 minutes. The combination of quasi-simultaneous data from the *Fermi* satellite and MAGIC covers an energy range from 100 MeV to 400 GeV. The high energy part of the resulting energy spectrum can be well-fitted to a simple power-law with a spectral slope of  $\Gamma = 3.75 \pm 0.27_{\text{stat}} \pm 0.2_{\text{sys}}$ , where the systematic uncertainties stem from the use of different unfolding algorithms, without apparent signs of a cut-off. When the spectrum is corrected for the effect of the absorption of VHE  $\gamma$ -rays by the Extragalactic Background Light (EBL) on their travel through Space, making use of the current generation of EBL models, the outcome is again compatible with a straight power-law, of spectral index  $\Gamma = 2.72 \pm 0.34_{\text{stat}}$ , when e.g. the currently most precise model by Domínguez et al. (2011) is used. The prolongation of the resulting de-absorbed spectrum joins smoothly the energetic part of the *Fermi* spectrum around 3 GeV. A cut-off in the overall spectrum of PKS 1222+21 below 130 GeV can therefore be excluded at 95% C.L. This finding, together with the detected fast variability in VHE  $\gamma$ -rays, cannot be explained by the current canonical scenario for the jet emission of this type of sources (Ghisellini and Tavecchio, 2009). The canonical scenario assumes that the  $\gamma$ -ray emission is released from

a jet region close to the central Black Hole, inside the Broad-Line Region (BLR) of the AGN, and predicts strong absorption of the  $\gamma$ -ray photons above a few GeV, due to the interaction of the VHE  $\gamma$ -rays with the optical-UV photons present in the BLR. The strong absorption by the BLR photon field can be circumvented by the proposed far-dissipation scenario (Sikora et al., 2008), where the emission is thought to result from a spherical region, with a diameter similar to the entire jet section, located beyond the BLR. However, this scenario is also incompatible with the MAGIC observation, due to the constraint set by the short time-scale of the variability.

In order to reconcile the observations with a revised understanding of the physical environment of the jets from FSRQs, two scenarios can be thought of: a strong re-collimation of the jet, which would allow small jet sections outside the BLR, or an internal jet structure. In this work, the second possibility has been explored. The developed model demonstrates that a two-zone emission scenario can account for the observed spectral features from infrared to  $\gamma$ -rays. The model is composed of two emitting regions located outside the BLR, in order to avoid the strong absorption of VHE  $\gamma$ -rays, and where the external photon field comes from the IR emission from the torus: one small and compact “blob” which has an important emission in VHE  $\gamma$ -rays and whose size is constrained by the variability time scale, and a larger emitting region modeled as standard sphere whose radius corresponds to the semi-aperture section of the jet which dominates emission at lower frequencies. As result, a negligible connection between these two emitting regions has been found which can thus be spatially separated. Therefore, the small “blob” has to remain beyond the BLR, but the emission region accounting for the lower energy part of the spectral energy distribution can be located inside or outside the BLR.

Also in this work, a second AGN, the BL Lac 1ES 1215+303, with two redshifts under debate ( $z = 0.13$  and  $z = 0.237$ ), has been discovered during an active period in the optical band in 2011. The analysis reveals a VHE spectrum extending up to energies  $>1$  TeV, which can be fitted by a power-law with spectral index  $\Gamma = (2.78 \pm 0.21_{\text{stat}} \pm 0.17_{\text{sys}})$ , where the systematic uncertainty stems from the variation of different unfolding algorithms. The de-absorption of the spectrum has been performed, as in the case of the previous source, resulting in a de-absorbed power-law spectral index of  $\Gamma = (2.24 \pm 0.26_{\text{stat}} \pm 0.13_{\text{sys}})$  and  $\Gamma = (1.71 \pm 0.32_{\text{stat}} \pm 0.23_{\text{sys}})$ , for the two redshift possibilities, respectively, where the systematic uncertainty results from the variation of the EBL models. A multi-frequency study of the variability of the source involving optical, UV, X-rays, High Energy and VHE  $\gamma$ -rays data has been performed, resulting in a hint of correlation between them on long term time-scales. Contrarily to the previously discussed FSRQ source, the findings of this source are well compatible with the currently favoured Synchrotron-Self-Compton (SSC) models (Maraschi et al., 1992) for BL Lacs if the assumed redshift is  $z = 0.13$ . In the framework of the SSC model, the high redshift  $z = 0.237$  is very unlikely and cannot be fitted by the model.

In the same FoV as 1ES 1215+303, a second VHE  $\gamma$ -ray source was detected during two observation campaigns carried out in 2010 and 2011, namely the BL Lac 1ES 1218+304, located at a redshift of  $z = 0.187$ , and seen at a distance of  $\sim 0.8^\circ$  from 1ES 1215+303. For the first time, two sources were detected in the same FoV of the MAGIC telescopes, and the data analysis has been adapted accordingly. A VHE spectrum with spectral index  $\Gamma = (2.81 \pm 0.10_{\text{stat}} \pm 0.04_{\text{sys}})$ , where the systematic uncertainty results from the use of dif-

ferent unfolding algorithms, extending to energies  $>1$  TeV, has been retrieved, compatible with previous observations of this source by MAGIC and VERITAS. Also the obtained flux levels are compatible with the assumption of a steady emission, during the 2010 and 2011 observations, and when compared to those from its discovery back in 2005 by MAGIC (Albert et al., 2006a).

All three sources have been used to test the current EBL models for their compatibility with physically allowed leptonic emission scenarios. The IR-UV photons of the EBL interact with the VHE  $\gamma$ -ray photons via pair production of electrons and positrons and produce hence a distortion of the observed VHE  $\gamma$ -ray spectrum. Despite of the large distances of the observed objects, and retrieved spectral points extending to energies  $>400$  GeV and  $>1$  TeV, for different sources, current EBL models could not be further constrained by these data. However, it has to be mentioned that the current status of EBL modelling has reached a point where the uncertainty of and the spread between models has already been greatly reduced. Nevertheless, both sources, 1ES 1215+303 and 1ES 1218+304 can be ideal future objects for the study of the EBL, with more sensitive telescopes, especially in the TeV domain, since they are distant sources whose emission extends to energies higher than 1 TeV. This is true especially in the case of 1ES 1218+304 which is detectable in VHE  $\gamma$ -rays in quiescent state and very stable long term activity. Moreover, even during a flare state, the spectral shape of this source has been observed to remain unaffected.

Finally, in the appendix, a detailed “cooking recipe” for stereoscopic data analysis can be found, which will hopefully be useful for future analyzers of MAGIC stereoscopic data.

## Outlook

The detection of PKS 1222+21 in VHE  $\gamma$ -rays, together with its fast variability found in this work, strongly challenges the present jet emission models of FSRQs. A first approximation of the solution to the problem has already been presented in a dedicated chapter, but a detailed multi-wavelength study must be carried out in order to test the new model. Especially the prediction of a time delay of several hours between a rise in optical activity and the subsequent  $\gamma$ -ray flare can be tested. Also the correlation (if any) between X-rays and  $\gamma$ -rays would answer the question if the small blob is emitting mainly in  $\gamma$ -rays or is also contributing substantially to the X-ray band emission. Simultaneous radio observations would offer the possibility to measured the bulk Lorentz factor and the aperture angle of the jet during a high flux state of the source.

A longer observation of PKS 1222+21 in VHE  $\gamma$ -rays during a flare state would shed more light on the proposed emission model of this object. A cut-off is expected around 1 TeV. If one extrapolates the observed spectrum by MAGIC, an observation of  $\sim 2$  hours would be enough to extend the spectrum up to  $\sim 1$  TeV, however at least 5 hours would be needed to detect the cut-off with sufficient significance in case a similar flare is observed. A better case for the future will be the Cherenkov Telescopes Array (CTA) with which  $\sim 40$  minutes of observation should be enough.

Longer or more sensitive observations in VHE  $\gamma$ -rays of 1ES 1215+303 and 1ES 1218+304 can be very useful for EBL studies. Also very convenient in order to derive EBL limits would be simultaneous *Fermi* data. This study is based on the fact that the VHE spectral index cannot be harder than the spectral index of the *Fermi* data since at such energies, they are

almost unaffected by the EBL absorption, and from there, the maximum absorption due to EBL can be derived or, in the end, the energy- and redshift dependent absorption, measured. Another approach could be applied to these two sources, especially to 1ES 1218+304, given its long term stability: by making use of simultaneous optical, X-ray and  $\gamma$ -ray observations by *Fermi*, the best fits of a SSC model of the spectral energy distribution, omitting the VHE  $\gamma$ -ray measurements can be found, since these data are not affected by the EBL if their redshifts are  $z \lesssim 1$ . Then, this result can be extrapolated to the VHE band. From the comparison between the expected value by the model and the observations at VHE, the EBL absorption can be inferred (Mankuzhiyil et al., 2010).

Besides the EBL, the intergalactic magnetic field can be tested by using distant sources emitting in the VHE domain. The absorption of VHE photons due to the EBL is produced by pair production. These electrons and positrons are relativistic and can interact via inverse Compton scattering with the cosmic microwave background photon field, resulting in the emission of GeV photons. Tavecchio et al. (2010) found that the spectrum and the flux level of the reprocessed emission is critically dependent on the intensity of the intergalactic magnetic field, that can deflect the pairs, thus diluting the intrinsic emission. They derived a relation for the reprocessed spectrum expected from a steady source as in the case of 1ES 1218+304 from where the intergalactic magnetic field intensity can be derived from the combination of contemporaneous Fermi and MAGIC data.

---

# 11

---

## Conclusiones y Trabajo Futuro

El sistema de telescopios MAGIC pertenece a la segunda generación de *Imaging Atmospheric Cherenkov Telescopes (IACT)* y son actualmente los mayores de su clase, contando con un espejo de diámetro de 17 m cada uno. Observan rayos  $\gamma$  de muy alta energía (VHE por sus siglas en inglés) y operan en el rango de energía desde  $\sim$ 50 GeV hasta pocas decenas de TeV. Los telescopios han operado en modo estereoscópico desde otoño de 2009, y desde entonces, varias nuevas fuentes han sido descubiertas. Este trabajo explica en detalle los actuales conceptos para el análisis de datos estereoscópicos tomados con MAGIC, aplicados a un amplio y diverso conjunto de nuevos datos. Además, varios análisis no estándar han sido utilizados en el análisis de datos observados en 2010 y 2011 que no habían sido obtenidos en condiciones óptimas de observación, éstos incluyen datos tomados bajo moderada luz de luna y fuentes que se encuentran en posiciones no estándar en la cámara de MAGIC.

El 17 de Junio de 2010, MAGIC descubrió la segunda fuente más distante detectada en rayos  $\gamma$  de VHE, con un *redshift* bien determinado de  $z = 0.432$ , y perteneciente a la clase *Flat Spectrum Radio Quasars (FSRQs)*. Sólo dos objetos de este tipo habían sido detectados hasta entonces en el dominio de VHE. MAGIC observó el aumento de intensidad más rápido detectado en FSRQs en VHE, en una escala temporal de unos 10 minutos. La combinación de datos prácticamente simultáneos tomados por el satélite *Fermi* y MAGIC cubren un rango de energía desde 100 MeV hasta 400 MeV. La parte más alta energética del espectro resultante puede ser ajustado por una ley de potencias con un índice espectral  $\Gamma = 3.75 \pm 0.27_{\text{stat}} \pm 0.2_{\text{sys}}$ , donde la incertidumbre sistemática deriva del uso de diferentes métodos de *unfolding*, sin signos de una caída exponencial. Cuando el espectro es corregido por el efecto de la absorción de rayos  $\gamma$  de VHE por la Luz Extragaláctica de Fondo (EBL por sus siglas en inglés) en su viaje a través del Espacio, haciendo uso de la actual generación de modelos de EBL, el resultado puede ser de nuevo ajustado por una ley de potencias de índice espectral  $\Gamma = 2.72 \pm 0.34_{\text{stat}}$  cuando, por ejemplo, se usa el modelo de EBL más preciso actualmente (Domínguez et al., 2011).

La prologanción del espectro deabsorbido resultante se une con la parte del espectro medido por *Fermi* aproximadamente a 3 GeV. Una caída exponencial del espectro de PKS 1222+21 por debajo de 130 GeV puede ser excluída con un nivel de confianza del 95%. Este hallazgo, junto con la rápida variabilidad detectada en rayos  $\gamma$  de VHE no

puede ser explicado por el actual escenario estándar para la emisión de *jets* de este tipo de fuentes (Ghisellini and Tavecchio, 2009). Dicho escenario estándar asume que la emisión de rayos  $\gamma$  es liberada por una región del *jet* situada cerca del agujero negro central, dentro de la *Broad-Line Region (BLR)* del AGN, y predice una fuerte absorción de fotones  $\gamma$  a partir de pocos GeV, debido a la interacción de los rayos  $\gamma$  de VHE con los fotones visible-UV presentes en la BLR. La fuerte absorción por parte de los fotones de la BLR puede ser evitada por los propuestos escenarios de “dissipación lejana” (Sikora et al., 2008), donde la emisión se cree que es producida por una región esférica con un diámetro similar a la sección del *jet*, y localizada fuera de la BLR. Sin embargo, este escenario es también incompatible con la detección de MAGIC, debido a la restricción impuesta por la variabilidad en una escala temporal tan corta.

Con el fin de conciliar las observaciones con un entendimiento revisado del entorno físico de los *jets* en FSRQs, se pueden sugerir dos escenarios: una fuerte recolimación del *jet* que podría permitir pequeñas secciones del mismo fuera de la BLR, o bien, la posibilidad de tener una estructura interna en el *jet*. En este trabajo, la segunda posibilidad ha sido explorada. El modelo desarrollado demuestra que un escenario con dos zonas de emisión puede dar cuenta de las características espectrales observadas desde infrarrojo hasta rayos  $\gamma$ . El modelo se compone de dos zonas de emisión localizadas fuera de la BLR, a fin de evitar la fuerte absorción de rayos  $\gamma$  de VHE, y donde el campo de radiación externo proviene de la emisión IR del toroide: una zona pequeña y compacta que tiene una emisión importante en rayos  $\gamma$  de VHE y cuyo tamaño viene definido por la escala temporal de la variabilidad, y una región de emisión más extensa modelada como una esfera estándar cuyo radio se corresponde con la sección de semi-apertura del *jet* y que domina la emisión a bajas frecuencias. Como resultado, se ha obtenido que la conexión entre las dos regiones de emisión es despreciable y pueden estar espacialmente separadas. Por tanto, la región pequeña tiene que permanecer igualmente fuera de la BLR, pero la región de emisión que da cuenta de la parte de bajas energía de la distribución espectral de energía puede estar localizada tanto dentro como fuera de la BLR.

También en este trabajo, un segundo AGN, el BL Lac 1ES 1215+303, cuyo *redshift* es objeto de debate ( $z = 0.13$  y  $z = 0.237$ ), ha sido descubierto durante un periodo activo en el visible durante 2011. El análisis revela un espectro en VHE que se extiende hasta energías superiores a 1 TeV, que puede ser ajustado por una ley de potencias con un índice espectral  $\Gamma = (2.78 \pm 0.21_{\text{stat}} \pm 0.17_{\text{sys}})$ , donde la incertidumbre sistemática proviene de la variación de diferentes algoritmos de *unfolding*. El espectro deabsorbido ha sido calculado como en el caso anterior, y resulta en una ley de potencias con índice espectral  $\Gamma = (2.24 \pm 0.26_{\text{stat}} \pm 0.13_{\text{sys}})$  y  $\Gamma = (1.71 \pm 0.32_{\text{stat}} \pm 0.23_{\text{sys}})$ , para los dos *redshifts* posibles respectivamente, donde las incertidumbres sistemáticas derivan de las diferencias de los diferentes modelos de EBL. Se ha llevado a cabo un estudio multifrecuencia de la variabilidad de la fuente usando datos tomados en visible, UV, rayos X, rayos  $\gamma$  de alta energía (HE) y muy alta energía (VHE), dando como resultado un indicio de correlación entre las distintas frecuencias a larga escala temporal. Al contrario que en el caso del FSRQ previamente discutido, los resultados de esta fuente son compatible con el actual modelo estándar Synchrotron-Self-Compton (SSC) para BL Lacs asumiendo un *redshift*  $z = 0.13$ . En el contexto del modelo SSC, el *redshift*  $z = 0.237$  es muy poco probable y la distribución espectral de energías no puede ser ajustada por dicho modelo.

En el mismo campo de visión de 1ES 1215+303, una segunda fuente de rayos  $\gamma$  de VHE fue detectada durante las dos campañas de observación llevadas a cabo en 2010 y 2011, el BL Lac 1ES 1218+304, situado a un *redshift*  $z = 0.187$ , y a una distancia de  $\sim 0.8^\circ$  de 1ES 1215+303. Por primera vez, dos fuentes han sido detectadas en el mismo campo de visión de MAGIC, y el análisis de los datos ha sido adaptado para ello. Un espectro en VHE con índice espectral  $\Gamma = (2.81 \pm 0.10_{\text{stat}} \pm 0.04_{\text{sys}})$ , donde la incertidumbre sistemática proviene del uso de diferentes algoritmos de *unfolding*, extendiéndose hasta energías  $> 1$  TeV, ha sido obtenido, compatible con observaciones previas de esta fuente con MAGIC y VERITAS. Además, el nivel de flujo obtenido es compatible con la hipótesis de una emisión estable durante las observaciones llevadas a cabo en 2010 y 2011, y cuando se compara con los resultados obtenidos en el descubrimiento de la fuente en 2005 con MAGIC (Albert et al., 2006a).

Las tres fuentes han sido usadas para testear los modelos actuales de EBL y su compatibilidad con los escenarios propuestos por los modelos de emisión leptónicos. Los fotones IR-UV del EBL interaccionan con los fotones de rayos  $\gamma$  de VHE mediante la producción de pares de electrones y positrones, distorsionando el espectro observado en rayos  $\gamma$  de VHE. A pesar de ser objetos lejanos, y habiéndose detectado puntos espectrales hasta energías  $> 400$  GeV y  $> 1$  TeV para las diferentes fuentes, los actuales modelos de EBL no puede ser acotados por estos datos. Sin embargo, hay que mencionar que el estado actual de los modelos de EBL ha llegado a un punto en el que las incertidumbres y las diferencias entre los diferentes modelos se han reducido notablemente. No obstante, ambas fuentes, 1ES 1215+303 y 1ES 1218+304, pueden ser objetos ideales para futuros estudios de EBL con telescopios más sensibles, especialmente en el dominio de TeV, puesto que son fuentes lejanas cuya emisión se extiende hasta energías mayores de 1 TeV. Esto se cumple especialmente en el caso de 1ES 1218+304 puesto que es detectable en rayos  $\gamma$  de VHE incluso en estado de baja actividad y es una fuente muy estable a largo plazo. Además, incluso durante periodos de actividad, el índice espectral de la fuente permanece inalterado.

Finalmente, en el apéndice se encuentra una detallada “receta de cocina” para el análisis de los datos estereoscópicos, que espero sea de utilidad para futuros analizadores de datos observados con MAGIC.

## Trabajo futuro

La detección de PKS 1222+21 en rayos  $\gamma$  de VHE, junto con la rápida variabilidad encontrada en este trabajo, supone un gran desafío para los actuales modelos de emisión de *jets* en FSRQs. Una primera aproximación a la solución del problema ha sido propuesta en uno de los capítulos de este trabajo, pero un estudio multifrecuencia detallado ha de llevarse a cabo con el objetivo de testear el nuevo modelo propuesto. En especial, la predicción de un retraso de varias horas entre el aumento de actividad en visible y el posterior aumento de actividad en rayos  $\gamma$  puede ser testeado. Además, la correlación entre rayos X y rayos  $\gamma$  podría responder a la pregunta sobre si la pequeña zona de emisión del modelo emite principalmente en rayos  $\gamma$  o también contribuye sustancialmente en la emisión de rayos X. Observaciones simultáneas en radio podrían ofrecer la posibilidad de medir el *bulk Lorentz factor* y el ángulo de apertura del *jet* durante un estado activo de la fuente.

Una observación de más larga duración de PKS 1222+21 en rayos  $\gamma$  de VHE durante

una fase de actividad podría arrojar más luz sobre el modelo de emisión propuesto para este objeto. Una caída exponencial en el espectro es esperado a 1 TeV aproximadamente. Extrapolando el espectro observado por MAGIC, una observación de unas 2 horas sería suficiente para extender el espectro hasta  $\sim 1$  TeV, sin embargo, al menos 5 horas serían necesarias para poder detectar dicha caída con suficiente significancia, en caso de que la fuente fuese observada durante un periodo de actividad similar al detectado. En el futuro, haciendo uso del Cherenkov Telescopes Array (CTA), unos 40 minutos de observación debería ser suficiente.

Observaciones de más larga duración o usando telescopios más sensibles en rayos  $\gamma$  de VHE de 1ES 1215+303 y 1ES 1218+304 pueden ser muy útiles para estudios de EBL. Muy conveniente también para derivar límites en el EBL serían datos simultáneos observados por *Fermi*. Este estudio está basado en el hecho de que el índice espectral medido en VHE no puede ser más duro que el índice espectral medido por *Fermi* puesto que a estas energías el espectro no está prácticamente afectado por absorción del EBL, y de ahí, la máxima absorción debida al EBL puede ser calculada o, en último término, la dependencia de la absorción con la energía y el *redshift*. Otro enfoque puede ser aplicado a estas dos fuentes, especialmente a 1ES 1218+304, debido a su estabilidad a largo plazo: haciendo uso de datos simultáneos en visible, rayos X y rayos  $\gamma$  observados por *Fermi*, se puede encontrar el mejor ajuste a un modelo SSC de la distribución espectral de energía, omitiendo las medidas de rayos  $\gamma$  de VHE, puesto que estos datos no están afectados por EBL para fuentes con  $z \lesssim 1$ . Después, el resultado del ajuste puede ser extrapolado hasta la banda de VHE. A partir de la comparación entre el valor esperado por el modelo y las observaciones en rayos  $\gamma$  de VHE, la absorción debida al EBL puede ser calculada (Mankuzhiyil et al., 2010).

Además del EBL, el campo magnético intergaláctico puede ser testeado usando fuentes lejanas que emiten en el dominio de VHE. La absorción de fotones de VHE debido al EBL es producida mediante la producción de pares. Estos electrones y positrones son relativistas y pueden interaccionar mediante dispersión *inverse Compton* con los fotones del fondo cósmico de microondas, resultando en una emisión de fotones con energías de GeV. Tavecchio et al. (2010) han encontrado que el espectro y el nivel de flujo de la emisión reprocesada depende fuertemente de la intensidad del campo magnético intergaláctico, que puede desviar los pares, y por tanto diluir la emisión. También derivan una relación para el espectro reprocesado esperado de una fuente estable, como es el caso de 1ES 1218+304, a partir de la cual la intensidad del campo magnético intergaláctico podría ser calculado a partir de la combinación de datos contemporáneos de Fermi y MAGIC.

---

# A

---

## Appendix

The aim of this appendix is to give a detailed review, from the analyzer's point-of-view, of how to run the different programs in the MARS framework for the analysis of wobble stereo data. Even if I start to explain the calibration and the image cleaning, these steps are usually performed by the Onsite Analysis at La Palma. The analyzer can then start with the data quality selection. Nevertheless, for some especial cases, the image cleaning should be performed directly by the analyzer.

You need to install in your pc ROOT<sup>1</sup> and MARS<sup>2</sup>, which require two enviromental variables to be set: *ROOTSYS* and *MARSSYS*, containing the paths to both packages, respectively, in the shell configuration file as follow:

```
setenv ROOTSYS "your_ROOT_path";
setenv LD_LIBRARY_PATH "$ROOTSYS/lib";
setenv DYLD_LIBRARY_PATH "$ROOTSYS/lib";
setenv PATH "$ROOTSYS/bin:$PATH";

setenv MARSSYS "your_MARS_path";
setenv LD_LIBRARY_PATH "${MARSSYS}: ${LD_LIBRARY_PATH}";
setenv DYLD_LIBRARY_PATH "${MARSSYS}: ${DYLD_LIBRARY_PATH}";
setenv PATH "${MARSSYS}: ${PATH}";
```

This configuration works only for *cshrc* shells, if you want to use a *bash* shell, the command *setenv* should be replaced by the command *export*.

### A.1 Searching the data

The data can be searched from the following website: <http://magic.pic.es/priv/database>. Different options are available for the search, such as the source name, the observation date,

---

<sup>1</sup>A ROOT version can be downloaded from: <http://root.cern.ch/drupal> data analysis framework, version 5.26.00, for the latest MARS versions ROOT 5.26 has to be used.

<sup>2</sup>You can get a MARS version from: <http://magic.pic.es/priv/cvs>, usually you should use the lastest version available.

observation mode, the zenith distance, etc. Once you have found the data you are interested in, you can retrieve them from the data center at PIC<sup>3</sup> via a web site<sup>4</sup> (typically a *wget* command is used) or from the GRID<sup>5</sup>. They can be downloaded at different stages of the analysis, from calibrated files to the output of *melibea*. Typically, the standard analysis starts with *star* files, but I will explain how to run the analysis starting from calibrated files.

We need not only the data from the source which we want to analyze, but also an Off data sample and Monte Carlo simulations. In order to select a proper Off data set and MC data, we have to make sure that these cover a similar zenith angle range as the source data. The Off data can be downloaded from the same site as the source data. As these Off data will not be used to subtract the background from the source data, they can be dedicated Off data or data which have been already analyzed and no signal was found, no matter if they were observed in wobble or On/Off mode. Regarding the MC files, can be downloaded from: [http://magic.pic.es/priv/wiki/index.php/MC\\_production](http://magic.pic.es/priv/wiki/index.php/MC_production), where you have to check the kind of observation (On/Off or wobble), the trigger configuration and the zenith angle. Also there, you can find a MC production of simulated  $\gamma$ -rays from random directions (the so-called *diffuse MC*), which is used for the analysis of the off-axis sources and for extended sources.

Files are named with two characteristic numbers, the run and the subrun number. The number of runs is always the same for both telescopes, and typically a run starts with each new wobble position. In case of subrun numbers, these are not always the same for both telescopes, since M2 usually saves more information (due to the larger number of pixels in the camera, for instance) such that the number of subruns is larger for M2 data files.

As first quality check, it is a good practice to check the electronic runbooks of the observation. You can find them at <http://magic.pic.es/priv/data/CCdata> where you have to select the observation day. The runbooks are the files with the extension *.rbk*.

## A.2 Star

As explained in Sec. 5.4, the image cleaning and parameterization of single telescope images are performed by the program *star*. The standard *star* files (the output of *star*) can be downloaded from PIC, or you can run *star* by yourself. For standard analyses, the files available at PIC are adequate, but in case you want to run a special analysis for observations under moon light conditions, which require higher image cleaning levels, or if you want to try a different image cleaning algorithm, the *star* program has to be run by hand. As input, calibrated files are needed, denoted as *\*M1\*\_Y\_\** and *\*M2\*\_Y\_\**. The calibration is automatically performed at La Palma.

---

<sup>3</sup>Port d'informació científica, located in Barcelona.

<sup>4</sup><http://magic.pic.es/priv/data/Query> where you will find different versions of the calibrated data. As a general rule, you should take the lastest version available for each M1 or M2 data set. Information about the recommended version can be found at: [http://magic.pic.es/priv/wiki/index.php/Data\\_Center:Storage:Recommended\\_Versions](http://magic.pic.es/priv/wiki/index.php/Data_Center:Storage:Recommended_Versions)

<sup>5</sup>A PIC data center account and a GRID certificate is needed, you can find information about how to get it on [http://magic.pic.es/priv/wiki/index.php/PIC\\_Account](http://magic.pic.es/priv/wiki/index.php/PIC_Account) and [http://magic.pic.es/priv/wiki/index.php/Data\\_Center:Authentication:Obtaining\\_a\\_Grid\\_certificate](http://magic.pic.es/priv/wiki/index.php/Data_Center:Authentication:Obtaining_a_Grid_certificate)

*star* has to be run independently for both telescopes data. You can get information on how to run *star* using the command line:

```
$MARSSYS/star -h
```

Typically, *star* is run as:

```
$ENV{MARSSYS}/star -b -v5 --ind=*_M1_*root --out=./ \
--config=config_star.rc --log=outfile.log
```

In case of MC files, we have to add the option *-mc* to the command line. Since it will take some time, it is useful to run it in the background, using the shell command *nohup*.

In the previous command line, the following parameters have been used:

- **--ind=** are the calibrated input files for each telescope (of the type *\*M1\*\_Y\_\** or *\*M2\*\_Y\_\**).
- **--out=** is the output directory for the star files.
- **--config=** is the configuration file.
- **--log=** is the logfile where all the logging information is saved.

The configuration files are different for M1 and M2 data, default files are:

*\$MARSSYS/mrcfiles/star\_M1.rc* for M1, and *\$MARSSYS/mrcfiles/star\_M2.rc* for M2. In case you want to run the *sum cleaning* analysis the configuration files for both telescopes are *\$MARSSYS/mrcfiles/star\_sum.rc* and *\$MARSSYS/mrcfiles/star\_M2\_sum.rc*, respectively. In case of moon data, the image cleaning levels in the configuration files have to be changed.

The M1 and M2 configuration files mainly differ in the cleaning thresholds, the bad pixels settings and the cross-talk correction, which has to be applied for M2 data, due to interferences between different channels of the Domino readout chip. The program *star* has to be run for the source data, the Off data and the MC files. The configuration files are the same for all data sets, except for the M2 MC files, where we should deactivate the option for the cross talk correction and upscale the size by 10%. I will go through the configuration lines which may be changed in certain cases in the configuration files.

If there is a bright star in the FoV which can affect the cleaning, it can be excluded using the following options:

```
MJStar.ExcludeStar: yes
MJStar.MStarPosCalc.SourceRaDec: 5.627416 21.1425
MJStar.MStarPixels.StarRadius: 60
```

where the coordinates of the star and an approximation of the star radius measured in millimeter have to be set.

The standard cleaning levels for MAGIC-I data are:

```
MJStar.MImgCleanStd.CleanLevel1: 6
MJStar.MImgCleanStd.CleanLevel1: 3
```

and for MAGIC-II data:

```
MJStar.MImgCleanStd.CleanLevel1: 9
MJStar.MImgCleanStd.CleanLevel1: 4.5
```

In case of moon data, higher levels are needed. Usually, a good cleaning level is defined, if the remaining number of islands, due to noise is lower than 10%. You will find this value at the end of the *star* logfile.

Sometimes, the Starguider report is not found, or there are problems in the report, so that you will obtain an error “the calibration of the starguider is not possible”. In such a case, you can skip the starguider calibration by disabling the option in the configuration file:

```
MJStar.CalibStarguider: no
MJStar.UseStarguider: no
```

For M2 data, more settings may be modified, such as activating the cross-talk removal from the *Domino* readout chips:

```
MJStar.RemoveCrosstalk: yes
MJStar.PixelMappingFile: pixel_full_07032010.txt
MJStar.CrosstalkCoefficientsFile: xtalk_DRS_allchannels_07032010.txt
```

In case of MAGIC-II Monte Carlo data, the above lines should be commented out, however we need to add the following, in order to upscale the MC by a 10% due to a mismatch between the MC and the data:

```
MJStar.MSignalScale.ScaleFactor: 1.10
MJStar.UseScaling: yes
```

All data used for the data reduction, this is to say the source data, the Off data and the MC, have to be cleaned with the same cleaning levels, otherwise a later classification of the events will not be correct.

If we are analyzing data from different days, *star* should be run day-by-day independently. In case there is a big time gap in the data sample, the process will stop and we have to run it in different sub-samples.

After running *star*, the output files will be called *\*M1\*\_L\_\** (*\*M2\*\_L\_\**). An additional output file called *star.root* (see Sec. A.4) is created which can be viewed to check the quality of the data. In case you downloaded the files from PIC, you will find a *star.root* file per run number. This file can be viewed with the *showplot* command:

```
showplot star.root
```

### A.3 Checking the data

The information contained in the root files are stored in a tree structure. It is useful to check some data characteristics with ROOT. Let's see how to surf into the data.

The information can be checked in the individual files using a browser which is a friendly interface, typing in the terminal:

---

```
root
root [0] new TBrowser
```

Usually, we need to check the characteristics of a sample of files. Let's check, for example, the zenith angle of a given sample of data:

```
root
root [0] TChain *d= new TChain("Events")
```

(we select one of the trees called “Events” where all the information about the events is saved: size, width, pointing, etc.)

```
root [1] d.Add(2*M1*I_*root)
```

(we add the data)

```
root [2] d.Draw("MPointingPos.fZd")
```

(we draw the zenith angle covered by the data sample).

## A.4 Quality selection

It is convenient to do the quality selection at the *star* files level before running *superstar*, because there, files from all the subruns will be merged in a unique file. Otherwise, if you want to reject just a part of these subruns, due to some technical problem or bad weather, you would be forced to delete the entire run and not only the affected subruns. I will comment on what is important to check in order to select the good quality data. First, we should check the output logfile from *star*. If the process has finished properly, we should get something like “*3.2% of the images contain spurious islands only due noise*” at the end, the number of islands due to noise should be as low as possible, typically the limit is about 5-10 %. This number gives an estimation of the number of additional spurious islands in the image, only created by the upward fluctuation of noise from two neighbouring pixels. Images containing additional islands due to noise are usually useless. If this number exceeds the limits, then we should re-run *star* using higher cleaning levels. This is very frequent in case the data was taken during twilight or moon light.

Then, we can check some parameters from the output file *star.root*. There, you can see different tabs, containing plots which give information, not only about the data, but also about the subsystems. I will go through the more important ones, but there is a lot of additional information which is interesting to check.

In the first tab (Fig. A.1), we find the starguider information where we can check the zenith and azimuth angle coverage by the data sample. There are two important plots at the bottom: the number of recognized stars by the starguider in the FoV and the brightness of the sky. The blue line and arrow give us an idea of typical values in both cases.

In the second tab we find information about the discriminator thresholds (DTs) from the *level-0 trigger*, which depend on the light conditions and the FoV (if a bright star is

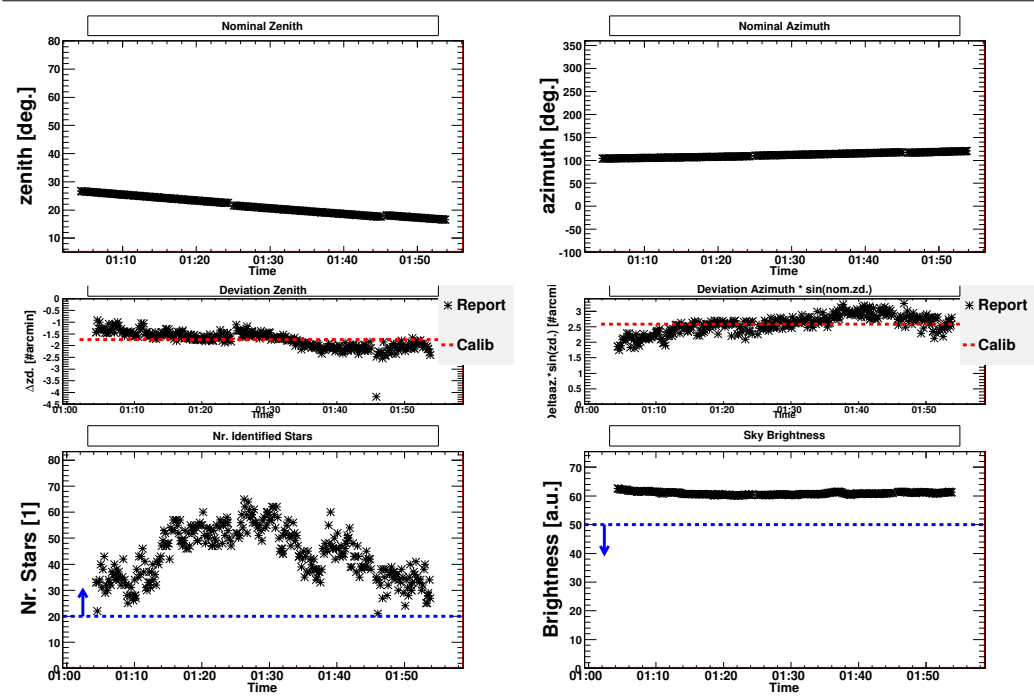


Figure A.1: The starguider information. See text for more information

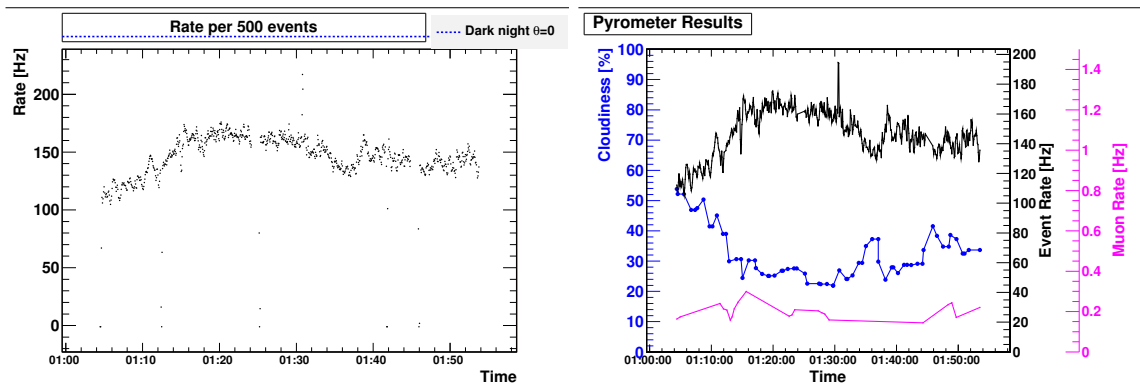


Figure A.2: Left: Events rate as a function of the time. Right: Different rates as function of the time. In blue, the cloudiness evolution is represented, in pink the muon rate and the black line represents the event rate.

found in the trigger region, the DTs will be higher in the case for data taken under moon light conditions).

Then, we can go to the *RateVsTime* tab (Fig. A.2, left), where we find the plot of the event rate vs. time. The rate should be constant around 200 Hz. It can be lower in case of twilight or moon data, but this is still acceptable if it remains constant. If this is not the case, it can be due to bad weather. For this reason, we should check the Pyrometer tab, here we can find the cloudiness plot vs. time (Fig. A.2, right). Usually, if there is a correlation in time between a higher cloudiness with a decrease of the event rate and the number of identified stars by the starguider, this means that the observation was probably disturbed by clouds. The cloudiness parameter is composed of the sky temperature measured by a commercial pyrometer, and the zenith angle of observation. It is not working at 100%, since there are particular cases in which the cloudiness parameter values are high without the presence of clouds in the FoV. In order to be sure, a typical anti-correlation between cloudiness, events rate and number of identified stars by the starguider is expected, as can be checked in Fig. A.1 and Fig. A.2.

In case that only part of the data are affected by clouds, we can exclude the data directly, or we can apply a cut in cloudiness later in the analysis.

We should also check the CoG (Center of Gravity) plot, distribution of the centers of the image ellipses in the camera. It should be more homogeneous in case of mono observations, compared to stereoscopic observations. Since the L3 trigger only accepts showers triggered by both telescopes, it will produce an inhomogeneity in azimuth, the so-called “L3-Blob”.

Also the image reconstruction efficiency of the showers should be checked, which is typically higher than 80%.

All this information should be checked for the source data, and for the Off data sample.

## A.5 Superstar

After running star, we get two sets of files one per telescope, which contain two different views of the same cleaned showers. The aim of *superstar* is to combine the information coming from both telescopes and reconstruct the stereoscopic parameters, which will be refined in a further analysis step. From this step onwards, instead to have one file per telescope, they will be combined into a single one containing the tag `*_S_*`. The parameters are renamed using underscores and the telescope number (e.g. `MHillas_1.fSize`, `MHillas_2.fSize`). *superstar* can be run using the following command line:

```
$ENV{MARSSYS}/superstar -b -q -f --config=config_superstar.rc \
--ind1=*_M1_*_I_*root --ind2=*_M2_*_I_*root --out=./ --log=outfile.log
```

where:

- `--config`= is the configuration file to be found at `$MARSSYS/mrcfiles/superstar.rc`.
- `--ind1`= are the M1 star files (`*M1*_I_*root`).
- `--ind2`= are the M2 star files (`*M2*_I_*root`).

This analysis step has to be run for all data sets (source data, MC files and Off data). In case of MC files, we have to add the option `-mc` to the command line.

## A.6 MC selection

Since the spectrum calculation depends on the effective collection area, which in turn depends on the zenith and azimuth angles, the MC should be selected such that it covers the same angle ranges as the source data. This can be done using the program `selectmc`.

In case of off-axis sources which are not at a standard wobble distance of 0.4 degrees from the camera center, or centered on the camera, we should select the corresponding position in the camera using the program `selectmcrho` for diffuse MC. This is because the sensitivity of the camera drops as a function of the distance to the camera center (see Fig. A.3). Also the program `selectmc` can be used setting by hand the distance to the camera center.

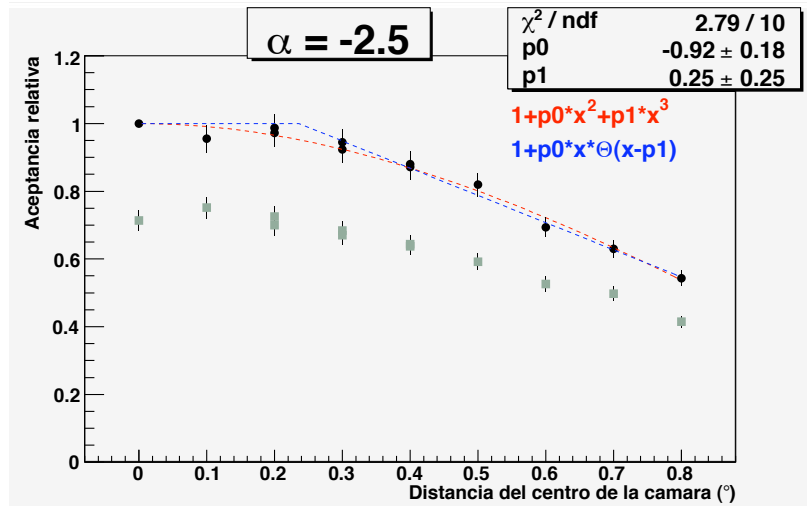


Figure A.3: Normalized camera sensitivity of MAGIC-I as function of distance to the camera center for a source with spectral slope -2.5, figure adopted from Becerra-González (2008).

The amount of needed MC events is huge, since most of them will be rejected by our selection criteria. Usually open cuts are needed due to the lack of statistics, instead of selecting the exact ranges, we should allow a generous range around the proper values. A tip for low statistics cases can be to use the proper data for the flux estimation and the rejected MC just for training. In principle, there should not be big difference in the training, but the proper effective area is much more important than an accurate training.

A typical command line looks like this:

```
$ENV{MARSSYS}/selectmc -selectmc -writerejected --pathData=<indir> \
--pathMC=<indir> --out=<outdir> --outname=<outname.root> --log=logfile.txt
```

where:

- **--writerejected** means the rejected events will be saved as well, if you don't plan to use them, it is better not to save them, since they take quite some disk space.
- **--pathData=** are the superstar source data files `*_S_*root`.
- **--pathMC=** are the superstar MC files.

As output, we will get a unique file which will contain all the events which satisfy the conditions.

The default binning of the histograms is 10 bins in Zenith (from  $\cos(\theta) = 0$  to  $\cos(\theta) = 1$ ), 12 bins in Azimuth (from 0 to  $2\pi$ ) and 12 bins in the angle of the source position around the camera center (from  $-\pi$  to  $+\pi$ ). If your statistics is not sufficient, you can change the number of histograms such that more events will be accepted by choosing less bins. This is achieved by using the following options in the command line:

- **--nbinsTh=** number of bins for the Zenith distribution.
- **--nbinsAz=** number of bins for the Azimuth distribution.
- **--nbinsPsi=** number of bins for the Psi distribution.

In case of *selectmcrho*, it is basically the same as *selectmc*, but you can select the source position in the camera for diffuse MC automatically. Of course, in that case you have to add the number of bins in  $\rho$  (distance to the camera center) or using in *selectmc* the parameters *rmin* and *rmax*.

As a result, you will get a MC belt centered on the source position. It is very important to check the number of selected MC events: if it is lower than 20.000 – 30.000 events, you should still open the cuts a bit more (i.e. decrease the number of bins).

## A.7 Calculation of the DISP parameter

The MC sample should be divided into two groups: one for training and a second one for testing purposes.

We will estimate the DISP parameter using the program *coach* as described in the next section, or the macro *train\_stereoDisp1.C* for M1 and *train\_stereoDisp2.C* for M2, which can be found in `$MARSSYS/mtemp/mmpi/macros/magic2`, where we only have to change the `*namemc` value, which is the training superstar MC sample. They are C++ macros which should be run<sup>6</sup> in ROOT. As output, we will get a matrix called *DispRF.root*<sup>7</sup> and a file called *DispRF\_gini.gif* which contains the so-called Gini-index plot (see Fig. A.4). There you can see the relative importance of the different used parameters for gamma/hadron separation.

---

<sup>6</sup>To run a C++ macro in ROOT, type in a ROOT console: `.x your_macro.C` or `root -q your_macro.C` from the terminal.

<sup>7</sup>Usually it is good practice to run the macros in different folders since the output will be saved with the same name as default.

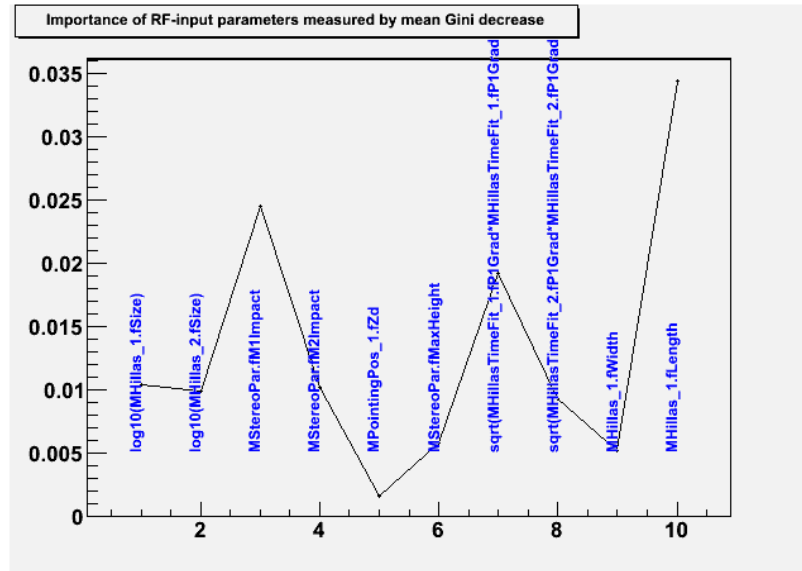


Figure A.4: Gini index of each parameter used in the DISP calculation.

## A.8 Random Forest

In case of an On/Off analysis you should divide the Off data sample in two different subsamples, like in the case of MC. In case of wobble data, you can use all the Off data sample for training, since these data will be used only for the gamma-hadron separation, but not for the background estimation. Since the images are the projections of the showers onto the camera plane, they depend on the zenith angle of the observation. Thus, it is very important to select the proper zenith angle in order to get the best gamma-hadron separation. From zenith angles 0 to 35 degrees, the showers look rather similar, but when we move to higher zenith angles, their appearance starts to change fast, so that we should divided the sample in smaller zenith angle ranges. You have to take care that the MC sample and the Off data sample cover the same zenith angle range and are similar to the source data, otherwise the separation will not be optimal and the macro will not warn you.

The Random Forest method has been adapted for MAGIC analyses. There are two different approaches in order run the Random Forest algorithm, using a macro or the MARS program *coach*<sup>8</sup>.

The macro can be found at  
`$MARSSYS/mtemp/mmpl/macros/magic2/mytrain.C`,  
where `*namemc` is the training MC sample in superstar format and `*namedata` is the Off data sample at superstar level. It is a *C++* macro that should be run in ROOT. As output, it will create a matrix called `RF.root` which contains the classification information. Also we will get a file called `gini.gif` which contains the so-called gini index plot. Typically, we get a peak at the `MaxHeight` parameter which means that this is the most important separation

<sup>8</sup>Compressed Osteria Alias Computation of the Hadronness parameter.

parameter between hadron and gamma-like showers.

The program *coach* can be run as follows:

```
$ENV{MARSSYS}/coach --config=coach.rc -RFgh -RFdisp
```

where:

- **--config**= is the configuration file.
- **-RFgh** is used for the gamma/hadron like separation.
- **-RFdisp** is used for the stereo DISP estimation

As output, we will get the file RF.root and the files DispRF.root for each telescope.

Concerning the configuration file, one needs to change only few files:

```
#Files path
RF.mcdata: ../GA*_S*.root (superstar MC files )
RF.data:   ../20*_S_*.root (superstar files for the Off data sample)
```

Selection of the zenith angle distribution:

```
RF.zdmin: 5.
RF.zdmax: 50.
```

The program *coach* apply a re-zenithing to the MC data and therefore, no splittings of the data depending on the zenith angle have to be done since the zenith angle is already included in the Random Forest procedure.

## A.9 Look-up tables

The standard tables can be found at `$MARSSYS/mtemp/mmpi/macros/magic2`, called `Energy_Table_M1.root` and `Energy_Table_M2.root`. They are the standard ones if you using the standard cleaning and standard cleaning levels. Otherwise, you should built your own energy tables. For this purpose you have to use the *C++* macro found at: `$MARSSYS/mtemp/mmpi/macros/magic2/create_Energy_table.C`, where *inputData* is the path to the training MC sample in *superstar* format. As output, you will get both energy tables for M1 and M2, respectively.

## A.10 Melibea

The program *melibea* has to be run for the source data and the MC test data. In this MARS routine, mainly three tasks are performed: the application of the gamma-hadron separation result from Random Forest, the calculation of the stereo DISP parameter and the energy reconstruction. In *melibea* all the stereo parameters are re-calculated and refined. These final results can be found in the tree `MStereoParDisp`.

As discussed in Chapter 5, *melibea* can be run using different methods connected to the ghost busting problem. As default, we will use the *Turbo buster* solution which until now gives the best results.

---

```
$ENV{MARSSYS}/melibea -b -q -f --ind=*_S_*root --out=./ \
--config=config_melibea.rc --stereo --rf --rftree=RF.root \
--calc-disp-rf --rfdisptree=DispRF.root --calc-disp2-rf \
--rfdisp2tree=DispRF.root --calcstereodisp --disp-rf-sstrained \
--outname=melibea.root
```

Where:

- **--ind**=is superstar files path (\*\_S\_\*).
- **--out**= is output directory for melibea files.
- **--config**= is configuration file.
- **--rftree**= is the Random Forest (RF) matrix for the gamma-hadron separation, typically called RF.root.
- **--rfdisptree**= is the DispRF.root file for M1.
- **--rfdisp2tree**= is the DispRF.root file for M2.

If you want to run *melibea* for MC files, you should use the option **-mc**.

The configuration file can be found at *\$MARSSYS/mrcfiles/melibea\_stereo.rc*, I will go through the main options which can be modified by the analyzer. If you want to use other than the default coordinates, this is the best place to do this. Of course, if you want to run the analysis for different source positions, you should run *melibea* once per pointing. This is only needed if you want to derive a flux or spectrum calculation, otherwise only for a signal search this is not necessary, since these coordinates can be set later.

```
MJMelibea.DefaultSourceRaDec: no
MJMelibea.SourceRaDec: 5.5755555555 22.014444444 (object coordinates)
```

There is a cloudiness cut which is set to 60 by default. The limit should be changed taking into account your preferred own data and your cloudiness values:

```
MJMelibea.MaxCloudiness: 60
```

The *Turbo buster* method is active by default, you can comment the following two lines in order not to use the method:

```
MJMelibea.StereoDispCalc.TurboBuster yes
MJMelibea.StereoDispCalc.MaxDispDiff2 0.05
```

For the energy estimation, the following lines should be active:

```
MJMelibea.StereoDispCalc.LUTableEnergyEstimate yes
MJMelibea.StereoDispCalc.ETab1 path/Energy_Table_M1.root
(path of the M1 Look-up table)
MJMelibea.StereoDispCalc.ETab2 path/Energy_Table_M2.root
(path of the M2 Look-up table)
```

As ouput, we will get the files tagged \*\_Q\_\*root and a file which contains information about hadronness and the hadronness cut efficiency, called *melibea.root*. The contained plots in this file can be viewed by the usual *showplot* command.

## A.11 Signal search

As has been presented in Sec. 5.11, there are mainly three powerful parameters to find a gamma-ray signal. The Alpha ( $\alpha$ ) distribution can be easily plotted using ROOT since this parameter has been already calculated in *star*. However, it cannot be used in case of mono data analysis. In case of  $\theta^2$  ( $\theta^2$ ) parameter, it has to be calculated using the different parameters previously estimated. This is performed by the program *odie*<sup>9</sup>.

The skymaps can be produced by two different routines, *caspar*<sup>10</sup> and the program *zinc*. These two tasks allow to produce skymaps for mono or stereoscopic data. There is a third option, called *celestina*<sup>11</sup> which can only produce skymaps for mono data, we will not talk about this program since by now the standard data is stereo, but you can find information at [http://magic.pic.es/priv/wiki/index.php/MAGIC\\_software:Celestina](http://magic.pic.es/priv/wiki/index.php/MAGIC_software:Celestina). Nevertheless, *celestina* is the only task in MARS which is able to perform skymaps for On/Off observations, while *caspar* and *zinc* can only work with wobble data, up to now.

From now on, unlike the previous steps (e.g. *star* or *melibea*) the data path and all the instructions are not given in the command line, but in the configuration file. All of these routines run over the source *melibea* files (MC and Off data will not be used for the signal search).

### A.11.1 Odie

Typically *odie* is run using the following command line:

```
$ENV{MARSSYS}/odie -b --config=odie.rc --log=odie.log
```

Let's see the configuration file (*\$MARSSYS/mrcfiles/odie.rc*) where all the paths and options are set:

*Odie.dataName: path/2\*\_Q\_\**, *melibea* source data path, for some of the options, it may be important to keep it in this format and not to finish with \*root.

Regarding the cuts, there are two options: we can use the standard cuts (which have been established from the concensus of different studies<sup>12</sup>) or we can directly set the desired cuts by hand. Any custom cuts should be optimized a priori using another data set, usually this is done using a Crab Nebula data sample observed at dates close to our source observation, following two objectives: to check the telescope performance using the best known  $\gamma$ -ray source in the sky and to optimize the cuts, such that our analysis is not affected by different trials.

Coming back to the configuration file, if you want to select the standard cuts you can choose three energy ranges:

*Low energy:*

<sup>9</sup>Odie is a fictional character in the Jim Davis comic strip Garfield.

<sup>10</sup>Caspar is the name of a German painter.

<sup>11</sup>The name is coming from a famous spanish novel, as well as *melibea*.

<sup>12</sup>More information can be found at:

[http://magic.pic.es/priv/wiki/index.php/MAGIC\\_software:Tasks:Collect\\_Cuts\\_used\\_by\\_people](http://magic.pic.es/priv/wiki/index.php/MAGIC_software:Tasks:Collect_Cuts_used_by_people).

---

```
Hadronness.fHadronness<0.28 && MHillas_1.fSize>55 \
&& MHillas_2.fSize>55
```

*Full energy range:*

```
Hadronness.fHadronness<0.16 && MHillas_1.fSize>125 && MHillas_2.fSize>125 \
&& MStereoParDisp.fEnergy>250
```

*High energy:*

```
Hadronness.fHadronness<0.17 && MHillas_1.fSize>300 && MHillas_2.fSize>300\
&& MStereoParDisp.fEnergy>1000
```

You should set the following line in the *odie* configuration file:

```
Odie.cuts: STANDARD
```

Afterwards, select the energy range, for which the set of cuts has been optimized: uncomment the lines which take care of the energy range and comment the rest. For example, if we want to run the analysis for *Low energy* range, it would look as follows:

```
# For low energy (LE) analysis
# Sensitivity ~ 3.0\% Crab
Odie.analysisEpoch: Jun10
Odie.eRange: LE
Odie.signalCut: 0.026
Odie.psf40: 0.10

# For full range (FR) analysis
# Sensitivity ~ 0.8\% Crab
#Odie.analysisEpoch: Jun10
#Odie.eRange: FR
#Odie.signalCut: 0.01
#Odie.psf40: 0.063

# For high energy (HE) analysis
# Sensitivity ~ 1.1\% Crab
# The signal cut is likely to be enlarged, see program output for recommendation
#Odie.analysisEpoch: Jun10
#Odie.eRange: HE
#Odie.signalCut: 0.01
#Odie.psf40: 0.053
```

As you can see, there are different options for each energy range: `Odie.analysisEpoch:` is the epoch of the defined set of cuts. Until now, only two definitions of standards cuts have been established. You should use the latter *Jun10*.

`Odie.eRange`: is the selected energy range, which can be LE (Low Energy), FR (Full Range) or HE (High Energy).

`Odie.signalCut`: is the value of the  $\theta^2$  value which optimizes the signal region. This value typically is close to zero and, depending on the energy range, its distribution can be narrower or broader. As you can see in the proposed values, for high energies this parameter is smaller which means the angular resolution is better, than for lower energies. Once you run the program, it will advise you on that number and you can re-consider it if your estimation is far from the appropriate one.

`Odie.psf40`: is the Point Spread Function (PSF). It follows the same behavior as the previous parameters: for higher energies, the PSF is smaller than for lower ones. The values shown here are the standards ones for different energy ranges.

Otherwise, custom cuts can be set by commenting out all the previous lines and setting, for example, the following line:

```
Odie.cuts: MHillas_1.fSize>100 && MHillas_2.fSize>100 \
&& MHadronness.fHadronness<0.1 && MStereoParDisp.fEnergy>150
```

A zenith angle cut can be performed by using:

```
Odie.minZenith: 0.
Odie.maxZenith: 35.
```

If no minimum and/or maximum zenith values are set, all the events will be used. The output name of the file where the  $\theta^2$  plots will be saved, can be set as:

```
Odie.outFileName: Output_odie.root
```

You should select if the data are stereoscopic data (TRUE) or mono data (FALSE)

```
Odie.stereo: TRUE
```

As discussed in Chapter. 5, we can decide to use the DISP parameter or not, and depending on this option, the output of some estimated parameters as the position and the estimated energy, will be saved in different containers in melibea files. If we use the DISP parameter, we should use the following lines (otherwise you should just keep commented the following two lines):

```
Odie.posContainer: MStereoParDisp
Odie.eContainer: MStereoParDisp
```

If you want to use different coordinates from the default ones, you should set them as follows:

```
Odie.sourceRa: 6.2786
Odie.sourceDec: 22.53
```

The Off events are taken from a camera region, where no source is expected. If you select one Off position, it will take as Off these events in the camera at  $180^\circ$  from the source position, called anti-source position. This anti-source off position is the most trustable estimation of the background since the wobble position is change every 20 minutes between these two positions. In case you select 3 Off regions, these will be at  $90^\circ$ ,  $180^\circ$  and  $270^\circ$ , etc. If the camera was perfectly homogenous we could select as many Off regions as we can to improve the statistics, until part of the signal from the source starts to leak into the Off regions. However, problems appear due to the inhomogeneity of the camera. A good practice is to test different Off numbers and check the plots (see Fig. A.5). If the background events is compatible within a statistical uncertainty lower than  $1\sigma$ , we can use several Off positions, otherwise as default only one Off region should be used. The number of Off regions can be set as follows:

```
Odie.nWobbleOff: 1
```

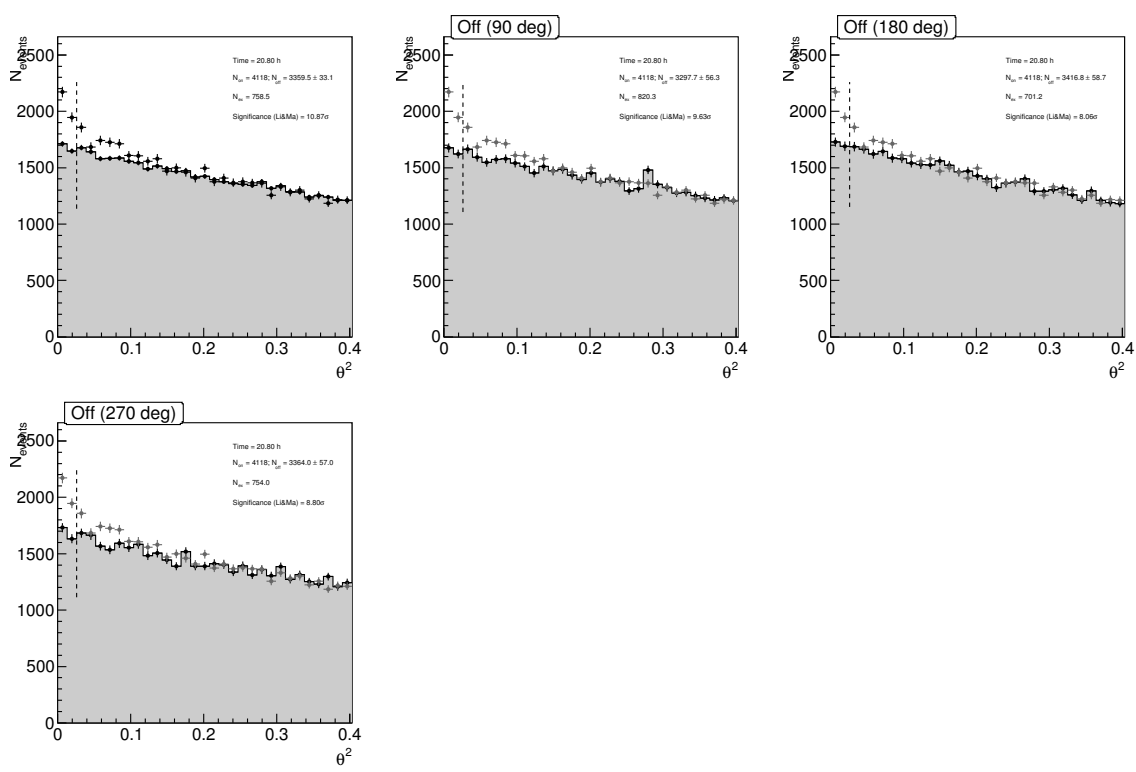


Figure A.5:  $\theta^2$  plot from 1ES 1215+303, using 3 Off regions. The first plot shows the combined  $\theta^2$  distribution, while in the rest only Off events from a given position are used ( $90^\circ$ ,  $180^\circ$  and  $270^\circ$ , respectively).

A useful option allows to reject one of the Off regions in case there is a hole in the signal region or maybe a contamination from another source in the FoV. We can decide not to

use this position in the background estimation (i.e. in the case of 3 Off regions, 1 = 90°, 2 = 180° and 3 = 270°).

```
Odie.nWobbleSkip: 2
```

Nevertheless, there are cases in which the On and Off distributions do not match properly. This can be due to camera inhomogeneity problems or in case of off-axis sources which are far from the camera center where the sensitivity can be lower and we are taking Off positions from more or less sensitive parts of the camera positions. We can solve this problem by forcing the program to select those Off events from the same camera position as the On events, the so-called Wobble Partner method<sup>13</sup> (in that case we should select only one Off position):

```
Odie.OffFromWobblePartner: TRUE
Odie.WobblePair0: 0.4, 0, 0.4, 180 (or other wobble partners)
Odie.ReWeightWobble: TRUE
```

Outside of the defined signal region, the number of On and Off events are normalized since they are expected to be similar. You can skip the normalization setting this option to FALSE. This normalization factor is only useful for strong sources, otherwise the normalization factor can be wrong due to the lack of statistics.

```
Odie.normAbove: 0.15 (theta^2 from where the On and Off will be normalized)
Odie.skipNormalization: TRUE
```

In order to change the range of the plot you can use:

```
Odie.rangeTh2: 0.4 (in theta^2 units)
```

These are the main options of the program, but you can get more information at [http://magic.pic.es/priv/wiki/index.php/MAGIC\\_software:Odie](http://magic.pic.es/priv/wiki/index.php/MAGIC_software:Odie)

Once you have generated your  $\theta^2$  plots, *odie* offers the possibility to combine them. It is a good option when you have different data samples which you do not want to mix a priori because you want to use different cuts, for example. You can run it as follows:

```
$ENV{MARSSYS}/odie -s --config=odie_stack.rc --log=odie_stack.log
```

The new needed configuration file is *\$MARSSYS/mrcfiles/odie\_stack.rc* where you should define the files you want to combine. You can use any wildcard understandable by bash, e.g.:

```
Odie.dataName: path/Output_odie_zd[1-7].root
```

The PSF also should be set as:

```
Odie.psf40: 0.09
```

---

<sup>13</sup>More details can be found at [http://magic.pic.es/priv/wiki/index.php/MAGIC\\_software:Tasks:OFF\\_from\\_Wobble\\_Partner](http://magic.pic.es/priv/wiki/index.php/MAGIC_software:Tasks:OFF_from_Wobble_Partner)

The significance of the signal is calculated using the Li&Ma formula (Li and Ma, 1983) from the number of On and Off events in the signal region. As has been established in the astro-particle field, we can talk about a firm detection, when the signal is above a significance of  $5\sigma$ . Nevertheless, starting from  $\sim 3\sigma$ , it can be considered a hint of a signal.

### A.11.2 Caspar

The program *caspar*<sup>14</sup> produces a background model which will be compared later with the event distribution from the source data in sky coordinates. It follows a similar philosophy as *odie*, using the same *odie* standard cuts, and the names of the common variables are the same. One of the most important parameters to check is the PSF since the smearing of the histogram depends directly on it.

In the configuration file, we can choose how the background model is generated. A blind map can be generated if the background model is created without assuming a source position, otherwise the so-called wobble map can be produced if the source is assumed to be where expected. It can be chosen with the following option:

```
Caspar.wobbleMap: TRUE (or FALSE for blind map)
```

It is run using the following command line:

```
$ENV{MARSSYS}/caspar --config=caspar.rc --log=caspar.log
```

The most important output of *caspar* is the skymap (see Fig. 6.2, for an example) from where we can check if there is an extended source, or if there are more sources in the FoV, etc. Also as output we get the relative flux plot (Fig. A.6) and the test statistics distribution (Fig. A.7) which compares the null hypothesis distribution with the real events distribution and gives an estimation of the significance of the signal. As you can see in the Fig. A.7, the dashed red line represents the null hypothesis (i.e. the distribution follows the null hypothesis in case no signal is found, and only random fluctuations are present).

As in the case of *odie*, *caspar* can also stack different skymaps. You can run it using the option **-s** and the proper configuration file *\$MARSSYS/mrcfiles/caspar\_stack.rc*.

### A.11.3 Zinc

The program *zinc* provides skymaps as well. It is different to *caspar* w.r.t. the technical implementation, but the results are similar. Besides, *zinc* produce a  $\theta^2$  plot which allows us to check accordingly the significance distribution and a residual plot. *zinc* is run with the following command line:

```
$ENV{MARSSYS}/zinc --config=zinc.rc --log=zinc.log
```

---

<sup>14</sup>More details can be found at [http://magic.pic.es/priv/wiki/index.php/MAGIC\\_software:Caspar](http://magic.pic.es/priv/wiki/index.php/MAGIC_software:Caspar).

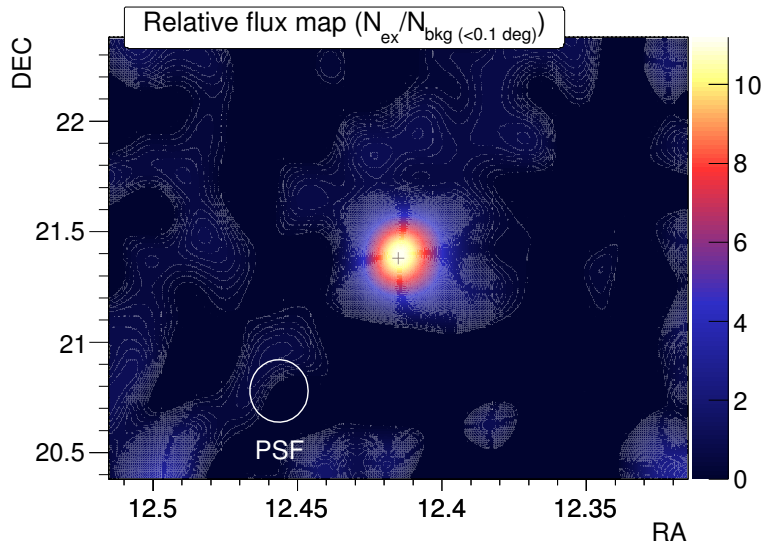


Figure A.6: Relative flux from PKS1222+21 during the flare on 17th of June 2010.

The most important options of the configuration file are:

We can select the source position in order to build the  $\theta^2$  plot. Otherwise, if we keep the coordinates at zero, the  $\theta^2$  plot will be produced at the point with the largest excess.

`Zinc.starRa: 0`

`Zinc.starDec: 0`

Select the FoV: It is defined in the declination axis in degrees.

You can set it to `$-1$` to get the maximum FoV, but it will be slow.

`Zinc.range: 2.8`

Define the PSF: If you keep the value in negative the default values will be used (0.1 deg for MI, 0.06 deg for stereo data)\\

`Zinc.psf: -1`

The data path points to the melibea source files:

`Zinc.dataName: path/2*_Q_*root`

In case of `zinc` there are no standard cuts pre-defined, they have to be set by the user:

`Zinc.cuts: MHadronness.fHadronness<0.2&&MHillas_1.fSize>100\\&&MHillas_2.fSize>100&&MStereoParDisp.fEnergy>200`

The output file name can be set as:

`Zinc.outFileName: zincOutput.root`

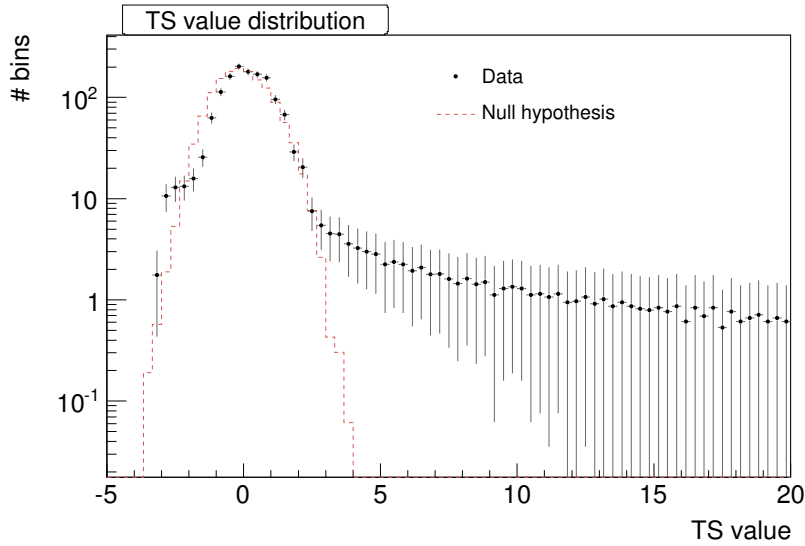


Figure A.7: Distribution of test statistics, compared with the null hypothesis (red dashed line) of PKS1222+21 on 17 of June 2010.

## A.12 Fluxlc

The program *fluxlc* is responsible for the calculation of the differential energy spectrum, the flux and light curve or flux upper limits in case no significant signal is found.

The typical command line looks as follows:

```
$ENV{MARSSYS}/fluxlc --config=fluxlc_stereo.rc --log=fluxlc.log
```

As in previous cases, everything is defined in the configuration file located at  
`$MARSSYS/mrcfiles/fluxlc_stereo.rc`

The main parameters are:

```
FluxLC.mcdata: path/G*Q*root (melibea test MC sample)
FluxLC.data: path/2*Q*root (melibea source data sample)
FluxLC.offdata: path/2*Q*root
(Melibea off data sample in case of On/Off observations,
for wobble data analysis it is not used)
```

```
Output file name:
FluxLC.outname: spectr_stereo_L3_Crab.root
```

```
Select if it is Stereo data (TRUE) or mono data (FALSE):
FluxLC.Stereo: TRUE
```

```
The number of bins for zenith angle distribution
(it is not important if you already selected the proper MC distributions)
```

```

FluxLC.zabins: 1

Zenith angle range:
FluxLC.za_edges: 0., 30.

Number of azimuth bins (not important if you already selected the
proper MC distributions):
FluxLC.finebinsphi: 1

```

The energy bins for the spectrum are selected in equal logarithmic bins. Typically, we use 28 bins but if the signal is strong enough, you can try to set smaller energy bins (larger number of bins), but be careful, since the statistical uncertainty of the spectral points depends on the uncertainty in the number of gamma-like excess events and the uncertainty of the effective area. The smaller the bins, the smaller becomes the statistics and the larger are the errors.

FluxLC.nBinsEnergyEst: 28

Select if the data have been taken in Wobble (TRUE) or in On/Off mode (FALSE)

FluxLC.WobbleData: TRUE

If it is wobble data, and the MC sample does not contain zbin0<sup>15</sup>, you can select to choose zbin1 to be copied to zbin0. Typically, we use TRUE, since there are no substantial differences between zbin0 and zbin1.

FluxLC.WobbleNoZbin0: TRUE

You can select to use (TRUE) or (FALSE) Off data. This will be the proper Off data for the case of On/Off data, or Off data taken from the Off positions in case of wobble data. As a standard, this option is set to TRUE.

```

FluxLC.UseOffData: TRUE
#Should the fit to the OFF data be used to determine the background?\\
FluxLC.UseFittedBackground: FALSE

```

Typically the *FittedBackground* option is set to FALSE, since the fit to the background is statistically not justified and produce high systematic uncertainty.

```

# Angular variable to be used in the extraction of the signal.
FluxLC.AngleType: Alpha
FluxLC.AngleType: Theta2

```

As default, this is *theta*<sup>2</sup>, since it is the standard for the stereo data analyses. In case of mono data, you can choose between alpha or theta2.

```

# Determine cuts (hadronness, alpha) from efficiency:
FluxLC.FindCutsFromEfficiency: FALSE

```

---

<sup>15</sup>Zbins are defined as  $1 / \cos(zd \cdot \pi / 180)$ .

The cuts can be optimized (TRUE), using the MC files. This optimization does not introduce trials in the analysis, since the source data are not used in the process. If you select the cut optimization, you should set the following lines:

```
# Efficiency of hadronnes and alpha (theta2) cuts:  
FluxLC.AlphaEffi: 0.7  
FluxLC.HadEffi: 0.6
```

which are the efficiency on the angular cut (theta2 or alpha), and the efficiency of the hadronness cut, respectively. Also the minimum values of the parameters should be set:

```
# Minimum allowed hadronness cut in case cuts are determined  
# from the gamma efficiency:  
(this minimum has priority over the efficiency constrain!)  
FluxLC.MinHadronness: 0.07  
# Minimum allowed Alpha and Theta2 cuts in case cuts are determined  
# from the gamma efficiency  
(this minimum values have priority over the efficiency constrain!):  
FluxLC.MinAlpha: 8.  
FluxLC.MinTheta2: 0.01
```

Only the previously selected angular parameter will be used.

Otherwise, you can set by hand a cut per energy bin (28 pairs of cuts, if you use the default settings, but you should change them according to the selected number of energy bins):

```
FluxLC.had: 0.9, 0.9, 0.9, 0.9, 0.9, 0.9, 0.7, 0.6, 0.5, 0.4, 0.3, 0.2, 0.2,  
0.2, 0.2, 0.2, 0.2, 0.2, 0.2, 0.3, 0.4, 0.5, 0.6, 0.6, 0.6, 0.6, 0.6  
FluxLC.alp: 0.1, 0.1, 0.1, 0.1, 0.1, 0.1, 0.05, 0.04, 0.03, 0.02, 0.02, 0.02,\  
0.02, 0.02, 0.02, 0.02, 0.02, 0.02, 0.02, 0.02, 0.02, 0.02, 0.02, 0.02, 0.02,\  
0.02, 0.02, 0.02
```

The two lines refer to the hadronness and angular cuts (theta or alpha), respectively. If you had previously selected the determination of the cuts from efficiency (TRUE), these values will be not taken into account.

```
# Tentative slope of the (assumed power-law) differential energy spectrum.  
FluxLC.SpectralSlope: -2.6
```

A kind of unfolding is performed on the LC values, and the value of the spectral slope is used in the process, so it is good to give a realistic value.

```
#Range for the spectrum fit  
FluxLC.fitRangeLow: 200.  
FluxLC.fitRangeUp: 2000.
```

The spectral points will be fitted by a simple power-law, and here you can select the fit range, which you should define a posteriori, once you have an estimate on where your good spectral points, those with small uncertainties are.

The normalization between On and Off can be done in general using the same value for all energy bins (TRUE) or differently for each energy bin (FALSE).

```
# Same normalization factor for all energy bins?
FluxLC.CommonNormFactor: TRUE
```

Another possibility for the normalization is to use only a geometrical normalization taking into account the number of selected Off regions (only for wobble data)

```
# For wobble data, apply just "geometrical" normalization
#(1/3 for instance, in case 3 OFF regions are used) in the Spectrum ?
FluxLC.WobGeomNorm: TRUE
```

Definition of the number of Off regions:

```
FluxLC.NumberOfWobbleOff: 1
```

If you run the analysis for a Crab Nebula data sample, you can calculate the sensitivity by setting the following line to TRUE.

```
FluxLC.SensitivityFromTheseCrabData: FALSE
```

Light curve settings:

```
#Select if the light curve is determined or not:
FluxLC.Lightcurve: TRUE
```

Select the energy ranges for the light curve estimation: as you can see in Fig. A.8, the effective area is constant at high energies, while for lower energies, it shows a steep slope, so that a small error in the effective area estimation can produce large errors in the flux calculation. For the light curve calculation, it is therefore better to use the safe part of the effective area, usually starting from 150-200 GeV.

```
FluxLC.LowELC: 200.
FluxLC.UpELC: 50000.
```

Selection of the normalization type for the light curve:

```
# For wobble data, apply just "geometrical" normalization
#(1/3 for instance, in case 3 OFF regions are used) in the Light curve ?
FluxLC.WobLCGeomNorm: TRUE
```

Define the time bins for the light curve, measured in minutes. If you want to estimate the total flux instead of a light curve, just set a big number of minutes or set 1440 minutes for night-by-night light curve:

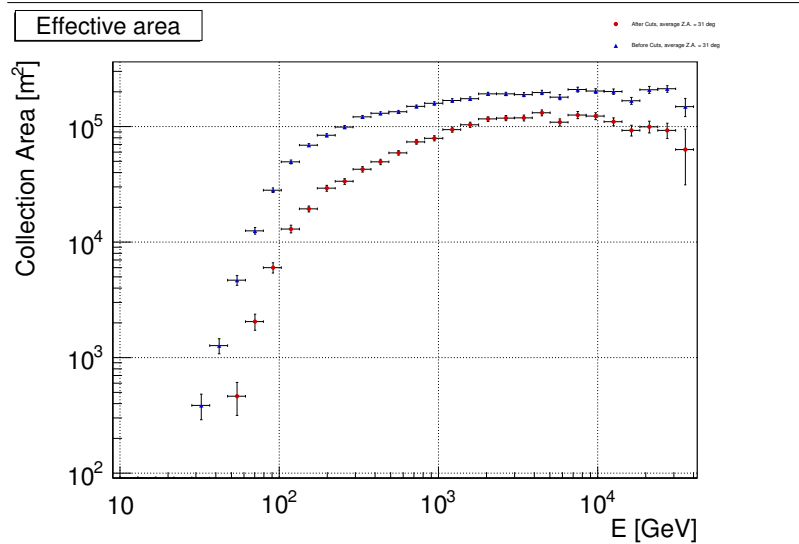


Figure A.8: Effective area, estimated from MC, before (blue) and after (red) the application of the cuts.

```
FluxLC.LCTimeScale: 10.
```

```
#Cuts used for the light curve (in degree or $degree^2$):
```

```
#FluxLC.AlphaCutForLC: 8.
```

```
FluxLC.Theta2CutForLC: 0.02
```

```
#You can select if you use the Off data (TRUE) or not (FALSE)
for the light curve calculation.
```

```
FluxLC.UseOffDataLC: TRUE
```

```
#Time format of the light curve; MJD (Modified Julian Days),
HMS (Hours Minutes Seconds) or dmy (day month year).
```

```
FluxLC.TimeFormat: HMS
```

*Fluxlc* also offers the possibility to calculate upper limits in case that no source is detected (see details on [http://magic.pic.es/priv/wiki/index.php/MAGIC\\_software:Fluxlc](http://magic.pic.es/priv/wiki/index.php/MAGIC_software:Fluxlc)).

```
#Select 95\% differential upper limit calculation (TRUE), otherwise FALSE:
FluxLC.DifferentialUpperLimit: TRUE
```

Select the energy range, in which the UL will be estimated. Since the UL calculation depends on the spectral characteristics of the assumed, but not detected, source, especially in an energy range where the collection area is not flat, the bins should be as small as possible, but retain enough statistics, e.g.:

```
FluxLC.DiffULMinEest: 200.
```

```
FluxLC.DiffULMaxEest: 500.
```

---

```
#The assumed power law will be used for the UL calculation so we should give
# a realistic value.
FluxLC.DiffULPowerIndex: 2.

#95\% Integral upper limit can be calculated setting to TRUE and giving the
#following spectral parameters:
FluxLC.IntegralUpperLimit: FALSE
FluxLC.IntULFunction: 6.e-10*pow(x/300.,-2.31-0.26*log10(x/300.))
FluxLC.IntULMinEst: 300.
```

Due to the systematic uncertainty of the overall normalization of the collection area, the ULs are affected. Moreover, higher levels of background light result in a worsening of the MAGIC collection area over the entire energy range. Corresponding correction factor can be obtained using the MARS class *mtools/MEfficiencyCorrections*, based on average *level-0 trigger* discriminator threshold (DT) values. As standard default values (0.3, 1.0) are used, in case of standard observations these values are fine, but in case of observations with high DTs values (e.g. during moon observations), we should check these numbers:

```
FluxLC.ULEfficiencyError: 0.3
FluxLC.ULEfficiencyCorrection: 1.0
```

From the output of *fluxlc*, it is important to check the cut efficiencies, which should be higher than 50%, otherwise it is advisable to further open the cuts. Looser cuts reduce the effect of systematic uncertainties between data and Montecarlo events, which is important for the estimation of the effective collection areas. In such a way, the spectrum is less affected by the residual discrepancy between data and Montecarlo. Loose cuts have also the advantage to allow for a larger statistics of excess events, given the larger collection area.

Since the number of excess from which the flux will be estimated, is obtained from *theta<sup>2</sup>* distributions, we should carefully check these plots (see Fig. A.9 and Fig. A.10), especially the *theta<sup>2</sup>* plot for each energy bin. Typically the *theta<sup>2</sup>* plots shown in this tab are very small, but they can be enlarger using the following procedure: open a new canvas, click on the desired plot with the right button of the mouse and select “Draw clone”. Then the single plot will appear in the new canvas and from there you can change the size with the mouse.

Later the spectral points can be checked, an example can be found in Fig. A.11.

In the last tab of the output file, the light curve can be found (see Fig. A.12). The minimum time bin acceptable for a light curve will be the one, where at least a significance of  $3\sigma$  is obtained per bin. In order to check the significance per time bin, we have to check a previous plot, as shown in Fig. A.13.

## A.13 Unfolding

The unfolding is performed using the macro *\$MARSSYS/macros/CombUnfold.C*, which uses the configuration file *\$MARSSYS/mrcfiles/combunfold.rc*. For the unfolding, a signif-

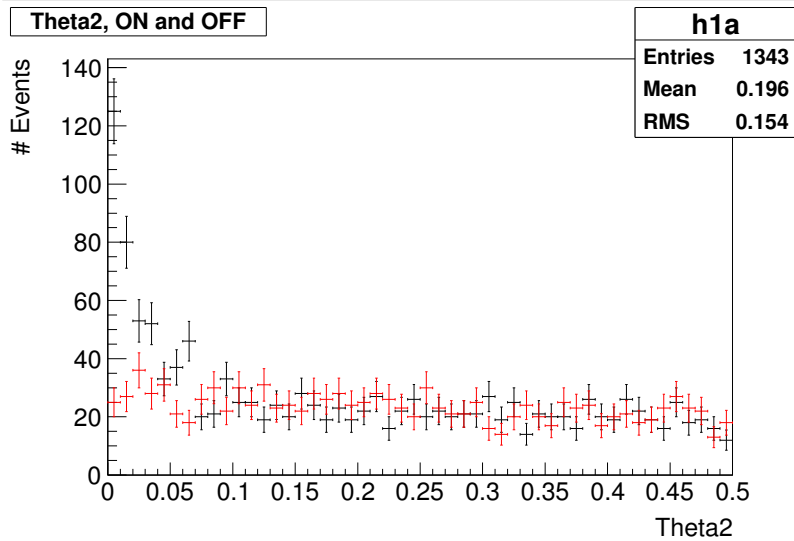


Figure A.9: Overall  $\Theta^2$  distribution, obtained from *fluxlc*.

icant signal is required at least in some consecutive energy bins of the spectrum. The main options in the configuration file are the following:

You can combine different spectra by averaging properly the collection areas and observation times. The energy bins should be the same for the different samples, otherwise you should re-run *fluxlc*. For that issue, you should select the proper number of files:

```
MCombineDataForUnfolding.NumFiles: 2
```

and hand over the files as:

```
MCombineDataForUnfolding.InputFiles[0]: yourpath/spectr_1.root
MCombineDataForUnfolding.InputFiles[1]: yourpath/spectr_2.root
```

Select the name of the output file:

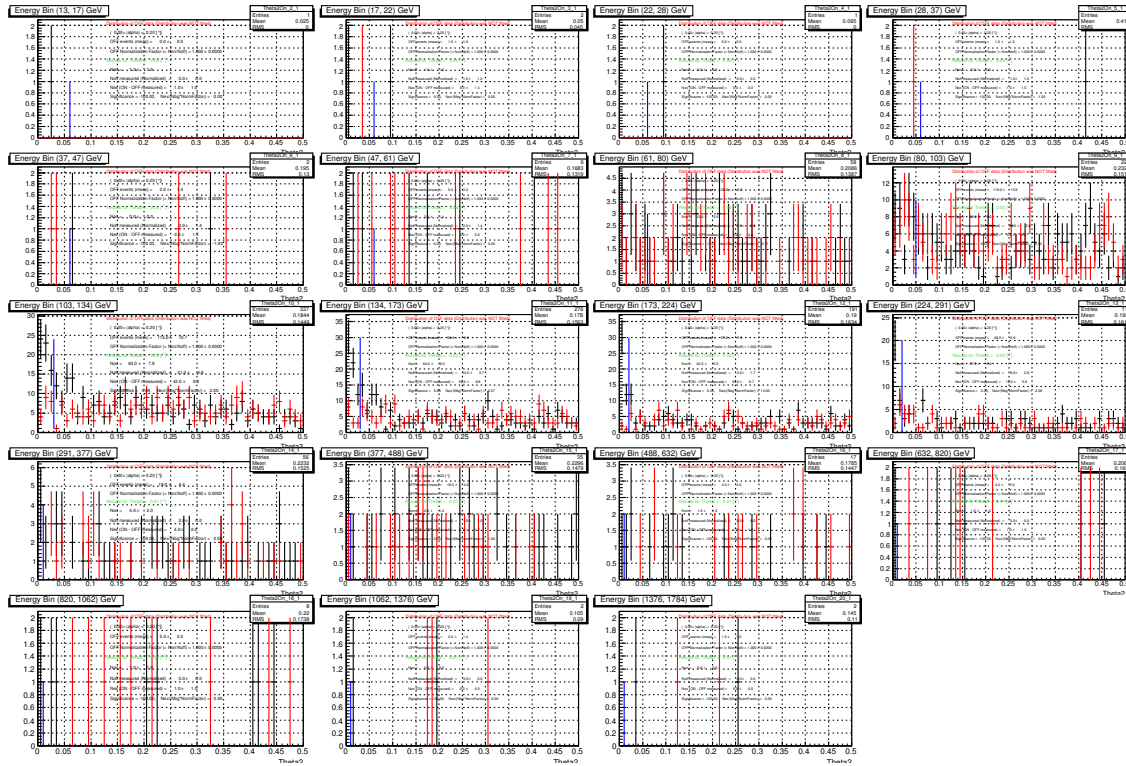
```
MCombineDataForUnfolding.OutputFile: yourpath/combined.root
```

Since the method is recursive, you can select the number of spectrum iterations (typically 1 or 2 is fine):

```
MCombineDataForUnfolding.NSpectrumIterations: 1
```

Using this macro, not only the unfolding can be done but also the de-absorption of the spectrum. This option can be used, once you have a stable unfolded spectrum (meanwhile keep the line commented). You will need to give the EBL absorption coefficient, from the following line:

```
MCallUnfold.AttFactorFile: yourpath/exptau_z0.045_modelKneiskeBest.dat
```

Figure A.10:  $\Theta_{\text{had}\nu}$  distribution per energy bin.

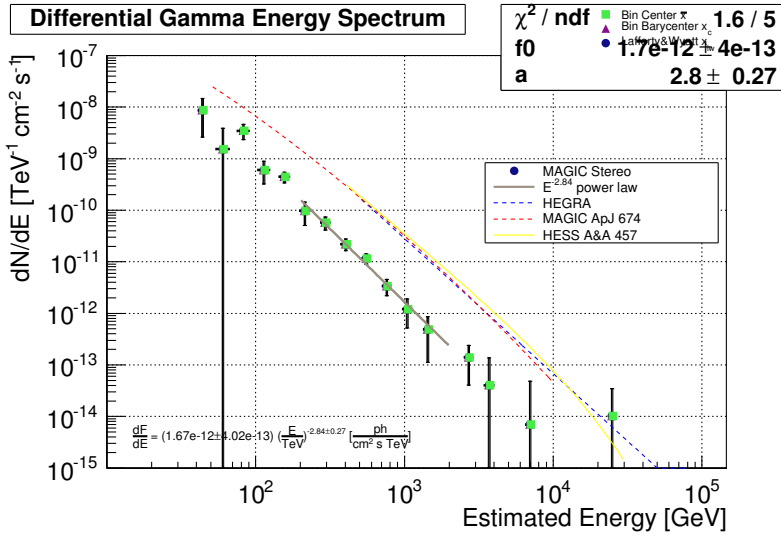
Selection of the a priori assumed spectrum shape and spectral slope. The assumed spectrum should be as similar as possible to the real one. Then, the convergence of the method will be fast (this option is only used if you select the forward unfolding method) :

```
#      FlagPrior      = 1  constant
#                      2  power law with power index Gamma
#                      3  from input
#                      4  rebinned ha_orig (measured distribution)
MCallUnfold.FlagPrior:        4

# if FlagPrior = 2  Gamma is the power index
MCallUnfold.Gamma:           3.0
```

There are several unfolding methods implemented (see Albert et al., 2007a). Typically, the easiest approach is the forward unfolding, which does not use the spectral points, but an assumed spectral shape. Even if it cannot be considered as reliable as the other methods it yields a good first approximation. You can select the different unfolding methods by selecting the proper number from the following list:

```
#      FlagUnfold     = 1  Schmelling (minimization by Gauss-Newton method)
```

Figure A.11: An example of a spectrum from *fluxlc*.

```

#      2 Tikhonov (minimization by MINUIT)
#      3 Bertero (appropriate for under-constrained case)
#      4 Forward unfolding
#      5 Schmelling (minimization by MINUIT)
#      6 BerteroW (appropriate for over-constrained case)
MCallUnfold.FlagUnfold:    4

```

Usually, the analyzer should run the unfolding using all the methods and check if the unfolded spectrum is stable. If this is not the case, and you get different results from different unfolding methods, this means that the spectrum cannot be unfolded, most probably due to a lack of statistics.

The noise component of the unfolded distribution should not be much higher than the noise component of the measurements. That is why we typically select the criteria number 5 in order to select the solution:

```

# Criterion for choosing the best weight
#   FlagCriterion = 1 biggest increase of trace(Sigma),
#                   2 LSQ solution (very large weight, many iterations)
#                   3 chi2 = # of sign. measurements,
#                   4 chi2 = rank of G,
#                   5 Trace(Sigma)/Trace(C) = 1,
#                   6 D2bar minimal (only MC)
#                   7
#                   8 choose the weight given by the bin IterBin
MCallUnfold.FlagCriterion:  5

```

For the forward unfolding, this flag has no meaning.

After having run the unfolding, we should check in the output file the tab shown in Fig. A.14

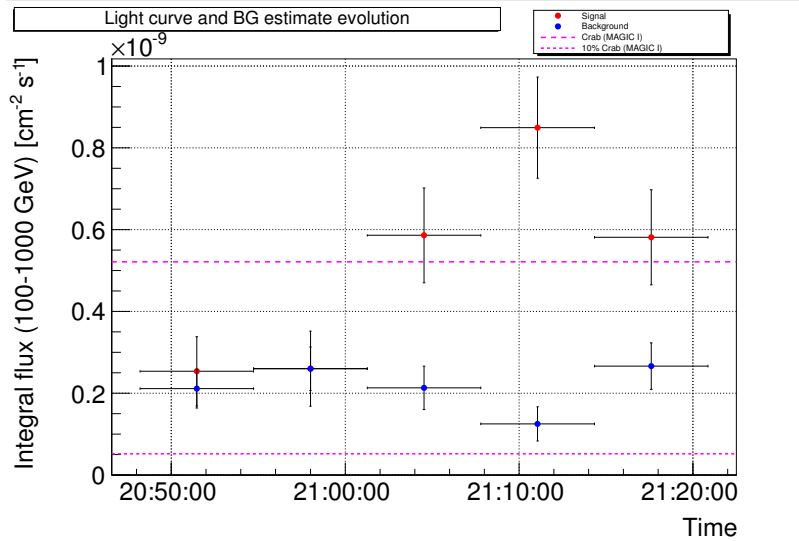


Figure A.12: An example of a light curve. The blue points represent the background, while the red ones the signal from the source.

where the selected bin should not be found at extreme values. Otherwise, you should select by hand the corresponding bin number, in that case you should set:

```
MCallUnfold.FlagCriterion: 8
MCallUnfold.IterBin:      17 (number of desired bin)
```

The energy range should be selected, firstly we can run the forward unfolding and use an automatic energy selection:

```
MCallUnfold.RangeAutoSelectA: 1
```

Then, we should go to Fig. A.15 and check the estimated energy bins in which positive counts are found. It is very important that there are no gaps in the middle. You can move the green lines by clicking and drawing with the mouse, in the reconstructed energy plot and in the inverted matrix. In the migration matrix, the relation is given between the measured energy and the true energy distribution, calculated using MC simulations. The horizontal green lines mean the true energy can be adjusted, make sure that the biggest part of the matrix lies inside the green lines. Another point to take into account is that the effective areas should be greater than 0 for entire the selected range. The acceptance should be high (higher than 80% typically).

You can select the type of function to fit the unfolding spectrum:

```
# Type of function to be fitted to the fluxes
#          or to be used in the Forward unfolding
#    F1Type = 1 power law                      (Npar = 3)
#          2 for power law with cutoff           (Npar = 4)
```

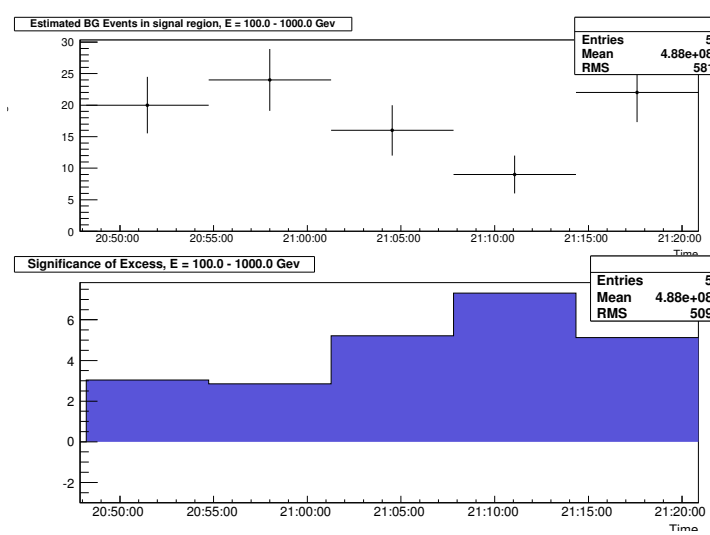


Figure A.13: Upper plot: Number of excess events per time bin. Lower plot: Significance per time bin.

```

#           3   for power law with VARIABLE POWER INDEX (Npar = 5)
#           4   for power law with VARIABLE POWER INDEX and cutoff
#                   (Npar = 5)
#           5   for broken power law                               (Npar = 6)
#           6   for broken power law
#                   with variable alpha1                         (Npar = 7)
#           7   for broken power law
#                   with a cutoff                                (Npar = 7)
#           8   for broken power law with variable
#                   alpha1 and cutoff                           (Npar = 8)

MCallUnfold.F1Type: 1

# these are values for Type 1
#                                     f0          alpha        r
MCallUnfold.Npar: 3
MCallUnfold.ParamVinit: 0.4e-10    -2.0      1.0
MCallUnfold.ParamStep:  1.e-12     0.2       0.0
MCallUnfold.ParamLimlo: 1.e-15    -10.0     0.0
MCallUnfold.ParamLimup: 1.e-7     10.0      0.0
MCallUnfold.ParamFix:   0          0         1

```

where  $f_0$  is the flux at the normalization energy ( $r$ , measured in TeV) and  $\alpha$  the starting guess for the spectral slope.

`MCallUnfold.ParamFix` is 0, if the variable is not fixed and has to be found, and 1 if it is fixed in the fit. Important are the flux limits (`MCallUnfold.ParamLimlo` and `MCallUnfold.ParamLimup`). Usually, the normalization energy is fixed, we should fix it at

a point where we have enough statistics.

We can evaluate how good the fitting is using the  $\chi^2$  value. A good fit result yields a  $\chi^2/\text{NDF} \sim 1$ .

Depending on the fit function type you selected you should set its initial parameters (uncomment the lines which refer only to the selected function). Typically, a simple power-law or a power-law with a cut-off is used. You should check the output (Fig. A.16) to judge which function describes your unfolded spectrum better.

At the end of the configuration file, you can set the energy range (measured in GeV) for the fitting (in order to exclude points with large error, for example).

```
MCallUnfold.FitMinUser: 200
MCallUnfold.FitMaxUser: 1000
```

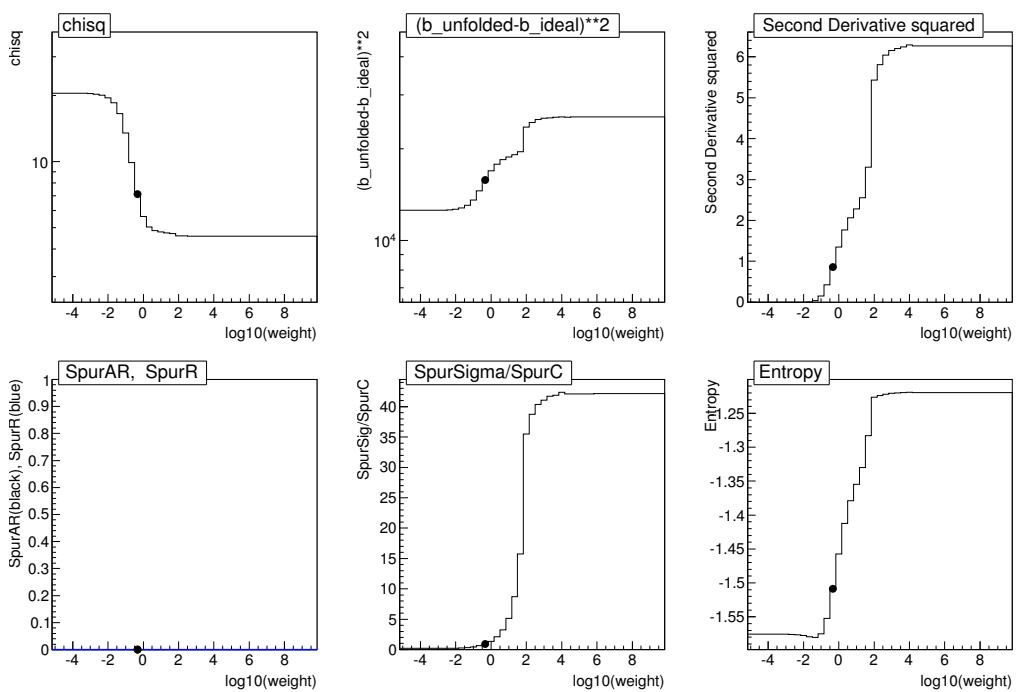


Figure A.14: Distribution to choose the best weight.

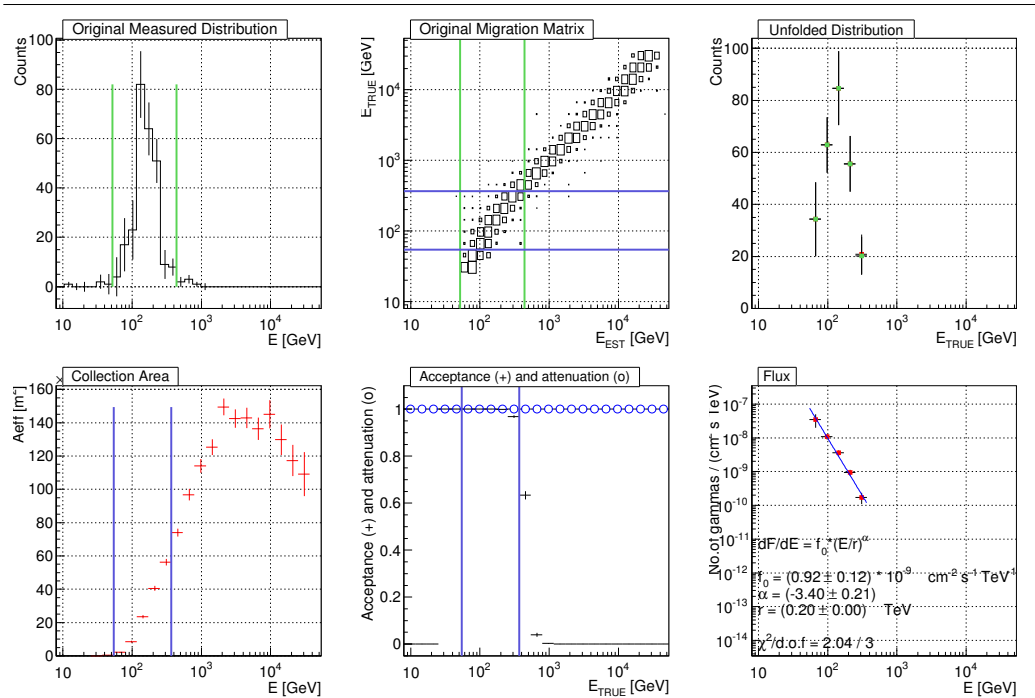


Figure A.15: In the first row from left to right: the event distribution as a function of reconstructed energy, the migration matrix, the unfolded distribution in true energy. In the second row: the collection area, the acceptance of the camera and the attenuation in circles in case you de-absorb a spectrum and finally, the unfolded spectrum.

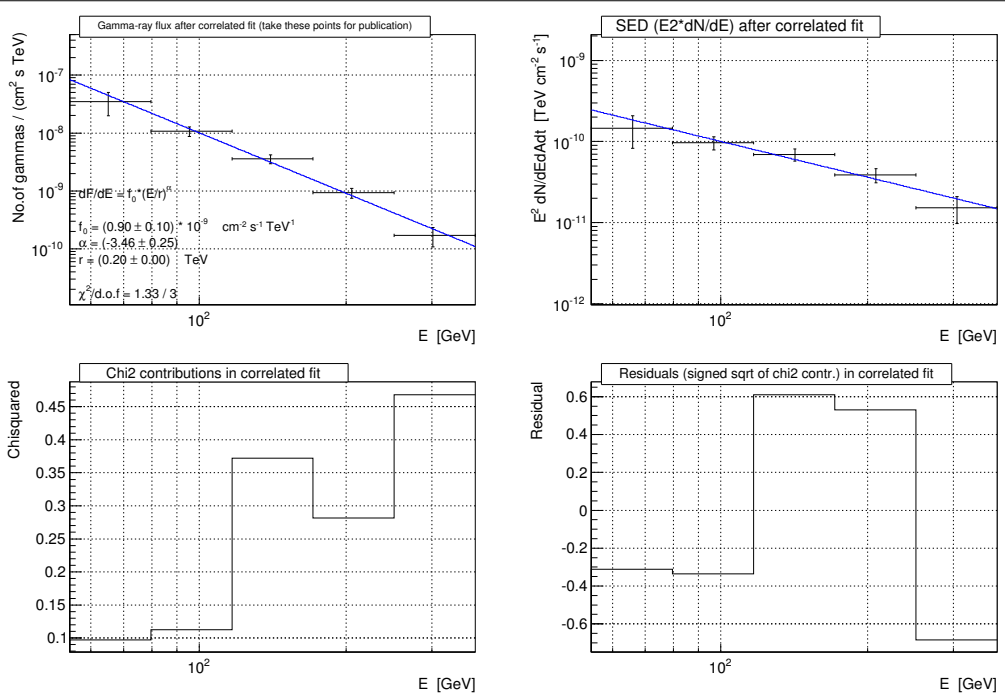


Figure A.16: In the upper part: the unfolded spectrum and the spectral energy distribution. In the lower part: the  $\chi^2$  of the fit and the residuals.



# List of Figures

1.1	All particle cosmic rays spectrum, taken from <a href="http://www.physics.utah.edu/\protect\unhbox\voidb@x\penalty\@M\{}whanlon/spectrum.html">http://www.physics.utah.edu/\protect\unhbox\voidb@x\penalty\@M\{}whanlon/spectrum.html</a> .	7
1.2	Sketch of the main $\gamma$ -ray emission processes.	8
1.3	Sky map of discovered VHE sources, taken from <a href="http://www.mpp.mpg.de/\protect\unhbox\voidb@x\penalty\@M\{}rwagner/sources">http://www.mpp.mpg.de/\protect\unhbox\voidb@x\penalty\@M\{}rwagner/sources</a> .	10
1.4	VHE survey of the galactic plain by HESS (Hinton and Hofmann, 2009).	11
1.5	The Crab Nebula is one of the most studied and strongest VHE $\gamma$ -ray emitters in the sky. Here, a picture taken from the Hubble Space Telescope in the optical is shown. Taken from <a href="http://hubblesite.org/newscenter/archive/releases/2005/37/image/a/">http://hubblesite.org/newscenter/archive/releases/2005/37/image/a/</a> .	12
1.6	Artistic view of a microquasar. Taken from <a href="http://www.daviddarling.info/encyclopedia/M/microquasar.html">http://www.daviddarling.info/encyclopedia/M/microquasar.html</a> .	13
2.1	AGN classification scheme.	18
2.2	Skymap of the extragalactic VHE $\gamma$ -ray emitters, taken from <a href="http://www.mpp.mpg.de/\protect\unhbox\voidb@x\penalty\@M\{}rwagner/sources/index.html">http://www.mpp.mpg.de/\protect\unhbox\voidb@x\penalty\@M\{}rwagner/sources/index.html</a> .	19
2.3	A cartoon of the AGN structure: the dusty torus has to be thought of as donut-like around the inner most region and is displayed here as cross section.	21
2.4	Simulated views of AGNs and their host galaxies for different orientations. Taken from <a href="http://en.wikipedia.org/wiki/Active_galactic_nucleus">http://en.wikipedia.org/wiki/Active_galactic_nucleus</a> .	21
2.5	Doppler factor as a function of the angle between the velocity vector and the line-of-sight to the observer for different values of the Lorentz factor.	23
2.6	Single particle spectrum due to synchrotron radiation.	26
2.7	The total Klein-Nishina cross section as a function of energy. The dashed line is an approximation at high energies.	28
2.8	Spectrum shape of a single electron spectrum due to <i>inverse Compton</i> scattering. The different color lines represent different $\gamma$ values (denoted on the top) in an isotropic and monochromatic radiation field.	30
2.9	Average SEDs from Fossati et al. (1998), showing the blazar sequence. The different colors denote different types of blazars.	33
2.10	Cross-section for pair creation process as a function of the energy of the photons.	34

2.11 Spectrum of the cosmic background radiation(Hauser and Dwek, 2001). . . . .	36
2.12 A comparison of recent EBL models, adopted from Domínguez et al. (2011). . . . .	38
2.13 Gamma-ray energy as a function of the redshift for some models and data from different sources. The detection from 3c279 in 2006 constrained the $\gamma$ -ray horizon (Albert et al., 2008a). . . . .	40
3.1 Atmospheric transmission at different energy ranges. Adopted from <a href="http://www.astro.queensu.ca/\protect\unhbox\voidb@x\penalty\OM\{}hanes/PHYS015-2010/Notes/T05-Pt04-Full-Spectrum.html">http://www.astro.queensu.ca/\protect\unhbox\voidb@x\penalty\OM\{}hanes/PHYS015-2010/Notes/T05-Pt04-Full-Spectrum.html</a> . . . . .	42
3.2 Sketch of an electromagnetic shower. . . . .	43
3.3 Longitudinal development of an electromagnetic shower for different values of $\ln(E_0/E_c)$ . The X-axis represents the radiation length ( $t$ ) while in the Y-axis the number of electrons (and positrons) is represented in logarithmic values. Taken from Gaug (2006). . . . .	44
3.4 Sketch of a hadronic shower. . . . .	45
3.5 Projection in the camera plane of showers from different progenitor particles. From left to right: an electromagnetic shower, a hadronic shower and a muon ring. Taken from Gaug (2006). . . . .	46
3.6 Vertical flux of different particles as a function of atmospheric depth. . . . .	46
3.7 Polarization sketch of a dielectric medium through which a charged particle moves. On the left, the effect produced by a particle travelling with a velocity lower than the speed of light in the medium and on the right, by a particle travelling faster than the speed of light in the medium. . . . .	47
3.8 <i>Cherenkov light pool</i> produced as the overlap of different Cherenkov emission cones. . . . .	48
3.9 Part of the Cherenkov spectrum emitted from an AS (dotted line) and the detected one (solid line). The difference is due to atmospheric effects (see the text for more information). . . . .	49
3.10 Simulations for a photon (left) and proton (right) generated AS, assuming an energy of 100 GeV and observed at zenith. The upper plots represent the shower evolution while the bottom ones are the projected view at ground (taken from F. Schmidt, ‘CORSIKA Shower Images’, <a href="http://www.ast.leeds.ac.uk/\protect\unhbox\voidb@x\penalty\OM\{}fs/showerimages.html">http://www.ast.leeds.ac.uk/\protect\unhbox\voidb@x\penalty\OM\{}fs/showerimages.html</a> ). . . . .	51
3.11 Schematic view of <i>Cherenkov telescopes</i> , taken from Hinton and Hofmann (2009). . . . .	53
4.1 The MAGIC telescopes. Taken from <a href="http://magic.mppmu.mpg.de/gallery/index.html">http://magic.mppmu.mpg.de/gallery/index.html</a> . . . . .	56
4.2 A MAGIC-I reflector panel composed of four mirrors is shown. . . . .	57
4.3 Pictures and schemes of the cameras of MAGIC-I and MAGIC-II. Taken from Tescaro (2010). . . . .	58
4.4 MAGIC-I camera sketch, where the colored regions represent different Sum Trigger patches. . . . .	60
4.5 MAGIC-I readout system (Goebel et al., 2007). . . . .	61

4.6	Domino board. . . . .	62
4.7	A photo of the Calibration box. Taken from Mazin (2007) . . . . .	62
4.8	Sketch of the denition of the signal (On) and background (Off) regions in wobble observations. The red circle represents the On position while the anti-source is located at 180°.Taken from Mazin (2007) . . . . .	63
5.1	Signal pulse time windows. Courtesy of Markus Gaug. . . . .	68
5.2	Left: Air shower image before cleaning. Right: Image after cleaning where the background light has been removed and the shower image parametrized.	69
5.3	Sketch of the Hillas parameters. . . . .	70
5.4	The ghost busting method scheme. . . . .	74
5.5	Sketch of the turbo buster method. . . . .	75
5.6	Sketch of decision trees. . . . .	76
5.7	Distribution of the Hillas parameters and hadronness for gamma-like showers represented by the yellow shaded are and hadron-like showers in blue shaded area. . . . .	77
5.8	Alpha distribution from a Crab Nebula data sample. Taken from Becerra-González (2008). . . . .	78
5.9	Integral MAGIC stereo system sensitivity. The grey solid line represents the integral sensitivity achieved by MAGIC-I while the black lines accounts for the integral sensitivity reached by the stereo system: the dashed line has been calculated using MC simulations and the solid one is the result from a Crab Nebula data sample analysis. . . . .	81
6.1	Distribution of the squared angular distance ( $\theta^2$ ) for events in the direction of PKS 1222+21 (black points) and normalized off-source events (grey histogram) for data taken on June 17 <sup>th</sup> . The signal is extracted in the $\theta^2$ -region denoted by the vertical dashed line. . . . .	85
6.2	Skymap from PKS1222+21 during a flare state on the 17 <sup>th</sup> of June 2010. . . . .	85
6.3	Differential energy spectrum of PKS 1222+21, as measured by MAGIC on June 17 <sup>th</sup> , 2010. Differential fluxes are shown as black points, upper limits (95% C.L.) as black arrows. The black line is the best fit to a power-law. The grey shaded area represents the systematic uncertainties of the analysis. The absorption-corrected spectrum and upper limits, using the EBL model by Domínguez et al. (2011), are shown by the blue squares and arrows; the dashed blue line is the best fit power-law. The blue area illustrates the uncertainties due to differences in the EBL models, cited in the text, by Kneiske and Dole (2010); Gilmore et al. (2009); Franceschini et al. (2008) and Albert et al. (2008a). . . . .	88
6.4	PKS 1222+21 light curve above 150 GeV for the whole observation campaign in nightly time bins. The blue points represent the flux calculated from the two detections of VHE $\gamma$ -rays by MAGIC, while the black arrows indicate flux U.L.s at 95% C.L., calculated form the non-detection of the source. . . . .	90

6.5 PKS 1222+21 light curve above 100 GeV during the VHE flare state on June 17 <sup>th</sup> , in 6 minutes time bins (black filled circles). The black solid line is a fit with an exponential function and the black dotted line a fit with a linear function. The grey open squares denote the equivalent fluxes from the background events and the grey dashed line is a fit with a constant function to these points. . . . .	91
6.6 Fermi daily light curve of PKS 1222+21 for E>100 MeV in the upper panel. The lower panel represents the photon index derived from a single power-law fitted to the LAT data. The red arrow represents the detection in VHE $\gamma$ -rays by MAGIC on 17 <sup>th</sup> June 2010, while the black arrows represent the epochs when two very high energy photons with energies above 100 GeV were detected by <i>Fermi</i> . Figure taken from Tanaka et al. (2011). The two red circles denote the detection of VHE $\gamma$ -rays by MAGIC. . . . .	92
6.7 The three different spectral energy distributions of PKS 1222+21, measured by <i>Fermi</i> corresponding to different periods of activity (red, blue and green filled circles). In grey diamonds, the spectrum of 3C 454.3 (one of the brightest sources detected in the $\gamma$ -rays band) is shown in flare state for comparison. Solid lines show the best-fit broken power-law models, while arrows indicate 95% upper limits. Figure taken from (Tanaka et al., 2011). . . . .	93
6.8 High energy SED of PKS 1222+21 during the flare of June 17 <sup>th</sup> , 2010 (MJD 55364.9), showing <i>Fermi</i> /LAT (squares) and MAGIC (circles) differential fluxes. A red bow tie in the MeV/GeV range represents the uncertainty of the likelihood fit to the <i>Fermi</i> /LAT data. The unfolded and deabsorbed spectral fit to the MAGIC data is shown as a red bow tie, extrapolated to lower and higher energies (dotted lines). A thick solid line (photon index $\Gamma = 2.7$ ) indicates a possible extrapolation of the MAGIC de-absorbed data to lower energies. The thick dashed line represents the EBL absorbed spectrum, obtained from the extrapolated intrinsic spectrum using the model of Domínguez et al. (2011). . . . .	95
6.9 Optical depth upper limits at 95% C.L. along the line of sight to PKS 1222+21 ( $z=0.432$ ) assuming the limiting intrinsic photon index $\Gamma_{\text{VHE}} = 2.4$ compared with optical depths predicted for the same redshift by different EBL models. Adapted from Aleksić et al. (2011c). . . . .	97
7.1 A sketch of the most simple model for an SSC spectral energy distribution. . . . .	103
7.2 Broken power-law distribution for electrons. . . . .	103
7.3 Spectral energy distribution for PKS 1222+21, see text for explanations. . .	105
7.4 Sketch of the geometrical arrangement assumed in the model. . . . .	106
7.5 Spectral energy distribution fit by the model considering two emitting regions outside the BLR with a $\Gamma = 20$ for the jet and $\Gamma_b = 50$ . . . . .	107
7.6 Spectral energy distribution fit to the model considering two emitting regions outside the BLR with $\Gamma = 20$ for the jet and $\Gamma_b = 70$ . . . . .	107

7.7	Spectral energy distribution fit to the model considering two emitting regions outside the BLR with $\Gamma = 20$ for the jet and $\Gamma_b = 70$ . Only the “blob” emission is represented by colored lines: the solid pink line represents the synchrotron emission part, the red line denotes the SSC, the green line is the EC emission due to the IR photon field and the dotted black line represents the EC emission due to the photon field of the jet. . . . .	108
7.8	Spectral energy distribution fit to the model considering the “blob” emitting outside the BLR with $\Gamma_b = 50$ and the jet inside the BLR with $\Gamma = 20$ . . . . .	109
7.9	Spectral energy distribution fit to the model considering the “blob” emitting outside the BLR with a $\Gamma_b = 70$ and the jet inside the BLR with $\Gamma = 20$ . . . . .	109
8.1	Sky region centered at the position of 1ES 1215+303 with approx. size of the trigger region of the MAGIC telescopes. By the yellow circle on the left side, the position in the sky of 1ES 1218+304 is represented. The red markers represent the wobble pointing positions. . . . .	114
8.2	$\theta^2$ distributions at the position of 1ES 1215+303 for the 2010 data. The top left plot shows the $\theta^2$ distribution calculated with data taken at 0 and 180 degrees, while in the top right plot, only data observed at 90 and 270 degrees have been taken into account. The combined distribution for the entire 2010 observation period is plotted in the bottom figure. . . . .	117
8.3	Skymap for the combined 2010 data, in which the source positions of 1ES 1218+304 and 1ES 1215+303 are not taken into account in the model background estimation. Only the bright source 1ES1218+304 is visible. . . . .	118
8.4	$\theta^2$ distribution of 1ES 1215+304 from the combined 2011 data, using standard cuts over the full energy range. . . . .	118
8.5	Skymap of the observed FoV of 1ES1215+303 from 2011 data, using standard cuts over the full energy range. One can see the presence of the bright second source 1ES 1218+304. . . . .	119
8.6	Light curve of 1ES 1215+303 from the data taken during the 2011 campaign for energies higher than 200 GeV. . . . .	120
8.7	Optical light curve in the R-band of 1ES 1215+303. The grey shaded areas represent the time windows observed by MAGIC during the 2010 and 2011 campaigns. . . . .	121
8.8	Optical light curve of 1ES 1215+303 in the R-band during the first MAGIC observation campaign in 2010. . . . .	122
8.9	Optical light curve of 1ES 1215+303 in the R-band during the second MAGIC observation campaign in 2011. . . . .	122
8.10	X-ray light curve of 1ES 1215+303 for the 2011 observation campaign, measured by <i>Swift</i> on a nightly time scale. . . . .	123
8.11	Time evolution of the spectral index for X-rays measured with <i>Swift</i> during the observation campaign of 1ES 1215+303 in 2011. . . . .	124
8.12	Light curves of 1ES 1215+303 on different bands observed by UVOT in 2011. The dashed blue light shows the reference value calculated for MJD 55168. . . . .	125
8.13	<i>Fermi</i> light curve for 1ES 1215+303 covering an energy range from 0.5 to 100 GeV during the 2011 MAGIC campaign in weekly time bins. . . . .	126

8.14 Time evolution of the spectral index measured by <i>Fermi</i> during the observation campaign of 1ES 1215+303 in 2011. . . . .	126
8.15 Differential energy spectrum from 1ES 1215+303 in 2011 assuming $z = 0.13$ . The black points represent the measured differential fluxes unfolded by Tikhonov algorithm. The solid black line represents the best fit to a power law and the grey shaded area the systematic uncertainties of the analysis. The blue points are the absorption corrected spectrum using different EBL models (see figure subtitles). The stripped blue line represents the best fit power law for the de-absorbed spectrum. And the blue shaded area in the first figure represents the uncertainty of Domínguez et al. (2011). . . . .	128
8.16 Differential energy spectrum from 1ES 1215+303 measured by MAGIC during the 2011 campaign assuming $z = 0.13$ . The black points represent the measured differential fluxes unfolded by the Tikhonov algorithm. The solid black line represents the best fit to a power law and the grey shaded area the systematic uncertainties of the analysis. The blue points are the absorption corrected spectrum using the EBL models from Primack et al. (2005). The stripped blue line represents the best fit power law for the de-absorbed spectrum and the blue area the spread of EBL models Domínguez et al. (2011), Franceschini et al. (2008), the “max high UV” EBL model described in Albert et al. (2008a), Kneiske and Dole (2010), Kneiske et al. (2002) and Primack et al. (2005). . . . .	129
8.17 Differential energy spectrum from 1ES 1215+303 in 2011 assuming $z = 0.237$ . The black points represent the measured differential fluxes unfolded by Tikhonov algorithm. The solid black line represents the best fit to a power law and the grey shaded area the systematic uncertainties of the analysis. The blue points are the absorption corrected spectrum using different EBL models (see figure subtitles). The stripped blue line represents the best fit power law for the de-absorbed spectrum. And the blue shaded area in the first figure represents the uncertainty of Domínguez et al. (2011). . . . .	131
8.18 Differential energy spectrum from 1ES 1215+303 measured by MAGIC during the 2011 campaign assuming $z = 0.237$ . The black points represent the measured differential fluxes unfolded by the Tikhonov algorithm. The solid black line represents the best fit to a power law and the grey shaded area the systematic uncertainties of the analysis. The blue points are the absorption corrected spectrum using the EBL models from Primack et al. (2005). The stripped blue line represents the best fit power law for the de-absorbed spectrum and the blue area the spread of EBL models Domínguez et al. (2011), Franceschini et al. (2008), the “max high UV” EBL model described in Albert et al. (2008a), Kneiske and Dole (2010), Kneiske et al. (2002) and Primack et al. (2005). . . . .	132
8.19 Spectral energy distribution for 1ES 1215+303. . . . .	135
8.20 Spectral energy distribution for 1ES 1215+303 modeled by a SSC model assuming a redshift of $z = 0.13$ and a Lorentz factor of $\Gamma = 20$ . . . . .	136

8.21 Spectral energy distribution for 1ES 1215+303 modeled by a SSC model assuming a redshift $z = 0.237$ and a Lorentz factor of $\Gamma = 20$ , which was obtained by the fit to the lower energy bump on the left side. . . . .	138
9.1 $\theta^2$ distributions, obtained from the 2010 data at $0^\circ$ , $90^\circ$ , $180^\circ$ and $270^\circ$ wobble angles w.r.t. the position of 1ES 1215+303 and the combined distribution, respectively. Standard low energy cuts have been used. . . . .	141
9.2 $\theta^2$ distributions obtained from 2011 data at $90^\circ$ and $270^\circ$ wobble angles w.r.t. the position of 1ES 1215+303 and the combined distribution, respectively. Standard cuts for low energies have been used. . . . .	142
9.3 $\theta^2$ distribution, obtained from combined 2010 and 2011 data, using standard cuts at low energies. . . . .	143
9.4 Skymap for the combined 2010 and 2011 data, using standard cuts at low energies. The BL Lac 1ES1215-303 is also present in this map, see chapter 8.	145
9.5 Measured VHE spectrum of 1ES 1218+304 from the 2011 data set from the two different pointings. In blue, the spectral points and the best fit of the spectrum measured in 2011 from data taken at 0.86 degrees from the camera center. The black points and fit are the ones derived from the analysis of the data set observed at 1.16 degrees from the camera center. Both shaded areas, blue and grey, account for the systematic uncertainties derived from the use of different unfolding methods. . . . .	147
9.6 Comparison between the spectra of 1ES 1218+304 from 2010 and 2011. The black points represent the spectral points derived from the 2010 data set, and the solid black line is the best fit to the 2010 data. In blue points, the differential energy spectrum from 2011 is shown, and the dashed blue line is the best fit to the 2011 spectral points. The shaded areas, grey and blue, represent the systematic uncertainties for the 2010 and 2011 data analysis, derived from the use of different unfolding algorithms. . . . .	147
9.7 VHE $\gamma$ -ray light curve from data taken in 2010. . . . .	148
9.8 VHE $\gamma$ -ray light curve from data taken in 2011. . . . .	149
9.9 Optical light curve for 1ES 1218+303 on a nightly time-scale. The flux has been measured in the R band. The grey shaded area represents the observation windows by MAGIC during both observation campaigns. . . . .	149
9.10 Optical light curve for 1ES 1218+303 for the 2010 observations on a nightly time-scale. The flux has been measured in the R band. . . . .	150
9.11 Optical light curve for 1ES 1218+303 for the 2011 observations on a nightly time-scale. The flux has been measured in the R band. . . . .	151
9.12 Differential energy spectrum from 1ES 1218+304 observed in 2010 and 2011. The black points represent the measured differential fluxes unfolded by the Tikhonov algorithm. The solid black line represents the best fit to a power-law and the grey shaded area represent the systematic uncertainties of the analysis. The blue points are the absorption corrected spectrum using different EBL models (see figure subtitles). The stripped blue line represents the best fit power-law to the de-absorbed spectrum. And the blue shaded area in the first figure represents the uncertainty of Domínguez et al. (2011). . .	152

---

9.13 Differential energy spectrum from 1ES 1218+304 observed in 2010 and 2011. The black points represent the measured differential fluxes unfolded by the Tikhonov algorithm. The solid black line represents the best fit to a power-law and the grey shaded area represents the systematic uncertainties of the analysis. The blue points are the absorption corrected spectrum using the EBL models from Primack et al. (2005). The stripped blue line represents the best fit power-law for the de-absorbed spectrum and the blue area represents the spread of EBL models Domínguez et al. (2011), Franceschini et al. (2008), the “max high UV” EBL model described in Albert et al. (2008a), Kneiske and Dole (2010), Kneiske et al. (2002) and Primack et al. (2005). . . . .	153
A.1 The starguider information. See text for more information . . . . .	168
A.2 Left: Events rate as a function of the time. Right: Different rates as function of the time. In blue, the cloudiness evolution is represented, in pink the muon rate and the black line represents the event rate. . . . .	168
A.3 Normalized camera sensitivity of MAGIC-I as function of distance to the camera center for a source with spectral slope -2.5, figure adopted from Becerra-González (2008). . . . .	170
A.4 Gini index of each parameter used in the DISP calculation. . . . .	172
A.5 $\theta^2$ plot from 1ES 1215+303, using 3 Off regions. The first plot shows the combined $\theta^2$ distribution, while in the rest only Off events from a given position are used ( $90^\circ$ , $180^\circ$ and $270^\circ$ , respectively). . . . .	178
A.6 Relative flux from PKS1222+21 during the flare on 17th of June 2010. . . . .	181
A.7 Distribution of test statistics, compared with the null hypothesis (red dashed line) of PKS1222+21 on 17 of June 2010. . . . .	182
A.8 Effective area, estimated from MC, before (blue) and after (red) the application of the cuts. . . . .	186
A.9 Overall $\Theta^2$ distribution, obtained from <i>fluxlc</i> . . . . .	188
A.10 $\Theta^2$ distribution per energy bin. . . . .	189
A.11 An example of a spectrum from <i>fluxlc</i> . . . . .	190
A.12 An example of a light curve. The blue points represent the background, while the red ones the signal from the source. . . . .	191
A.13 Upper plot: Number of excess events per time bin. Lower plot: Significance per time bin. . . . .	192
A.14 Distribution to choose the best weight. . . . .	193
A.15 In the first row from left to right: the event distribution as a function of reconstructed energy, the migration matrix, the unfolded distribution in true energy. In the second row: the collection area, the acceptance of the camera and the attenuation in circles in case you de-absorb a spectrum and finally, the unfolded spectrum. . . . .	194
A.16 In the upper part: the unfolded spectrum and the spectral energy distribution. In the lower part: the $\chi^2$ of the fit and the residuals. . . . .	195

## List of Tables

2.1	List of AGNs detected in VHE $\gamma$ -rays, ordered by date of discovery. LBL, IBL and HBL are Low, Intermediate and High-peaked BL Lacs respectively, FSRQ denotes Flat Spectrum Radio Quasar, RG is a Radio Galaxy and Starb. are Starburst galaxies. Those redshifts denoted by <sup>a</sup> have large uncertainties in their measurement or ambiguities in the identification of the optical absorption lines, while <sup>b</sup> means that two values for the redshift have been published. . . . .	20
2.2	Energy range photon target for the maximum absorption due to pair creation process during the interaction with $\gamma$ -rays. . . . .	35
6.1	Nights with good quality data taken by MAGIC from PKS 1222+21. The dates refer to the beginning of each night. . . . .	86
6.2	Nightly significance of PKS 1222+21 calculated from the $\theta^2$ distribution, and U.L. for $E > 100$ GeV in case of significance $\sigma < 4$ . . . . .	87
6.3	Spectral fits for PKS 1222+21, using broken power-law models, with low and high energy spectral indices $\Gamma_{LE}$ and $\Gamma_{HE}$ , respectively, and the break photon energies $E_{br}$ (Tanaka et al., 2011). . . . .	94
7.1	Input parameters for the emission models shown in the figures. Out and in denotes the localization of the emitting region, belonging outside the BLR or inside, respectively. $\gamma_{\min}$ , $\gamma_b$ and $\gamma_{\max}$ are the minimum, break and maximum Lorentz factor of the electron population while $n_1$ and $n_2$ denote the low and high energy slopes of the broken power-law of the electron distribution. The magnetic field is represented by $B$ , the normalization of the electron distribution by $K$ and the radius of the emission region by $R$ . The last three columns show the power carried by cold protons (assuming one proton per emitting electron), relativistic electrons and the magnetic field in units of $10^{45}$ erg $\cdot$ s $^{-2}$ . . . . .	111

8.1	Summary of the MAGIC observations of 1ES 1215+303. The first part of the table shows the data taken during the 2010 campaign, while the second part shows the 2011 observations. The 2010 data were taken in wobble mode at angles 0 and 180 degrees, except for the data indicated with <sup>a</sup> which were observed at 90 and 270 degrees. In case of 2011, all data were taken at 90 and 270 degrees. The dates refer to the beginning of each night. The significance in the last column has been estimated from the $\theta^2$ distribution, using the standard full energy cuts ( $E > 250$ GeV). . . . .	115
8.2	Measured spectrum of 1ES 1215+303 from 2011 data, best fit to a power law for different unfolding algorithms. . . . .	119
8.3	Fluxes measured from 1ES 1215+303 by UVOT on MJD 55168. . . . .	123
8.4	De-absorbed spectrum of 1ES 1215+303 best fit to a power law for different EBL models assuming $z = 0.13$ . . . . .	130
8.5	De-absorbed spectrum of 1ES 1215+303 best fit to a power law for different EBL models assuming $z = 0.237$ . . . . .	133
8.6	Input parameters for the emission models shown in the figures. In the first column the redshifts are given. $\gamma_{\min}$ , $\gamma_b$ and $\gamma_{\max}$ are the minimum, break and maximum Lorentz factor of the electron population while $n_1$ and $n_2$ denote the low and high energy slopes of the broken power-law of the electron distribution. The magnetic field is represented by $B$ , the normalization of the electron distribution by $K$ and the radius of the emission region by $R$ . The last three columns show the power carried by cold protons (assuming one proton per emitting electron), relativistic electrons and the magnetic field in units of $10^{45}$ erg · s <sup>-2</sup> . . . . .	137
9.1	Distance of the observed position of 1ES 1218+303 to the camera center, measured in degrees, for the different wobble data samples. . . . .	140
9.2	MAGIC good quality observation data of 1ES 1218+304. The first part of the table are the data from the 2010 campaign, while the second part accounts for the 2011 observations. The 2010 data were observed at wobble angles 0 and 180 degrees around the position of 1ES 1215+303, except for the nights with <sup>a</sup> which were observed at 90 and 270 degrees. In case of 2011, all data were taken at 90 and 270 degrees. The column named P1 and P2 refers to the observations taken at 0 or 180 degrees wobble angle, depending on the observation pointing and , and P2 stands for observations at 90 or 270 degrees wobble angle, while the column named “Total” refers to the combined observing time or significance from the two different pointings. The results are based on the $\theta^2$ distributions, using the standard cuts at low energies. . . . .	144
9.3	Measured spectrum of 1ES 1218+304 from 2010 data, best fit to a power-law for different unfolding algorithms. . . . .	145
9.4	Measured spectrum of 1ES 1218+304 from 2011 data, best fit to a power-law for different unfolding algorithms. . . . .	146
9.5	Measured spectrum of 1ES 1218+304 from the combined data of 2010 and 2011, best fit to a power-law for different unfolding algorithms. . . . .	148

---

9.6 De-absorbed spectrum of 1ES 1218+304 best fit to a power-law for different EBL models. . . . .	154
--	-----



## References

- A. A. Abdo et al.: 2010, *ApJS* **188**, 405
- A. A. Abdo et al.: 2011, *Science* **331**, 739
- A. A. Abdo et al.: 2009, *ApJ* **700**, 597
- V. Acciari et al.: 2009a, *ApJ* **690**, L126
- V. A. Acciari et al.: 2009b, *ApJ* **693**, L104
- V. A. Acciari et al.: 2009c, *ApJ* **695**, 1370
- V. A. Acciari et al.: 2010, *ApJ* **709**, L163
- V. A. Acciari et al.: 2008, *ApJ* **684**, L73
- F. Acero et al.: 2009, *Science* **326**, 1080
- F. Aharonian et al.: 2004, *A&A* **421**, 529
- F. Aharonian et al.: 2009a, *A&A* **503**, 817
- F. Aharonian et al.: 2009b, *ApJ* **695**, L40
- F. Aharonian et al.: 2005, *A&A* **436**, L17
- F. Aharonian et al.: 2007a, *A&A* **475**, L9
- F. Aharonian et al.: 2007b, *A&A* **473**, L25
- F. Aharonian et al.: 2008, *A&A* **481**, L103
- F. Aharonian et al.: 2006a, *A&A* **448**, L19
- F. Aharonian et al.: 2006b, *Nature* **440**, 1018
- F. Aharonian et al.: 2006c, *ApJ* **636**, 777
- J. Albert et al.: 2008a, *Science* **320**, 1752
- J. Albert et al.: 2006a, *ApJ* **642**, L119

- J. Albert et al.: 2006b, *ApJ* **648**, L105
- J. Albert et al.: 2008b, *Nuclear Instruments and Methods in Physics Research A* **588**, 424
- J. Albert et al.: 2007a, *Nuclear Instruments and Methods in Physics Research A* **583**, 494
- J. Albert et al.: 2007b, *ApJ* **654**, L119
- J. Albert et al.: 2007c, *ApJ* **666**, L17
- J. Albert et al.: 2007d, *ApJ* **667**, L21
- J. Albert et al.: 2008c, *ApJ* **674**, 1037
- J. Aleksić et al.: 2010a, *A&A* **517**, A5+
- J. Aleksić et al.: 2010b, *A&A* **524**, A77+
- J. Aleksić et al.: 2011a, *ApJ* **729**, 115
- J. Aleksić et al.: 2011b, *A&A* **530**, A4+
- J. Aleksić et al.: 2011c, *ApJ* **730**, L8+
- E. Aliu et al.: 2009a, *ApJ* **692**, L29
- E. Aliu et al.: 2008, *Science* **322**, 1221
- E. Aliu et al.: 2009b, *Astroparticle Physics* **30**, 293
- R. Antonucci: 1993, *ARA&A* **31**, 473
- W. D. Apel et al.: 2010, *Nuclear Instruments and Methods in Physics Research A* **620**, 202
- H. Bartko et al.: 2005, *Nuclear Instruments and Methods in Physics Research A* **548**, 464
- Josefa Becerra-González: 2008, *Master's thesis*, Universidad de la Laguna
- M. C. Bentz et al.: 2009, *ApJ* **705**, 199
- R. D. Blandford and R. L. Znajek: 1977, *MNRAS* **179**, 433
- D. Borla-Tridon et al.: 2009, *arXiv:0906.5448*
- D. A. Bramel et al.: 2005, *ApJ* **629**, 108
- Leo Breiman: 2001, *Machine Learning* **45**, 5
- T. Bretz et al.: 2009, *Astroparticle Physics* **31**, 92
- I. W. A. Browne: 1971, *Nature* **231**, 515
- E. Carmona et al.: 2008, in *International Cosmic Ray Conference*, Vol. 3 of *International Cosmic Ray Conference*, pp 1373–1376

- M. Catanese et al.: 1998, *ApJ* **501**, 616
- P. M. Chadwick et al.: 1999, *ApJ* **513**, 161
- L. Costamante and G. Ghisellini: 2002, *A&A* **384**, 56
- T. CTA Consortium: 2010, *arXiv:1008.3703*
- E. S. Domingo-Santamaria and D. F. Torres: 2005, *Astronomy and Astroph.* **444**, 403
- A. Domínguez et al.: 2011, *MNRAS* **410**, 2556
- A.-C. Donea and R. J. Protheroe: 2003, *Astroparticle Physics* **18**, 377
- J. H. Fan and R. G. Lin: 1999, *ApJS* **121**, 131
- Z. Fan, X. Cao, and M. Gu: 2006, *ApJ* **646**, 8
- L. Ferrarese and H. Ford: 2005, *Space Sci. Rev.* **116**, 523
- J. D. Finke, S. Razzaque, and C. D. Dermer: 2010, *ApJ* **712**, 238
- L. Foschini et al.: 2011, *arXiv:1101.1085*
- G. Fossati et al.: 1998, *MNRAS* **299**, 433
- A. Franceschini, G. Rodighiero, and M. Vaccari: 2008, *A&A* **487**, 837
- M. Gaug: 2006, *Ph.D. thesis*, Universitat Autonoma de Barcelona Departament de Fisica
- G. Ghisellini: 2000, in B. Casciaro, D. Fortunato, M. Francaviglia, & A. Masiello (ed.), *Recent Developments in General Relativity*, pp 5–+
- G. Ghisellini and P. Madau: 1996, *MNRAS* **280**, 67
- G. Ghisellini and R. Svensson: 1991, *MNRAS* **252**, 313
- G. Ghisellini and F. Tavecchio: 2008, *MNRAS* **386**, L28
- G. Ghisellini and F. Tavecchio: 2009, *MNRAS* **397**, 985
- G. Ghisellini et al.: 2011, *MNRAS* pp 627–+
- D. Giannios, D. A. Uzdensky, and M. C. Begelman: 2009, *MNRAS* **395**, L29
- D. Giannios, D. A. Uzdensky, and M. C. Begelman: 2010, *MNRAS* **402**, 1649
- R. C. Gilmore et al.: 2009, *MNRAS* **399**, 1694
- F Goebel et al.: 2007, *arXiv:0709.2363*
- K. Greisen: 1956, *Prog. Cosmic Rays Physics* **3**, 1
- Kenneth Greisen: 1966, *Phys. Rev. Lett.* **16(17)**, 748

- R. C. Hartman et al.: 1999, *ApJS* **123**, 79
- M. G. Hauser and E. Dwek: 2001, *ARA&A* **39**, 249
- D. Heck et al.: 1998, *CORSIKA: a Monte Carlo code to simulate extensive air showers.*
- V.F. Hess: 1912, *Physikalische Zeitschrift* **13**, 1084
- HESS Collaboration et al.: 2010, *A&A* **520**, A83+
- A. M. Hillas: 1985, in F. Jones (ed.), *Proc. of the 19<sup>th</sup> International Cosmic Ray Conference, La Jolla*, pp 445–448
- J. A. Hinton and W. Hofmann: 2009, *ARA&A* **47**, 523
- W. Hofmann: 2010a, *The Astronomer's Telegram* **2743**, 1
- W. Hofmann: 2010b, *The Astronomer's Telegram* **3007**, 1
- W. Hofmann and S. Fegan: 2009, *The Astronomer's Telegram* **2293**, 1
- D. Horan et al.: 2004, *ApJ* **603**, 51
- D. Horan et al.: 2002, *ApJ* **571**, 753
- I. Horváth: 2002, *A&A* **392**, 791
- S. G. Jorstad et al.: 2001, *ApJS* **134**, 181
- S. Kaspi et al.: 2007, *ApJ* **659**, 997
- K. I. Kellermann et al.: 1989, *AJ* **98**, 1195
- A. D. Kerrick et al.: 1995, *ApJ* **452**, 588
- P. Kharb and P. Shastri: 2004, *A&A* **425**, 825
- T. M. Kneiske and H. Dole: 2010, *A&A* **515**, A19+
- T. M. Kneiske, K. Mannheim, and D. H. Hartmann: 2002, *A&A* **386**, 1
- H. Krawczynski: 2004, *AJ* **48**, 367
- M. Lampton, B. Margon, and S. Bowyer: 1976, *ApJ* **208**, 177
- T. P. Li and Y. Q. Ma: 1983, *Astrophys. Journal* **272**, 317
- M. L. Lister et al.: 2009, *AJ* **138**, 1874
- H. T. Liu and J. M. Bai: 2006, *ApJ* **653**, 1089
- Malcolm S. Longair: 1992, *High Energy Astrophysics, Vol. 1*, Cambridge University Press
- Malcolm S. Longair: 1994, *High Energy Astrophysics, Vol. 2*, Cambridge University Press

- MAGIC Collaboration et al.: 2008, *Physics Letters B* **668**, 253
- P. Majumdar et al.: 2005, in *International Cosmic Ray Conference*, Vol. 5 of *International Cosmic Ray Conference*, pp 203–+
- M. P. Malmrose et al.: 2011, *ApJ* **732**, 116
- N. Mankuzhiyil, M. Persic, and F. Tavecchio: 2010, *ApJ* **715**, L16
- K. Mannheim: 1993, *A&A* **269**, 67
- L. Maraschi, G. Ghisellini, and A. Celotti: 1992, *ApJ* **397**, L5
- L. Maraschi and F. Tavecchio: 2003, *ApJ* **593**, 667
- M. Mariotti: 2010a, *The Astronomer's Telegram* **2753**, 1
- M. Mariotti: 2010b, *The Astronomer's Telegram* **2510**, 1
- M. Mariotti: 2010c, *The Astronomer's Telegram* **2967**, 1
- M. Mariotti: 2011, *The Astronomer's Telegram* **3100**, 1
- M. Mariotti and MAGIC Collaboration: 2010a, *The Astronomer's Telegram* **2910**, 1
- M. Mariotti and MAGIC Collaboration: 2010b, *The Astronomer's Telegram* **2916**, 1
- Daniel Mazin: 2007, *Ph.D. thesis*, Technische Universitat
- A. Moralejo et al.: 2009, *arXiv:0907.0943*
- M. Mose Mariotti: 2010, *The Astronomer's Telegram* **2684**, 1
- D. W. Murphy, I. W. A. Browne, and R. A. Perley: 1993, *MNRAS* **264**, 298
- K. Nalewajko and M. Sikora: 2009, *MNRAS* **392**, 1205
- A. Neronov, D. Semikoz, and I. Vovk: 2011, *A&A* **529**, A59+
- K. Nilsson et al.: 2003, *A&A* **400**, 95
- K. Nilsson et al.: 2008, *A&A* **487**, L29
- T. Nishiyama: 1999, in *International Cosmic Ray Conference*, Vol. 3 of *International Cosmic Ray Conference*, pp 370–+
- R. Ong: 2009a, *The Astronomer's Telegram* **1941**, 1
- R. A. Ong: 2009b, *The Astronomer's Telegram* **2301**, 1
- R. A. Ong: 2009c, *The Astronomer's Telegram* **2084**, 1
- R. A. Ong: 2009d, *The Astronomer's Telegram* **2260**, 1

- R. A. Ong: 2010a, *The Astronomer's Telegram* **2786**, 1
- R. A. Ong: 2010b, *The Astronomer's Telegram* **2968**, 1
- R. A. Ong and P. Fortin: 2009, *The Astronomer's Telegram* **2272**, 1
- R. A. Ong et al.: 2010, *The Astronomer's Telegram* **2486**, 1
- D. E. Osterbrock and R. W. Pogge: 1987, *ApJ* **323**, 108
- P. Padovani and P. Giommi: 1995, *ApJ* **444**, 567
- R. Pegna et al.: 2006, *Nuclear Instruments and Methods in Physics Research A* **567**, 218
- P. Picozza, R. Sparvoli, and PAMELA Collaboration: 2011, *Astrophysics and Space Sciences Transactions* **7**, 85
- J. Poutanen and B. Stern: 2010, *ApJ* **717**, L118
- J. R. Primack, J. S. Bullock, and R. S. Somerville: 2005, in F. A. Aharonian, H. J. Völk, & D. Horns (ed.), *High Energy Gamma-Ray Astronomy*, Vol. 745 of *American Institute of Physics Conference Series*, pp 23–33
- M. Punch et al.: 1992, *Nature* **358**, 477
- J. Quinn et al.: 1996, *ApJ* **456**, L83+
- M. Raue et al.: 2009, *The Astronomer's Telegram* **2350**, 1
- A. Reimer: 2007, *ApJ* **665**, 1023
- B. Rossi: 1952, *High Energy Particles*, Prentice-Hall, Inc., Englewood Cliffs, NJ
- M. Rüger, F. Spanier, and K. Mannheim: 2010, *MNRAS* **401**, 973
- T.Y. Saito and J. Sitarek: 2009, *Improvement of the Theta2 analysis by using the Random Forest method in the DISP estimation*, Technical report, MPI
- M. A. Sánchez-Conde et al.: 2009, *Phys. Rev. D* **79(12)**, 123511
- M. Sikora, R. Moderski, and G. M. Madejski: 2008, *ApJ* **675**, 71
- R. S. Somerville et al.: 2008, *MNRAS* **391**, 481
- F. W. Stecker, M. A. Malkan, and S. T. Scully: 2006, *ApJ* **648**, 774
- G. Superina et al.: 2008, in *International Cosmic Ray Conference*, Vol. 3 of *International Cosmic Ray Conference*, pp 913–916
- Y. T. Tanaka et al.: 2011, *arXiv:1101.5339*
- M. Tavani et al.: 2011, *Science* **331**, 736

- F. Tavecchio et al.: 2011, *arXiv:1104.0048*
- F. Tavecchio and G. Ghisellini: 2008, *MNRAS* **386**, 945
- F. Tavecchio et al.: 2010, *MNRAS* **406**, L70
- F. Tavecchio, L. Maraschi, and G. Ghisellini: 1998, *ApJ* **509**, 608
- F. Tavecchio and D. Mazin: 2009, *MNRAS* **392**, L40
- Diego Tescaro: 2010, *Ph.D. thesis*, IFAE
- M. Teshima: 2009, *The Astronomer's Telegram* **2098**, 1
- M. Teshima et al.: 2008, *The Astronomer's Telegram* **1500**, 1
- The Pierre AUGER Collaboration et al.: 2010, *Nuclear Instruments and Methods in Physics Research A* **620**, 227
- C. M. Urry and P. Padovani: 1995, *PASP* **107**, 803
- VERITAS Collaboration et al.: 2009, *Nature* **462**, 770
- B. Wagner, S. & Behera: 2010, *10th HEAD Meeting, Hawaii BAAS* **42**, 2, 07.05
- S. J. Wagner and HESS collaboration
- J.-M. Wang, B. Luo, and L. C. Ho: 2004, *ApJ* **615**, L9
- M. Weidinger and F. Spanier: 2010, *A&A* **515**, A18+
- G T Zatsepin and V A Kuzmin: 1966, *Soviet Journal of Experimental and Theoretical Physics Letters* **4**, 78



## Acknowledgements

Como no podría ser de otra manera, esta última sección empieza con nombres propios, Antonio Becerra y Francisca González, los *welys*, porque sin su ayuda esto no hubiera sido posible. No puedo dejar de recordar aquí aquellas noches de invierno, en las que mi padre salía de la cama sólo para llevarme a una montaña cercana a contemplar todos esos puntitos brillantes que despertaban en mi tanta curiosidad.

Agradezco al Instituto de Astrofísica de Canarias y a mis directores de tesis por ofrecerme la posibilidad de llevar a cabo este proyecto, así como apoyar las iniciativas que han ido surgiendo a lo largo de estos casi cuatro años. Muy especialmente tengo que agradecer a Markus Gaug su gran ayuda, no sólo como director, sino como amigo. También agradecer a Karsten Berger su corrección de la tesis incluso durante sus vacaciones.

I want to thank to the MAGIC collaboration for its fruitful and friendly work environment. Nevertheless, I cannot let pass by the opportunity to thank especially some of you, I apologize in advance if I forget someone. I would like to thank to the “PKS 1222+21 friends team”: Antonio Stamerra, Koji Saito, Daniel Mazin, Fabrizio Tavecchio, Tomislav Terzic and Laura Maraschi. Also the “1ES 1218+303 and 1ES 1215+304 team”: Elina Lindfors, Julian Sitarek, Pierre Collin and Saverio Lombardi. Thanks to Abelardo Moralejo for teaching me how to play mus and, of course, thanks for finding always time to answer my questions. I want to acknowledge Stefan Klepser for useful discussions during my stay at IFAE as well as Juan Cortina, Ignasi Reichardt, Roberta Zanin, Alicia López, Jelena Aleksić, Javier Rico, Michele Doro, Gianluca Giavitto and all the IFAE group for a very nice stay. It was a pleasure to work with Elisa Prandini, thanks for a funny walk around Munich without one of your shoes, and for sharing with me our friend PKS 1424+240. Thanks to Hajime Takami for our endless search for a new source of gamma-rays, Giacomo Bonnoli for providing me the Fermi data analysis and Alessandro Carosi for his collaboration searching the lucky GRB. A well-deserved thanks goes to the Onsite analysis group, without you the detection of fast flares in AGNs would not be possible. A very special thanks to Daniel Mazin for introducing me to the “EBL world” and to Fabrizio Tavecchio, Laura Maraschi, Antonio Stamerra and Gabriele Ghisellini for teaching and guiding me through the universe of the jet physics and for interesting physics discussions that gave meaning to this work. I would like also to thank to Ramesh Narayan for useful comments and discussion.

Y este trabajo no sólo ha sido posible gracias a los múltiples colaboradores, sino también a toda esa gente que han estado ahí. En primer lugar, quiero agradecer a mis hermanas por no enfadarse cuando me olvido de sus cumpleaños, y ya de paso, por estar siempre ahí

dispuestas a echar una mano. Gracias también a mi casi segunda madre, mi tía María, a mis primos y mi sobrina María del Valle.

Sin lugar a dudas, este nuevo párrafo sólo puede abrirlo una persona, Julio Carballo, porque cuando “no veo” me acuerdo de ti, y porque sin tu apoyo, paciencia, risas y también lágrimas hoy no estaría escribiendo esto. Por supuesto, también tengo que agradecer muy especialmente a Nayra Rodríguez, principalmente a ver si con la emoción se le olvidan los 20 céntimos que le debo, y “ya que estamos”, por haber estado en momentos difíciles y por tener siempre una sonrisa que ofrecer. Es el turno de la estrella, del cazador sideral, el auténtico, el genuino...redoble de tambores...Jesús Corral, gracias por todo sin olvidar J 1859. Por las risas, y por el apoyo moral le debo un abrazo a “mgg”, el nuevo show televisivo que desbanca a *En clave de ja o ...* será Miriam García? No me puedo olvidar de las chicas de la resi, por dejarse “engañar” tantas noches y pasárlas conmigo en el centro de cálculo. Y la mención especial del jurado es para Davinia González, por “Y cuando creo que no puedo soportarlo más, aguanto un segundo y entonces sé que puedo soportarlo todo”, gracias por ser, por estar, por las discusiones y por aprender contigo.

Tengo que agradecer a Almudena Frias, porque a pesar del tiempo y la distancia, sigues sin dejarme sola bajo la lluvia. A Patricia Carrera, por las muffins, los tardes de lluvia en el Starbucks y porque “goby” sólo hay una. A Ane Garcés, porque al final todas os llamais igual, pero tú sigues vistiendo diferente. A Julia Redondo y Pura Campos porque cuando tengo la suerte de encontrarnos todo sigue siendo igual.

Quiero agradecer a M. Jesús Arévalo la oportunidad de tomar contacto con la docencia, y aún más por su cercanía y sus palabras de aliento. También al grupo de Astropartículas, a los doctorandos por amenizar los largos días en el IAC, a “Karsten’s jaus pipol” por hacer desaparecer el vino de mi copa y a Eva Bejarano por tener siempre una sonrisa.

Finalmente, no quiero acabar la tesis sin mencionar el I.E.S. Pintor Jose M. Fernández, por acercarme y potenciar mi interés por la astronomía.